Editorial

Foreword to the special volume on "New Approaches to Study of the Structure and Magmatism in the Eger Graben"

The Eger (or Ohře) Graben (or Rift) represents a prominent tectonic, magmatic and sedimentary feature of the post-Variscan Bohemian Massif. Even though the rocks and geological phenomena therein have been studied for over two centuries, many aspects of origin and evolution of this structure remain enigmatic. Fortunately, the methods and interpretations advanced during past few decades and the Eger Graben hosted several interesting scientific projects and detailed geological mapping. This was our motivation to invite experts to present their results in this thematic issue of the *Journal of Geosciences*.

The issue begins with contribution by **Babuška and Plomerová**, whose paper summarizes current knowledge on structure of Upper Mantle beneath the western Bohemia, where three principal Variscan units – Saxothuringian, Moldanubian and Teplá–Barrandian – all meet in a "triple point". The crust in western Bohemia remains seismically active and the area hosts the youngest (Late Pleistocene) volcanoes of the Bohemian Massif. There is evidence that the Eger Graben follows the contact of mantle lithosphere domains. The Variscan mantle boundaries played an important role in magma ascent of both Late Variscan and Cenozoic magmatic phases.

In the following paper, **Novotný et al.** present interpretation of deeper geological setting based on geophysical data from the S04 seismic profile crossing the Eger Graben near Teplice. Their geological model is also supported by gravity and aeromagnetic data. The subsurface extent of granitic and ultrabasic bodies was constrained using the geophysical data. Possible magmatic centres for Altenberg–Teplice Caldera and Cenozoic volcanic complexes are also outlined.

Detailed image of the tectonic setting in the western part of the České středohoří Mts. is presented by **Cajz and Valečka**. This paper, forming a "bridge" between known tectonic settings of the Most Basin and the central part of the České středohoří Volcanic Complex, underlines the true complexity of the tectonic network. The faults are described and classified in terms of their relative age, which is useful for further discussions on evolution of the regional stress field influencing the development of Eger Graben.

The largest at least partly preserved volcano in the Bohemian Massif is situated within the Eger Graben and its immediate neighbourhood. The geometry of the Czech part of this Late Carboniferous Altenberg–Teplice Caldera was reconstructed by **Mlčoch and Skácelová**. The model shows more prominent subsidence in the eastern part and maximum thickness of the rhyolitic ignimbrite, which fills up the caldera, in the southeastern part.

The Cenozoic magmatism and volcanism did not occur solely inside the graben. Significant volume of alkaline magmas erupted on its shoulders. The basaltic rocks on the German side of the Erzgebirge Mts. (Saxothuringian Unit) attracted **Rönick and Renno** for detailed study dealing with clinopyroxene phenocrysts. Two distinct volcanic suites (Ti-rich and Ti-poor) host seven different types of clinopyroxene phenocrysts, some of them displaying signs of magma mixing.

The presence of subvolcanic rocks in the central part of the Doupovské hory Volcanic Complex is known for over a century, but nobody has brought a detailed description of this suite yet. **Holub et al.** present petrological, geochemical and geochronological data giving the general overview of this small, but multifarious intrusive body built by two distinct suites. More alkaline, "dry" suite includes ijolitic rocks, urtite and sodalite-phyric phonolite, whereas the less alkaline, "wet" suite consists mainly of essexites, foid monzonites and foid syenites. The entire intrusive body was emplaced at *c.* 29 Ma ago.

The follow-up manuscript by **Haloda et al.** deals more in detail with crystallization history of the most primitive intrusive rocks found at Doupov. The composition of olivine cores in melteigite is in equilibrium with bulk rock chemistry at conditions near to liquidus – and thus no olivine was added as a cumulate. The development of the melteigitic magma started as equilibrium crystallization at *c.* 4 kbar, later followed by Rayleigh-type fractionation crystallization near the surface. The slightly more evolved magma of Ol-free ijolite experienced a LP fractional crystallization.

The number of maar volcanoes in the Eger Graben became reduced since the times of Kopecký, mostly due to modified interpretation. Geometry and structure of two selected maar volcanoes in northern Bohemia were studied by **Skácelová et al.** Combination of magnetic, gravity and electric conductivity measurements detected the extents of diatremes and geometry of their feeder dyke systems. Different country-rock setting (hard crystalline units *vs.* soft Cretaceous marine sediments) resulted in different geometry of the two diatremes[†].

Vladislav Rapprich[1] and Jiří Málek[2]
[1] Czech Geological Survey, Prague, Czech Republic
[2] Institute of Rock Structure and Mechanics ASCR, v.v.i., Prague, Czech Republic
[Guest Editors]

[†] Due to page limitations, this paper will appear in following issue (*Journal of Geosciences,* vol. 55, no. 4). Even though not printed here, the contribution represents an integral part of the thematic set.

Foreword

North Bohemian volcanics as lifelong love – In memory of Lubomír Kopecký

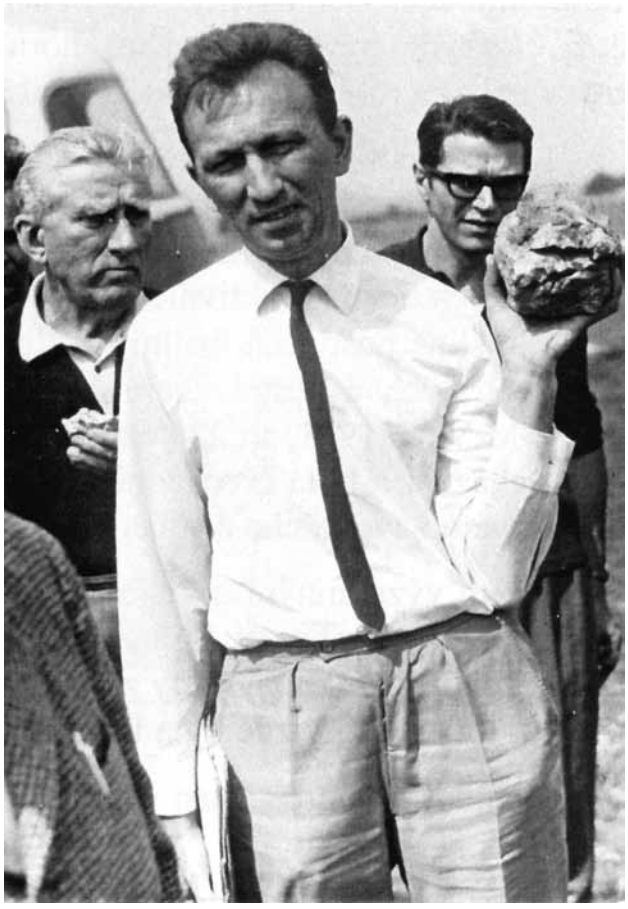

Lubomír Kopecký demonstrating marlstone xenolith from the Hnojnice diatreme in 1971 (photo reproduced from Váně 1999).

The small North Bohemian village of Oleško in the Labe-river lowland offers a ravishing view on the majestic volcanic hills of the České středohoří Mountains. Here, the outstanding geologist, petrologist and volcanologist Lubomír Kopecký was born on December 19th, 1924 and also here, on January 8th, 2010 his rich and fruitful life came to an end.

Graduating from geology at Charles University in 1949, he got employed at the State Geological Survey, to which he remained faithful till his retirement in 1991. Already as a university student he started to be professionally interested in Cenozoic alkaline volcanics, having elaborated the first complex volcanological model for the Doupovské hory Volcanic Complex and defended it successfully as his dissertation thesis. He continued the research on the Cenozoic volcanic rocks as a member of the State Geological Survey as the exclusive specialist in the country at the time. In 1964, geological maps 1 : 200 000 and explanatory booklets for the whole state territory as well as the concise monograph "Geology of Czechoslovakia" were presented to the participants of the 22nd International Geological Congress in India. All the work concerned with the Cenozoic volcanics of the Bohemian Massif was done by Kopecký on his own. Maars, diatremes, phreatic explosions, kimberlite-related pipes, volcanic role of rifting, phase development of volcanism and many other features, until then unknown in Czech geology, were discovered and introduced for North Bohemia by him. Many detailed modern geological maps of Czech volcanic areas bear the signature of his authorship and the number of his archival expert reports is enormous. Problems of the genesis of alkaline volcanics led him to the study of carbonatites about which he organized a successful international conference in Prague. He devoted much energy to establish the concept of cryptovolcanic origin of some craters both in Europe and overseas against the impact model. One of his achievements must be especially mentioned: he was the founder of a new Czech industrial branch – the petrurgy, applying melting of basaltic rocks for cast products. Uncompromising in his ideas, he always remained steady even at the cost of being a little isolated.

Admirable dynamism and untiring scientific activity characterized him till his last days and his whole life work represents the fundamental pillar of the knowledge of Bohemian Cenozoic volcanism. Kopecký's masterpiece, summarizing his almost two hundred original papers in the extensive "České středohoří Mts. and Ambient Young Alkaline Volcanic Complexes of the Ohře Rift, Czech Republic: Volcanology, Petrology and Rift Evolution" (Czech Geological Survey, 2010) unfortunately appeared in print only after his death. It is quite natural that the personality and work of Kopecký is commemorated in this thematic issue of the *Journal of Geosciences* focused on Ohře Rift (Eger Graben), in which Lubomír Kopecký spent all his scientific life.

Ferry Fediuk
Geohelp, Prague, Czech Republic

References

Váně M (1999) Geology of the Louny Area for the Third Millennium. Edited by the author, Chomutov, pp 1–476 (in Czech)

Journal of Geosciences, 55 (2010), 171–186 DOI: 10.3190/jgeosci.070

Original paper

Mantle lithosphere control of crustal tectonics and magmatism of the western Ohře (Eger) Rift

Vladislav BABUŠKA*, Jaroslava PLOMEROVÁ

Geophysical Institute, Academy of Sciences of the Czech Republic, Boční II/1401, 141 31 Prague 4, Czech Republic; babuska@ig.cas.cz
* *Corresponding author*

This paper summarizes our recent research on the relationship between tectonics of the mantle lithosphere and of the upper crust in the western Bohemian Massif. The rejuvenated Variscan junction of three mantle domains, the Saxothuringian, Moldanubian and Teplá–Barrandian, delimited by different orientation of seismic anisotropy reflecting a consistent fossil olivine orientation and belonging to originally separated microplates, plays important role in the crustal architecture of the region. The crust above the mantle junction is the most active part of the BM characterized by periodic earthquake swarms and mofettes emitting gases of mantle origin. Detected offsets of surface boundaries of the three units from their mantle counterparts indicate a detachment of the rigid upper crust from the mantle lithosphere. Locations of major tectonic features like the Ohře (Eger) Rift, the West Bohemian Shear Zone and the Mariánské Lázně Fault were probably predisposed by the boundaries of the mantle lithosphere domains. We have suggested that the sublithospheric mantle of the western BM acted as a major provider for heat and partial melts and the Variscan mantle boundaries served as magma conduits for the late-orogenic granitic magmatism and, after their rejuvenation, also for the Cenozoic volcanism. Similarly, the boundaries may have pre-determined the subsequent locations of sedimentary basins. It is possible that also in other regions some of these so called intra-plate phenomena can be related to partly healed up and later rejuvenated microplate boundaries.

List of abbreviations: BM – Bohemian Massif, BOHEMA – International project "BOhemian Massif HEterogeneity and Anisotropy", BP – Bor Pluton, CHB – Cheb Basin, DEKORP Deutsches Kontinentales Reflexionsseismisches Programm, DP – Doupovské hory Mts., DU – Dyleň Unit, ECC – Erzgebirge (Krušné hory) Crystalline Complex, ECRIS – European Cenozoic Rift System, ER – Ohře (Eger) Rift, HSU – Horní Slavkov Unit, KH – Komorní Hůrka, KHF – Krušné Hory (Erzgebirge) Fault, KU – Kladská Unit, KVP – Karlovy Vary Pluton, MD – Moldanubian Unit, MLC – Mariánské Lázně Complex, MLF – Mariánské Lázně Fault, PF – Plesná Fault, SB – Sokolov Basin, SP – Smrčiny (Fichtelgebirge) Pluton, ST – Saxothuringian Unit, T-junction – "triple" junction of the ST/TB/MD mantle lithospheres, TB – Teplá–Barrandian Unit, TCC – Teplá Crystalline Complex, TP – Tirschenreuth Pluton, WBSZ – West Bohemian Shear Zone, ZEV – Zone of Erbendorf–Vohenstrauss, ZH – Železná Hůrka, ŽP – Žandov (also Lesný–Lysina or Kynžvart) Pluton.

Keywords: mantle lithosphere domains, seismic anisotropy, Ohře (Eger) Rift, mantle sutures, control of crust architecture
Received: 7 April 2010; accepted: 8 September 2010; handling editor: J. Málek

1. Introduction

The area of our study – the western Ohře (Eger) Rift (ER) – is a part of the European Cenozoic Rift System (ECRIS, Prodehl et al. 1995). This system of graben structures and volcanic fields spreads over a distance of about 1000 km, including the French Massif Central, the Upper Rhine Graben, the Eifel, the North Hessian Depression, the Vogelsberg, the Ohře (Eger) Rift and the Pannonian Basin. The widespread rifting and associated volcanism in the foreland of the Alpine orogen is usually related to the effects of Alpine collision (e.g. Ziegler 1992). On the other hand, Granet et al. (1995) suggested that the ECRIS may have a common source of a 'plume-like' volcanism in the mantle, manifested by the existence of 'baby-plumes' beneath the Variscan massifs. Teleseismic tomography studies have imaged such relatively narrow plumes beneath the French Massif Central (Granet et al. 1995) and the Eifel (Ritter et al. 2001).

From the point of geodynamics, the western ER is the most active part of the Bohemian Massif (BM). Active tectonics is primarily manifested by Cenozoic volcanism (Ulrych et al. 2000), gas emanations containing high proportions of mantle-derived CO_2 and He (Weinlich et al. 1999), as well as by the periodic occurrence of shallow earthquake swarms (Horálek and Fischer 2008) and neotectonic crustal movements (Bankwitz et al. 2003; Schunk et al. 2005). The question of a possible source of mantle fluids is important namely in relation to the recent increase of $^3He/^4He$ ratios observed by Bräuer et al. (2005). The authors interpreted the observation as an evidence for ascending mantle-derived melt and as an indication of a possible future unrest in this presently inactive volcanic region.

The concentration of various ongoing geodynamic phenomena in a small area of the western ER called for a study focused on the interaction between near-surface tectonics and geodynamic processes at depth. Geoscientists from 10 institutions in the Czech Republic, Germany and France cooperated within the BOHEMA project (BOhemian Massif HEterogeneity and Anisotropy, Babuška et al. 2003) to study the structure and dynamics of the lithosphere and asthenosphere of the western BM. Central to the BOHEMA project was a passive seismic experiment in 2001–2003, which provided important set of data for the high-resolution teleseismic tomography down to a depth of about 250 km and for a model of large-scale seismic anisotropy of the mantle lithosphere in the western BM (Plomerová et al. 2007; Babuška et al. 2008).

This paper summarizes major results on fabrics of the mantle lithosphere retrieved up to now from passive seismic experiment of the BOHEMA international project (Babuška et al. 2003). We have focused on the western ER above the junction of three mantle lithospheres, the Saxothuringian (ST), Moldanubian (MD) and the Teplá–Barrandian (TB) units, delimited by mapping their seismic anisotropy at the dense BOHEMA network of temporary stations (Plomerová et al. 2007; Babuška et al. 2008). Tectonics of the mantle lithosphere most probably predisposed formation of the western ER, affected paths for late Variscan and Cenozoic magmatism as well as the location of sedimentary basins. We coin the idea that it is important to look beneath the Moho discontinuity when we want to understand geodynamic processes recorded in tectonics and in magmatic products of the complex crustal structure. The paper does not have ambitions to solve a complicated tectonic development of the region and it does not present details of geophysical methods used to infer structure of the mantle lithosphere published elsewhere (see references to individual results). The paper aims at providing a review of seismological results on deep lithosphere structure of the region to contribute to a holistic view and better understanding of the coupling between tectonic processes near the surface and deep-seated dynamics of the mantle lithosphere. Such approach is important for developing future models, which will realistically consider the entire lithosphere in tectonic history of the complex Variscan collision zone.

2. Mantle investigations of the western Bohemian Massif by teleseismic methods

Most of constrains on the upper mantle structure of the western BM come from teleseismic body waves travelling through the entire Earth and recorded at dense networks of stations in the region. Changes in seismic wave velocities, both with depth as well as laterally, are retrieved from deviations of the travel times of longitudinal P waves and from polarization of shear-waves. Deviations in seismic wave propagation relative to a radial Earth velocity reference model are exploited in seismic tomography resulting in isotropic images of the Earth interior. We also model a large-scale anisotropy (fabric) of the upper mantle by analysing directional variations of the P-wave travel times and polarization of shear waves (shear-wave splitting).

2.1. Seismic tomography

Plomerová et al. (2007) presented initial tomographic model of the upper mantle beneath the whole BM down to 250 km, with variance improvement of 71 % and the highest resolution in the western part of the massif. For this paper we selected velocity perturbations in three layers of the model comprising the mantle lithosphere beneath the BM along with two perpendicular vertical cross-sections (Fig. 1). Depth of the model depends on lateral size of the array of seismic stations and the resolution depends on a density of crossing rays within the investigated volume. Therefore, not only a sufficient amount of data, but also a good azimuthal and incidence angle coverage is needed. Data for the tomography (P-wave arrival times) were measured on the BOHEMA network recordings of more than 240 teleseismic earthquakes, which provided 13 500 rays for the tomographic inversion, with a lateral resolution of about 20 km in the upper mantle.

The sufficient lateral resolution allowed searching for a hypothetical narrow (~ 50 km in diameter) and vertical low-velocity anomaly beneath the ER, which would be similar to plumes found beneath the other Variscan massifs – the French Massif Central and the Eifel (Granet et al. 1995; Ritter et al. 2001). In general, velocity perturbations in the tomographic images (Fig. 1) are weak and correlate with large-scale tectonic features. But they did not image any distinct low-velocity heterogeneity down to 250 km, which could be interpreted as a magma chamber or a mantle plume. There are weak negative perturbations in the mantle beneath the western part of the ER, which can be traced down to the bottom of the model. But they do not form any tube-like low-velocity heterogeneity, which could be associated with a narrow uprising plume below the rift at these depths. Moreover, this tomography, which is corrected for crustal effects, shows such well-resolved negative perturbations of comparable amplitudes also in other parts of the model (Fig. 1) though their resolution may be lower due to a lower number of stations. However, incorporating the stations in the eastern and southern BM is important for resolving the mantle down to 250 km below the ER. We interpret the negative perturbations in the western BM by

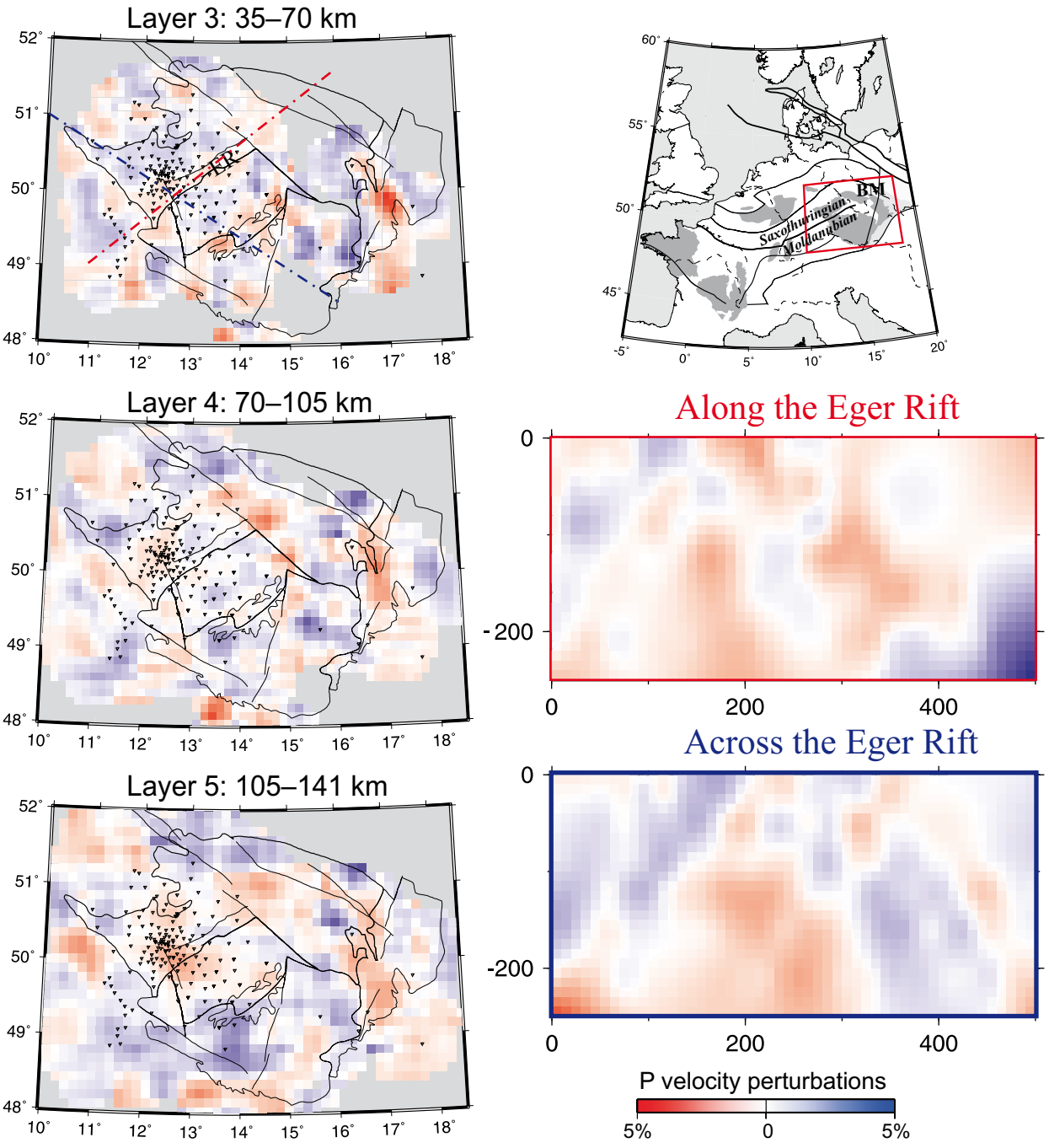

Fig. 1 Plane views of tomographic images of smoothed P-velocity perturbations in the lithosphere–asthenosphere system of the Bohemian Massif (BM) selected for three deep layers (left) from Plomerová et al. (2007) and projections of the seismic stations (triangles). Two vertical cross-sections (see Layer 3 for their location) through the velocity perturbation model (right) along and across the Ohře (Eger) Rift (ER) indicate the lithosphere thinning beneath the rift. Major Variscan massifs in central–western Europe are shaded (top right).

a lithosphere thinning along the whole ER and the positive perturbations in the southern BM by a lithosphere thickening to the south beneath the Moldanubian Unit.

To show velocity variations related to the ER, Plomerová et al. (2007) constructed two cross-sections through the velocity perturbation model – along and across the rift (Fig. 1). The low-velocity perturbations form a broader, ridge-parallel anomaly, which can be interpreted as an asthenosphere updoming (a lithosphere thinning), mapped there also, for instance by Babuška and Plomerová (2001) and derived by Heuer (2006) and Geissler et al. (2010) from receiver function studies.

2.2. Mapping of seismic anisotropy

Seismic anisotropy provides key information to our understanding of tectonic fabric of the lithosphere–asthenosphere system (Babuška and Cara 1991). Thanks to systematic preferred orientation of olivine crystals and their elastic anisotropy, the mantle lithosphere exhibits a consistent large-scale seismic anisotropy of domains in dimensions of several hundred kilometres (Babuška and Plomerová 2006, for review) observed in directional variations of longitudinal-wave velocities and in shear-wave splitting. Teleseismic shear-wave splitting, the analogy of the light birefringence, is generally considered as a proof of the upper mantle anisotropy, and represents the most common method to study the seismic anisotropy (see, e.g., Savage 1999, for review). The presence of seismic anisotropy, as an almost ubiquitous property of the mantle, is now documented by extensive sets of data from temporary arrays of seismic stations covering a large variety of tectonic settings. We use two methods to evaluate anisotropic parameters of body waves. Directional variations of the parameters we then invert to retrieve 3D anisotropic self-consistent models of the mantle lithosphere (Šílený and Plomerová 1996).

If seismic waves propagate through anisotropic media (Fig. 2), we record early arrivals (negative residuals) for waves propagating in high-velocity directions and delayed arrivals (positive residuals) for waves propagating in low-velocity directions. To show the spatial variations of relative P velocities and to study the P-velocity anisotropy, we construct for each station a P-residual sphere showing azimuth-incidence angle dependent terms (directional terms) of relative residuals in a lower hemisphere projection. All the calculations are related to a velocity mean – a directional mean which represents an isotropic velocity in the volume beneath a station**.** As the directional mean forms a reference level in each sphere, the P spheres can be compared easily, regardless of differences in the lithosphere thickness, which is the dominant high-velocity heterogeneity in the uppermost mantle and affects the station means. To reduce effects due to sediments and variable crustal thickness and velocities, we apply crustal corrections derived from results of deep seismic soundings and receiver function analysis in the first step of calculations, i.e., in computing the absolute P residuals as differences between the observed travel time and the travel time calculated according to a reference radial Earth model. We have used the IASP91 Earth model (Kennett 1991). For details of the method we refer to, e.g., Babuška and Plomerová (1992).

Similarly to other regions, also in the BM we often observe the so-called 'bipolar' pattern of the P spheres, where negative directional terms consistently prevail in one half of the hemisphere, while positive ones dominate in the other half. Relating the early and delayed arrivals with the high- and low-velocity directions, we interpret such bipolar pattern in the P spheres as a result of propagation through a dipping olivine fabric of the mantle lithosphere and model them by peridotite aggregates with dipping foliations (b-axis models) or lineation (a-axis models; for details see Babuška et al. 2008).

The P-sphere patterns can be affected to some extent by a presence of crustal anisotropy and by a trade-off between the anisotropy and velocity heterogeneities. The trade-off makes it difficult to separate out the respective contributions and we can rely only on indirect indications. Sources of seismic anisotropy in the crust (cracks, bedding/lamination of sediments, foliation of metamorphic rocks) differ from the upper mantle anisotropy, caused mainly by a large-scale olivine preferred orientation in large volumes of relatively homogeneous fabrics. Small-size (relative to seismic wavelengths) varying anisotropy in the crust behaves as a heterogeneous volume and, similarly to non-compensated small-size crustal heterogeneities (e.g., due to a varying density of rock complexes), can appear as localized singular distortion in otherwise smooth pattern of the P spheres. The smooth and consistent pattern of seismic anisotropy can extend laterally up to several hundreds kilometres. Its change is often linked with prominent tectonic sutures or dominant faults cutting the whole lithosphere (Babuška and Plomerová 2006). Different P-sphere patterns on both sides of a suture often turns to "no P pattern" right above a suture, as the waves sample both differently oriented fabrics. It would be difficult to explain sudden changes of the P-sphere pattern associated with prominent tectonic boundaries by velocity heterogeneities in the deep mantle. Such characteristics of the P spheres described above, along with geographical and back-azimuth variations of the shear-wave splitting, allow us to associate the directional velocity variations with seismic anisotropy of the mantle lithosphere.

Two shear waves propagate within an isotropic medium with identical velocity and no preferred polarization. When entering an anisotropic medium, such waves separate (split) into the fast and slow waves with polarizations in mutually perpendicular planes. Shear-wave splitting parameters – fast shear (S) wave polarization and delay time (δt) of the slow S wave – reflect a strength, symmetry and axes orientation of the anisotropic medium. By analyzing lateral and azimuthal variations of the splitting parameters and by inverting these variations, jointly with P anisotropic parameters, we can model a lithosphere fabric. Joint inversion/interpretation of independent data (e.g., deviations in travel times, shear-wave splitting, surface-wave dispersions, receiver functions) reduces a set of potential models which could explain the observations and thus favour more realistic solutions (Fouch and Rondenay 2006; Vecsey et al. 2008).

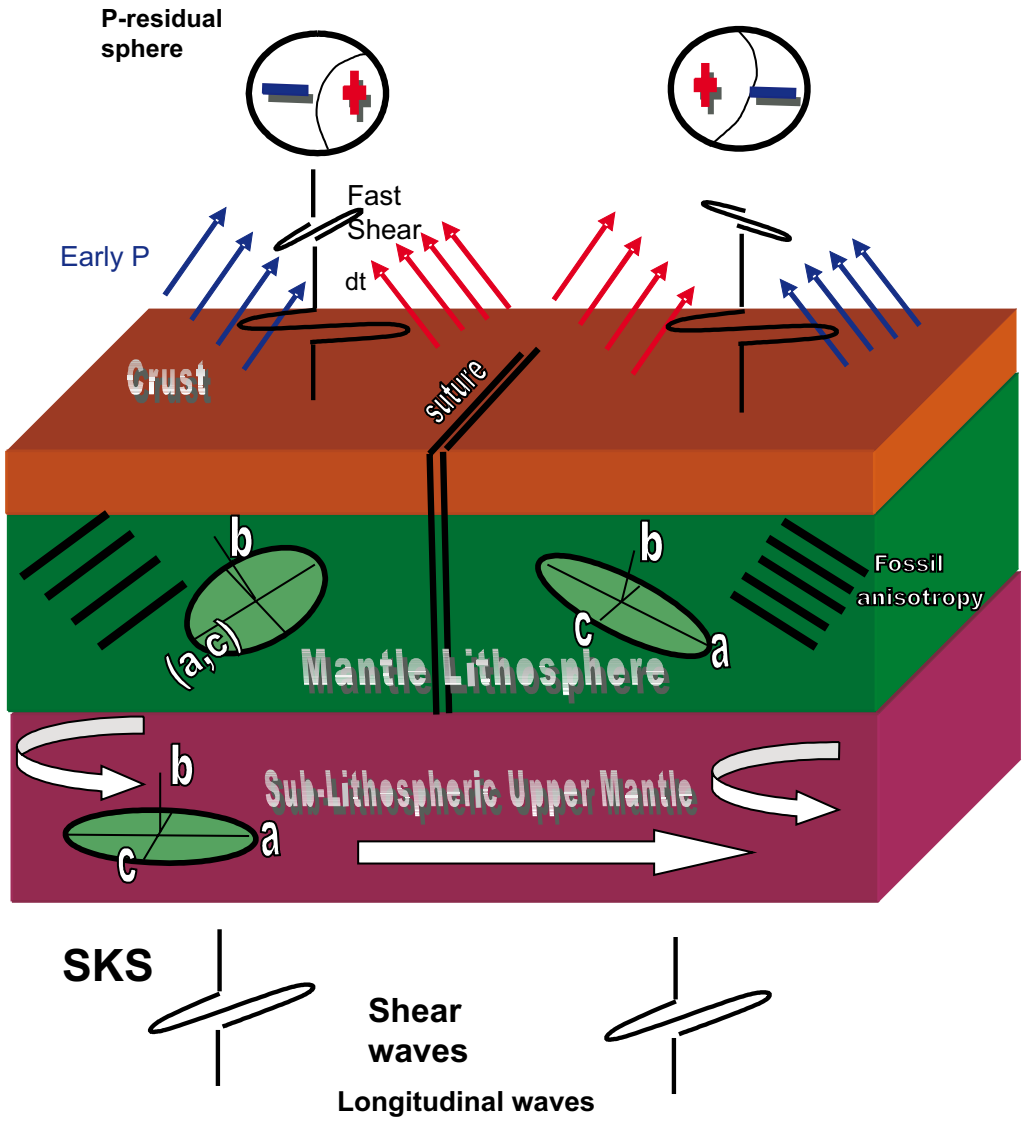

Fig. 2 Schematic block-diagram showing principles of the 3D modelling of seismic anisotropy from a directional dependence of relative residuals of longitudinal (P) waves and from shear-wave (SKS) splitting. Both types of waves arrive at seismic stations from teleseismic distances. Seismic anisotropy in the asthenosphere can be related to systematic orientation of olivine due to a slow sub-horizontal flow. Two domains of the mantle lithosphere, separated by a suture cutting the entire lithosphere, are characterized by differently oriented anisotropic fabrics approximated by olivine aggregates of hexagonal (left, *(a,c)* is the plane of high P velocities), or orthorhombic symmetry (right, axis *a* is the high-velocity direction). Strength of velocity anisotropy is derived from the fabric of peridotite xenoliths (see, e.g., Ben Ismail and Mainprice 1998). The anisotropy orientation and its symmetry are modelled by a joint inversion of body-wave anisotropic parameters. The diagrams above schematically show anisotropic parts of P residuals in a lower-hemisphere projection. Relative high-velocity directions (blue arrows) project as early P arrivals (negative residuals, blue) and relative low-velocity directions (red arrows) as delayed P-arrivals (positive residuals, red). The P residual is a difference between aa observed travel time and a theoretical travel time calculated for a standard radial Earth model.

Babuška et al. (2008) analysed splitting of shear-waves on recordings of about 130 earthquakes with magnitude larger than 5.6 at epicentral distances larger than 85° with respect to the centre of the BOHEMA array. The selected waveforms have a large signal/noise ratio and well separated shear phases. The shear-wave splitting was evaluated with code SPLIT (Vecsey et al., 2008) based on a 3D approach by Šílený and Plomerová (1996). Shear-wave splitting analysis detected only small but systematic changes of the prevailingly E–W fast split polarizations over the whole western BM with average delay times of 1.2 s (Fig. 3). On the other hand, the P-velocity anisotropy has recognized three distinctly different orientations of fabrics in the mantle lithosphere of the three tectonic units – the Saxothuringian (ST), Moldanubian (MD) and Teplá–Barrandian (TB) (Plomerová et al. 2007). The ST pattern

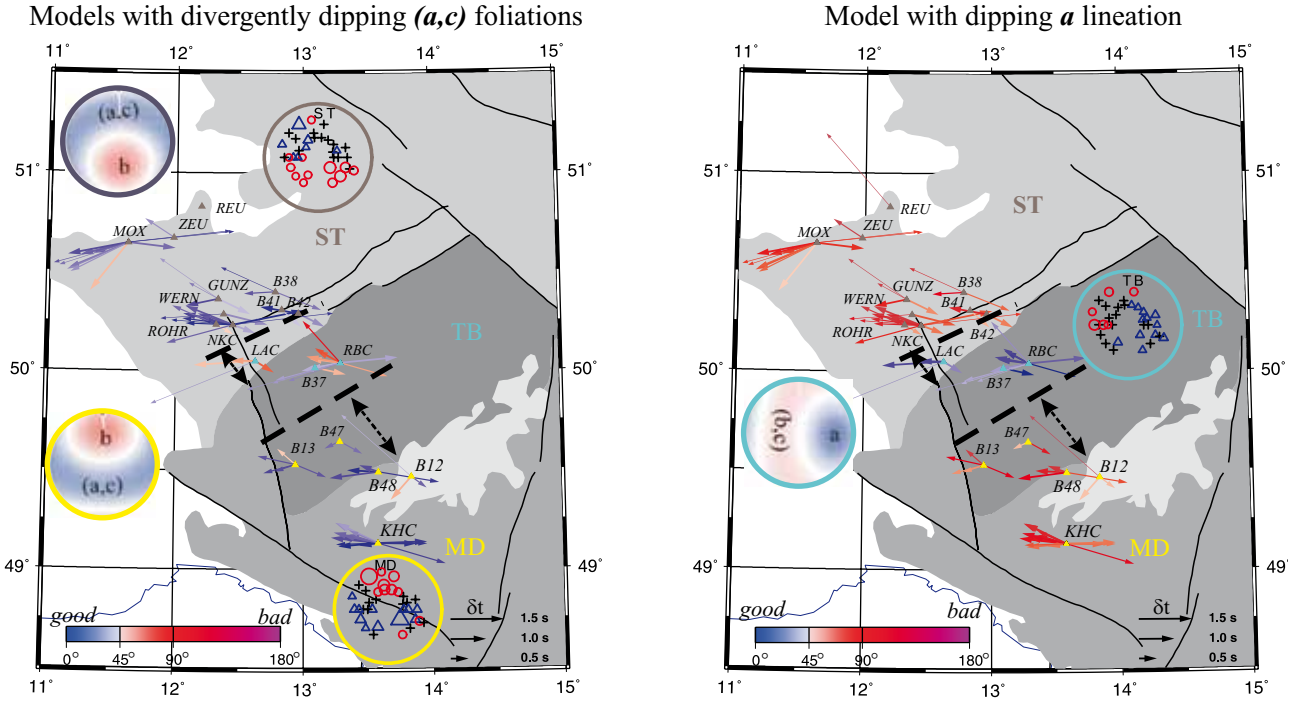

Fig. 3 Conformity of the observed and synthetic shear-wave splitting calculated for the aggregates represented by velocities in the lower hemisphere projection and by the symmetry axes. Orientations of the aggregates were retrieved by inversions of the P-residual spheres (the spheres with symbols, where red circles – positive terms of the relative residuals – mark the low-velocity directions of wave propagation and blue triangles – negative terms – stand for the high-velocity directions of propagation relative to a velocity mean. Black crosses mark directions with residual terms close to zero, in interval (–0.1s, 0.1s). The conformity is expressed as a difference between the observed and synthetic fast shear-wave polarization azimuths. The observed fast shear-wave azimuths Φ and split delay times δt (thick arrows – good evaluations, thin arrows – fair evaluations), coloured according to the conformity, are shown for the broad-band stations (for details see Babuška et al. 2008). The orientations of the hexagonal *b*-axis model (left) explain well directional variations of the splitting within the Saxothuringian (ST) and Moldanubian (MD), while this symmetry fails to explain the splitting at stations located above the Teplá–Barrandian (TB) mantle lithosphere. On the other hand, the hexagonal *a*-axis model (right) fits the polarizations at the three TB stations, while it fails to model the observations at stations in the ST and MD. The dashed lines approximate the TB mantle domain boundaries, which are north-westerly shifted (dashed double arrows) relative to the crustal boundaries of the units and indicate a possible thrusting of the MD mantle lithosphere beneath the south-eastern rim of the TB.

exhibits the negative residuals for northern propagation directions, the MD pattern is characterized by negative residuals (relatively high-velocity directions) for southern propagation, and the TB pattern by negative residuals for waves arriving from NE–SE (Fig. 3). We have modelled fabrics of the mantle lithosphere of the three units by peridotite aggregates of hexagonal symmetry with easterly dipping lineations *a* (TB) and divergently dipping foliations (*a,c*) (to the N–NW in the ST, to the S–SW in the MD). Such self-consistent 3D anisotropic models result from inversion and joint interpretation of the P residual spheres and shear-wave splitting synthetics. The resolved fabrics are compatible for the two independent datasets of anisotropic parameters (Babuška et al. 2008).

3. Tectonic predisposition of the Ohře (Eger) Rift

During the Variscan orogeny the lithosphere of the BM was assembled by collisions of independent blocks (e.g., Franke 2006), which apparently retained in the mantle lithosphere their olivine fabric that predated incorporation of these microplates into the Variscan Orogen (Babuška and Plomerová 2006). Moreover, during the post-orogenic re-equilibration of the lithosphere/asthenosphere system, the mantle lithosphere was not significantly thinned and thus preserved its olivine fabric. This is compatible with limited Mesozoic subsidence of the BM.

Most papers dealing with the process of rifting accept that tectonic forces are insufficient to disrupt continental lithosphere, unless the lithosphere has been weakened prior to rifting (e.g., Bailey and Wooley 1999). Also the essentially Miocene ER is superimposed on the Variscan suture zone between the ST in the north and the TB/MD in the south. This suture has been identified on the basis of both geological (Jindřich 1971; Kopecký 1978; Franke et al. 1995; Zulauf et al. 2002) and geophysical (Krawczyk et al. 2000; Švancara et al. 2000; Šrámek 2001) data. The very complex crustal structure beneath the westernmost part of the graben structure of the ER is reflected in a large variability of interpretations and

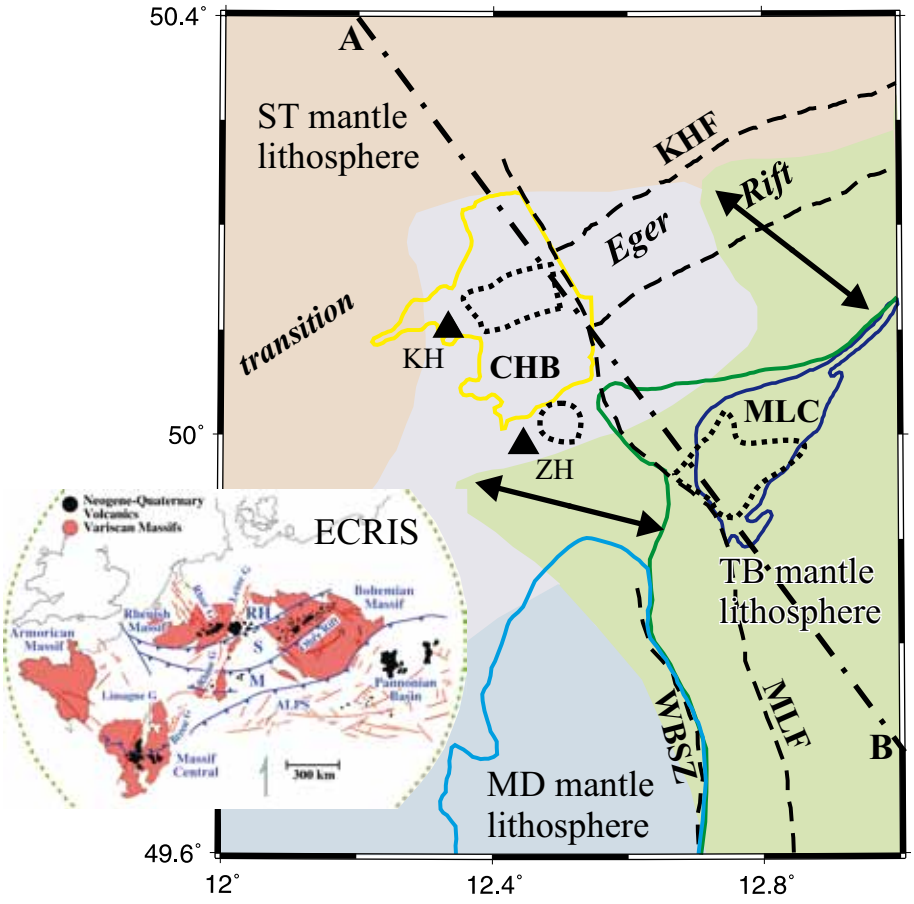

Fig. 4 Three mantle lithosphere domains defined by different orientation of seismic anisotropy and their transition (colour provinces), along with the contours of the crystalline basement of the Saxothuringian (ST), Moldanubian (MD) and Teplá–Barrandian (TB) tectonic units. Profile A–B locates the cross-section in Fig. 5. The inset of the European Cenozoic Rift System (ECRIS) is from Prodehl et al. (1995). For additional abbreviations see caption to Fig. 6.

in changes of Moho depths which vary (depending on the used method due to their different sensitivity on various physical parameters) from *c.* 27 km beneath the CHB (Geissler et al. 2005; Heuer 2006) to *c.* 33 km (Hrubcová et al. 2005), or even 35 km in the near surroundings (Grad et al. 2008). To explain the complexity of the crust, already Tomek et al. (1997) suggested on the basis of the 9HR deep seismic reflection profile that the middle and lower crust of the Saxothuringian Terrane is thrust beneath the TB crust. Positions of the boundaries of the ST, TB and MD units mapped on the surface and their upper-mantle equivalents, as identified by different directional dependences of P-wave velocities (Fig. 4) indicate a detachment of the rigid upper crust from the lower crust and the mantle lithosphere (Plomerová et al. 2007) and a very complicated geometry of the boundaries of the units (Babuška and Plomerová 2008).

Occurrences of Cenozoic sediments and volcanics in Bavaria (e.g., Kämpf et al. 2005) clearly indicate a

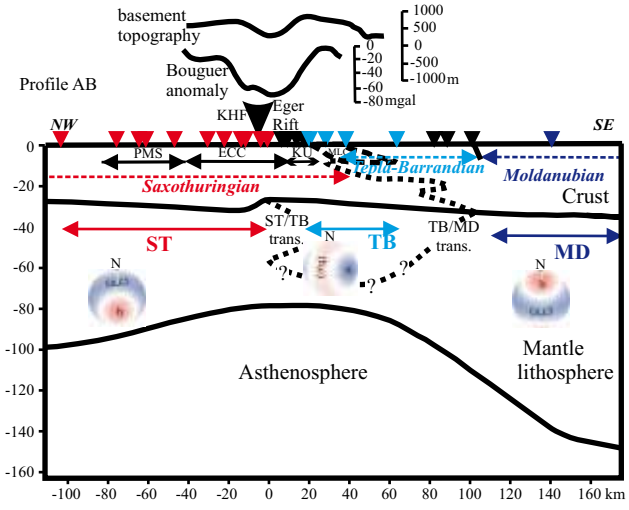

Fig. 5 Lithosphere cross-section along Profile A–B (see Figs 4 and 6 for location) showing three mantle lithosphere fabrics derived from seismic anisotropy. Anisotropic structure of the mantle lithospheres (Plomerová et al. 1998; Babuška et al. 2008) is approximated by peridotite aggregates with strength of P anisotropy ~ 6 % and with the high-velocity *a* axis dipping to the E (in the TB), or with the high-velocity *(a,c)* foliation plane dipping to the NNW (in the ST), or to the S (in the MD). The velocity distribution is presented in polar projections of the lower hemisphere, blue – high velocity directions (max. v_p = 8.6 km/s), red – low velocity directions (min. v_p = 7.8 km/s). KHF – Krušné Hory Fault, PMS – Paleozoic Metasediments, ECC – Erzgebirge Crystalline Complex, KU – Kladská Unit, MLC – Mariánské Lázně Complex. Underthrusting of the ST crust is according to Tomek et al. (1997) and the Bouguer anomalies are after Šrámek (2001).

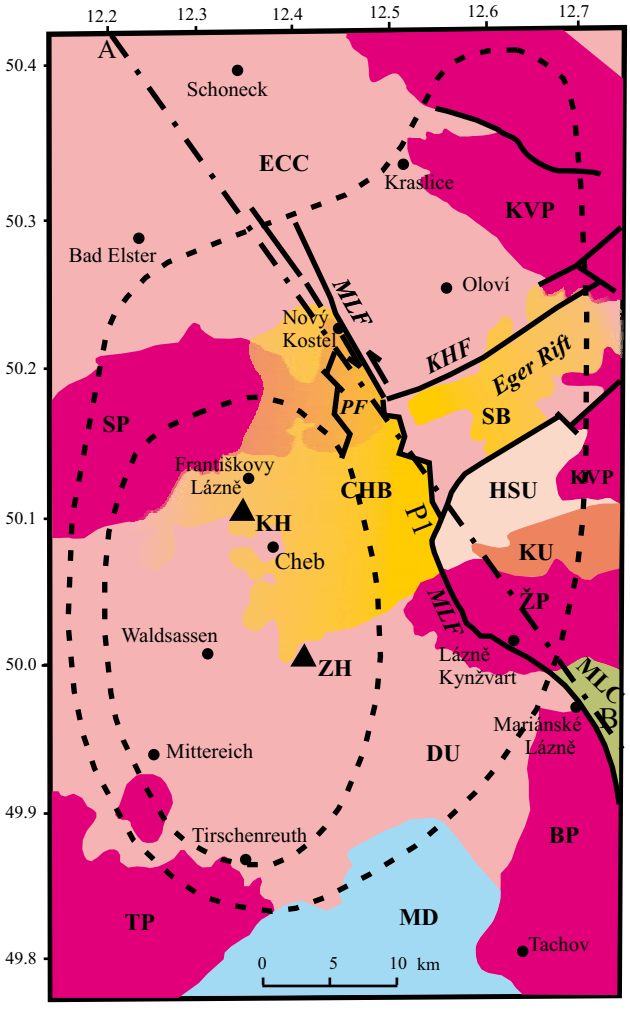

Fig. 6 Geological map of the ST–TB–MD junction simplified from Kachlík (1997), Zulauf et al. (2002), Mlčoch (2003) and Schunk et al. (2005). *Saxothuringian*: ECC – Erzgebirge (Krušné hory) Crystalline Complex, DU – Dyleň Unit, HSU – Horní Slavkov Unit, KU – Kladská Unit; *Teplá-Barrandian*: MLC – Mariánské Lázně Complex; MD – *Moldanubian*. Variscan granitoids: SP – Smrčiny (Fichtlgebirge) Pluton, KVP – Karlovy Vary Pluton, ŽP – Žandov Pluton, BP – Bor Pluton, TP – Tirschenreuth Pluton. CHB – Cheb Basin, SB – Sokolov Basin. KHF – Krušné Hory Fault, MLF – Mariánské Lázně Fault, PF – Plesná Fault (Schunk et al. 2005). Quaternary volcanoes: KH – Komorní hůrka and ZH – Železná hůrka. The dashed contours show the crust thinning to less than 30 km (outer curve) and to 28 km (inner curve) beneath the Cheb Basin (Heuer 2006).

continuation of the ER to the south-west, where the rift signatures developed above the ST/MD contact, but without a significant Ohře graben-like structure on the surface. Babuška et al. (2010) suggested that, unlike the sharp contact of the ST and TB mantle lithospheres east of the CHB, the ST/MD mantle junction in NE Bavaria is a complex transition of both units extending to about 150 km toward the south from their surface boundary (Babuška and Plomerová 2001). Though the ST/MD contact is also marked by lithosphere thinning (Plomerová et al. 1998), similar to that beneath the ER proper east of the CHB (Fig. 1), the asymmetric graben morphology (e.g., Grygar et al. 2006) did not develop above the broad slanting contact of both units.

A model lithosphere section perpendicular to the western ER shows the observations of lateral changes of the anisotropy patterns, together with major geological features and changes in the surface topography and Bouguer gravity anomalies (Fig. 4). In the regional gravity field, the ST/TB suture is characterized by a strong gradient between the distinctly negative gravity field of the ST and only slightly negative or even positive gravity field of the TB (Plaumann and Švancara 1996). The contact of both units is marked by a chain of local positive gravity anomalies, which start from the MLC and continue to the NE (Šrámek 2001). The crustal structure (Fig. 6) reflects the abrupt change of the mantle fabrics. The area of the TB adjacent to the suture represents a Variscan inclined crustal section (Zulauf et al. 1997). During the Early Viséan (~340 Ma), a significant vertical uplift of more than 10 km in the NW segment resulted in the juxtaposition of upper-crustal rocks of the TB unit against lower-crustal rocks of the Ohře Crystalline Complex (Zulauf et al. 2002).

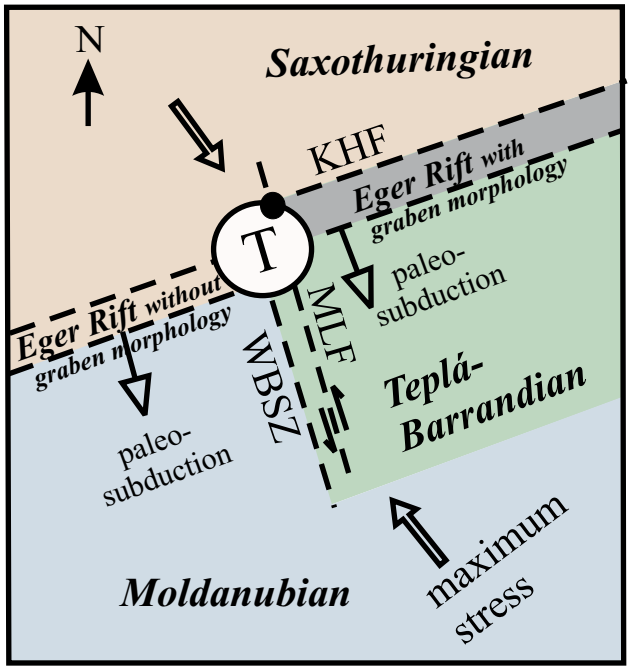

Fig. 7 Tectonic sketch showing a present-day situation of the "T (triple) junction" of the mantle lithosphere domains representing most probably remnants of three microplates assembled during the Variscan orogeny. From the point of geodynamics the junction at the northwest tip of the Teplá–Barrandian microplate is the most active part of the Bohemian Massif with the Nový Kostel swarm area marked by the black dot (see also Fig. 8). Stress orientation in the uppermost crust is according to Müller et al. (1992). For abbreviations see caption to Fig. 6.

Divergently dipping fabrics of the ST and MD mantle lithospheres were recognized throughout the whole BOHEMA array (Plomerová et al. 2007) and also modelled in the westernmost rim of the BM in Bavaria (Plomerová et al. 1998), where both units juxtapose each other. The most prominent feature of the lithosphere section is the location of the CHB and the western ER above the transition between the ST and TB mantle lithospheres. The "mantle triple junction" has a shape of capital T, with the ST mantle lithosphere to the north and the mantle lithospheres of the MD and TB units to the south-west and south-east from their mantle boundary (WBSZ, Fig. 7) projected into the MLF–KHF intersection on the surface.

4. Discussion

4.1. Mantle control of the Saxothuringian–Teplá-Barrandian microplate boundary deformation

Our previous results (Plomerová et al. 2005, 2007; Babuška et al. 2008) proved that the TB unit has its own mantle lithosphere though its thickness is probably smaller than that of the ST and MD units. A model of juxtaposition of the three domains of mantle lithosphere, each bearing a consistent fossil olivine fabric, is shown in a schematic block-diagram in Fig. 8. The TB, the best preserved fragment of the Cadomian orogen in central Europe (Franke 2000), probably played a key role in the plate-tectonic development of the region as a median massif between the ST and MD units intervening during the Variscan orogeny from opposite sides (Franke 2006). The mantle boundary between the TB and the ST, and its crustal equivalent rimmed with mantle rocks (Mlčoch 2001), represent a Variscan suture later copied by the ER. Previously Kopecký (1986) suggested that the ER developed by Alpine remobilization of an older heterogeneity in the deep crystalline basement. We also showed that the late Variscan mantle transition between the ST and TB units is characterized by a lithosphere thinning to ~80–90 km (Plomerová et al. 1998; Babuška and Plomerová 2001). However, the crystalline basement of the western ER belongs to the ST unit (Tomek et al. 1997; Mlčoch 2003; Mlčoch and Konopásek 2010), which is in allochtonous position above this mantle transition.

It is generally accepted that after a complete subduction of the ST oceanic lithosphere, the process continued by a continental collision accompanied by subduction and a subsequent exhumation at the north-western margin of the TB unit (Babuška et al. 2010). The MLC and its equivalent beneath the Doupovské hory Mts. (Mlčoch 2003), both being thrust over the ST crust, indicate a collision of the two plates with a complicated shape of their margins. Both high-grade metamorphic complexes represent a mixture of *c.* 540 Ma oceanic rocks juxtaposed at depth with lower-crustal rocks of the structurally overlying TB unit (Tomek et al. 1997; Timmermann et al. 2004). We can speculate that the subducting ST microplate was colder and stronger than the overriding TB plate, which was tilted to the SE exposing deeper crustal levels at the ST/TB collision zone (Zulauf et al. 1997). However, in both plates rigid parts of the crust were detached from the mantle, which was probably "welded" in 'crocodile-type' intercalations of both mantle lithospheres.

There are at least three observations indicating the crust/mantle detachment in the western ER. First, it is documented by ~25 km shift between the ST/TB boundary mapped on the crystalline surface and its mantle counterpart (Plomerová et al. 2007 and Fig. 4). It is interesting to note that Kachlík (1997) estimated a thrust movement of the MLC over the Kladská Unit (KU, Fig. 6) for at least 25 km. The second indication is in the crustal section derived from the 9HR refraction profile (Tomek et al. 1997; Švancara and Chlupáčová 1997, also Fig. 8), where the ST crust is thrust beneath the TB crust to a distance of about 100 km, southward of the northern rim of the MLC. Third, detachments of rigid pieces of the upper crust are also reflected in the thin-skinned tectonics documented by the Zone of Erbendorf–Vohenstrauss (ZEV). Tectonic, petrological and geochronological features of the ZEV are directly comparable with those of the TB unit (O'Brien 1997) situated about 50 km eastward.

Laminated lower crust revealed by refraction/reflection profiling in the western BM, and mostly in its ST part (DEKORP Research Group 1994; Hrubcová et al. 2005), supports such detachment along a ductile zone in the lower crust, observed also in several west European regions (Müller et al. 1997). The latter authors suggest that a weak constant shear stress develops in the lower crust due to a differential velocity of the motion between the brittle upper crust and the mantle lithosphere. The model of the crust, which was decoupled from the mantle, implies to some extent an independent tectonics of both parts of the present-day lithosphere of the western BM. On the other hand, the present geodynamic activity indicates that both layers intimately link via reactivated Variscan boundaries.

The periodic occurrence of earthquake swarms (Horálek and Fischer 2008) and neotectonic crustal movements (Bankwitz et al. 2003; Schunk et al. 2005) indicate that the crust deformation continues even nowadays. It is interesting to note that almost all earthquakes in the western BM occur within the ST crust (Figs 6 and 8) and are located within a small focal area near Nový Kostel (Babuška et al. 2007). About 90 % of seismic energy estimated for a period 1991–1999 by Horálek et al.

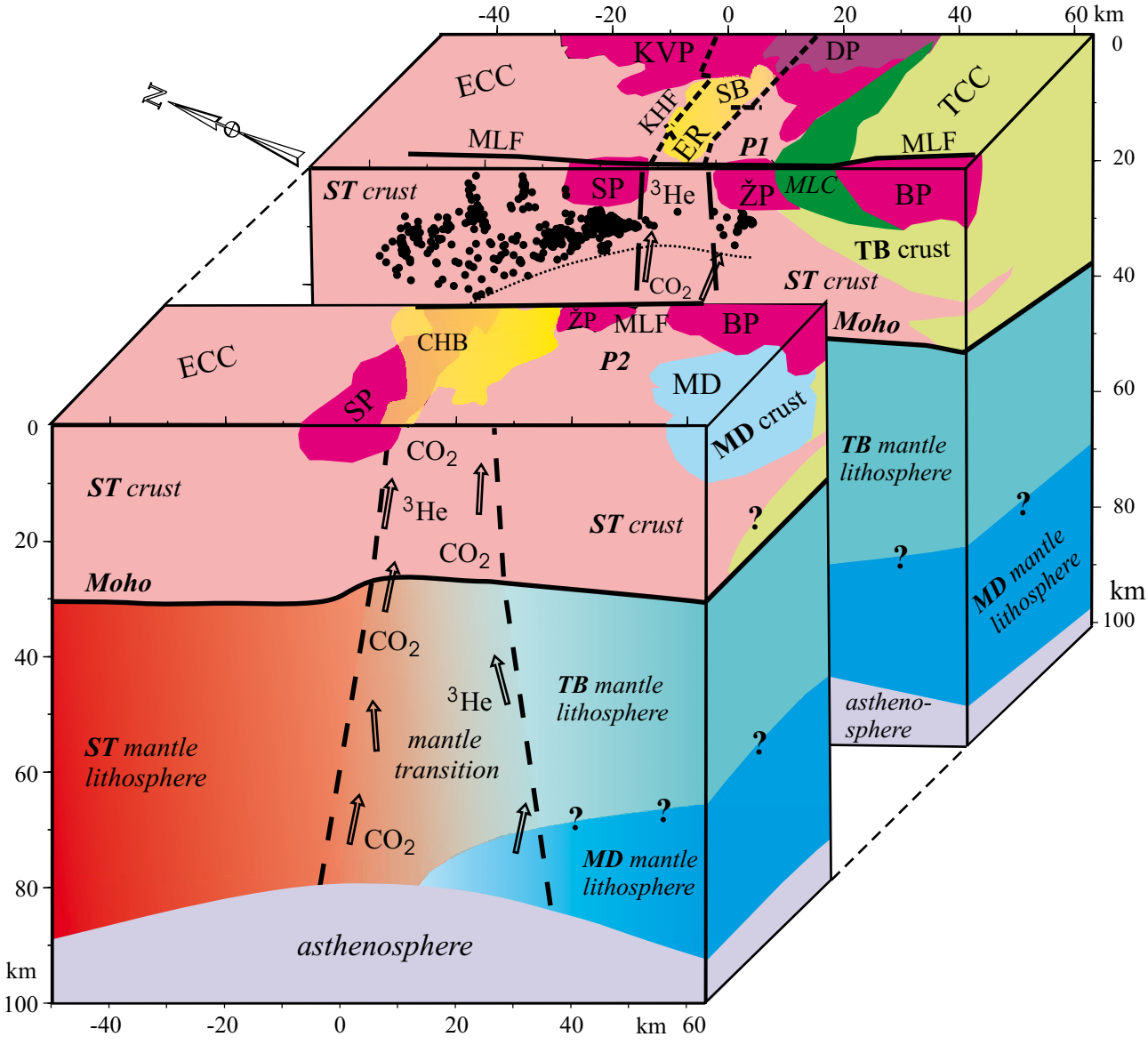

Fig. 8 Schematic cartoon showing the near surface geology (see Fig. 6 for explanation of symbols) and deep tectonics of the western Bohemian Massif. Model structure of the mantle lithosphere is based on observations of seismic anisotropy (Plomerová et al. 2007; Babuška et al. 2008). The lateral transition in the mantle indicates the boundary zone between the Saxothuringian (ST) and Teplá–Barrandian (TB) mantle lithospheres. Thicknesses and shapes of the MLC, SP and ŽP are according to Tomek et al. (1997), Hecht et al. (1997) and Blecha et al. (2009). Black dots are earthquake foci according to Fischer and Horálek (2003), the brittle-ductile transition in the crust (the dashed curve) follows the deepest foci of the earthquake swarms. Note that the earthquake foci are located mainly in the Ohře (Eger) Rift flanks and only in the ST crust, which is thrust over the ST/TB mantle transition and under the TB crust.

(2000) for the whole seismically active part of the Vogtland/western BM was released in the Nový Kostel area situated above the ST/TB mantle transition (Fig. 6), near the crossing of the KHF and the MLF. These faults represent the crustal expression of the ST/TB mantle suture and the NNW oriented MD/TB mantle boundary (Fig. 4). The long-term crustal deformation of the area is also indicated by a higher metamorphic grade of the block situated eastward of Nový Kostel (uplifted by at least 1 km, J. Fiala, pers. comm. 2005). Similarly, major emanations of mantle-derived fluids (CO_2 and helium, Bräuer et al. 2005; Babuška and Plomerová 2008) concentrate within the CHB situated above the mantle T-junction (Fig. 7). Therefore, we can assume that the mantle boundaries of the microplates, assembled during the Variscan orogeny and rejuvenated in the Cenozoic, most probably control the present-day geodynamic activity in the region, regardless the ST crust thrust over.

4.2. Close spatial relationship between mantle sutures and magmatism

4.2.1. Variscan magmatism

In this part we focus on locations and orientations of granitoid massifs in the western BM in relation to the previously described mantle boundaries. Petford et al. (2000) studied 3D geometries of granitic plutons and concluded that they mostly appear as flat-lying to open funnel-shaped structures with central or marginal feeder zones with a small number of conduits. This is also true for the major body of the Late-Variscan Smrčiny (Fichtelgebirge) Pluton (SP in Fig. 6), which was emplaced along the WSW continuation of the Krušné Hory Fault (KHF) above the ST/MD mantle suture and from a feeder channel situated near the KHF/MLF crossing (Hecht et al. 1997), located directly above the mantle T-junction (Figs. 6 and 7). Also the Žandov Pluton (ŽP) and the Bor Pluton (BP) seem to be closely related to the MLF and to the West-Bohemian Shear Zone (WBSZ, see also Siebel et al. 1999; Zulauf et al. 2002), where we map the mantle boundary between the TB and MD units (Fig. 4). We expect that several seismic stations newly installed in Bavaria above the TB/MD mantle junction will provide additional data for constraining a course of this mantle boundary and help to clarify a relation of both parallel fault zones (WBSZ and MLF).

Blecha et al. (2009) examined from gravity data the shape of the Late-Variscan Karlovy Vary Pluton (KVP) and of the Žandov Pluton, called by the authors as the Lesný–Lysina (Kynžvart) Massif, separated from the KVP. Such separation can be explained by different ways of magma supplies. The ŽP is located near the MLF and the mantle T-junction, which may have served as ascent paths for granitic magmas. On the other hand, Blecha et al. (2009) deduced from the elongation of the outcropping granite bodies of the KVP, that magma conduits may have been identical to, or parallel with, the Jáchymov Fault, paralleling the MLF at about 50 km eastward, and in the southern part of the KVP with the ER. By analogy with the KVP, Weinberg et al. (2004) pointed out that 'en cornu' shaped plutons in north-eastern Brazil were particularly emplaced where regional-scale shear zones intersect major lithological boundaries. Our suggestion of the mantle boundaries as major magma feeders is in accord with the models of emplacement of granite plutons (Petford et al. 2000; Cruden 2006; Blecha et al. 2009) by successive additions of sheet-like intrusions in repeated magma pulses.

Though we do not discuss the Krušné hory granite Batholith which is outside the area covered by the present study, it is worth mentioning that Kováříková et al. (2007) pointed out an importance of the mantle component in the intrusions forming this batholith, as well as a significant role of mantle-derived mafic magmas in heating of the sources of granitic melts. Also Siebel et al. (2003) found that mantle-related magmatism in NE Bavaria postdated the final convergence stage of the Variscan orogen (see also Finger et al. 2009).

4.2.2. Alkaline magmatism

Because the teleseismic tomography down to 250 km did not image any distinct heterogeneity which could be interpreted as a narrow mantle plume (Plomerová et al. 2007), the asthenosphere became a major candidate as a potential source of the Cenozoic volcanism in the western BM. This has been confirmed by Haase and Renno (2008) who observed no systematic changes in compositions of Cenozoic lavas across the lithospheric boundaries in the area of the western ER and concluded that the asthenosphere was the most common magma source. Wilson and Downes (2006) suggested that in general, melt generation in the asthenosphere and at the base of the lithosphere is a consequence of decompression partial melting, triggered by upwelling of the lithosphere–asthenosphere transition. In the western ER both the lithosphere (Plomerová et al. 1998; Plomerová and Babuška in press) and the crust (Geissler et al. 2005; Heuer 2006) are thinned to about 80 km and 27 km, respectively.

The asthenospheric origin of melts also indicates that the flux channels are obviously interconnected through the whole lithosphere. For alkaline magmatism and the present-day "post-volcanic" phenomena in the western BM, permissive release of a heat and materials flux from the asthenosphere is the essential factor. The flux is probably easily channelled to relatively narrow zones along the boundaries of mantle lithosphere. The largest flux of the mantle CO_2 is observed in the Cheb Basin directly above the mantle T-junction (Babuška and Plomerová 2008 and Fig. 8).

Two Quaternary volcanoes – Komorní hůrka and Železná hůrka (KH and ZH in Fig. 6), which are situated above the T-junction of the mantle lithospheres, are located along the mantle boundary between the TB and MD expressed on the surface by the WBSZ. Location of the volcanoes suggests that the junction was a major zone of weakness providing open channels for ascending magmas (Babuška and Plomerová 2008). Also in the French Massif Central a mantle suture, hidden beneath an allochtonous crust and reactivated during the Cenozoic extension of the thinned lithosphere, provided a space for major volcanism (Babuška et al. 2002).

In a broader European context, Wilson and Downes (2006) suggested that boundaries between east–west trending terranes (Rhenohercynian, Saxothuringian, Moldanubian) may be regions of anomalously thin, irregular

or weak lithosphere. Such deep, laterally persistent fault zones appear to have exerted a significant control on the location of subsequent Cenozoic magmatism, possibly acting as pathways for magma ascent through the lithosphere.

4.3. Deep-seated predisposition of sedimentary basins

Location of sedimentary basins of the western ER also indicates a possible influence of the deep lithosphere structure on basin formation (Babuška et al. in press). We suggest that a better knowledge of the mantle structure can contribute to the understanding of why a basin originated at a particular place and developed in a certain way.

The asymmetric Cheb Basin (CHB), which is superimposed on the western limit of the graben part of the ER (Figs 4 and 6), formed during the Pliocene and early Pleistocene (4.5–1.5 Ma) (Špičáková et al. 2000) by reactivation of the intersecting fracture systems of the ENE trending Krušné Hory Fault (KHF) and the NNW trending Mariánské Lázně Fault (MLF). This intersection is above the T-junction of the ST, TB and MD mantle lithospheres (Plomerová et al. 2007). The eastern margin of the CHB is defined by the northern part of the MLF along which the depot centre of the basin developed. The CHB belongs to the ER, but it lies outside the morphologically distinct graben structure of the rift (Fig. 6). Babuška et al. (2010) suggested that this is because the graben has developed above the mantle suture between the ST and TB units, while the CHB position was predestined by the crustal and lithosphere thinning above the "triple junction" of the ST/TB/MD mantle lithospheres. The NNW striking WBSZ, as a deep boundary between the TB and MD mantle lithospheres in the western BM (Plomerová et al. 2007), and the sub-parallel MLF probably played a very important role in the CHB development. The MLF forms the ENE limit of the CHB, but it finds no morphological expression of its zigzag course above the ST–TB mantle transition zone. On the other hand, the MLF is straight with escarpments expressed in 200–400 m heights above the flanks of this transition (Schunk et al. 2005 and Fig. 6), i.e., above the rigid rims of the ST and TB mantle lithospheres.

5. Conclusions

Boundaries of the mantle lithosphere domains with consistent fabrics play important role in the crust architecture and the present-day geodynamic activity. This paper reviews most of our research on the deep lithosphere structure in the western part of the Bohemian Massif (BM).

- Mapping the three-dimensional seismic anisotropy of the mantle lithosphere from anisotropic parameters of teleseismic body waves, shear-wave splitting parameters and directional terms of P residuals, identified three mantle domains in the western BM. Their boundaries are delimited by a change in orientation of seismic anisotropy, consistent within the individual domains. The observed anisotropy reflects a fossil olivine preferred orientation which most probably formed prior to the Variscan assembly of the originally separated microplates – the Saxothuringian (ST), Moldanubian (MD) and Teplá–Barrandian (TB).
- The mantle boundaries are locally shifted from their surface counterparts indicating thus a crust/mantle detachment. The part of the Ohře (Eger) Rift (ER) characterized by the graben morphology developed above the steep lithosphere-scale Variscan suture between the ST and TB mantle domains. Unlike this sharp and steep suture, the ST/MD mantle contact in NE Bavaria is an inclined southward dipping transition. This is probably a reason why the typical graben morphology did not develop in the SW continuation of the ER, though some Cenozoic sediments and volcanic rocks indicate a continuation of the rift structure south-west of the Cheb Basin (CHB).
- The most distinct effects of the deep lithosphere on the near surface tectonics seem to be found above the T-shape mantle 'triple junction' separating the ST mantle lithosphere from the MD and TB mantle lithospheres situated to the southwest and the southeast, respectively. Due to a Cenozoic rejuvenation of this junction, the area is from the point of geodynamics the most active part of the BM.
- Architecture of the mantle lithosphere probably plays important role also in the location of the late-orogenic granitoid massifs. The boundaries of the accreted lithospheric blocks may have acted as magma feeders providing successive additions of sheet-like intrusions in repeated magma pulses. The feeder of the major part of the Smrčiny (Fichtelgebirge) Pluton located at the crossing of the Krušné Hory and Mariánské Lázně faults above the mantle T-junction can serve as an example.
- The seismic tomography did not reveal a narrow plume in the upper mantle as a possible source of the Cenozoic volcanism in the region. Therefore, the asthenosphere upwelling in the western ER is the most probable source of magmas which may be channelled to the surface along partly open boundaries of the lithospheric blocks. The two Quaternary volcanoes (Komorní hůrka and Železná hůrka; KH, ZH in Fig. 6) and the major present-day emanations of large volumes of mantle gases are located above the mantle T-junction.
- Though the Cheb Basin is situated within the ST crust, it developed above the mantle T-junction, outside the morphologically distinct ER graben.

- We have suggested that the sublithospheric mantle of the western BM could have acted as major provider for heat and partial melts tapped by boundaries of the lithospheric microplates. The mantle boundaries of individual blocks represent weakened zones and partly open conduits into the crust and to the surface. Therefore, several phenomena often vaguely described as intraplate, like the magmatism, volcanism and earthquakes, can be directly linked with healed up paleoplate boundaries. This finding may also apply to other continental regions.

Acknowledgements. We thank Čestmír Tomek and an anonymous second reviewer for their constructive comments and suggestions how to improve the original manuscript. The research was supported by the Grant Agency of the Czech Republic project 205/07/1088 and by grant No. IAA300120709 of the Grant Agency of the Czech Academy of Sciences.

References

Babuška V, Cara M (1991) Seismic anisotropy in the Earth. Kluwer Academic Publishers, Dordrecht, pp 1–217

Babuška V, Plomerová J (1992) The lithosphere in central Europe – seismological and petrological aspects. Tectonophysics 207: 141–163

Babuška V, Plomerová J (2001) Subcrustal lithosphere around the Saxothuringian–Moldanubian Suture Zone – a model derived from anisotropy of seismic wave velocities. Tectonophysics 332: 185–199

Babuška V, Plomerová J (2006) European mantle lithosphere assembled from rigid microplates with inherited seismic anisotropy. Phys Earth Planet Inter 158: 264–280

Babuška V, Plomerová J (2008) Control of paths of Quaternary volcanic products in western Bohemian Massif by rejuvenated Variscan triple junction of ancient microplates. Stud Geophys Geod 52: 607–629

Babuška V, Plomerová J, Vecsey L, Granet M, Achauer U (2002) Seismic anisotropy of the French Massif Central and predisposition of Cenozoic rifting and volcanism by Variscan suture hidden in the mantle lithosphere. Tectonics 21: 11-1 – 11-20

Babuška V, Plomerová J, Bohema Working Group (2003) BOHEMA seismic experiment: search for an active magmatic source in the deep lithosphere in central Europe. EOS, Trans AGU 84: 409–417

Babuška V, Plomerová J, Fischer T (2007) Intraplate seismicity in the western Bohemian Massif (central Europe): a possible correlation with a paleoplate junction. J Geodyn 44: 149–159

Babuška V, Plomerová J, Vecsey L (2008) Mantle fabric of western Bohemian Massif (central Europe) constrained by 3D seismic P and S anisotropy. Tectonophysics 462: 149–163

Babuška V, Fiala J, Plomerová J (2010) Bottom to top lithosphere structure and evolution of western Eger Rift (central Europe). Int J Earth Sci 99: 891–907

Babuška V, Plomerová J, Vecsey L (in press) Links between the structure of the mantle lithosphere and morphology of the Cheb Basin (Eger Rift, central Europe). Int J Earth Sci; DOI 10.1007/s00531–010–0531–4

Bailey DK, Wooley AR (1999) Episodic rift magmatism: the need for a new paradigm in global dynamics. Geolines 9: 15–20

Bankwitz P, Schneider G, Kämpf H, Bankwitz E (2003) Structural characteristics of epicentral areas in Central Europe: study case Cheb Basin (Czech Republic). J Geodyn 35: 5–32

Ben Ismail W, Mainprice D (1998) An olivine fabric database: an overview of upper mantle fabrics and seismic anisotropy. Tectonophysics 296: 145–157

Blecha V, Štemprok M, Fischer T (2009) Geological interpretation of gravity profiles through the Karlovy Vary Granite Massif (Czech Republic). Stud Geophys Geod 53: 295–314

Bräuer K, Kämpf H, Niedermann S, Strauch G (2005) Evidence for ascending upper mantle-derived melt beneath the Cheb Basin, central Europe. Geoph Res Lett 32: L08303; DOI 10.1929/2004GL022205

Cháb J, Stráník Z, Eliáš M (2007) Geological map of the Czech Republic 1:500 000. Czech Geological Survey, Prague

Cruden AR (2006) Emplacement and growth of plutons: implications for rates of melting and mass transfer in continental crust. In: Brown M, Rushmer T (eds) Evolution and Differentiation of the Continental Crust. Cambridge University Press, pp 455–519

DEKORP Research Group (1994) The deep reflection seismic profiles DEKORP 3/MVE–90. Z geol Wiss 22: 623–684

Finger F, Gerdes A, René M, Riegler G (2009) The Saxo–Danubian Granite Belt: magmatic response to post-collisional delamination of mantle lithosphere below the south-western sector of the Bohemian Massif (Variscan orogen). Geol Carpath 60: 205–212

Fischer T, Horálek J (2003) Space–time distribution of earthquake swarms in the principal focal zone of the NW Bohemia/Vogtland seismoactive region: period 1985–2001. J Geodyn 35:125–144

Fouch MJ, Rondenay S (2006) Seismic anisotropy beneath stable continental interiors. Phys Earth Planet Inter 158: 292–320

Franke W (2000) The mid–European segment of the Variscides: tectonostratigraphic units, terrane boundaries and plate tectonic evolution. In: Franke W, Haak V, Oncken O, Tanner D (eds) Orogenic Processes: Quantification

and Modelling in the Variscan Belt. Geological Society London Special Publications 179: 35–61

Franke W (2006) The Variscan orogen in Central Europe: construction and collapse. In: Gee DG, Stephenson RA (eds) European Lithosphere Dynamics. Geological Society London Memoirs 32: 333–343

Franke W, Dallmeyer Rd, Weber K (1995) Geodynamic evolution. In: Dallmeyer RD, Franke W, Weber K (eds) Pre–Permian Geology of Central and Eastern Europe. Springer-Verlag, Berlin, pp 579–593

Geissler WH, Kämpf H, Kind R, Bräuer K, Klinge K, Plenefisch T, Horálek J, Zedník J, Nehybka V (2005) Seismic structure and location of a CO_2 source in the upper mantle of the western Eger (Ohře) Rift, central Europe. Tectonics 24: TC5001; DOI 10.1029/2004TC001672

Geissler WH, Sodoudi F, Kind R (2010) Thickness of the European lithosphere as seen by S receiver functions. Geophys J Int 181: 604–634

Grad M, Guterch A, Mazur S, Keller GR, Špičák A, Hrubcová P, Geissler WH (2008) Lithospheric structure of the Bohemian Massif and adjacent Variscan belt in central Europe based on profile S01 from the SUDETES 2003 experiment. J Geophys Res 113: B10304; DOI 10.1029/2007JB005497

Granet M, Wilson M, Achauer U (1995) Imaging a mantle plume beneath the Massif Central (France). Earth Planet Sci Lett 17: 1109–1112

Grygar R, Grmela A, Jelínek J, Pöpperl J, Galek R (2006) Tectonic setting of Sokolov Basin in relation to prediction of thermal water discharge zones. Geolines 20: 44–45

Haase KM, Renno AD (2008) Variation of magma generation and mantle sources during continental rifting observed in Cenozoic lavas from the Eger Rift, Central Europe. Chem Geol 257: 192–202

Hecht L, Vigneresse JL, Morteani G (1997) Constrains on the origin of zonation of the granite complexes of the Fichtelgebirge (Germany and Czech Republic). Evidence from gravity and geochemical study. Geol Rundsch 86: 93–109

Heuer B (2006) Lithospheric and upper mantle structure beneath the western Bohemian Massif obtained from teleseismic P and S receiver functions. Scientific Technical Report STR06/12, GeoForschungsZentrum Potsdam, ISSN 1610–0956, pp 1–149

Horálek J, Fischer T (2008) Role of crustal fluids in triggering the West Bohemia/Vogtland earthquake swarms: just what we know (a review). Stud Geophys Geod 52: 455–478

Horálek J, Fischer T, Bouškova A, Jedlička P (2000) The western Bohemia/Vogtland region in the light of the WEBNET network. Stud Geophys Geod 44: 107–125

Hrubcová P, Sroda P, Špičák A, Guterch A, Grad M, Keller GR, Brueckl E, Thybo H (2005) Crustal and uppermost mantle structure of the Bohemian Massif based on CELEBRATION 2000 data. J Geophys Res 110, B11305; DOI 101029/2004JB003080

Jindřich V (1971) New views in tectonic significance of platform sediments in the Bohemian Massif, Czechoslovakia. Geol Soc Am Bull 82: 763–768

Kachlík V (1997) The Kladská Unit. In: Vrána S, Štědrá V (eds) Geological Model of Western Bohemia Related to the KTB Borehole in Germany. Sbor geol věd, Geol 47: 70–80

Kämpf H, Peterek A, Rohrmüller J, Kümpel HJ, Geissler WH (2005) The KTB Deep Crustal Laboratory and the western Eger Graben. In: Koch R, Röhling HG (eds) GeoErlangen 2005 System Earth – Biosphere Coupling, Regional Geology of Central Europe, Exkursionsführer. Schriftreihe Dt Ges Geowiss 40: 37–107

Kennett BLN (1991) IASPEI 1991, Seismological Tables. Research School of Earth Science, Australian National University, Canberra, pp 1–167

Kopecký L (1978) Neoidic taphrogenic evolution and young alkaline volcanism of the Bohemian Massif. Sbor geol věd, Geol 31: 91–107

Kopecký L (1986) Geological development and block structure of the Cenozoic Ohře Rift (Czechoslovakia). In: Aldrich Jr MJ, Laughlin AW (eds) Proceedings of the 6th International Conference on Basement Tectonics, Santa Fe, USA, Sept. 16–20, 1985. International Basement Tectonics Association, Salt Lake City, pp 111–124

Kováříková P, Siebel W, Jelínek E, Štemprok M, Kachlík V, Holub FV, Blecha V (2007) Petrology, geochemistry and zircon age for redwitzite at Abertamy, NW Bohemian Massif (Czech Republic): tracing the mantle component in Late Variscan intrusions. Chem Erde 67: 151–174

Krawczyk CM, Stein E, Choi S, Oettinger G, Schuster K, Götze HJ, Haak V, Prodehl C, Schulze A (2000) Geophysical constraints on exhumation mechanisms of high-pressure rocks: the Saxo–Thuringian case between the Franconian Line and Elbe Zone. In: Franke W, Haak V, Oncken O, Tanner D (eds) Orogenic Processes: Quantification and Modelling in the Variscan Belt. Geological Society London Special Publications 179: 303–322

Mlčoch B ed (2001) Investigation of Crystalline Formations in Deep Basement Structures of the Doupov Complex and its Broad Surroundings. Unpublished final Report, Czech Geological Survey, Prague, pp 1–121 (in Czech)

Mlčoch B (2003) Character of the contact between the Saxothuringian and Teplá–Barrandian unit. Geolines 16: 75

Mlčoch B, Konopásek J (2010) Pre-Late Carboniferous geology along the contact of the Saxothuringian and Teplá–Barrandian zones in the area covered by younger sediments and volcanics (western Bohemian Massif, Czech Republic). J Geosci 55: 81–94

Müller B, Wehrle V, Zeyen H, Fuchs K (1997) Short-scale variations of tectonic regimes in the western European stress province north of the Alps and Pyrenees. Tectonophysics 275: 199–219

O'Brien JP, Duyster J, Grauert B, Schreyer W, Stöckert B, Weber K (1997) Crustal evolution of the KTB drill site: from oldest relics to the late Hercynian granites. J Geophys Res 102: B8, 18 203–18 220

Petford N, Cruden AR, McCaffrey KJW, Vigneresse JL (2000) Granite magma formation, transport and emplacement in the Earth's crust. Nature 408: 669–673

Plaumann S, Švancara J (1996) Tschechisch–deutsche Schwerekarte 1:500.000 um Erzgebirge und Böhmerwald (Krušné hory, Český les). Unpublished manuscript, Hannover/Brno

Plomerová J, Babuška V (in press) Long memory of mantle lithosphere fabric – European LAB constrained from seismic anisotropy. Lithos; DOI 10.1016/j.lithos.2010.01.008

Plomerová J, Babuška V, Šílený J, Horálek J (1998) Seismic anisotropy and velocity variations in the mantle beneath the Saxothuringicum–Moldanubicum contact in central Europe. Pure Appl Geophys 151: 365–394

Plomerová J, Vecsey L, Babuška V, Granet M, Achauer U (2005) Passive seismic experiment MOSAIC – a pilot study of mantle lithosphere anisotropy of the Bohemian Massif. Stud Geophys Geod 49: 541–560

Plomerová J, Achauer U, Babuška V, Vecsey L, Bohema Working Group (2007) Upper mantle beneath the Eger Rift (Central Europe): plume or asthenosphere upwelling? Geophys J Int 169: 675–682

Prodehl C, Müller S, Haak V (1995) The European Cenozoic rift system. In: Olsen KH (ed) Continental Rifts: Evolution, Structure, Tectonics. Elsevier, Amsterdam, pp 133–212

Ritter JRR, Jordan M, Cristensen UR, Achauer U (2001) A mantle plume below the Eifel volcanic fields, Germany. Earth Planet Sci Lett 186: 7–14

Savage MK (1999) Seismic anisotropy and mantle deformation: what have we learned from shear wave splitting? Rev. Geophysics 37: 65–106

Schunk R, Peterek A, Reuther CD (2005) Second day: active processes of the western Eger Graben system, Stop 6a–c. In: Kämpf H, Peterek A, Rohrmüller J, Kümpel HJ, Geissler W (eds) The KTB Deep Crustal Laboratory and the Western Eger Graben. Schriftreihe Dt Ges Geowiss 40: 66–71

Siebel W, Breiter K, Wendt I, Höhndorf A, Henjes–Kunst F, René M (1999) Petrogenesis of contrasting granitoid plutons in western Bohemia (Czech Republic). Mineral Petrol 65: 207–235

Siebel W, Chen F, Satir M (2003) Late-Variscan magmatism revisited: new implications for Pb-evaporation zircon ages on the emplacement of redwitzites and granites in NE Bavaria. Int J Earth Sci 92: 36–53

Šílený J, Plomerová J (1996) Inversion of shear-wave splitting parameters to retrieve three-dimensional orientation of anisotropy in continental lithosphere. Phys Earth Planet Inter 95: 277–292

Špičáková L, Uličný D, Koudelková G (2000) Tectonosedimentary evolution of the Cheb Basin (NW Bohemia, Czech Republic) between Late Oligocene and Pliocene: a preliminary note. Stud Geoph Geod 44: 556–580

Šrámek J (2001) Gravimetry. In: Mlčoch B (ed) Investigation of Crystalline Formations in Deep Basement Structures of the Doupov Complex and Broader Surroundings. Czech Geological Survey, Prague, pp 1–10 (in Czech)

Švancara J, Chlupáčová M (1997) Density model of geological structure along the profile 9HR. In: Vrána S, Štědrá V (eds) Geological Model of Western Bohemia Related to the KTB Borehole in Germany. Sbor geol věd, Geol 47: 32–36

Švancara J, Gnojek I, Hubatka F, Dědáček K (2000) Geophysical field pattern in the west Bohemian geodynamic active area. Stud Geoph Geod 44: 307–326

Timmermann H, Štědrá V, Gerdes A, Noble SR, Parrish RR, Dörr W (2004) The problem of dating high-pressure metamorphism: a U–Pb isotope and geochemical study of eclogites and related rocks of the Mariánské Lázně Complex, Czech Republic. J Petrol 45: 1311–1338

Tomek Č, Dvořáková V, Vrána S (1997) Geological interpretation of the 9HR and 503M seismic profiles in western Bohemia. In: Vrána S, Štědrá V (eds) Geological Model of Western Bohemia Related to the KTB Borehole in Germany. Sbor geol věd, Geol 47: 43–50

Ulrych J, Cajz V, Pivec E, Novák JK, Nekovařík Č (2000) Cenozoic intraplate alkaline volcanism of western Bohemia. Stud Geoph Geod 44: 346–351

Vecsey L, Plomerová J, Babuška V (2008) Shear-wave splitting measurements – problems and solutions. Tectonophysics 462: 178–196

Weinberg RF, Sial AN, Mariano G (2004) Close spatial relationship between plutons and shear zones. Geology 32: 377–380

Weinlich FH, Bräuer K, Kämpf H, Strauch G, Tesař J, Weise SM (1999) An active subcontinental mantle volatile system in the western Eger Rift, Central Europe: gas flux, isotopic (He, C, and N) and compositional fingerprints. Geochim Cosmochim Acta 63: 3653–3671

Wilson M, Downes H (2006) Tertiary–Quaternary intraplate magmatism in Europe and its relationship to mantle dynamics. In: Gee DG, Stephenson RA (eds) European Lithosphere Dynamics. Geological Society London Memoirs 32: 147–166

Ziegler PA (1992) European Cenozoic rift system. Tectonophysics 208: 91–111

Zulauf G (1997) Von der Anchizone bis zur Eklogitfazies Angekippte Krustenprofile als Folge der cadomischen und variscischen Orogenese im Teplá–Barrandium (Böhmische Masse). Geotekt Forsch 89: 1–302

Zulauf G, Dörr W, Fiala J, Vejnar Z (1997) Late Cadomian crustal tilting and Cambrian transtension in the Teplá–

Barrandian unit (Bohemian Massif, Central European Variscides). Geol Rundsch 86: 571–584

Zulauf G, Buess C, Dörr W, Vejnar Z (2002) 10 km minimum throw along the West Bohemian shear zone: evidence for dramatic crustal thickening and high topography in the Bohemian Massif (European Variscides). Int J Earth Sci 91: 850–864

Journal of Geosciences, 55 (2010), 187–199 DOI: 10.3190/jgeosci.073

Original paper

Crustal structures beneath the Saxonian Granulite Massif, the České středohoří and the Doupovské hory Mts. based on the depth-recursive tomography

Miroslav NOVOTNÝ[1*], Zuzana SKÁCELOVÁ[2], Bedřich MLČOCH[2]

[1] *Geophysical Institute, Academy of Sciences of the Czech Republic, Boční II/1401, 141 31 Prague 4, Czech Republic; mn@ig.cas.cz*
[2] *Czech Geological Survey, Klárov 3, 118 21 Prague 1, Czech Republic*
[*] *Corresponding author*

The P-wave velocity distribution, obtained recently by the depth-recursive tomography along the S01 refraction profile of the SUDETES 2003 seismic experiment, correlated fairly well with other geophysical results known in the area of the KTB deep drilling site. The S01 velocity model also provided a reliable velocity image of the upper and middle-crustal structures along the Eger Graben. In the present paper we will use the results of the depth-recursive tomography applied to the crossing S04 profile to derive a 3-D picture of structures near the S04 and S01 intersection.
The NW–SE trending S04 profile starts in the Saxonian Granulite Massif and intersects the Eger Graben in the region of Altenberg–Teplice Caldera. The depth-recursive tomography, applied to the S04 profile, also produced a velocity model allowing, together with the derived S01 velocities, a reliable 3-D interpretation down to the depths of 15–20 km. Besides the P-wave velocities, gravity, aeromagnetic and petrophysical data support the presented geological interpretation. Using the velocity and gravity data we identified the subsurface granitic and ultrabasic bodies in wider surroundings of the Saxothuringian and Teplá–Barrandian contact zone and also possible magmatic centers for the Teplice–Altenberg Caldera as well as for the Doupovské hory and the České středohoří volcanic complexes.

Keywords: Depth-recursive refraction tomography, SUDETES 2003 seismic profiles S04 and S01, Bohemian Massif, Saxonian Granulite Massif, Altenberg–Teplice Caldera, České středohoří and Doupovské hory volcanic complexes
Received: 29 April 2010; accepted: 10 September 2010; handling editor: J. Konopásek

1. Introduction

Two refraction profiles S01 and S04 were recorded in the Western Bohemia as a part of the recent international seismic experiment SUDETES 2003 (Grad et al. 2003). They intersect in the Eger Graben near the Altenberg–Teplice Caldera gravity minimum, southwest of Litoměřice (Fig. 1). The S01 profile starts near the KTB site, then follows the SW–NE oriented Eger Graben (Fig. 1) and further NE crosses the Elbe Zone and the geological structures in the Lusatian Complex. Recently, Grad et al. (2008) used the S01 wide-angle seismic data to derive a velocity model involving the whole crust. Based only on the distinct first breaks of refraction waves along the S01 line, Novotný et al. (2009) applied the DRTG method (Depth Recursive Tomography on Grid) to derive a P-wave velocity image of upper and middle crust yielding here a higher resolution. The DRTG inversion of the refraction first arrivals was performed using a regular network of refraction grid rays that allowed a statistical assessment of the resolution: the lateral sizes of the velocity anomalies to be resolved were derived depending on their depths, velocity excesses and desired confidence level. Thus, for the 68% confidence and 5% excess, we can resolve the velocity anomalies in the S01 pattern with the minimum size from 7.5 to 20 km depending on their depth positions from 0 to 20 km (see Novotný et al. 2009, fig. 10 and accompanying text). The S01 velocity features proved to be consistent with Vertical Seismic Profiling (VSP) and log measurements at the KTB site.

Profile S04 starts in the region of the Saxonian Granulite Massif, crosses the Krušné hory Mts, then the Eger Graben and continues SE across the boundaries of the main units in the Bohemian Massif (Saxothuringian, Teplá–Barrandian, Moldanubian and Moravian units) to the West Carpathians. Růžek et al. (2007) developed a special two-step inverse procedure for inverting the refracted Pg, Pn and reflected Pm phases. They derived velocity models down to the Moho along eight refraction profiles from recent seismic experiments in the Bohemian Massif. Based on their error analyses, Růžek et al. (2007) considered the S04 and other obtained models reliable down to a 15 km depth, where only the velocity anomalies exceeding 5 % can be reliably detected.

Within the range of 0–350 km, the S04 seismic data were acquired in the most detailed average inter-shot and inter-station spacing of 34.5 km and 3 km, respectively. Using the DRTG method only for the distinct first arrivals

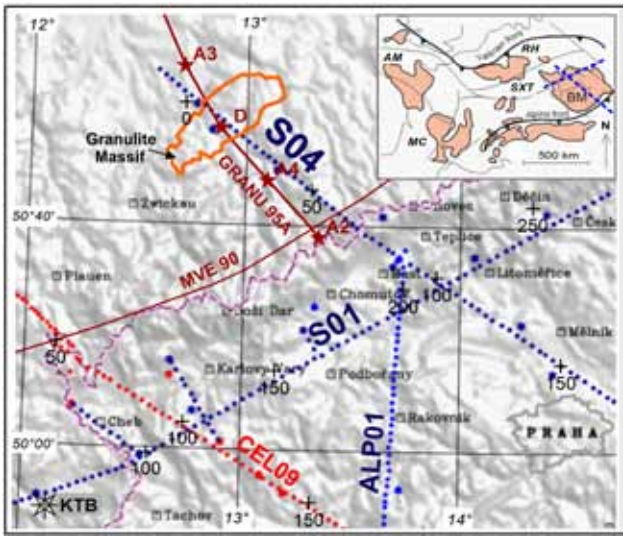

Fig. 1 The seismic profiles of the SUDETES 2003, ALP 2002, CELEBRATION 2000 refraction experiments (Guterch et al. 2003) and the DEKORP 3 and GRANU 95 projects in the Bohemian Massif. The circles and stars show the locations of the stations and shot points in the related seismic measurements. The ticks with a step of 50 km mark the distance scales along the individual profiles. The background topography is from the US Geological Survey TOPO 30 model by Švancara et al. (2005*)*. Inset shows the position of S04 within the European Variscides. BM – Bohemian Massif, AM – Armorican Massif, MC – Massif Central, SXT – Saxothuringian Zone, RH – Rhenohercynian Zone (adapted after Pitra et al. 1999).

of refraction waves in this range, a P-wave velocity image was obtained with the resolution comparable to that attained by DRTG tomography on the S01 profile. For the compared 68% confidence, the 5% velocity anomalies are resolvable in the S04 velocity pattern if their minimum lateral sizes amount 5–17 km at the depths of 0–6 km or 16–24 km at the depths of 12–15 km. Velocity anomalies under 5 % can be then also detected if their lateral sizes exceed the minimum limit specified for the desired confidence level. A peculiarity of the S04 refraction tomography is that there is the 6–11 km depth belt with frequent occurrence of low-velocity zones causing the zero statistical resolution. For more details see Novotný (in prep.).

The target of the SUDETES 2003 seismic experiment was to decipher the lithospheric structure of the Central Europe, especially in the Bohemian Massif as the easternmost part of the European Variscides. Relatively good quality of the S04 first arrivals allowed investigation of the shallower structures relevant for regional geology. The consistence and lateral resolution attained in both S04 and S01 velocity cross-sections near their junction allows delineation of crustal structures occurring under the Altenberg–Teplice Caldera (ATC) and the České středohoří Mts. Based on the presented P-wave velocity and gravity models and extensive borehole data in the region (e.g. Mlčoch and Konopásek 2010), a subsurface geological model along the S04 line is composed. The model involves partially the root zone of the Saxonian Granulite Massif, further the southwestern margin of ATC structures and the collision zone of the Saxothuringian and the Teplá–Barrandian units.

2. Geological setting, gravity and magnetic image

The S04 profile intersects the S01 profile near the contact of the Saxothuringian Zone (SXT) and the Teplá–Barrandian Unit (TBU) that were interpreted as the two major terranes of the Bohemian Massif – see e.g. Matte et al. (1990) and Fig. 2. The SW–NE trending contact zone is pronounced in the regional gravity image (Fig. 3). The striking horizontal gravity gradient observed between the negative (SXT) and the positive (TBU) gravity anomalies defines the Litoměřice Deep Fault (LDF) that is not demonstrated at the present surface (see e.g. Bucha and Blížkovský 1994).

The geophysical image of the studied area is complex. The most pronounced gravity minimum lies north of Bílina in the region of the Altenberg–Teplice Caldera. The S04 profile passes the southwestern flank of the ATC gravity minimum. An important role in the geophysical characteristics plays the Bílina Fault placed at the southeastern margin of the ATC gravity anomaly. Two local minima of Bouguer anomaly are pronounced in the north (Fig. 3). The former, located in the NW, reflects the Fláje Pluton (Fig. 2). The Fláje anomaly reaches its minimal value at the northern margin of the Most Basin that has the maximal thickness of sediments here. The latter, in the N–NE parts of the ATC, likely corresponds to a rather large accumulation of granites: Schellerhau Granite Complex and Cínovec–Krupka Composite Massif (e.g. Štemprok et al. 2003; Müller et al. 2005). On the other hand, a gravity high is caused by metabasites and ultramafic rocks cropping out in the Porta Bohemica area west of Litoměřice. The

⇨

Fig. 2 Geological sketch of the Early Carboniferous and older rocks with the profile network. Crystalline basement below the Late Paleozoic and younger strata after Mlčoch and Konopásek (2010) is shown in color. **Geological units:** SXT – Saxothuringian Zone, TBU – Teplá–Barrandian Unit, ATC – Altenberg–Teplice Caldera, LP – Louny Pluton, LSP – Lusatian Pluton, NEP – Nejdek–Eibenstock Pluton, SP – Smrčiny Pluton, FP – Fláje Pluton, TR – Teplice rhyolite, MLC – Mariánské Lázně Complex, EMLC – equivalent of the Mariánské Lázně Complex below the Doupovské hory Mts., LVRP – Lower Vltava River Pluton after Fediuk (2005), WN – Wildenfels nappe. FN – Frankenberg nappe. **Faults:** BF – Bílina Fault, CSF – České středohoří Fault, CHF – Chomutovka Fault, JF –Jáchymov Fault, KHF – Krušné hory Fault, LF – Liboc Fault, LSF – Lusatian Fault, SF – Střezov Fault, STF – Stráž Fault.

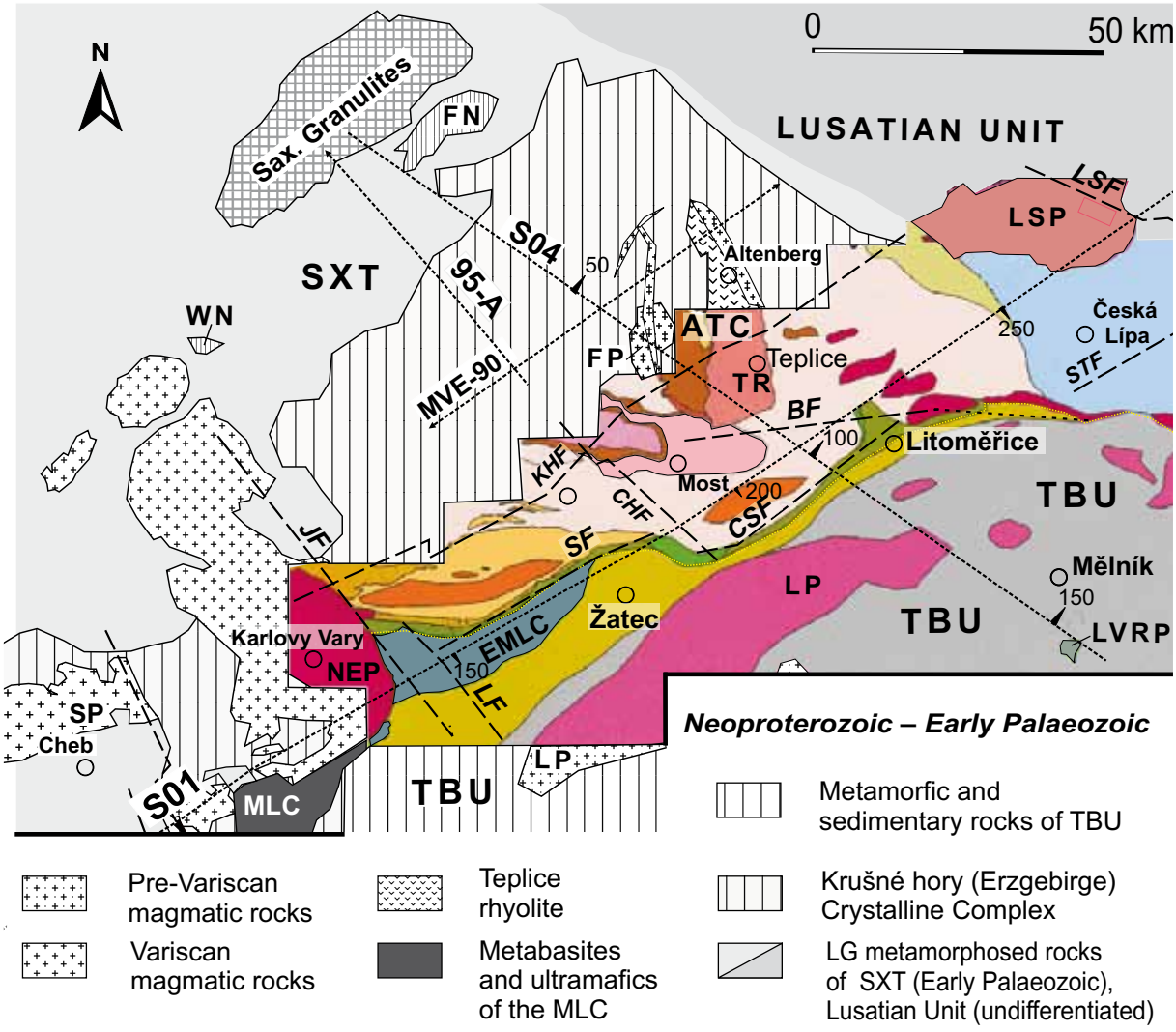

Saxothuringian Zone

- Variscan magmatic rocks
- Pre-Variscan magmatic rocks
- Lower Vltava River Pluton
- orthogneiss, metagranite
- granulite
- rhyolite of Altenberg–Teplice Caldera

Lusatia

- orthogneiss
- phyllite
- mica-schist
- amphibolite
- gneiss paragneiss
- metabasites and ultramafics of the MLC and EMLC
- phyllite, greenschist
- phyllite of Elbtal -Schiefergebirge (Early Palaeozoic)

Teplá–Barrandian Unit

- metamorphic and sedimentary rocks of the TBU
- Teplá Crystalline Complex

- SXT–TBU lithological boundary
- faults
- extent of the crystalline basement after Mlčoch and Konopásek (2010)

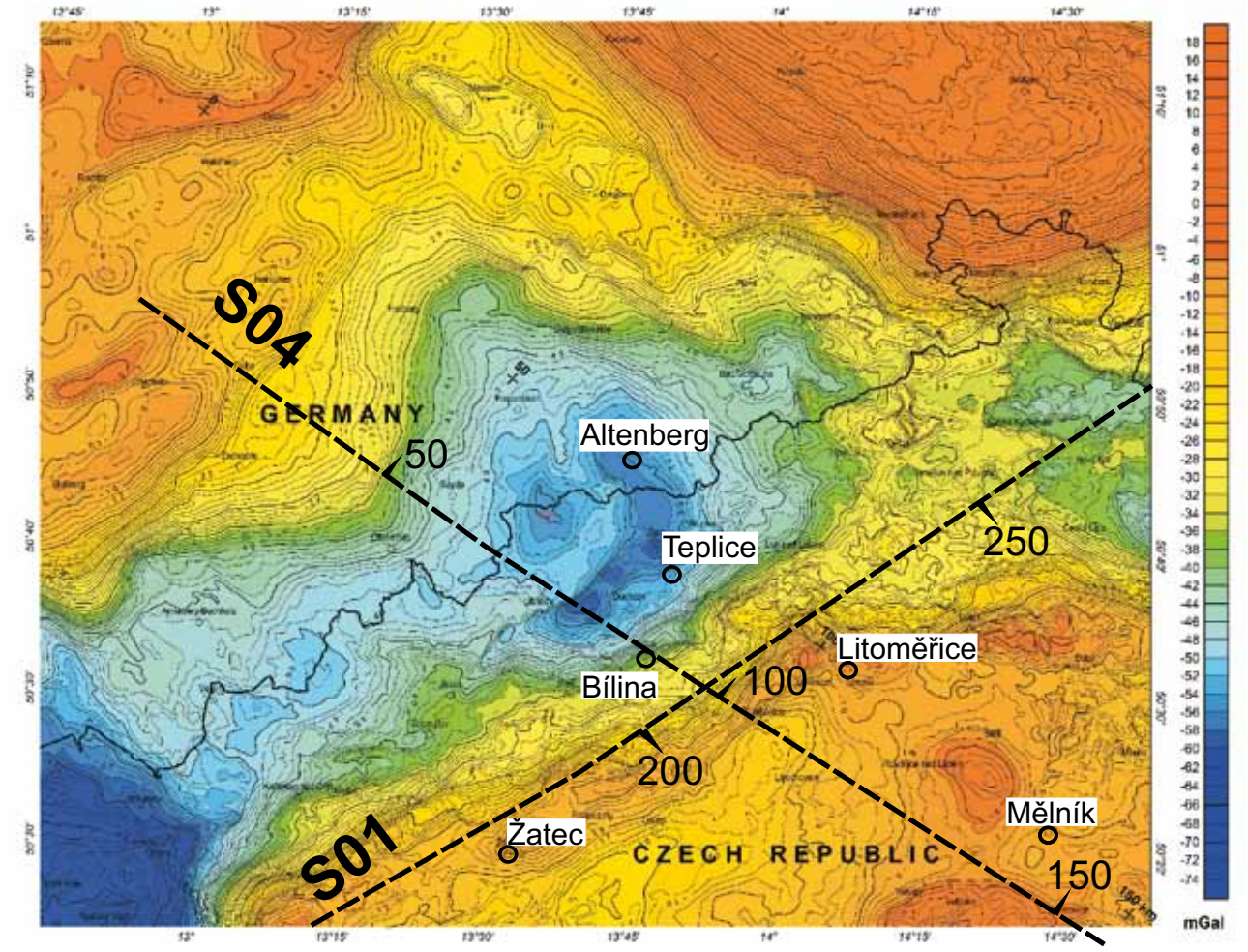

Fig. 3 Gravity map of the Altenberg–Teplice Caldera region with the profile network (after Sedlák et al. 2009).

TBU region, southeast of the LDF, is characterized by significantly increased values of the gravity field. The magnetic map (Šalanský 1995) shows distinct major positive anomalies occurring in both geological units near their contact. The small isolated positive anomalies are more intense and correspond to the Tertiary volcanic rocks of the České středohoří Mts. Švancara et al. (2005) derived the analytical continuation of magnetic anomalies for the half-space level of 10 km. It indicates that the regional positive magnetic anomaly along the LDF may be caused by accumulation of mafic and ultramafic rocks at the depths greater than 5 km.

3. S04 and S01 cross-sections

3.1. S04 velocity pattern

The S04 velocity model that will be interpreted together with the S01 cross-section is depicted in Fig. 4 and complemented by real geological observations. It is a part of the velocity model derived by Novotný (in prep.) for an extended distance range (0–350 km). We also refer to this work for the lateral resolution achieved by the DRTG method and the model ambiguity inherent to any refraction tomographic method if low-velocity zones are present. Refraction tomography cannot determine the velocities within such zones, i.e. in the regions with negative velocity depth gradient preventing refraction waves to return to the surface. The main advantage of the DRTG method is that it updates and verifies the derived velocity models for every grid node of the imaged model domain. In Fig. 4, the P-wave velocities are contoured in a 100 $m.s^{-1}$ step. The grid nodes, where the model velocities were verified, are denoted by dots. The low-velocity zones (LVZs) with a weak or negative velocity gradient, occurring mostly in the 6–11 km depths, are not verified inside (no dots in grid nodes), but by the refraction grid rays crossing LVZs. They yielded the best fit for this model thanks to the involved LVZs. The same grid sampling (Δx = 5000 m and Δz = 500 m) was used as in the case of the S01 model.

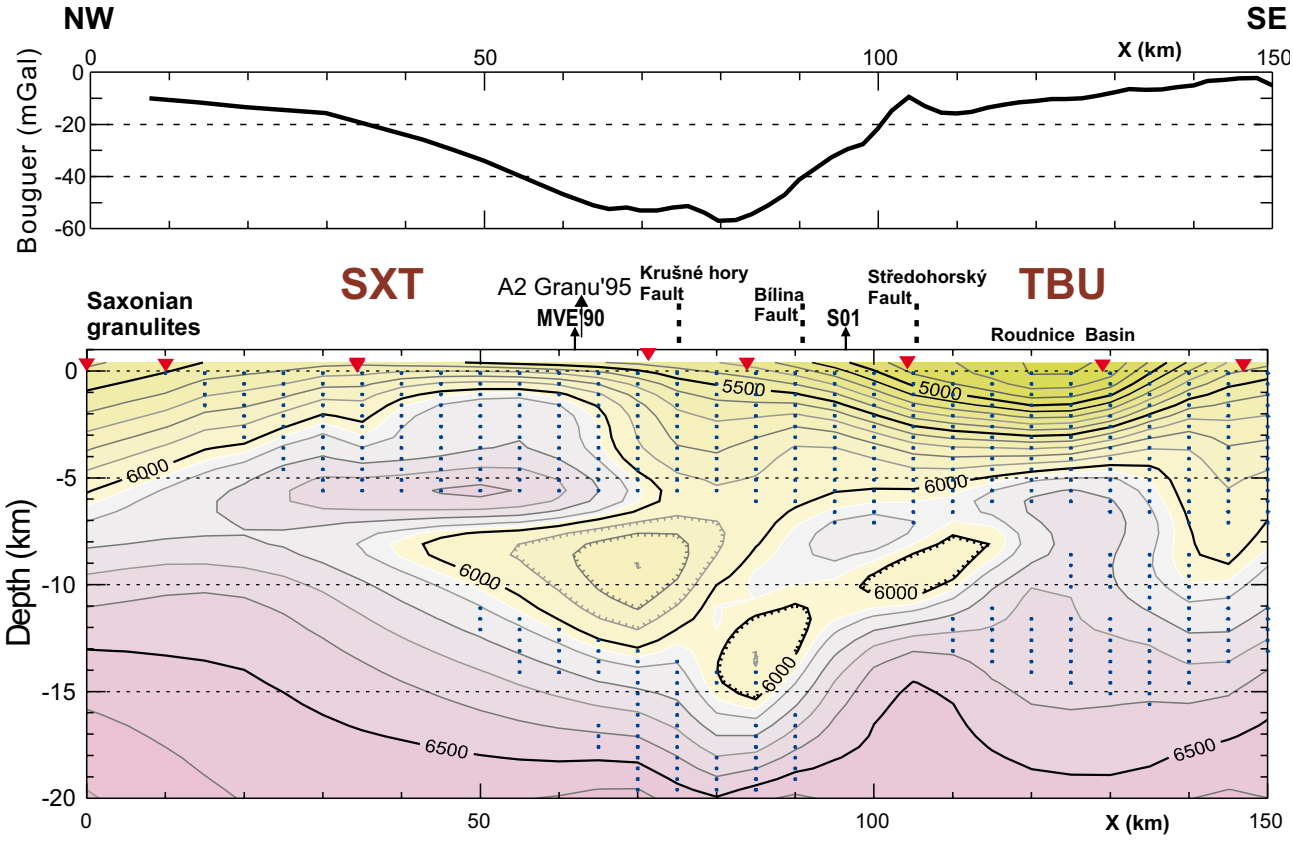

Fig. 4 Bouguer anomalies for a reduction density of 2.67 g.cm^{-3} (top) and P-wave velocities along S04 profile contoured at the 100 m.s^{-1} step. Inserted is the 6050 isovelocity – just colored. The dots denote the grid nodes verified by the refraction grid rays. Intersections with the profiles MVE-90 and S01 are marked. Triangles stand for the shot point positions at the S04 distance scale. SXT – Saxothuringian Zone, TBU – Teplá–Barrandian Unit.

The DRTG velocity features encountered in the 0–150 km range are also confirmed by independent geophysical methods, namely by the inverse gravity modeling and by the forward ray-tracing modeling on two near collateral profiles. For inverse gravity modeling along the S04 line, we use the Bouguer gravity anomaly (top of Fig. 4) derived by Švancara et al. (2005) for the reduction density of 2.67 g.cm^{-3}.

Recently, Sedlák et al. (2009) studied the gravity response of igneous rocks in the southeastern Saxony and northwestern Bohemia. In a previous study aimed at the geothermal drilling near Litoměřice, Sedlák et al. (2007) derived a 2-D density model down to 12 km depth along a NW–SE trending profile that passed the geothermal borehole LT–1 located 13 km NNE of the S04 line (km ~105). The densities and block interfaces inferred by the inverse gravity modeling near the LT–1 borehole reflected fairly well the blocky structure that is in accord with the S04 velocity pattern. In particular, they involve the minor HV (high-velocity) and LV (low-velocity) anomalies at the contact zone of the Saxothuringian and the Teplá–Barrandian units. Their deeper positions, if compared with the density model by Sedlák et al. (2007), are in agreement with the trend (dipping southwest) detected in the crossing S01 profile (see the S01 velocity pattern near the S04 intersection in Fig. 6). The gravity modeling performed directly along the S04 line is presented later, in Chapter 4.

The northwestern end of the S04 profile reaches the Saxonian Granulite Massif. This region was covered by several refraction and reflection profiles, performed within the framework of two seismic projects DEKORP 3/MVE 90 and GRANU 1995 – see DEKORP Research Group (1994) and Enderle et al. (1998). The DEKORP 3/MVE 90 surveyed the Variscan structures of the Rhenohercynian and the Saxothuringian zones while the GRANU 1995 seismic profiles targeted the Saxothuringian Zone and the Saxonian Granulite Massif. The reflection profile MVE–90 East was measured along the northwestern Czech border (Fig. 1). It intersects the S04 line at km ~61. The DEKORP and GRANU seismic profiles provided basic data for the studies of the geological development of the Saxothuringian Zone (e.g. Krawczyk et al. 2000; Franke and Stein 2000).

The GRANU 95A seismic profile intersects the S04 line between the shot points A3 and D in the Saxonian Granulite Massif (Figs 1 and 5). It diverges under a low angle to the southeast related to the S04 line – its shot

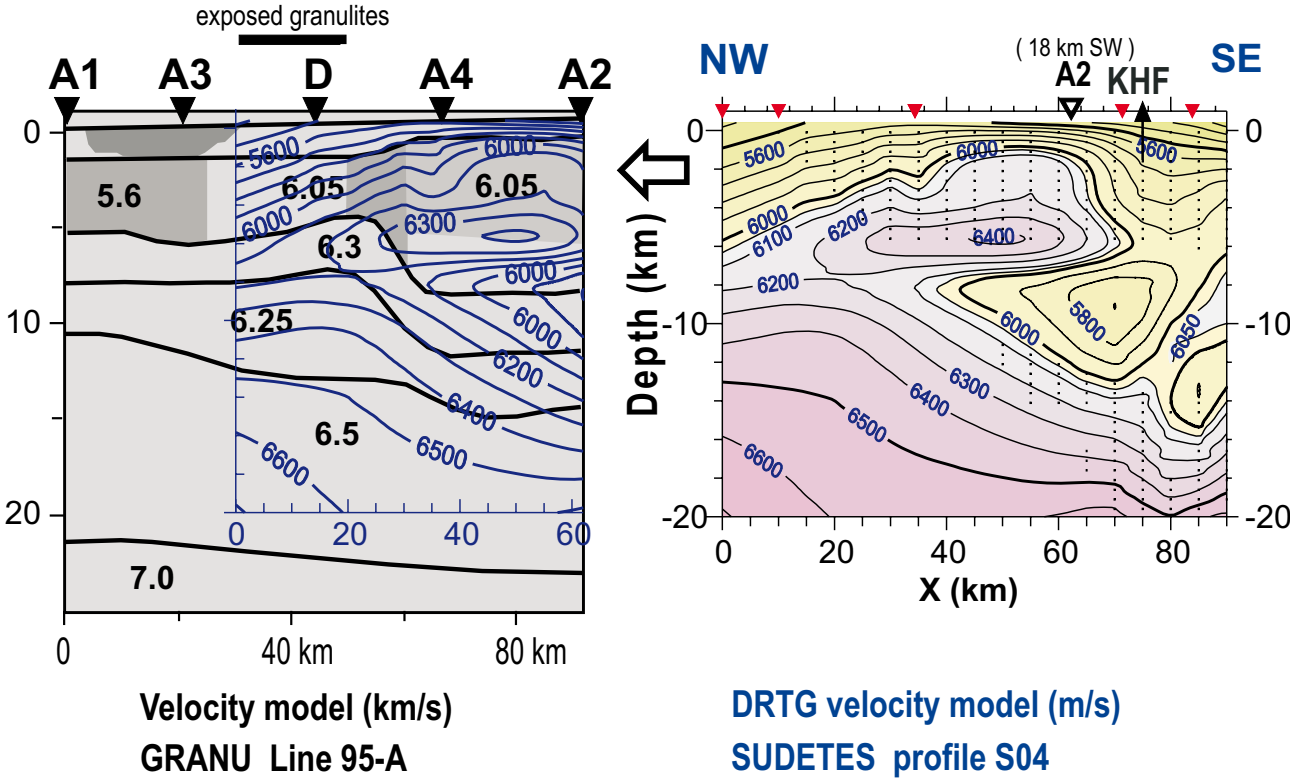

Fig. 5 Comparison of the GRANU 95A and S04 velocity sections. The GRANU 95A model was adapted after Enderle et al. (1998). The GRANU shot point A2 is projected to the S04 distance scale at km 62, the profile intersection lies between the shot points A3 and D. KHF – Krušné hory Fault.

point A2 is placed at ~18 km southwest of the S04 line. It is interesting to compare the overlapping parts of the S04 model and the GRANU 95A model derived by forward modeling (Enderle et al. 1998). Figure 5 presents the P-wave velocity distribution along the overlapping sections. The S04 profile intersects the 95–A line between the A3 and D shot points. The A2 shot point is located at the southeastern end of the 95–A line and is projected to km ~62 of the S04 distance scale. Since the GRANU 95A model used a special (blocky) representation, it can be only partially compared with the regular S04 isovelocities as presented in Fig. 4. However, the basic features can be seen in both models: the HV body at ~6 km depth and the underlying LV zone extending down to about 12 km depth below and southeast of the exposed granulites.

3.2. S01 velocity pattern

The S01 profile range of interest is depicted in Fig. 6. The curve of Bouguer anomalies was derived by Švancara et al. (2005) for the reduction density of 2.67 g.cm^{-3}. The P-wave velocities are contoured at an interval of 100 m.s^{-1} over the verified model nodes extending down to the 20 km depth. As expected, no verification by refraction grid rays was obtained directly in the low-velocity zones. However, their conservation by the DRTG imaging yielded better travel-time fits of refraction rays passing through. Thanks to the results of detailed exploration at and near the KTB site, the S01 velocity model was proved to be consistent with other geophysical and geological evidence, particularly with the log velocities down to ~8 km. We refer to Novotný et al. (2009) for the detailed derivation of the S01 velocity model by the DRTG method and its geological interpretation.

As the most striking velocity features in the investigated S01 range, we observe two extensive elevations of 6600–5900 m.s^{-1} isovelocities under the Doupovské hory and the České středohoří volcanic complexes (Fig. 6). They obviously correspond to the velocity/density contrast of the ultramafic underplate which could have formed during the extensive volcanic activity related to the Eger Graben (Ulrych et al. 1999, 2002). The DHVC and CSVC represent two major centers of intra-plate alkaline volcanism in the Bohemian Massif active from the Late Cretaceous to Quaternary (Ulrych and Pivec 1997; Cajz et al. 2009). The intermediate depression down to 14 km corresponds to pre-Variscan granites forming the basement of the Žatec Basin (TBU) and of the Bílina Block in the Saxothuringian Zone. The subvertical trend of the 6100 m.s^{-1} isovelocity is interpreted as the northeastern margin of the Nejdek–Eibenstock Pluton at km 140 and the southwestern margin of the Lusatian Block at km 250 (Novotný et al. 2009).

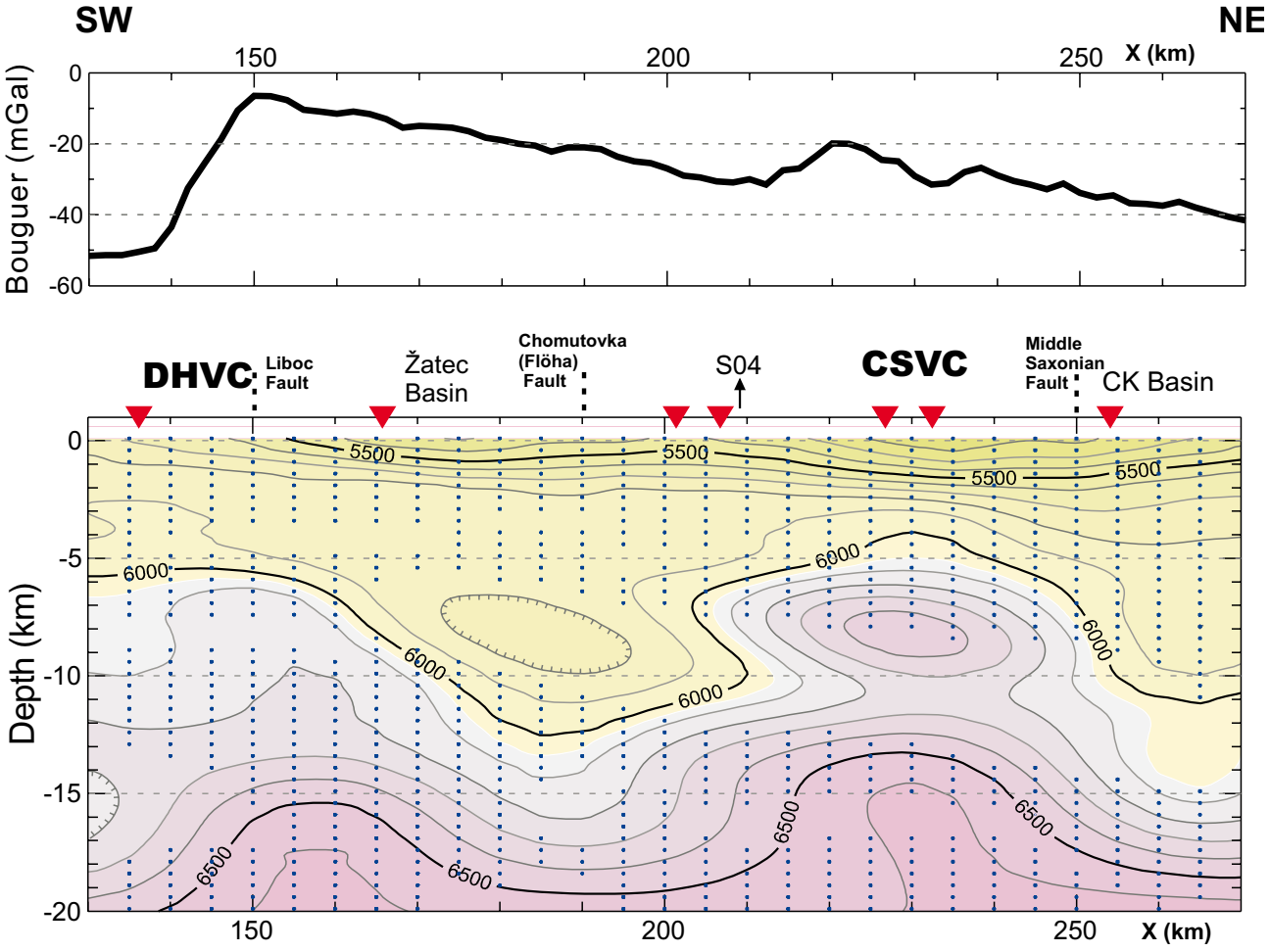

Fig. 6 The P-wave isovelocities at the 100 m.s^{-1} step along the S01 profile range of 130–270 km. The grey color starts at the 6050 isovelocity. The Bouguer anomalies were derived for a reduction density of 2.67 g.cm^{-3} (top). The dots denote the grid nodes verified by the refraction grid rays. The intersection with the S04 profile and the shot-point positions (triangles) are marked. Abbreviations: DHVC – Doupovské hory Volcanic Complex, CSVC – České středohoří Volcanic Complex, CK Basin – Česká Kamenice Basin.

The particular target of the following interpretation is the buried HV body that appears between 200–250 km or 90–140 km on the S01 or S04 distance scales, respectively.

4. Interpretation of crossing velocity patterns

The S01 profile in the 130–250 km range under investigation runs close to the contact of the Saxothuringian Zone with the Teplá–Barrandian Unit (Fig. 2). It crosses two volcanic complexes of the Doupovské hory and the České středohoří Mts. and at km ~250 it enters the Lusatian Unit (Fig. 6). The S04 profile starts in the Saxonian Granulite Massif, passes the ATC structures near their southwestern margin, then intersects perpendicularly the contact between SXT and TBU and continues to the Late Paleozoic Roudnice sedimentary Basin hidden today below the Cretaceous sediments (Figs 2 and 7). As follows from the Bouguer anomaly curve presented in Fig. 4, the S04 range is chosen to involve a wider environment of the ATC gravity minimum. The S01 and S04 intersection is located in the Bílina Block that belongs to the SXT, 10 km NW of the SXT–TBU contact. Table 1 summarizes the physical properties of main encountered rock types.

4.1. Geological model

Figure 7 presents a geological sketch based on the S04 velocity model. In the 20–60 km range, a high-velocity layer (6200–6400 m.s^{-1}) is located at depths of 4–7 km. Its occurrence is also confirmed by the forward modeling on the GRANU 95A refraction profile (Fig. 4). The underlaying low-velocity block (5800–6000 m.s^{-1}) at depths of 7–10 km may correspond to metamorphosed granitic rocks of the Saxothuringian Zone, as the labo-

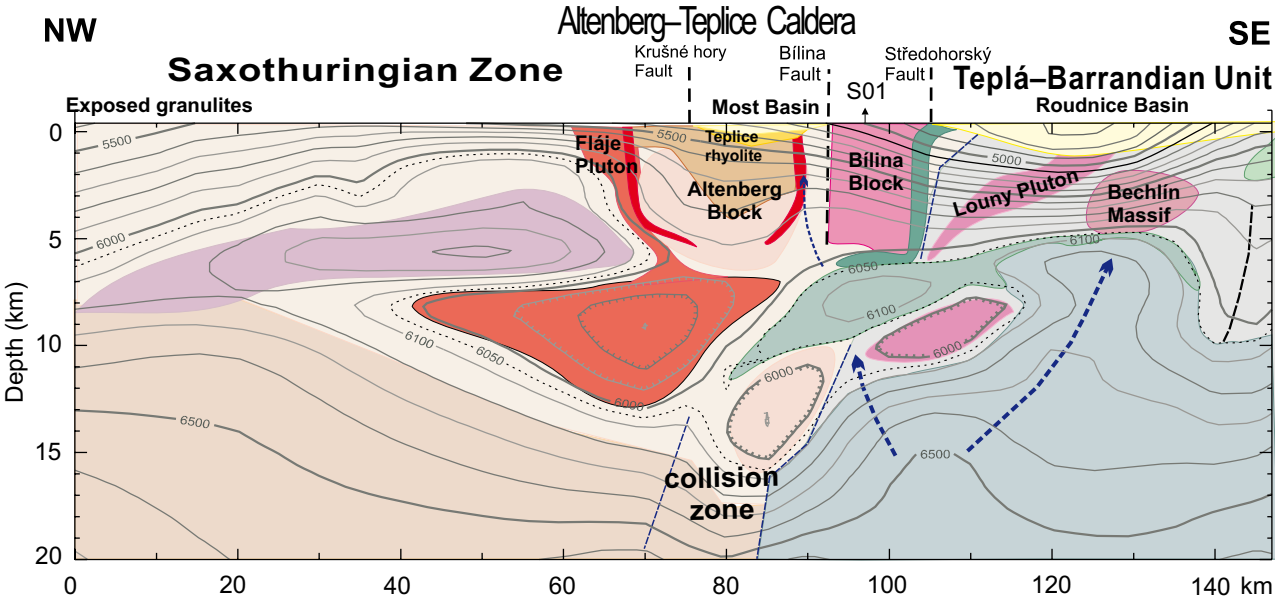

Fig. 7 Geological model inferred from the S04 isovelocities. Contour step 100 m.s^{-1}.

ratory P-wave velocities of orthogneisses are *c.* 5800–5900 m.s^{-1}. The P-wave isovelocity of 6200 m.s^{-1} characterizes the basement, top boundary of which at the depths of 8–15 km dips steeply to the SE. The maximal depth of the basement (~15 km) is reached at the collision zone between the Saxothuringian and Teplá–Barrandian units.

The S04 high and low-velocity anomalies at km 61 (Fig. 4) correlate well with the high and low reflective zones of the crossing MVE–90 time section. The intersection is located at the geophone position ~8240 (i.e. km ~362) northeast of the Flöha Zone in the Sayda orthogneiss block – see fig. 3.10, p. 704 in Behr and DEKORP Research Group B (1994). In particular, the granitic complex beneath the Sayda orthogneisses found in the MVE–90 cross-section for geophone positions of 8140–8410 reaches the Two-Way Time (TWT) down to ~1 s which agrees fairly well with the top of the uppermost high-velocity anomaly in Fig. 3 near the MVE intersection. The transparent zone of decreased reflectivity in TWT of 2.2–4.7 s, i.e. at ~6.6–15 km depth, corresponds to the intermediate LVZ. The deeper high-reflectivity zone starting from TWT ~4.7 s (i.e. from ~15 km depth) corresponds to the basement at 6200 m.s^{-1} reaching ~15 km depth at the intersection (km 61) with the MVE–90 (Fig. 7). Note that the geological interpretation of MVE–90 time section (illustrated by the above-mentioned fig. 3.10 of Behr and DEKORP Research Group B 1994) has shown that the transparent zone extends over the Flöha Zone, as far as 12–17 km southwest of the S04–MVE intersection.

Further southeast (60–90 km along the profile), the S04 velocity pattern images the southwestern margin of the Altenberg–Teplice Caldera that represents the largest region of the Late Paleozoic acidic volcanism in the Bohemian Massif. Recent studies (e.g. Štemprok et al. 2003) distinguished two phases of felsic magmatism in this area. The Fláje Pluton represents an older intrusion, whereas the younger granitic magmatism is represented by a series of granitic intrusions (e.g. the Cínovec–Krupka Composite Massif) accompanying the Teplice rhyolite and the granite porphyry dykes, also referred to as Altenberg–Frauenstein microgranites.

Based on thermobarometric study of melt inclusions in quartz phenocrysts, Müller et al. (2005) deduced at least two distinct depth ranges of magma storage, namely at 6–13 km and 17–24 km. The deep magma reservoir of the Eastern Erzgebirge Magmatic Complex was considered as a main source for the Teplice rhyolite, Schellerhau granite and granite porphyry (Altenberg–Frauenstein microgranite). Except for the northern margin, the granitic Bílina Block is fringed by metabasites and ultramafic rocks that are exposed in the Porta Bohemica area (see the bedrock edition of the geological map by Mlčoch 1994). A narrow ultramafic rim of the Bílina Block is also indicated in the gravity field (Figs 5 and 8). In agreement with the S04 velocity features (Fig. 7) and the results of inverse gravity modeling (Fig. 8), the contact zone between the Saxothuringian and the Teplá–Barrandian units is located under the Bílina Block at depths of 5–10 km. The collision zone generally dips to the northwest, which is in accord with the geological interpretation of this part of the SXT–TBU boundary by Mlčoch and Konopásek (2010).

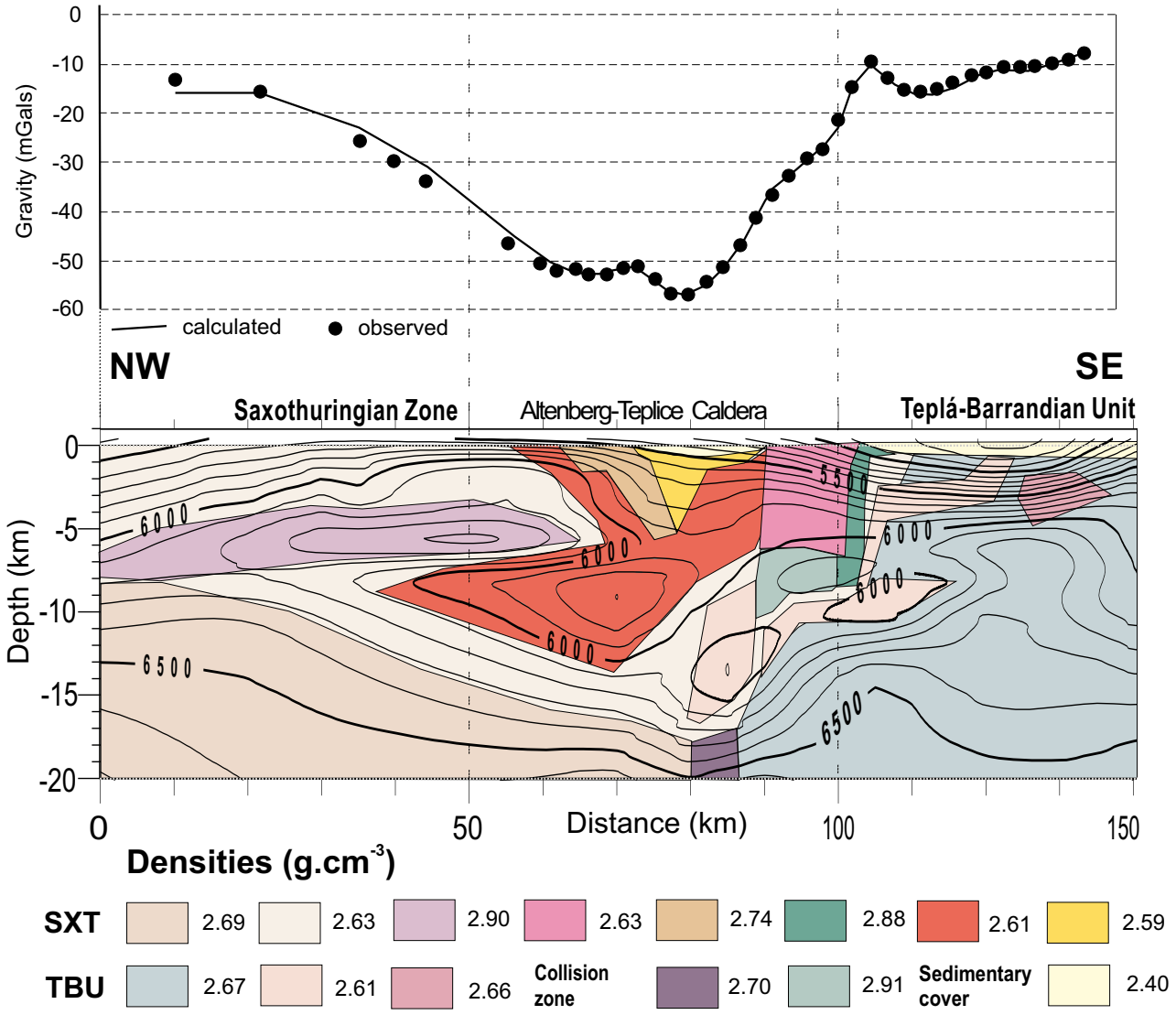

Fig. 8 S04 density model fitting the ATC gravity minimum. Block densities in g.cm^{-3}. Overlain are the S04 isovelocities (km.s^{-1}).

4.2. Density model

The S04 velocity model and its correlation with the deep reflection MVE–90 profile and gravity data constrain the position and thickness of the ATC structures. Mlčoch and Skácelová (this volume) describe a shallow geological model of the ATC based on the borehole database and reflection seismic data. To verify the P-wave velocities at the S04 cross-section we deduced a simple density model (Fig. 8) that fits the Bouguer anomaly along the S04 line near the ATC gravity minimum. The densities used for the single model blocks are in conformity with the physical properties (apparent bulk density D_o, mineralogical density D_m, porosity and velocity Vp – see Tab. 1) of the assumed rock types – granites and orthogneisses. At depths 10 to 12 km, the density model involves the occurrence of rocks with low P-wave velocities (5500–6000 m.s^{-1}) and low densities of *c.* 2.62–2.63 g.cm^{-3}. Similarly, the previous interpretation of MVE–90 transect (DEKORP 1999) estimated the thicknesses of the Fláje, Schellerhau and Sadisdorf granites to be 9–12 km and of the Teplice intrusion zone with the Altenberg granite porphyry dykes to 10–15 km.

4.3. Magmatic emplacement

Generally, the velocity image best records the high-density (mantle-derived) magmatic intrusions that show

Tab. 1 Bulk (D_o) and mineralogical density (D_m), directional P-wave velocities of representative rock types in the individual geological units

Rock type	Density D_o g.cm^{-3}	Density D_m g.cm^{-3}	Porosity %	P-wave velocities (m.s^{-1}) mean	max	min	Number of samples
granite (Čistá–Jesenice Composite Pluton)	2.63	2.64	0.8	5700	–	–	22
granodiorite (Čistá–Jesenice Composite Pluton)	2.62	2.66	1.1	5900	–	–	76
Bechlín diorite (Čistá–Jesenice Composite Pluton)	2.84	2.87	0.6	6400	–	–	128
Teplice rhyolite (Altenberg–Teplice Caldera)	2.63	2.66	1.0	6200	–	–	18
granite (Cínovec–Krupka Composite Massif)	2.60	2.64	1.1	6000	–	–	115
phyllite (Teplá-Barrandian Unit)	2.72	2.76	1.4	–	6300	5200	10
metabasite (Teplá–Barrandian Unit)	2.90	2.95	1.7	7400	–	–	26
orthogneiss (Saxothuringian Zone)	2.59	2.66	2.6	5700	–	–	110
paragneiss (Saxothuringian Zone)	2.66	2.73	2.6	–	6200	5400	92
amphibolite (Porta Bohemica, Saxothuringian Zone)	2.86	2.92	1.9	6300	–	–	8
dark granulite (Saxothuringian Zone)	2.87	2.92	1.5	–	6700	6000	5
light granulite (Saxothuringian Zone)	2.63	2.67	0.9	5310	–	–	7
gabbro	2.95	3.10	0.4	6500	–	–	4
pyroxene diorite	3.10	3.10	0.5	6700	–	–	2

a distinct density/velocity contrast against the surrounding lower density crustal rocks. Gravity differentiation in the ascending magmas causes a considerable decreasing velocity gradient along the magma ascent path or, more precisely, along the magmatic channels axes. The created contrast may persist after the solidification of magma and we can observe it, e.g., as positive P-wave velocity anomalies bound to these magma-ascent conduits.

Let us search such signatures near the ATC region in the middle crust. According to the lateral resolution achieved in the velocity sections, our analyses may document (multiphase) magmatic channels of regional scale, rather thousands than hundreds of meters wide, in dependence also on the persisting velocity contrasts.

Distinct elevations on the 6600–6300 m.s^{-1} isovelocities at the depths of 15–13 km can be observed in both S04 and S01 sections at km 105 and 230, respectively (Figs 4 and 6). Their depth range corresponds to the deeper magma reservoir assumed by Müller et al. (2005) for the ATC volcanic region. Moreover, next velocity elevations on the 6000–5500 m.s^{-1} isovelocities can be traced at the S04 cross-section along a conduit aiming at the ATC region – see the assumed magma paths marked by arrows in Fig. 7.

The root path of magma is divided at ~15 km depth into two branches: the northwestern one, leading towards the ATC, and the southeastern one, reaching as shallow level as ~3 km near the Bechlín Massif (Figs 2, 7 and 8). At 85–130 km, both branches create a magmatic body doming from 9 to 5 km depth at the 6050 ms^{-1} isovelocity (Fig. 4). This magmatic body in the S01 cross-section acquires a rather diapir-like shape – see the 6050 ms^{-1} isovelocity near the S04 intersection in the S01 velocity pattern (Fig. 6). It may correspond to the shallower ATC reservoir, whose existence was predicted by Müller et al. (2005). According to the density model (Fig. 8) it could have supplied lighter, crust-derived melts in accord with the acidic volcanism observed in the ATC region. As follows from the S04 velocity image (Fig. 4), the northwestern conduit feeding the shallow magma reservoir is disrupted at ~ 11 km depth. Then it continues into upper crust at km 90 as marked by the elevations on the 6050 up to 5500 ms^{-1} isovelocities. The conspicuous interruption of this magma conduit at ~11 km is likely caused by faulting in the collision zone (Fig. 7) and perhaps also by stoping processes, presumably in later phases of magmatic emplacement. The low-velocity host rocks in the crossing S01 profile were interpreted as pre-Variscan granites (Novotný et al. 2009).

The S04 velocity pattern delineates the upper-crustal conduit (km 85–95) aiming at the ATC region located further to the NW. The elevations observed on the 6050–5500 m.s^{-1} isovelocities trend upward along the Bílina Fault and mark a magma ascending path (Fig. 7). The Bílina Fault at km 90 separates the crystalline rocks of the Bílina Block from the Tertiary sediments of the Most Basin (see Fig. 2 for its trace in the crystalline basement). The magma channel confined to this fault zone is assumed to have supplied the crust-derived melts.

The S01 velocity pattern portrays the discussed magma reservoirs in the SW–NE transect (Fig. 6). Their upper boundary, marked by the 6050 ms^{-1} isovelocity, rises upward at km 230. Here, the S01 velocity image reveals an upwelling under the Doupovské hory and České středohoří volcanic complexes – see, for instance, Ulrych et al. (1999) with Cajz et al. (2009). The local maxima of depicted 6000 and 5900 ms^{-1} isovelocities (Fig. 6) indicate magma conduits trending upwards into the volcanic regions. They may also be the sources of the ultramafic and mafic rocks (peridotite, serpentinite,

pyroxene granulite and charnockite) found as xenoliths in the Tertiary volcanic rocks of the České středohoří Mts. (Opletal and Vrána 1989). Based on the S01 and S04 sections, the reservoir covers an extensive subsurface area of 40×50 km^2.

5. Discussion and conclusions

The Altenberg–Teplice Caldera region is located near the contact zone where the Saxothuringian rock assemblages were thrust over the Teplá–Barrandian Unit (Mlčoch and Konopásek 2010). The contact is represented by the gravity-defined Litoměřice Deep Fault (e.g. Šťovíčková 1973) following the escarpments of the České středohoří and Střezov faults (Fig. 2). According to the geological map, an 8 km shift of the SXT–TBU contact is observed between the steep gravity gradient at the depth and the actual geological boundary (Mlčoch 2003; Mlčoch and Konopásek 2010). The boundary below the Bílina Block is documented in the velocity and density model (Fig. 8). Within the presented velocity and density models (Figs 7 and 8), the SXT–TBU collision zone can be further traced under the ATC region down to ~20 km depth.

As documented by the S04 and S01 cross-sections, rather complex velocity image of the SXT–TBU collision zone probably results from several phases of magmatic activity and associated stoping processes affecting the host rocks and ascending melts during magmatic intrusions. The magmatic body discovered close to the S04–S01 intersection was interpreted as a shallower subvolcanic magmatic reservoir for the Altenberg–Teplice Caldera and the České středohoří Volcanic Complex. Contouring by the 6050 ms^{-1} isovelocity, it covers a subsurface area of *c.* 2000 km^2 at 9–5 km below the surface. Another deeper reservoir demonstrated by a pronounced elevation on the 6500 ms^{-1} isovelocity at the 15–13 km depth is assumed to feed the shallower reservoir observed in 9–5 km depths. The depth ranges of both reservoirs are in agreement with the two levels of magma storage predicted by Müller et al. (2005) for Eastern Erzgebirge Volcano–Plutonic Complex. The feeding channels are clearly manifested in the S04 and S01 velocity images by the sequences of elevations on P-wave velocity contours whose maxima delineate the ascending paths of intruded magma.

The interpretation of the key velocity features obtained by the 2-D refraction tomography is neither comprehensive nor unique. The DRTG method however yielded relatively consistent results at the intersection of the S04 and S01 profiles. Figure 9 presents the depth velocity curves extracted from the DRTG models at their intersections: 96 km at S04 and 209 km at S01 distance scales. A fair correlation can be seen in the whole depth range. Particularly, both DRTG sections consistently imaged the

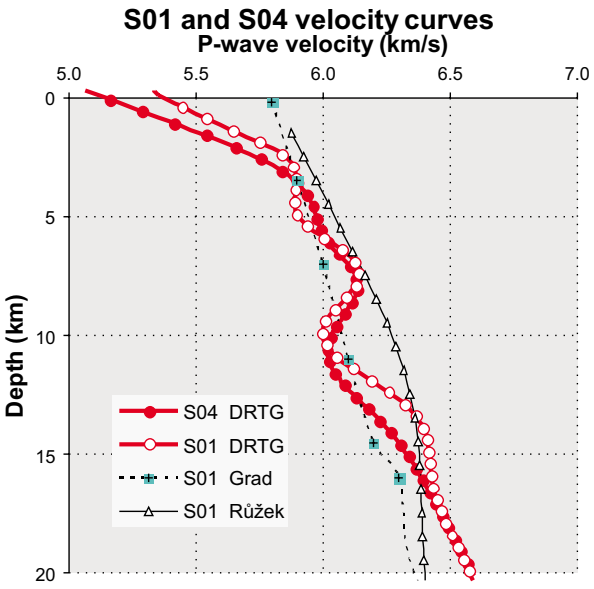

Fig. 9 P-wave velocities at the S01 and S04 intersection obtained by the DRTG and other methods – see text for details.

LVZ most profound at 10–12 km depths. The northwestern continuation of this LVZ was also found by forward ray-tracing in the GRANU 95A profile (Fig. 4) and is thus confirmed independently.

For the sake of completeness, Fig. 9 shows the results of the previous interpretations by Růžek et al. (2007) and Grad et al. (2008) derived from their final S01 models. Although the comparison of these models just for one x-coordinate may not be representative on the whole, the sweeping out of the LVZ in both previous models can be inferred. For further discussion of low-velocity zones imaging by refraction tomography we refer to Novotný et al. (2009).

We believe that the consistent results of the DRTG tomography on both the S01 and S04 transects provide a reliable P-wave velocity image of magmatic centers below the Altenberg–Teplice Caldera and volcanic complexes of the Eger Graben.

The velocity model derived on the nearby GRANU95A profile was used for the geodynamic study of high-pressure granulites exhumation in the Saxothuringian Zone (Franke and Stein 2000). Since the S04 velocity pattern represents a southeastern continuation of the GRANU-95A section, the presented velocity patterns allow extension of the geodynamic model toward the southeast, across the collision zone with the Teplá–Barrandian Unit.

Acknowledgments. This study was supported by the Project No A300460602 of the Grant Agency of the Academy of Sciences of the Czech Republic. The research was further financed by the Ministry of Education, Youth and Sports of the Czech Republic through

the Research Centre 1M0554 "Advanced Remedial Technologies and Processes". The acquisition of the used S01 and S04 seismic data within the SUDETES 2003 Refraction Experiment were supported by the Research Project No 630/3/02 funded by the Ministry of Environment of the Czech Republic. The authors are grateful to O. Novotný, O. Krentz and R. Keller for their careful reviews, which contributed to improvement of this paper. Our thanks also belong to V. Janoušek and J. Konopásek for their thorough editorial work and useful critical comments.

References

Bucha V, Blížkovský M eds (1994) Crustal Structure of the Bohemian Massif and West Carpathians. Academia, Prague and Springer-Verlag, Berlin, pp 174–177

Cajz V, Rapprich V, Erban V, Pécskay Z, Radoň M (2009) Late Miocene volcanic activity in the České středohoří Mountains (Ohře/Eger Graben, northern Bohemia). Geol Carpath 60: 519–533

Behr HJ and DEKORP Research Group B (1994) Crustal structure of the Saxothuringian Zone: results of the deep seismic profile MVE–90 (East). Z geol Wiss 22: 647–769

DEKORP and Orogenic Processes Research Groups, Krawczyk CM correspondent (1999) Structure of the Saxothuringian granulites: geological and geophysical constraints on the exhumation of high-pressure/high-temperature rocks in the mid-European Variscan belt. Tectonics 18: 756–773

Enderle U, Schuster K, Prodehl C, Schulze A, Bribach J (1998) The refraction seismic experiment GRANU95 in the Saxothuringian belt, SE-Germany. Geophys J Int 133: 245–259

Fediuk F (2005) The Lower Vltava River Pluton: a semi-hidden intrusive complex in Neoproterozoic at the northern outskirts of Prague, Central Bohemia. J Czech Geol Soc 50: 71–78

Franke W, Stein E (2000) Exhumation of high-grade rocks in the Saxo–Thuringian belt: geological constraints and geodynamical concept. In: Franke W, Haak V, Oncken O, Tanner D (eds) Orogenic Processes: Quantification and Modelling in the Variscan Belt. Geological Society London Special Publications 179: 337–354

Grad M, Špičák A, Keller GR, Guterch A, Brož M, Brückl E, Hegedüs E (2003) SUDETES 2003 seismic experiment. Stud Geophys Geod 47: 681–689

Grad M, Guterch A, Mazur S, Keller GR, Špičák A, Hrubcová P, Geissler WH (2008) Lithospheric structure of the Bohemian Massif and adjacent Variscan belt in central Europe based on profile S01 from the SUDETES 2003 experiment. J Geophys Res 113: B10304, DOI: 10.1029/2007JB005497.

Guterch A, Grad M, Špičák A, Brückl E, Hegedüs E, Keller GR, Thybo H (2003) An overview of recent seismic refraction experiments in central Europe. Stud Geophys Geod 47: 651–657

Krawczyk CM, Stein E, Choi S, Oettinger G, Schuster K, Götze HJ, Haak V, Oncken O, Prodehl C, Schulze A (2000) Geophysical constraints on exhumation mechanisms of high-pressure rocks: the Saxo–Thuringian case between the Franconian Line and Elbe Zone. In: Franke W, Haak V, Oncken O, Tanner D (eds) Orogenic Processes: Quantification and Modelling in the Variscan Belt. Geological Society London Special Publications 179: 303–322

Matte P, Maluski H, Rajlich P, Franke W (1990) Terrane boundaries in the Bohemian Massif: result of large-scale Variscan shearing. Tectonophysics 177: 151–170

Mlčoch B (1994) The geological structure of the crystalline basement below the North Bohemian brown coal Basin. KTB Report 94 (3): 39–46

Mlčoch B (2003) Character of the contact between the Saxothuringian and Teplá–Barrandian Unit. Geolines 16: 75

Mlčoch B, Konopásek J (2010) Pre-late Carboniferous geology along the contact of the Saxothuringian and Teplá–Barrandian zones in the area covered by younger sediments and volcanics (western Bohemian Massif, Czech Republic). J Geosci 55: 81–94

Mlčoch B, Skácelová Z (2010) Geometry of the Altenberg–Teplice Caldera revealed by the borehole and seismic data in its Czech part. J Geosci 55: 217–229

Müller A, Breiter K, Seltmann R, Pécskay Z (2005) Quartz and feldspar zoning in the eastern Erzgebirge volcano–plutonic complex (Germany, Czech Republic): evidence of multiple magma mixing. Lithos 80: 201–227

Novotný M (in prep.) P-wave velocity image of Bohemian Massif at the S04 transect. To be submitted.

Novotný M, Skácelová Z, Mrlina J, Mlčoch B, Růžek B (2009) Depth-recursive tomography along the Eger Rift using the S01 profile refraction data: tested at the KTB super drilling hole, structural interpretation supported by magnetic, gravity and petrophysical data. Surv Geophys 30: 561–600

Opletal M, Vrána S (1989) Charnockite xenoliths in the Tertiary volcanites of the České středohoří Mts., northern Bohemia. Sbor geol věd, Geol 44: 51–78 (in Czech)

Pitra P, Burg JP , Guiraud M (1999) Late Variscan strike-slip tectonics between the Teplá–Barrandian and Moldanubian terranes (Czech Bohemian Massif). J Geol Soc, London 156: 1003–1020

Růžek B, Hrubcová P, Novotný M, Špičák A, Karousová O (2007) Inversion of travel times obtained during active seismic refraction experiments CELEBRATION 2000, ALP 2002 and SUDETES 2003. Stud Geophys Geod 51: 141–164

Sedlák J, Gnojek I, Zabadal S (2007) Zhodnocení anomálií gravitačního a magnetického pole v okolí vrtu PVGT LT–1. Assessment of gravity and magnetic anomalies near the PVGT LT-1 borehole. Unpublished manuscript, Geomedia Ltd., Prague and Miligal Ltd., Brno, (in Czech)

Sedlák J, Gnojek I, Zabadal S, Scheibe R, Zabadal S (2009) Gravity response of igneous rocks in the northwestern part of the Bohemian Massif. J Geosci 54: 325–342

Šalanský K (1995) Magnetic map of the Czech Republic 1:500 000. Czech Geological Survey, Prague

Štemprok M, Holub FV, Novák JK (2003) Multiple magmatic pulses of the Eastern Volcano–Plutonic Complex, Krušné hory/Erzgebirge Batholith, and their phosphorus contents. Bull Geosci 78: 277–296

Šťovíčková N (1973) Hlubinná zlomová tektonika a její vztah k endogenním geologickým procesům. Deep fault tectonics and their relation to endogenous processes. Academia, Prague, pp 1–198 (in Czech)

Švancara J , Špaček P, Hubatka F (2005) Geophysical image of regional geological structures and verification of crustal velocity models. In: Novotný M (ed) SLICE-Seismic Lithospheric Investigation of Central Europe (Chapter 3). Unpublished final report, Czech Geological Survey–Geofond, Prague, pp 1–215 (in Czech)

Ulrych J, Pivec E (1997) Age-related contrasting alkaline volcanic series in North Bohemia. Chem Erde 57: 311–336

Ulrych J, Pivec E, Lang M, Balogh K, Kropáček V (1999) Cenozoic intraplate volcanic rock series of the Bohemian Massif: a review. Geolines 9: 123–135

Ulrych J, Svobodová J, Balogh K (2002) The source of Cenozoic volcanism in the České středohoří Mts., Bohemian Massif. Neu Jb Mineral, Abh 177: 133–162

Journal of Geosciences, 55 (2010), 201–215 DOI: 10.3190/jgeosci.075

Original paper

Tectonic setting of the Ohře/Eger Graben between the central part of the České středohoří Mts. and the Most Basin, a regional study

Vladimír CAJZ[1*], Jaroslav VALEČKA[2]

[1] *Institute of Geology, Academy of Sciences CR, Rozvojová 269, 165 02 Prague 6, Czech Republic; cajz@gli.cas.cz*
[2] *Czech Geological Survey, Klárov 3, 118 21 Prague 1, Czech Republic*
[*] *Corresponding author*

The paper presents the results of a new detailed survey in the SW part of the České středohoří Mts. (a section of the Ohře/Eger Graben/Rift), focused on its tectonic setting. Courses of the SE marginal graben faults are traced in detail. This limiting fault zone is described as a horst, with the graben fill being structured into rhomboidal blocks; older known faults are specified, and new faults are depicted. Respecting the age ranges of the preserved stratigraphic units, fault movements are classified into those older than 36 Ma, younger than 24 Ma and younger than 16 Ma (with a possible age less than 9 Ma), based on different lithologies and abrupt lithological changes (i.e., the rock boundaries). The faults are compared with the earlier defined paleostress fields. Fault reversals were detected on several faults. An important role of crystalline basement ridges during the graben formation was identified: three complex tectonic structures are spatially associated with these ridges. Two areas with distinct tectonic and geological development were defined within the Ohře/Eger Graben. The Saxothuringian – Teplá–Barrandian terrane boundary was found to be less important for graben formation during the Cenozoic. This disagrees with simplified riftogenic model of the Ohře/Eger Graben. The supposed *"Litoměřice Deep-seated Fault"*, possibly representing a first-order terrane boundary, could not be confirmed in the post-Paleozoic rocks – this structure did not function as a fault during Cenozoic times.

Keywords: surface-detected faults, timing of tectonic activity, Ohře/Eger Graben/Rift, Bohemian Cretaceous Basin, České středohoří Volcanic Complex, Most Basin
Received: 28 May 2010; accepted: 15 September 2010; handling editor: V. Kachlík

1. Introduction

Since the papers of Kopecký (1974, 1978), the Ohře/Eger Graben has been believed to represent a rift structure. This idea was a modern one at its time; nevertheless, it has not been generally accepted. An unclear tectonic setting was one of the main reasons for rejection of the rift idea, especially by geologists with detailed knowledge from the field (e.g., Hurník and Havlena 1984; Malkovský 1987). Contrary to their opinion, the rift concept is accepted worldwide (Wilson and Downes 1991; Ziegler 1992; Dèzes et al. 2004; Haase and Renno 2008). Such situation calls for a regional research aimed at the character and timing of tectonic activity. This is one of the possible approaches which can contribute to better knowledge of the origin of this graben.

At present, the courses of fault zones limiting the Ohře/Eger Graben (EG) are generally well known. The direction of the České středohoří Fault Zone (CSFZ – limiting the EG in the southeast) became better defined during the detailed survey on scale 1:10 000 (Šebesta et al. 1997; Valečka et al. 2003, 2008). The course of the Krušné hory Fault Zone (limiting the EG in the northwest) and the related movements were identified very well in the area of lignite mining.

Internal tectonic structure of the EG is still much less known compared to that of the limiting fault zones. Cajz et al. (2004) published newly discovered faults in the central and eastern parts of the České středohoří Volcanic Complex (CSVC) and Rajchl et al. (2009) clarified tectonic conditions during sedimentation of the Most Basin (MB) fill. This paper tries to combine these two separate areas inside the graben, presenting the results of a detailed survey from the region in between. It should be emphasized that the current study deals with tectonic deformations visible only in the post-Paleozoic sediments and volcanic products. Moreover, it is based on faults identified in outcropping geological units. It is not the aim of this paper to compare these structures with the supposed tectonic setting of the basement.

New faults were found in the area defined approximately by the cities of Bílina, Teplice, Ústí nad Labem and Lovosice, i.e., between the central part of the CSVC and the sedimentary fill of the MB (Fig. 1). The course of several faults belonging to the CSFZ was specified more precisely. The faults are vertical or very steeply inclined. Dip-slip faults were mostly detected, but strike-slip and combined movements are also present. Typically, some of the faults were reactivated several times during the history and the movements on their fault planes may

have undergone reversals. Unfortunately, the fault planes could not be traced along their full length and only their near-surface segments are described.

Much of the volcanic material has been eroded from the studied region. Rocks of Variscan basement and Cretaceous sediments beneath the volcanics are exposed, being partly covered by sediments of the MB and by the youngest volcanic products. This setting is complicated by tectonic movements during the formation of nearly all geological units. The result of possible movements on the fault – i.e., the vector sum – can be determined based on the field survey and the evaluation of borehole data. The timing of the movements can be estimated from the age of the stratigraphic units deformed. The authors wish to emphasize that the vertical movement attributed to the individual faults and their parts is time-dependent and the total displacement magnitude as observed today only expresses the vector sum. Unfortunately, not all data necessary for an accurate interpretation are always available from the survey and borehole evaluation.

2. Lithostratigraphic units used for fault detection

Saxothuringian crystalline basement is exposed in the Oparno Valley, in the city of Bílina and its close surroundings and several isolated bodies are located south of the highest peak, Milešovka Hill. Carboniferous rocks are represented mainly by rhyolite deposited as a pyroclastic flow (ignimbrite) produced from the Teplice–Altenberg Caldera. Less frequent are conglomerates. These rocks are exposed especially in the Oparno Valley, covering the crystalline basement, and in the Bílina area.

Upper Cretaceous rocks are present in a complete succession described by Čech et al. (1980). Paleogene sediments have been preserved over a small area only. Volcanics of the CSVC are developed in all formations as defined by Cajz (2000) and Cajz et al. (2009). Sediments of the Most Basin are represented by sands of the Bílina delta. Typical fine-grained basinal sediments are developed as well, especially in the northern and northwestern part of the study area.

2.1. Upper Cretaceous

Facial and spatial development, together with the uniform thicknesses of the lithostratigraphic units described below, indicate tectonic stability of the study area during the Late Cretaceous sedimentation. The area got involved in the Bohemian Cretaceous Basin (BCB) mainly due to long-term rise of global sea level; subsidence played a subordinate role. This is in great contrast to the zone farther NE (closer to the Lusatian Massif) where a rapidly subsiding zone (depocentre) developed immediately at the beginning of sedimentation (Valečka 1989; Uličný et al. 2009a). In that zone, the thicknesses of sedimentary units increase almost by the factor of five. The exceptional tectonic stability came to an end in the Coniacian. Then, the study area was subjected to the same tectonic regime as the other parts of the BCB. The relatively rapid and continuous subsidence resulted in high thicknesses of monotonous calcareous pelites of the Březno Fm.

The ***Peruc–Korycany Fm***. *(Cenomanian)* consists of the Peruc and Korycany members. The Peruc Mb. (thickness max. 23.7 m), filling only narrow depressions in the basement, is characterized by upwards-fining fluvial cycles. The cycles begin with sandstones or conglomerates and end with claystones, locally with high amount of organic matter. Sandstones of the Korycany Mb. (thickness max. 40–50 m) cover a wider area but are missing at basement elevations.

The ***Bílá hora Fm***. *(Lower–Middle Turonian)* (max. 73.5 m) is mainly developed in the form of silicified spiculitic marlstones or spongolites ("*opuka*" in Czech). These rocks pass downward to mudstones, and to glauconitic, calcareous sandstones, 1–3 m thick, at the top of the formation. Near the Most–Teplice Elevation (see below), sandstones predominate, and shallow-water biosparitic limestones were locally deposited.

The ***Jizera Fm***. *(Middle–Upper Turonian)* is represented by marlstones, less frequently by biomicritic limestones, 2.5–40 m thick. They progressively overlap the top of the Most–Teplice Elevation. In places, basal conglomerates with blocks of material abraded from local basement rocks occur at several levels, indicating several transgression phases (Čech and Valečka 1991).

The ***Teplice Fm***. *(Upper Turonian–Lower Coniacian)* consits of alternation of marlstones and biomicritic limestones, representing a characteristic development; the thickness reaches 35–55 m. In the lower part, the limestones concentrate to a sequence 7–12 m thick. A distinct basal bed with high glauconite content, phosphatic nodules, phosphatised fauna and coprolites, with a sharp, erosive lower contact represents a correlative horizon in the whole BCB.

Rohatce Member *(Coniacian)* – marlstones with hard, silicified limestone beds as a typical marker; max. thickness 25 m. They occur in the eastern and central parts of the area. To the west, the hard beds wedge out and pass into marlstones.

The ***Březno Fm.*** *(Coniacian–Lower Santonian)* in the development of monotonous marlstones or calcareous claystones attains a complete thickness of 220–240 m.

The ***Merboltice Fm***. *(Santonian)* occurs as relics of sandstones preserved only in the southern surroundings of Ústí nad Labem in max. thickness of 70–80 m.

Quaternary

- anthropogenic deposits and excavated areas
- fluvial sediments
- coluvial sediments
- loess

Tertiary

- sediments of the Most Basin
- fossil weathered ol. basalts
- solid olivine-bearing basalts
- altered ol. basalts
- volcaniclastics of ol. basalts
- olivine-free basalts
- volcaniclastics of olivine-free basalts
- phonolites and trachytes
- quartzites

Upper Cretaceous

- Merboltice Fm. sandstones
- Březno Fm. calcareous claystones
- Rohatce Mb. marlstones, silicified limestones
- Teplice Fm. marlstones, limestones
- Jizera Fm. marlstones
- Bílá hora Fm., spongolites (opuka)
- Peruc–Korycany Fm. sandstones

Carboniferous

- rhyolite (ignimbrite)

Saxothuringian Zone

- gneisses

- faults (arrows in the subsided blocks)

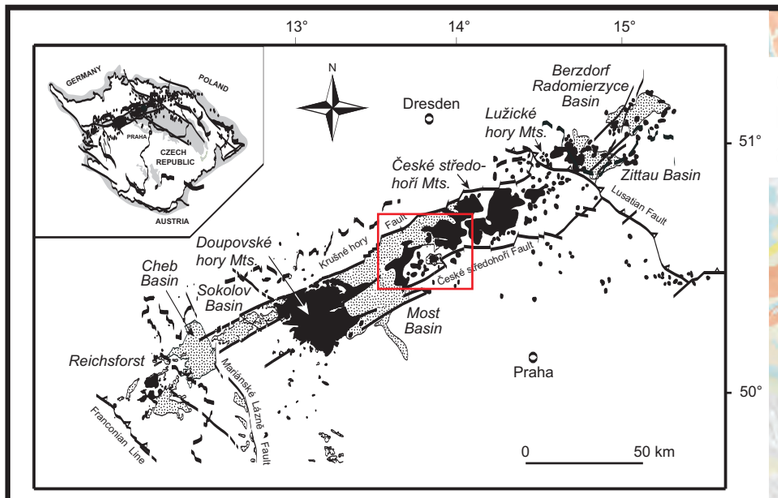

Cajz V. & Valečka J. – Tectonic setting of the Ohře/Eger Graben between the central part of the České středohoří Mts. and the Most Basin, a regional study.

BBE – Bílina Basement Elevation
OBE – Oparno Basement Elevation
OBH – Oparno–Břvany Horst
BTN – Bořislav Tectonic Node
MTN – Milešov Tectonic Node
HMFS – Hlince–Milešov Fault System

Fig. 1
A tectonic sketch of a geological map from the new detailed survey (Šebesta et al. 1997; Valečka et al. 2003, 2008).

2.2. Pre-volcanic Tertiary

The ***Staré Sedlo Fm***. *(Paleogene)* includes remnants of fluvial sediments of an ancient stream network. The drainage pattern was very different from the present one, transecting the course of the later formed Ohře/Eger Graben. Fluvially redeposited material of the Merboltice Fm. sandstones has been reported from Dolní Zálezly in the Labe/Elbe River valley (Šebesta et al. 1997). Relics of quartzites from several areas in the České středohoří Mts. and their close surroundings are supposed to represent a silcrete, i.e., a weathering product from hot climate in the Paleogene. In the study area, quartzites representing strongly silicified conglomeratic sandstones occur only near Lužice, overlying the Březno Fm. marlstones (Valečka et al. 2008).

2.3. České středohoří Volcanic Complex

The studied region is transitional between the central part of the complex and its margin in the Louny area. A different erosion rate can be presumed for the central and marginal parts of the complex. In addition, stratigraphy of volcanic units is more complicated than that of Cretaceous sediments, showing much less continuity. Longer periods of volcanic quiescence occurred between the depositions. The time spans of the two oldest formations partly overlap, which is caused by problems of K–Ar dating method and evaluation of its results: geological criteria show a different relationship. It is important for the survey that the two formations are easily recognizable and obey the Principle of superposition. Only the phonolitic intrusions are problematic because they may belong to either of the two oldest formations. They are, however, not fundamental in fault detection. As all these units are of continental origin, the erosion destroyed their rocks continuously during dormant periods but also during the volcanic activity. Moreover, the study area is unique by the presence of the youngest volcanic activity subsequent to the basin fill sedimentation (Cajz et al. 2009).

Ústí Fm. *(Uppermost Eocene–Lower and Middle Oligocene; 37–28 Ma)* – basanitic volcanism produced mostly into water environment (syngenetic alteration) includes sedimentary intercalations (with diatomites and lignite), fault-controlled vents and occasional terrestrial volcanoes of Strombolian type. Effusive products covered large areas in general.

Děčín Fm. *(Middle and Upper Oligocene; 31–25 Ma)* – tephritic to trachybasaltic terrestrial volcanism, large central composite volcano, many parasitic vents over a wide area, explosive and effusive activity (stratovolcanic style). Explosive and effusive products covered large areas but only remnants are present now.

Dobrná Fm. *(Upper Oligocene–Lower Miocene; 24–19 Ma)* – scattered Strombolian volcanoes of basanitic production. They were spread across the CSVC and beyond; only vents and relics of cinder cones and lavas survive.

Štrbice Fm. *(Middle and Upper Miocene; 13–9 Ma)* – isolated, mostly Strombolian volcanoes of basanitic chemistry and their subvolcanic apparatuses concentrated in the study area. The youngest volcanism of the CSVC.

2.4. Sediments of the Most Basin

Střezov Fm. *(Paleogene–Neogene)*. A lithological definition as volcanic, volcaniclastic and mixed volcaniclastic and sedimentary material below the Most Fm. is too wide, as is the stratigraphic extent. The rocks of this formation originated by weathering and transport of CSVC volcanics, and by rare volcanic activity in the area of the MB. They can be paralleled with the Ústí, Děčín and partly with Dobrná formations of the CSVC.

Most Fm. *(Neogene)* – we substitute this regular stratigraphic term by informal "sedimentary or basin fill". We do not subdivide the formation into members and we do not distinguish separate lithofacies as it is not necessary for our tectonic considerations.

3. Pre-Cretaceous relief and Late Cretaceous sedimentation

In the relief of the basement, two positive morphological forms with no sedimentation of the Peruc–Korycany Fm. can be recognized: the Oparno and Bílina basement elevations (Fig. 2). These elevations, developed already in some form before the sedimentation, strongly influenced the spatial distribution, thickness and lithofacies development of the Peruc–Korycany, Bílá hora and Jizera formations. These elevations are present in the area of the Bílina Block which is defined in the basement (*sensu* Mlčoch ed. 2001). In further text, we use names for these elevations – parts of basement outcrops because the morphological function of these older structures was very important for Cretaceous sedimentation. Both of them are parts of previously described larger structures in the basement.

The eastern ***Oparno Basement Elevation*** (OBE) is elongated in the WNW–ESE direction. It is a relatively low elevation characterized by a progressive, slow transgression of the Bílá hora Fm. The thickness of the transgressive Bílá hora Fm. attains only 1 m on top of this elevation. Far to the east from the Elbe River, the OBE continues as the Litoměřice–Maršovice–Bezděz Elevation (Vejlupek 1984; Vejlupek and Novák 1986). To the W, the OBE is linked with the Most–Teplice Elevation (Čech and Valečka 1991).

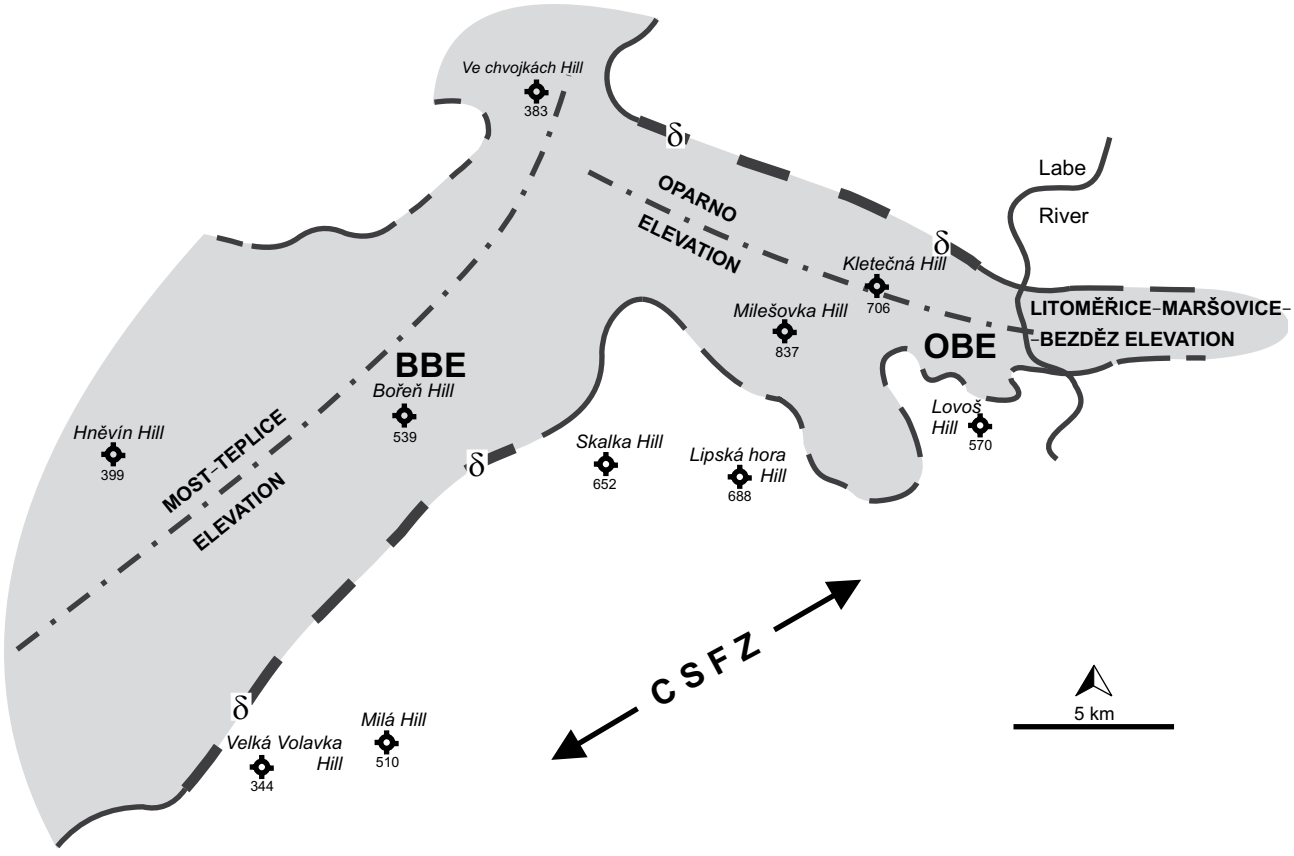

Fig. 2 Basement elevations below Cretaceous sediments. Most–Teplice and Oparno elevations boundaries: dot-and-dash line – elevation axes; grey – area of an "island" during the Peruc–Korycany Fm. sedimentation; thick dashed line with a ***δ*** symbol – elevation margins of (old ?) tectonic origin. BBE – Bílina Basement Elevation, OBE – Oparno Basement Elevation, CSFZ – České středohoří Fault Zone.

The Most–Teplice Elevation is elongated NE–SW; it was the highest elevation in the entire BCB. Its upper part is covered by the Jizera Fm. marlstones, thickness of which is reduced to 2.5 m on the top. The uncovered part of the Most–Teplice Elevation near Bílina is herein called the ***Bílina Basement Elevation*** (BBE). Its SE slope is relatively steep, possibly of tectonic origin. At the foot of the slope, a narrow depression (paleovalley) is situated with fluvial fill of the Peruc Mb. The depression is elongated in the NE–SW direction. A similar depression with the Peruc Mb. (Stebno paleovalley *sensu* Uličný et al. 2009b), oriented W–E or WNW–ESE, is present near the northern margin of the OBE, indicating its possible tectonic character.

4. Tectonic development during the latest Cretaceous and earliest Tertiary

No Cretaceous sediments younger than the Merboltice Fm. sandstones (Santonian) are present either in the study area or in the BCB. The development before the deposition of the Staré Sedlo Fm. (Paleogene) is therefore difficult to assess: it was dominated by erosion. Data from the central part of the CSVC suggest that the Paleogene fluvial sediments are composed of the same material as the Santonian sandstones. Fluvial re-deposition possibly resulted in a relative increase in kaolin proportion in the sediment in some areas. Unfortunately, the Staré Sedlo Fm. sediments are rare in the area of the CSVC, and the reconstruction of the drainage pattern is thus impossible.

Superficial rocks of the CSVC overlie the Cretaceous sediments, especially those of the Merboltice and Březno fms. In the study area, relics of the Merboltice Fm. sandstones, max. 50–70 m thick, are limited to a small area S of Ústí nad Labem. Almost as a rule, superficial rocks of the CSVC overlie the monotonous claystones of the Březno Fm., preserved commonly in the thickness of 60 to 120 m, so the identification of tectonics is very problematic. The nearly total erosion of the Merboltice Fm. sandstones and the erosion of a large part of the Březno Fm. claystones contrast with the central part of the CSVC where great volumes of these sandstones are preserved in thicknesses of up to 200 m. It can be therefore assumed that the relative tectonic uplift of most of the study area occurred before the onset of volcanic activity. Tectonic

style with rhomboidal blocks, similar to that detected in the central part of the CSVC (Cajz et al. 2004), can be supposed. This tectonic activity was followed by a long period of peneplanation, leaving no sedimentary record. The peneplanation created flat morphology with shallow depressions, due to the stream network draining the area. This time was coeval with the deposition of the Staré Sedlo Fm. Superficial rocks of the CSVC therefore overlie the Cretaceous sediments with a flat or only slightly inclined topography. Tectonic disintegration into blocks can be deduced from the erosion intensity of Cretaceous sediments preserved below the superficial volcanic products of the CSVC. The borehole data evaluation resulted in the definition of two large tectonically contrasting areas resulting from pre-volcanic tectonic activity.

The beginning of volcanism was accompanied by the onset of another phase of tectonic activity. Low topography in the central part of the CSVC caused the presence of water reservoirs – most probably shallow lakes as a part of a drainage system. This was the host environment for primitive magmas of the Ústí Fm. The most subsided area was situated approximately between the Ploučnice Fault (F.) in the NE (beyond the study area) and a line between the OBE and BBE in the SW. This area can be understood as the real central part of the CSVC: it represents the oldest Tertiary depocentre in the graben, situated transverse to the EG course. Volcanism of the Ústí Fm. was accompanied by continued tectonic activity. Formation of deep and narrow syn-volcanic depressions is known at several places (Cajz et al. 2004).

5. Description of individual faults

The tectonic scheme drawn in a geological map (Fig. 1) is based on a new detailed survey and evaluation of borehole data. Generally, the structures can be subdivided into faults pertaining to the CSFZ in the SE and other structures of the internal part of the graben. Alternatively, they can be subdivided into parallel and transverse ones relative to the general graben course.

5.1. Faults parallel to the general Ohře/Eger Graben course (ENE–WSW)

5.1.1. Faults of the CSFZ

Müller (1924) for the first time, and consequently Hibsch (1926), coined the term České středohoří Fault to describe the single but morphologically prominent tectonic structure apparently limiting the České středohoří Mts. in the SE. Later, this term was used by Malkovský (1977, 1979). The same fault was named Litoměřice Fault by Váně (1985, 1999) and Herčík et al. (2003). Štovíčková et al. (1973), Kopecký (1978) and Malkovský (1979) considered this fault to represent the epitectonic manifestation of an old suture in the crystalline basement (the Saxothuringian – Teplá–Barrandian terrane boundary), designated as *"Litoměřice Deep-seated Fault"*. Similar idea was invoked by Pešek (1996) to explain the supposed northern tectonic limit of the Permo-Carboniferous sedimentary basins underlying Cretaceous sediments. Moreover, the rift concept of the EG (Kopecký 1978) was based on the existence of this deep structure and especially on its activation during the Cenozoic. Lastly, Cháb (2008) assumed the České středohoří Fault and the Ohře Fault, or a Fault Zone (more to the SE), to represent tectonic manifestations of the "Ohře/Eger Rift".

Our new detailed survey proved the existence of a complicated fault zone on the SE foot of the České středohoří Mts., but its origin can be hardly connected with rifting as directly as has been assumed. We use the term České středohoří Fault Zone, but we describe its course in a considerable detail and decipher its different tectonic development. This structure only very generally parallels the České středohoří or the Litoměřice faults of previous authors. We traced the course of the CSFZ from the valley of the Labe/Elbe River between Lovosice and Litochovice in the NE to Břvany in the SW (see Fig. 1). The zone consists of four to six parallel or nearly parallel faults, and is intersected by several younger transverse faults. The CSFZ strikes NE–SW between the Labe River valley and Třebenice; far to the SW, the strike changes for ENE–WSW. The width of this zone is very high in the E (5 km between Velemín and Lovosice) but decreases to 2.5–3 km in the SE. Some faults in the zone branch off, some vanish. The vertical displacement of the southern blocks is very moderate, reaching a few tens of meters only. The CSFZ is an asymmetrical structure. Blocks uplifted to the highest tectonic position in the whole area concentrate only approximately along the northern border of the CSFZ, forming a horst structure. We call this structure the ***Oparno–Břvany Horst*** (OBH). The uplifted blocks of the OBH are composed of spiculitic marlstones and spongolites (opukas) of the Bílá hora Fm., locally with relics of the Jizera Fm. marlstones. In some blocks in Oparno–Velemín area, gneisses and migmatites of the Krušné hory/Erzgebirge Crystalline Complex (Saxothuringian Zone) are exposed beneath Carboniferous rhyolitic ignimbrites and Cretaceous opukas. The strike of the OBH does not follow the course of the CSFZ in detail, it coincides only very generally. The width of the OBH is 1.5–1.7 km between the Labe River valley and Velemín, in a segment striking ENE–WSW. The strike of the OBH turns to NE–SW between Velemín and Podsedice, with the width locally reduced to 100 m. In this part, the OBH is fragmented into many small blocks, displaced by transverse strike-slip faults (Fig. 3).

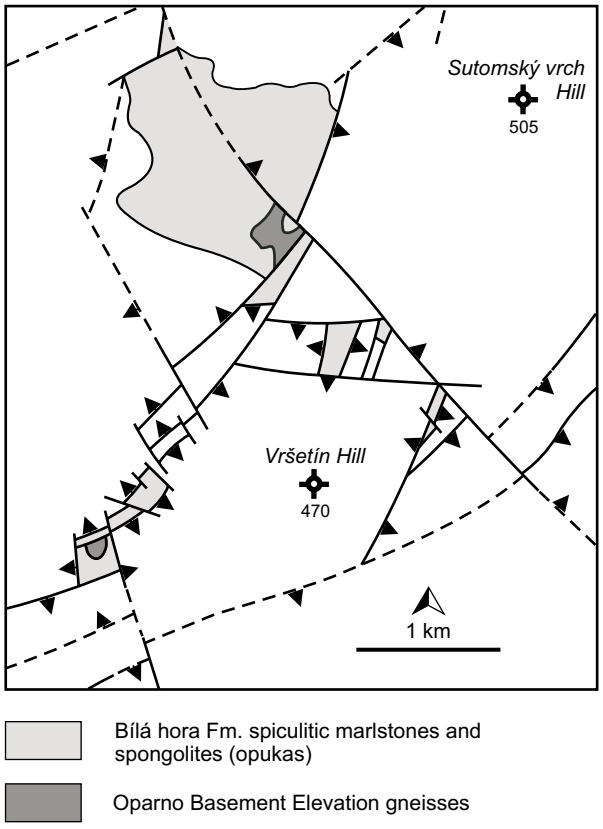

Fig. 3 Detail of the Oparno–Břvany Horst (OBH) in the surroundings of Vlastislav.

At Podsedice, the horst merges with the common course of the CSFZ, returning to the ENE–WSW strike. In the segment between Podsedice and Břvany, the structure of the CSFZ is simpler, consisting of only two border faults. The OBH is one of the most prominent tectonic structures in the study area. Only its part near Břvany has been described before: Váně (1999) reported an uplifted "horst-like" block limited by the ***Břvany*** and ***Hrádek faults***, having a width of up to 2.5 km. We adopted these names for the border faults of the OBH along most of its course between Břvany and the Vlastislav–Teplá area. Between the Labe River valley and Velemín, the border of the OBH is linked with the ***Litochovice F.*** (Vejlupek and Kaas 1986) and the newly documented Chotiměř F. (Kycl et al. 2009). On the Litochovice F., relative subsidence of the northern block attains the highest value – approx. 150–200 m. This is the place, where the strike of the OBH is parallel to the axis of the OBE in the basement. In the Velemín area, the horst departs from this elevation generally to the S and proceeds as far as to Třebenice. From Třebenice to the W, the horst strikes ENE–WSW again. From Velemín, relative subsidence of blocks N and NW of the OBH decreases to several tens of meters only. The high vertical displacement magnitude on the Litochovice F. splits into several faults of different strikes. This very complicated point is herein called the ***Milešov Tectonic Node*** (MTN).

The general strike of the CSFZ only partly coincides with the "*Litoměřice Deep-seated Fault*" idea. The detailed course of the OBH is completely different from the latter. This is why we cannot agree with the simplified model of tectonic setting of the graben, which led to the rift concept. We only agree with the idea of Pešek (1996), in which the southern border of the CSFZ coincides – for some fault segments – with the tectonic boundary of Permo–Carboniferous sedimentation and the Saxothuringian Crystalline basement. To the SW of Charvatce (beyond the study area), the CSFZ runs several kilometers to the north of this older tectonic boundary.

5.1.2. Faults inside the Ohře/Eger Graben and parallel to its course

This subgroup can be divided into semi- and subparallel faults. The most important semiparallel fault is the ***Litochovice F***., described above as the northern limit of the OBH in the OBE area. This is the fault with the largest vertical displacement in the whole study area, functioning as the southern limit of the oldest Cenozoic depocentre of volcanic products. Its continuation, the Velemín F. (as far as to the MTN), is ranked among transverse faults due to its E–W strike. The subparallel ***Štěpánov F***. represents the next continuation to the SW but its vertical displacement magnitude reaches only 50 m now, which is caused by younger movement of opposite sense detected in the volcanics. Farther to the SW, a fault of the same strike – the ***Hrobčice F***. – shows a subsided southern block and limits the area of crystalline rock outcrops SE of Bílina. Farther S and SW, the subparallel ***Skršín F***. and ***Dobrčice F***. were detected with subsided northern blocks. The ***Žichov F***. of the same strike shows an opposite sense of the sum of movement. The displacement magnitudes on these faults are several tens of meters. These three faults were formerly supposed to represent only a single one, which was called the Skršín F. over a larger distance (Valečka and Zelenka 2008).

Very important is the subparallel ***Kostomlaty F***. (see also below) which limits a rhomboidal and relatively small block of the Děčín Fm. volcanics, uniquely preserved in this area, which deeply subsided at the times of volcanic activity. An equivalent fault limiting this block from NW is the ***Bukovice F***. Another important subparallel ***Straky F***. is situated in the NW part of the study area, limiting basinal sediments in the NW. Other parallel faults are located in the northern part of the area and their strike and displacement are mostly constructed from borehole data evaluation. Among these, the ***Trmice F***. should be mentioned as the longest of the detected structures.

Ostrý F., which separates the vent and the cinder cone of the youngest volcano from its lava plateau, is characterized by a displacement of a few tens of meters with an uplift of the northern block. This fault movement ranks among the youngest in the area. This structure was activated much earlier with an opposite sense of movement. It forms the NW limit of a block with the most strongly eroded Březno Fm. claystones. The last structure worth mentioning is the ***Kletečná F***., which is covered by debris, material of slope movements and loess and thus difficult to detect on the surface. It runs across NW foothills of Kletečná and Milešovka hills with subsided NW blocks in the very complicated area of the ***Bořislav Tectonic Node*** (BTN). The course of the Kletečná Fault and tectonic reversals in its history were detected from borehole data. Pre-volcanic movements were characterized by a subsidence of the southern block, while the syn- or post-volcanic movements of even higher magnitude featured a subsidence of the northern block. The currently detectable displacement magnitude is nearly 150 m.

5.2. Faults transverse to the course of the Ohře/Eger Graben

5.2.1. Faults striking generally NW–SE

These faults in the CSFZ strike nearly perpendicular to its course, causing lateral offsets in either direction. The most important ones are (from the SW to the NE): the ***Měrunice F***. limiting one of the larger OBH blocks, with a subsided SW block. It continues to the NW with this block uplifted due to younger movement. Its further continuation is the ***Liběšice F***. (*sensu* Valečka and Zelenka 2008) with an inverted movement of the sunken SW block. This part of the Liběšice F. can be synonymized with the Želenice F. of Zahálka (1914). The ***Želkovice F***. (*sensu* Valečka and Zelenka 2008) limits the OBH with a subsided SW block; it continues to the NW as the newly detected ***Mukov F***. with the resulting opposite sense of movement. The ***Chrášťany F***. and the ***Teplá F***. form the limits of the narrowest, further segmented block(s) of the OBH in a similar manner. Their continuation to the NW was impossible to detect. The ***Vchynice F***. and the ***Žernoseky F***. offset the OBH very close to the OBE with a more easily detectable strike-slip movement (see Fig. 1).

Other transverse faults were detected in the central part of the graben. A complicated structure is typical of the westernmost part of the study area. The NNE–SSW-striking ***Sedlec F***. was activated in at least two periods, with opposite senses of movement. The ***Lužice F***. and the ***Korozluky F***. limit the extent of basinal sediments, the ***Lužice F***., together with the parallel ***Jánský F***., constitute a micrograben in volcanics where porcelanites (basinal sediments with a coal seam exposed to subaerial weathering) are preserved. In the centre of the study area, the ***Hlince–Milešov Faults System*** (HMFS) is developed between the MTN and the Kostomlaty F., moreover crossing the Kletečná F. Unfortunately, no magnitudes of the relative subsidence of NE blocks on the HMFS are available. Farther to the N, the ***Lbín F***. with the NE uplifted block and the ***Žalany F***. with the SW uplifted block limit the extent of the basin fill. The ***Žalany F***. terminates a deeply subsided volcanic block near Bukovice, as well. The NW–SE-striking ***Bystřany F***. and the ***Nechvalice F***. constitute a horst-like volcanic block uplifted from basinal sediments. In contrast, the ***Řehlovice F***. and the ***Habrovany F***. constitute a micrograben of the same trend filled with basinal sediments preserved among blocks with much older volcanics. Both faults possibly terminate at the Vaňov F.

In the Labe/Elbe River valley, several faults or segments of N–S strike were detected. They possibly determine the course of the river. Among them, only the Prackovice F. is important with the E block subsided by nearly 100 m. Other faults do not show any important vertical displacement, but rather a strike-slip component.

5.2.2. E–W trending faults

Faults of this trend were responsible for the Neogene formation of depocentres in the Most Basin (Rajchl et al. 2009). In the studied region, they are present but much less frequent than described from the neighboring area by the same authors. The ***Bílina Fault*** is supposed to represent one of the most important structures of the region. Unfortunately, this term has been used in different sense. The structure of the Bílina "Crevasse" was first described by Zahálka (1914) as an E–W-striking fault south of the town of Bílina with only 20 m vertical throw and a short along-strike length of max. 2 km. Hibsch (1924) used the name ***Bílina–Lyskovice F***. for a supposed fault limiting the extent of crystalline rocks and striking ENE–WSW, possibly running across the town of Bílina. Only two segments of this supposed fault are shown, 4 km apart, on the map of Hibsch (1924). It was proposed to separate the southern crystalline block from deeply subsided northern block with preserved Cretaceous and Miocene sediments. Later, during mining activities, the Bílina F. was indeed detected north of Bílina. It strikes ENE–WSW with a subsidence of the northern block by about 70 m (or up to 100 m) as far as to its junction with the E–W-striking Victoria Fault (old miners' name). From this point on, both faults show a subsidence of the northern block by only 35 m farther to the W or WSW. The Centrum F. (old miners' name), which is subparallel to the Victoria F., shows similar vertical displacement. The split of a large vertical displacement magnitude on one fault into several

faults with smaller throws is a situation analogous to that we have encountered at complicated tectonic points – tectonic nodes. Some authors (e.g., Brus and Hurník 1988; Rajchl et al. 2009) supposed an E–W strike of the Bílina F. The confusion in the definition of the strike comes possibly from Hibsch's text (1924) – *"... the Bílina F. is accompanied by several E–W trending faults ..."* – or from the general course of a suspected hidden structure (Mlčoch ed. 2001). In the latest printed map, Kopecký ed. (1990) considered the Bílina F. as running from Braňany to the northern environs of Bílina, with generally ENE–WSW strike. These authors described several faults (a fault zone) striking ENE–WSW and E–W as the Bílina Fault. Valečka (1990) suggested a continuation of the Bílina F. far to the E, as far as to the Labe River valley, evaluating boreholes in the Cretaceous sediments. The E–W-striking Bílina F. in the present concept runs farther to the E, forming an important tectonic structure in the basement (Mlčoch and Konopásek 2010). Unfortunately, it is impossible to track this fault in the volcano-sedimentary cover in the same way. Only our ***Štrbice F***. and ***Velemín F***. follow this direction over a relatively short distance. They both have deeply subsided northern blocks (over 100 m). Farther to the E, the Štrbice F. terminates at the Kostomlaty F. – the high values of vertical displacement can be tracked in a different strike subparallel to the graben axis.

Another important E–W structure was described as the ***Vaňov F***. (Cajz et al. 2004). In the Labe/Elbe River valley, the right-lateral strike-slip movement prevails on its planes and the effects of faulting are partly responsible for present slope movements in the river canyon. A similar situation is encountered where this fault reaches the Bílina River valley. Far to the W, this fault continues with a more distinct vertical displacement and a subsided northern block. An indication of a tectonic reversal during the fault history is locally present.

The formerly described Žim F. (Cajz et al. 2004) is better visible with an E–W strike on the left bank of the Labe/Elbe River. It can be followed for several hundred meters to the west, before it merges with the semiparallel Kletečná Fault. The N–S course of the river changes for the E–W in Ústí nad Labem. This is caused by a left-lateral strike slip along an E–W-striking fault with some vertical component. It splits a phonolite laccolith into the Mariánská skála Hill and the Kamenný vrch Hill parts (Ulrych et al. 2000).

6. Zones of largest vertical displacement and conclusions for riftogeny

The question of the position of the possible "*rift margin*", i.e. that of the largest-magnitude normal faulting, is very difficult to answer. In any case, it does not follow the terrane boundary where "*the main deep-seated fault driving the rift development*" (*sensu* Kopecký 1974 and others) has been expected. The ***Litochovice F***. with the largest known vertical displacement (min. 150–200 m) is semiparallel to this boundary and follows the ***OBE*** better (Fig. 4). Its continuation, the ***Velemín F***., is transverse (E–W) and this highest value is detectable as far as to the ***MTN*** only. From here, the ***Štěpánov F***. with a younger reduced vertical displacement magnitude continues semiparallel to the central part of the EG and disappears at the Mukov Fault. From the ***MTN***, the ***HMFS*** with NE subsided blocks is developed. The ***HMFS*** can be tracked as far as to the ***Kostomlaty F***. (with NW deeply subsided block, min. 100 m) and is connected with the ***Štrbice F***. (subsidence of northern block well exceeding 100 m). The Štrbice Fault follows the Bílina F. of modern definition in the basement (e.g. Mlčoch 2003; Mlčoch and Konopásek 2010) in the limitation of the Bílina Block.

Both these complicated orientations of the largest dip-slip are problematic from the viewpoint of the "*rift course*". The only structure roughly conformable with the "*rift course*" is the ***OBH*** (see Fig. 4). The subsidence of northern blocks was, however, very modest, reaching several tens of meters, much like at the CSFZ itself. Moreover, another zone of large vertical displacement magnitude (*c*. 100 m) is present, transverse to the graben axis. It is the ***Žalany F***. connected with the ***Kostomlaty F***., which are situated in the central part of the graben.

The movements on any deep structures responsible for the graben formation must be traced superficially, in the exposed rocks older than the tectonic remobilization. From this detailed study we can conclude that for the formation of the graben with Cenozoic volcanic infill was the existence of the ***Oparno*** and ***Bílina basement elevations*** much more important than the presence of the Variscan terrane boundary. This study permits to define two separate areas, distinct in their geological development, at least during the Cenozoic. The border between them is formed by a wider E–W-striking zone represented by the OBE in the E, and the BBE in the W. This zone can be paralleled with the basement Bílina F. (*sensu* Mlčoch and Konopásek 2010). In the general direction to the N to ENE of this border, deeply sunken areas are filled with products of the oldest volcanism. A very moderately subsided area in a shape of "dish" is present generally to the S to WSW. In terms of riftogeny, only the approximate course of the CSFZ (with SE dips on subparallel faults) may express the possible upwelling during the rift formation with some *"deep-seated"* structure partly involved. Thus, the importance of the CSFZ as a manifestation of any deep-seated structure seems to have been overestimated.

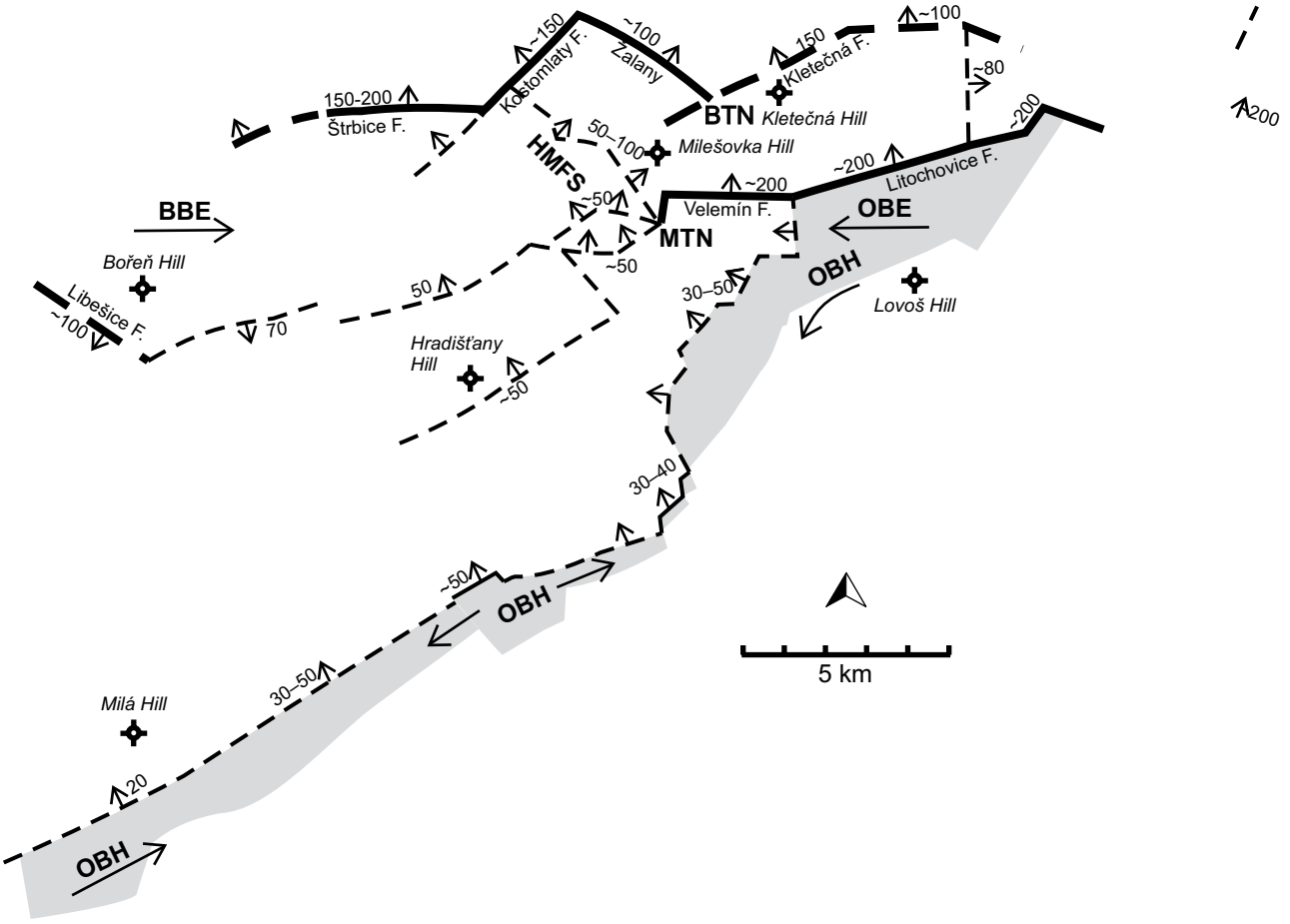

Fig. 4 Graben-forming faults: Oparno–Břvany Horst (OBH) – its highest blocks in grey; Oparno Basement Elevation (OBE); Bílina Basement Elevation (BBE). Also shown are tectonic nodes of Milešov (MTN) and Bořislav (BTN), as well as the complicated Hlince–Milešov Faults System (HMFS). The largest vertical displacement magnitudes on faults limiting the graben are given in meters. Arrows – resulting relative vertical movement of blocks (vector sum); arrow in the subsided block.

7. Timing of tectonic activity

Brittle deformation structures offset different stratigraphic units, which gives information on the age of the tectonic activity. This is, however, not exact enough. We also evaluated borehole data providing information on older movements, assuming that the stratigraphic unit is covered by a younger one. Other criteria are represented by paleogeomorphology and lithology of both sediments and volcanics. These are the reasons which permitted us to group the faults by the detected or assumed age into three groups. On the other hand, we know that the use of such criteria should be taken as a very rough time constraint only.

A) post-Cretaceous/pre-volcanic faults (Fig. 5) – formed before the volcanic activity, some of them being almost coeval with the onset of the volcanic activity. This group includes faults of the CSFZ and of the OBH. We believe that these "limiting" faults are older ones, with the major movements taking place prior to volcanic activity. Only the SE-dipping faults of the CSFZ may be partly caused by the subsequent possible upwelling of the region. Transverse faults segmenting both these structures are younger. Reaching the Labe/Elbe River, the strike of the CSFZ – parallel to the axis of the OBE – turns to the E. The existence of the basement ridge played an important role. The Litochovice F. is situated above the northern steep slope of the OBE which may be of (older?) tectonic origin as well. In its continuation, the Velemín and Štěpánov faults possibly also represent products of pre-volcanic tectonic activity. We therefore suppose their formation simultaneous with the CSFZ.

Faults with the largest dip-slip of the northern (NE to NW) blocks (see Fig. 4) can be assigned to this group, as well. They could have been partly coeval with the onset of volcanic activity. These faults are situated inside the graben. Based on the detected erosion of Cretaceous cover on the OBE, it can be assumed that the activity of the Štrbice (Bílina) F. also started at about the same time.

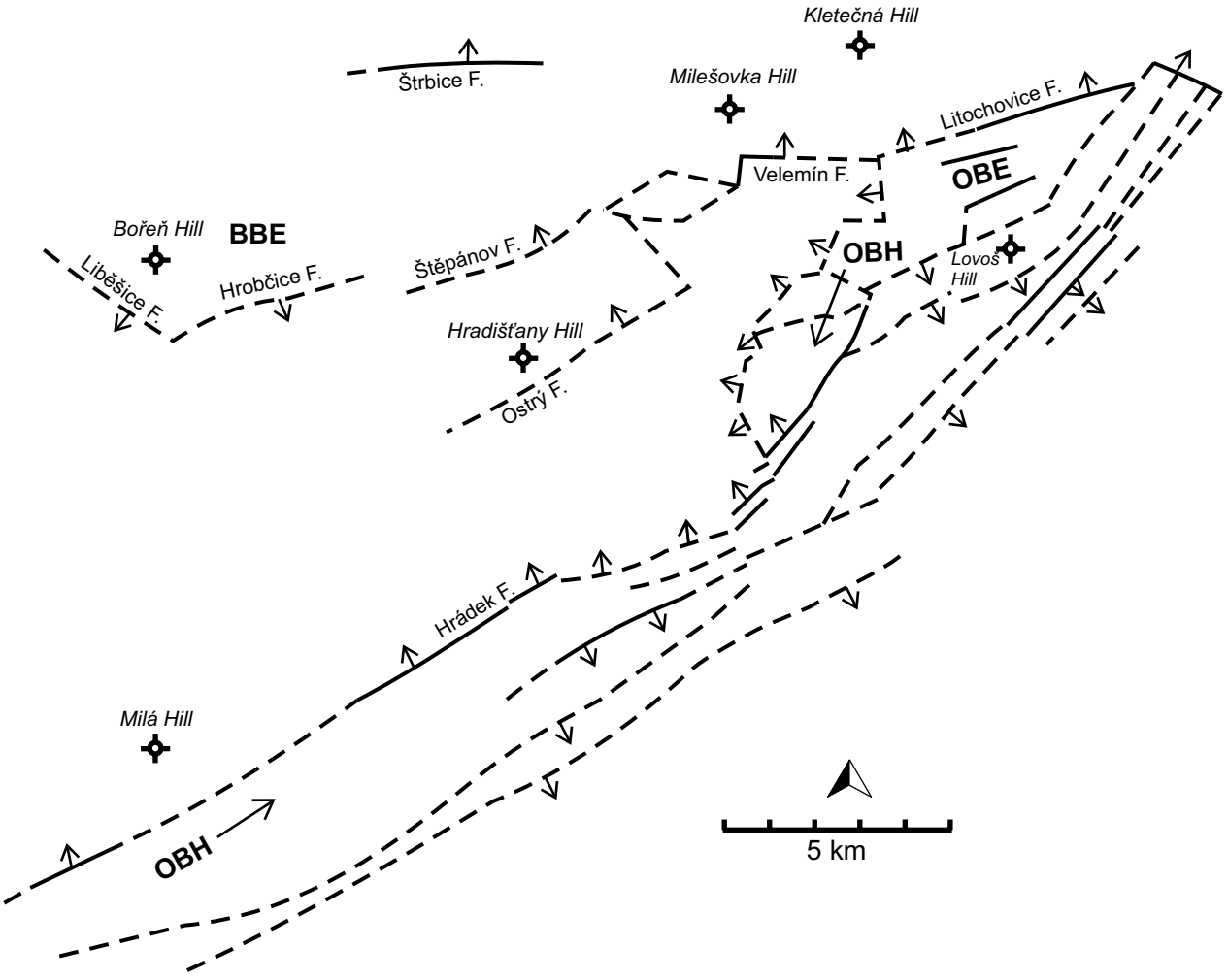

Fig. 5 "A" faults – post-Cretaceous/pre-volcanic, older than 36 Ma. Arrows – time-constrained relative vertical movement of blocks; arrow in the subsided block.

B) intravolcanic faults (Fig. 6) – younger than the Ústí and Děčín formations of the CSVC. Unfortunately, no accurate relationships are known between the faulting and the Dobrná Fm. volcanics. The age of these faults can be therefore supposed to be less than 24 Ma. This corresponds well with the idea of tectonic remobilization necessary for the Dobrná Fm. (24–19 Ma) magma ascent (Cajz 2000). It is important that the movements of this time were dominated by relative subsidence of northern blocks (NW to NE). The deeply subsided volcanic block near Bukovice was formed contemporaneously. It includes lahars and lavas of the Děčín Fm. composite volcano, exceptionally far from the central part of the complex. The E–W-oriented strike-slip movements, both right- and left-lateral, can be observed in older volcanics but their age may be younger. The most prominent among them is the Vaňov Fault. Tectonic reversals were found at the Štěpánov and Hrobčice faults. Movements on the Štrbice F. continued with the subsidence of northern block at this time.

C) post-depositional / ***post-volcanic faults*** (Fig. 7) – disrupting and/or limiting the basin fill and possibly younger than the Late Miocene volcanism (13–9 Ma). Faults activated at this time only accentuate the block setting. Smaller graben-like structures (Habrovany–Řehlovice and Lužice–Jánský faults) and horst-like structures (Nechvalice–Bystřany faults) were formed nearly perpendicular to the general graben course. Some of the movements were of opposite sense relative to older ones. This is most significant at the Žalany F., where the fault limited the deeply subsided Bukovice Block from the NE and subsequently determined the area of basinal sedimentation from the SW. The Štrbice F. was activated again. Demonstrably youngest are the last movements on the Ostrý F., which separates two blocks – one with a relict of a cinder cone and its vent, and another one with

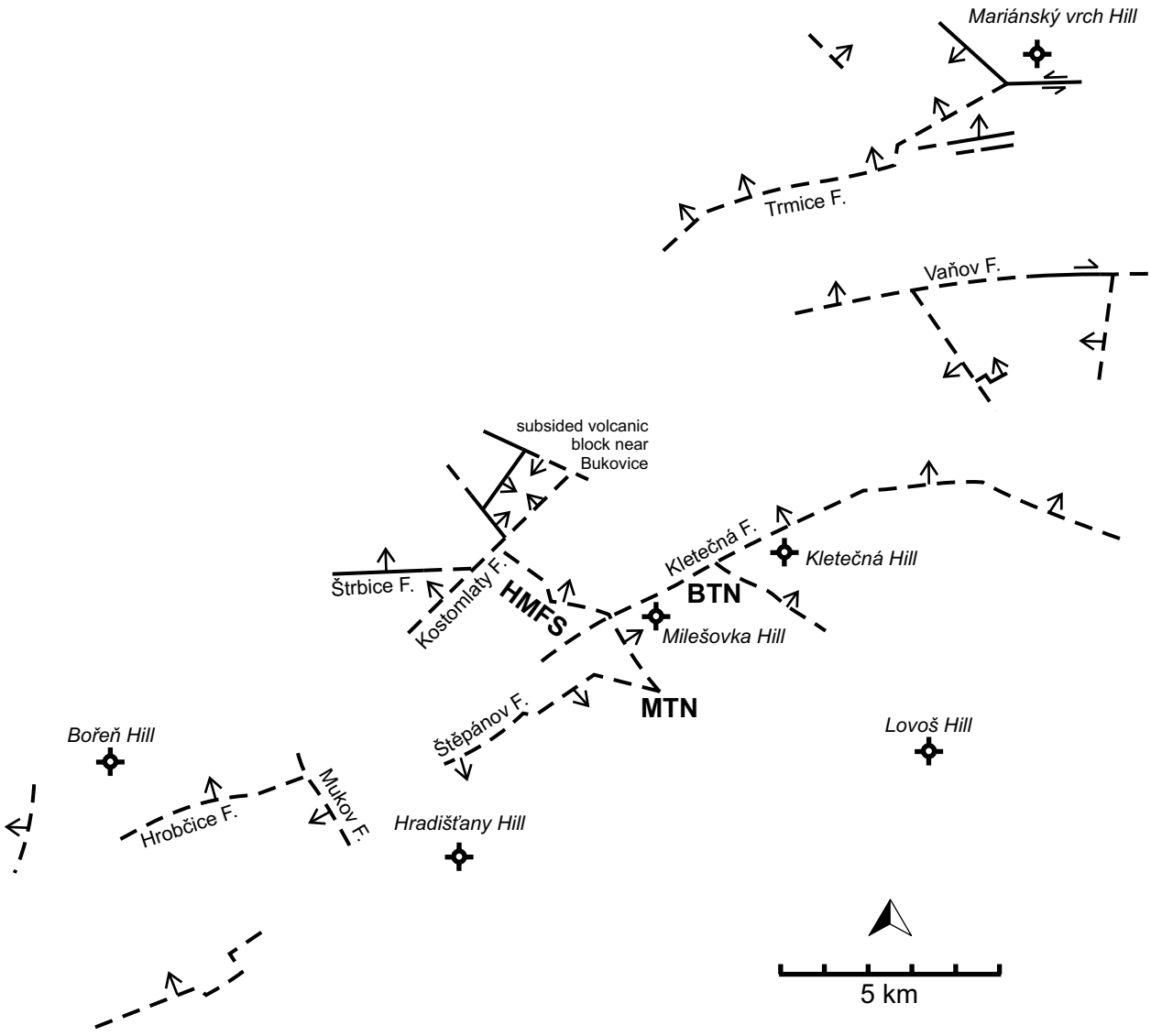

Fig. 6 "B" faults – syn-volcanic, younger than 24 Ma. Arrows – time-constrained relative vertical movement of blocks; arrow in the subsided block.

lava belonging to this vent. The uplifted NW block was detected due to the excessively high base of lava (Cajz et al. 2009) and verified by boreholes reaching different lithological boundaries in Cretaceous sediments. The age of the movements on faults of this group is less than 16 Ma, and possibly younger than the Štrbice Fm. volcanics – 9 Ma (at least at some of the faults).

8. Discussion

The above presented age categories of faults are based on the recognized movements on each of them; they represent time ranges with verified uppermost age constraint recorded in the current geological setting. As the topmost units have been eroded from the study area, there may have existed younger movements on these faults than those used for their age assignment. To be sure about the precise age constraints, study and evaluation of small-scale brittle tectonic phenomena is needed. A field survey itself cannot be used for the determination of the paleostress tensor during the fault activation. Nevertheless, the function of faults can be compared with the paleostress field reported to be in operation at the given time:

Our ***A-faults*** (post-Cretaceous/pre-volcanic; older than 36 Ma – see Fig. 5) coincide in time with tectonic phases $\boldsymbol{\beta}_1$ and $\boldsymbol{\alpha}_2$ of Adamovič and Coubal (1999, 2009). Since the dip orientations of the fault planes could not be

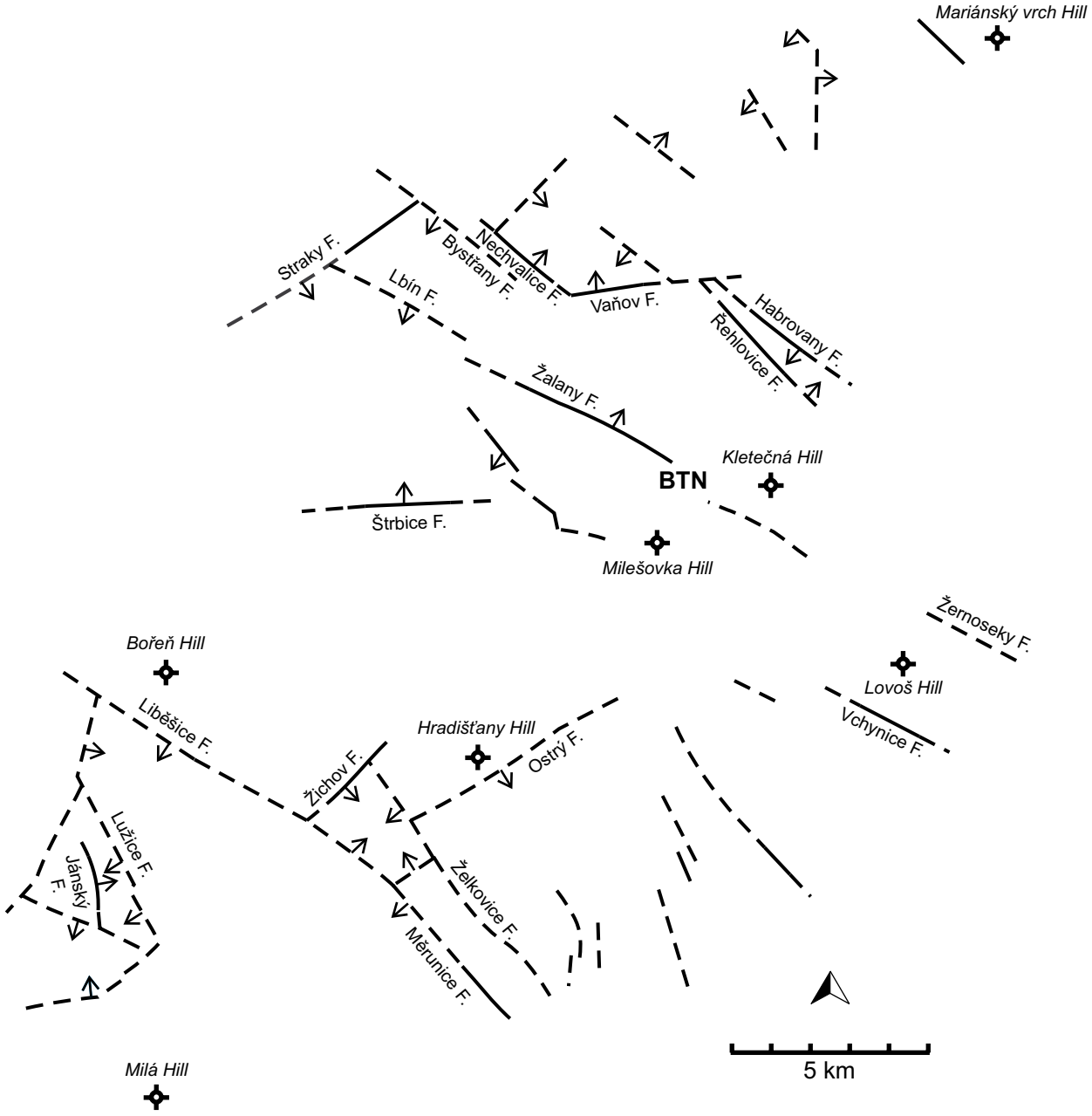

Fig. 7 "C" faults – post-depositional/post-volcanic, younger than 16 Ma (possibly 9 Ma). Arrows – time-constrained relative vertical movement of blocks; arrow in the subsided block.

studied in the field, their kinematics (normal vs. reverse faulting) could not be determined. Nevertheless, their preferred WSW–ENE to SW–NE strikes demand nearly perpendicular orientation of stress in both cases. Then, only α_2 can be applied, which would imply a reverse movement under NNW–SSE compression. Then, no extension can be expected on the CSFZ during upwelling, and the upwelling itself is questionable. From this point of view, the riftogenic model is difficult to apply. A better explanation is that the CSFZ formation resulted from the stress relaxation after the α compressive stress fields. This idea would apply an orientation of this tensor in a N–S or, even better, NNW–SSE direction, which is slightly different from what has been published. The ascent of primitive basaltic magmas (Ústí Fm.) would have been the most easily achieved under extensional conditions.

B-faults (intravolcanic; younger than 24 Ma – see Fig. 6) mostly coincide with β_3 NW–SE extension, and some of them may be slightly older to coincide with β_2 N–S extension. No preferred orientation in their courses

can be found. In extensional conditions, normal faults should develop. And extensional conditions are expected to allow the ascent of primitive magmas (Dobrná Fm.).

C-faults (post-depositional/post-volcanic; younger than 16 Ma and some of them possibly than 9 Ma – see Fig. 7) correspond in time to compressions γ and δ (from nearly E–W to N–S) or to the younger tensional field ε (Coubal and Adamovič 2000). The fault strikes are predominantly transverse to the graben axis and the constitution of smaller horst- and graben-like structures is characteristic. Formation of these structures is possible under the supposed stress field. The mostly short faults transverse to the CSFZ and causing its segmentation may belong to this fault group. Their strike is parallel to the dominant strikes of faults in the graben interior at this time. Compressional fields γ and δ could have produced both sinistral and dextral strike-slip movements on the transverse faults.

Exceptional is the Štrbice F. which was active in the same style (subsidence of N block) during all periods and during all paleostress fields. Normal movements on this fault are obvious, which corresponds with β_1, β_2 and β_3 fields but not with α_2 and γ –δ fields.

All the E–W-striking faults in the study area are of behavior distinct from those in the MB sedimentary fill. In the opinion of Rajchl et al. (2009), these faults in the MB belong to the older generation, having been overprinted by NE–SW-striking structures. Our results show a different situation: the E–W faults are not overprinted by the NE–SW ones. The CSFZ (NE–SW) in the study area represents some kind of a structural barrier for the E–W faults because it was not affected by their activity. A similar situation is displayed at the termination of the Štrbice F. (E–W) at the Kostomlaty F. (NE–SW) inside the graben. On the other hand, the Štrbice F. and the Velemín F. belong among the oldest faults, as determined by the onset of their activity. Both faults are spatially connected with the basement ridges.

We suppose that the faults striking NW–SE are more important than assumed in the area of the MB (Rajchl et al. 2009). They belong among the youngest, they limit the basinal sediments and they constitute small grabens and horsts. Some of them were probably active under a tensional stress field ε. In case they overprint the older faults, then they are definitely not E–W faults, but NW–SE faults.

9. Conclusions

The České středohoří Fault Zone (CSFZ) is only roughly parallel to the graben axis. The CSFZ consists of a system of parallel faults transected by younger strike-slip faults. Along the parallel faults, southeasterly blocks subsided; the highest blocks are concentrated to the northern part of the CSFZ and constitute here the horst (OBH). The CSFZ has not a direct relationship to the presumed *"Deep-seated Litoměřice Fault"*, the supposed rift margin. The existence of a morphological ridge in the basement (OBE–BBE) played a more important role during the origin of the CSFZ than a simplified course of the Variscan terrane boundary between the Saxothuringian and Teplá–Barrandian zones. It is also possible that the tectonic setting in the basement itself is much more complicated. We suppose a post-Cretaceous/pre-volcanic formation of the CSFZ. Its origin may have been associated with a possible upwelling under a tensional paleostress field (using the riftogenic model). A change in the paleostress field was necessary for the transverse segmentation of the CSFZ. The expected largest vertical displacement magnitude is not parallel to the graben course and again, it is closely connected with the pre-existing basement ridges (OBE, BBE). Moreover, the maximum vertical displacement is reached over a relatively short distance (at the N margin of the OBE) or, more frequently, the displacement magnitude is split to several faults of different strikes in the graben interior.

In geomorphological subdivision, the CSVC is a composite regional geological unit with different settings in its central part (Milešov and Verneřice areas) and the part around Louny. This is reflected in the CSVC development as well. The Dobrná Fm. volcanics are preserved to a higher degree compared to the Ústí Fm. ones in the Louny marginal area. Volcanic activity in this part of the CSVC seems to be younger on average.

In the study area, faults in the graben interior are of variable strike. They constitute an irregular network consisting of rhomboidal blocks, very much like in the central part of the CSVC. The usual vertical displacement reaches tens of meters; it exceeds one hundred meters on several faults only. Repeated movements on some of faults were documented, both of the same sense or inverse ones. Two tectonic nodes, i.e. complicated fault intersections with the break-up of one large dip-slip into several smaller sectional ones, were defined (KTN, BTN). Also the complicated structure of the HMFS, representing wider zone interconnecting two zones of large vertical movement, was observed. These structures were spatially connected with the ridges in the basement.

The E–W-striking faults are not as frequent as described in the MB, and their age seems to be intravolcanic or younger. The Štrbice and the Velemín faults, both connected to the older structures in the basement and activated several times, may be of older origin. The E–W-striking faults do not offset the CSFZ course. This is in contradiction with the idea of their importance, activity and age in the MB. Nevertheless, faults of this strike show some of the highest magnitudes of relative

subsidence of northern blocks in total. This may reflect an E–W oriented interconnection of basement ridges (OBE and BBE), which was significant for graben formation. In the internal part of the graben, this inherited structure separates the northern area (N to ENE) of large subsidence with large volumes of volcanic products from the southern area (S to WSW) with a dish-shaped shallow basin and probably primarily reduced volcanic activity.

Acknowledgements. This study was supported by the Grant Agency of the Academy of Sciences CR, Project No. IAA300460602 and falls within the Academic Research Plan AV0Z 30130516 of the Institute of Geology AS CR v.v.i. and Research Plan MZP 0002579801 of the Czech Geological Survey. The study was also partly supported by the Czech Science Foundation (205/07/0691). The new geological map involves results of three projects supported by the Ministry of Environment CR: ISPROFIN 215124-1, OH-18/01 (OG MŽP), PPŽP 630/1/97. The authors wish to acknowledge Karel Mach (Doly Bílina a.s.) and Jan Blín (Coal Services – former Mostecká uhelná a.s.) for tectonic data acquired during mining activities. Special thanks are due to Anna Trubačová for her great help with all figures, including the map. We also thank the two reviewers, Bedřich Mlčoch and Klaus Stanek, whose comments improved the manuscript significantly, and Jiří Adamovič and Vojtěch Janoušek for the language revision of the text.

At the end of this paper, allow the authors to commemorate Mr. Miroslav Váně, an outstanding expert in the geology and the tectonic structure of the Louny region, whose death in the early summer of this year was a sad loss for geology. This article draws on his findings and in many respects follows on from them. The authors would therefore like to devote this paper to the memory of Mr. Váně.

References

Adamovič J, Coubal M (1999) Intrusive geometries and Cenozoic stress history of the northern part of the Bohemian Massif. Geolines 9: 5–14

Adamovič J, Coubal M (2009) Time succession of Cenozoic stress fields in the northern part of the Bohemian Massif. In: Röhling HG, Linnemann U, Lange JM (eds) GeoDresden 2009 – Geologie der Böhmischen Masse, Kurzfassungen der Vorträge und Poster/Abstracts. Schriftreihe Dt Ges Geowiss 63: 269

Brus Z, Hurník S (1988) Faults in the North–Bohemian Brown Coal Basin: the review. In: Pešek J, Vozár J (eds) Coal–bearing Formations of Czechoslovakia. Thematic Volume Concerning IGCP Project 166. Dionýz Štúr Institute of Geology, Bratislava, pp 103–109

Cajz V (2000) Proposal of lithostratigraphy for the České středohoří Mts. volcanics. Bull Czech Geol Surv 75: 7–16

Cajz V, Adamovič J, Rapprich V, Valigurský L (2004) Newly identified faults inside the volcanic complex of the České středohoří Mts., Ohře/Eger Graben, North Bohemia. Acta Geodyn Geomater 134: 213–222

Cajz V, Rapprich V, Erban V, Pécskay Z, Radoň M (2009) Late Miocene volcanic activity in the České středohoří Mountains, Ohře (Eger) Graben, northern Bohemia. Geol Carpath 60: 519–533

Cháb J (2008) Brief Geology of the Basement of Bohemian Massif and its Carboniferous and Permian Cover. Czech Geological Survey, Prague, pp 1–283 (in Czech)

Coubal M, Adamovič J (2000) Youngest tectonic activity on faults in the SW part of the Most Basin. Geolines 10: 15–17

Čech S, Valečka J (1991) Important transgressions and regressions in the Bohemian Cretaceous Basin. Unpublished manuscript, Czech Geological Survey, Prague, pp 1–51 (in Czech)

Čech S, Klein V, Kříž J, Valečka J (1980) Revision of the Upper Cretaceous stratigraphy of the Bohemian Cretaceous Basin. Věst Ústř Úst geol 55: 277–296 (in Czech)

Dèzes P, Schmid, SM, Ziegler PA (2004) Evolution of the European Cenozoic Rift System: interaction of the Alpine and Pyrenean orogens with their foreland lithosphere. Tectonophysics 389: 1–33

Haase KM, Renno AD (2008) Variation of magma generation and mantle sources during continental rifting observed in Cenozoic lavas from the Eger Rift, Central Europe. Chem Geol 257: 195–205

Herčík J, Herrmann Z, Valečka J (2003) Hydrogeology of the Bohemian Cretaceous Basin. Czech Geological Survey, Prague, pp 1–91

Hibsch JE (1924) Erläuterungen zur geologischen Karte der Umgebung von Bilin. Státní geologický ústav Československé republiky, Prague, pp 1–148

Hibsch JE (1926) Erläuterungen zur geologischen Übersichtskarte des Böhmischen Mittelgebirges und der unmittelbar angrenzenden Gebiete zugleich in allgemein verständlicher geologischen Führer. Freier Lehrerverein, Děčín, pp 1–143

Hurník S, Havlena V (1984) The Krušné hory Mts. and brown–coal basin at their foot as a part of a neotectonic megafold structure. Čas Mineral Geol 29: 55–67 (in Czech)

Kopecký L (1974) Detection of faults and determination of their order in the region of platform volcanism. Sbor geol Věd, Geol 26: 197–226

Kopecký L (1978) Neoidic taphrogenic evolution and young magmatism of the Bohemian Massif. Sbor geol Věd, Geol 31: 91–107

Kopecký L ed (1990) Explanatory text to the basic geological map of ČSSR 1 : 25 000, sheet 02–341 Bílina. Czech Geological Survey, Prague, pp 1–112 (in Czech)

Kycl P, Rapprich V, Mlčoch B, Valečka J, Zelenka P, Čáp P, Havlíček P, Holásek O, Hradecká L, Šimůnek Z (2009) Documentation of the outcrops and geological phenomena along the highway D–8, section 0805 Lovosice–Řehlovice and their importance for the environmental factors. Unpublished manuscript, Czech Geological Survey, Prague, pp 1–22 (in Czech)

Malkovský M (1977) Important Faults in the Platform Cover of The N Part of the Bohemian Massif. Czech Geological Survey, Prague, pp 1–30 (in Czech)

Malkovský M (1979) Tectogeny of the Platform Cover of the Bohemian Massif. Czech Geological Survey, Prague, pp 1–176 (in Czech)

Malkovský M (1987) The Mesozoic and Tertiary basins of the Bohemian Massif and their evolution. Tectonophysics 137: 31–42

Mlčoch B ed. (2001) Research on the crystalline formations in the deep basement of the Doupovské hory Mts. Complex and its surroundings. Unpublished manuscript, Czech Geological Survey, Prague, pp 1–121 (in Czech)

Mlčoch B (2003) Correlation of the crystalline basement outcropping in the Porta Bohemica with Saxothuringian Unit. Zpr geol Výzk v Roce 2002: 31–32 (in Czech)

Mlčoch B, Konopásek J (2010) Pre–Late Carboniferous geology along the contact of the Saxothuringian and Teplá–Barrandian zones in area covered by younger sediments and volcanics (western Bohemian Massif, Czech Republic). J Geosci 55: 81–94

Müller B (1924) Geologische Sektion Niemes–Roll (Kartenblatt Böhmisch Leipa–Dauba). Sbor St geol Úst Čs republ 4: 231–288

Pešek J (1996) Geology of the Upper Paleozoic basins in the Central Bohemia. Czech Geological Survey, Prague, pp 1–95 (in Czech)

Rajchl M, Uličný D, Grygar, R, Mach K (2009) Evolution of basin architecture in an incipient continental rift: the Cenozoic Most Basin, Eger Graben (Central Europe). Basin Res 21: 269–294

Šebesta J, Moravcová O, Cajz V, Valečka J, Adamovič J, Kadlec J, Hroch Z, Burda J (1997) Slope movement hazards in the Labe (Elbe) River valley, Ústí nad Labem county. Unpublished manuscript, Czech Geological Survey, Prague, pp 1–62 (in Czech)

Šťovíčková N (1973) Deep-seated Tectonics and its Relation to Endogenic Geologic Processes. Academia, Prague, pp 1–198 (in Czech)

Uličný D, Laurin J, Čech S (2009a) Controls on clastic sequence geometries in a shallow–marine transtensional basin: the Bohemian Cretaceous Basin, Czech Republic. Sedimentology 56: 1077–1114

Uličný D, Špičáková L, Grygar R, Svobodová M, Čech S, Laurin J (2009b) Palaeodrainage systems at the basal unconformity of the Bohemian Cretaceous Basin: roles of inherited fault systems and basement lithology during the onset of basin filling. Bull Geosci 84: 577–610

Ulrych J, Novák JK, Langrová A, Melka K, Cajz V, Adamovič J, Pertlik F, Wiesner T, Žid L, Radoň M (2000) Tertiary phonolite laccolith of Mariánská hora Hill, N. Bohemia: Geological, petrological and mineralogical characteristics. Acta montana Series A 116: 5–44

Valečka J (1989) Sedimentology, stratigraphy and cyclicity of the Jizera Formation (Middle–Upper Turonian) in the Děčín area (N Bohemia). Věst Ústř Úst geol 64: 77–90

Valečka J (1990) Tectonic structures of the Upper Cretaceous rocks. In: Hradecký P (ed) Geological–Tectonic Evaluation of the Nuclear Power Plant North Bohemia – the Building Site Choice. Unpublished manuscript, Czech Geological Survey, Prague, pp 8–14 (in Czech)

Valečka J, Zelenka P (2008) Stratigraphy, lithology and tectonics of Cretaceous sediments in the surroundings of Bílina. Zpr Stud Reg Muz (Teplice) 27: 85–93 (in Czech)

Valečka J, Cajz V, Kycl P, Mlčoch B, Rapprich V, Valigurský L, Zelenka P (2003) Slope movement hazards in the SE part of the České středohoří Mts., in the Litoměřice region. Part B –Geology, geological map. Unpublished manuscript, Czech Geological Survey. Prague, pp 1–36 (in Czech)

Valečka J, Cajz V, Rapprich V, Zelenka P, Mlčoch B (2008) Geology, geological map and explanations (Documentation and specialized survey on slope movements – the České středohoří Mts. region, 2004– 2007). Unpublished manuscript, Czech Geological Survey, Prague, pp 1–28 (in Czech)

Váně M (1985) The geological structure of the Krušné hory-piedmont Graben and its tectonogenesis. Sbor Geol Věd, Geol 40: 147–181 (in Czech)

Váně M (1999) Geology of the Louny Area for the Third Millennium. Edited by the author, Chomutov, pp 1–476 (in Czech)

Vejlupek M (1984) Permo–Carboniferous in the basement of the Cretaceous NE of Litoměřice. Věst Ústř Úst geol 59: 173–177 (in Czech)

Vejlupek M, Novák J (1986) Tectonics of the platform sediments in the Úštěk region. Věst Ústř Úst geol 61: 103–107 (in Czech)

Vejlupek M, Kaas A (1986) Tectonic structure of the Cretaceous of the Roudnice area. Čas Mineral Geol 31: 279–284 (in Czech)

Wilson M, Downes H (1991) Tertiary–Quaternary extension-related alkaline magmatism in Western and Central Europe. J Petrol 32: 811–849

Zahálka Č (1914) Cretaceous System in the České středohoří Mts. Edited by the author, Roudnice, pp 1–465 (in Czech)

Ziegler PA (1992) European Cenozoic rift system. Tectonophysics 208: 91–111

Journal of Geosciences, 55 (2010), 217–229 DOI: 10.3190/jgeosci.071

Original paper

Geometry of the Altenberg–Teplice Caldera revealed by the borehole and seismic data in its Czech part

Bedřich MLČOCH[1*], Zuzana SKÁCELOVÁ[2]

[1] *Czech Geological Survey, Klárov 3, 118 21 Prague 1, Czech Republic; bedřich.mlčoch@geology.cz*

[2] *Czech Geological Survey, Erbenova 348, 790 01 Jeseník, Czech Republic*

[*] *Corresponding author*

The Altenberg–Teplice Caldera (ATC) in the eastern Krušné hory Mts./Erzgebirge (Czech Republic, Germany) is the largest centre of Late Palaeozoic acid volcanism in the Bohemian Massif. Previous studies were focused mainly on its exposed part in the north, as the southern part is covered by Tertiary sediments. Borehole data, geological mapping and geophysical survey enabled to gain a new image of its areal and vertical extent and to construct a digital model of individual geological units. The evaluation of the Czech Geological Survey – Geofond borehole database and 3D modelling of the crystalline relief and of the rhyolite complex enabled to reconstruct the geometry of the Czech part of the ATC.

Keywords: Saxothuringian Zone, Eastern Krušné hory Mts./Erzgebirge Volcano–Plutonic Complex, Altenberg–Teplice Caldera, borehole, seismic data, erosion level

Received: 21 May 2010; accepted: 9 September 2010; handling editor: M. Štemprok

1. Introduction

Calderas belong to important volcanic structures and many recent studies deal with their experimental analogue modelling, anatomy and development (e.g. Walter and Troll 2001; Troll et al. 2002; Cole et al. 2005; Holohan at al. 2008). An uplift and collapse of the caldera shape its structure and cause deformations with the fault systems specific for each region. One of the possible approaches is to focus on the geometry of the caldera structure revealed by the analysis of a digital elevation model (Spinks at al. 2005) and by geophysics (in particular the seismic and gravity data). These methods enable to interpret the position of the faults and decipher the tectonic development. In particular, earlier volcanic structures are not easy to reconstruct without the aid of the accurate digital elevation model of geological units and the knowledge of their geological development.

The Altenberg–Teplice Caldera (ATC) in the eastern Krušné hory Mts./Erzgebirge (Czech Republic and Germany) is thought to be a giant collapse caldera, where the eruptions of rhyolitic lavas and ignimbrites of Carboniferous age were accompanied by granite and granite porphyry (microgranite) intrusions (Fig. 1). This volcano–plutonic complex crops out only in its northern part; further southwards it is covered by the sediments of the North Bohemian Basin. Moreover, a tectonically sunken block of the Saxothuringian crust (the Altenberg Block) occurs inside the ATC.

Moesta (1928) interpreted as the first this large volcanic and sub-volcanic complex as a relic of a Late Variscan caldera. Holub (1980) studied the petrography in the deep borehole B/Le 127 Ledvice and found out that the "quartz porphyries" actually corresponded to ignimbrites. Jiránek et al. (1987) summarized the results of previous detailed geological, petrological and geochemical studies in the Czech part of the Teplice rhyolite body. Benek (1991) described the ATC as a palaeo-caldera of trapdoor type.

The assessment of the actual size of the caldera has been hampered by the fact that its southern part is covered by Cretaceous and Tertiary sediments. The recent evaluation of the boreholes that reached bedrock of the North Bohemian Basin with detailed geological mapping (Mlčoch ed. 1989) made it possible to define the probable extent of the caldera and also enabled the compilation of geological map of the crystalline basement (Fig.1 after Mlčoch 1994; Mlčoch ed. 2001). Seltmann and Schilka (1995) evaluated new geochemical and geochronological data giving thus significant information "about the role of volcanics in the petrogenetic and metallogenic evolution of this crustal unit". This was followed by a number of detailed geochemical studies concerned with the evolution of the ATC volcano–plutonic complex (e.g. Breiter 1997; Breiter et al. 2001; Müller and Seltmann 2002; Štemprok et al. 2003). The granites in the Krušné hory Mts./Erzgebirge have been divided traditionally into two major suites (Lange et al 1972); the Older Intrusive Complex (OIC) and the Younger Intrusive Complex (YIC). The results of dating and mutual relationships of Late Variscan magmatites of the eastern part of the Krušné hory Mts./Erzgebirge are summarized e.g. in the articles by Štemprok et al. (2003), Müller et al. (2005), Romer et al.

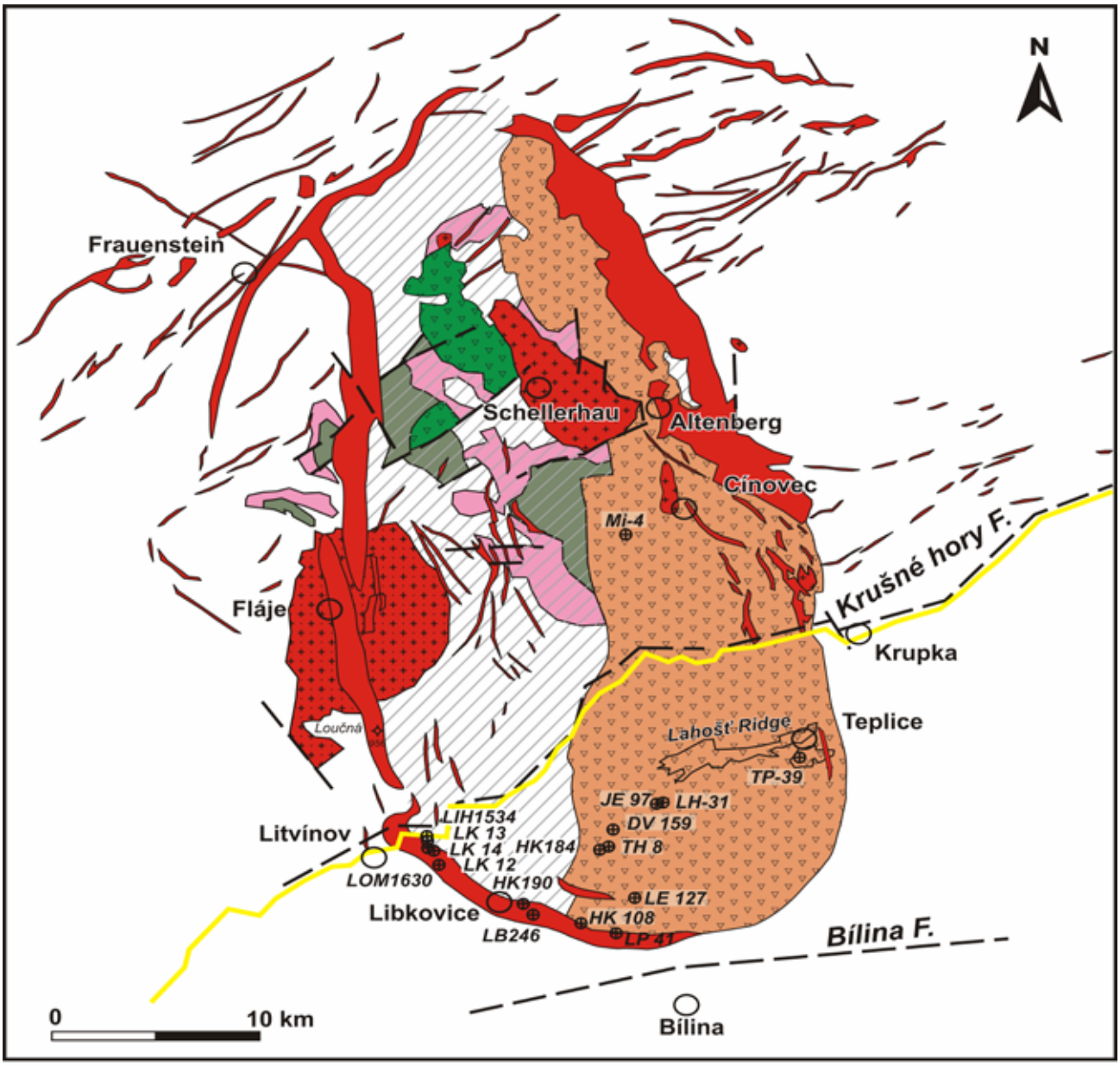

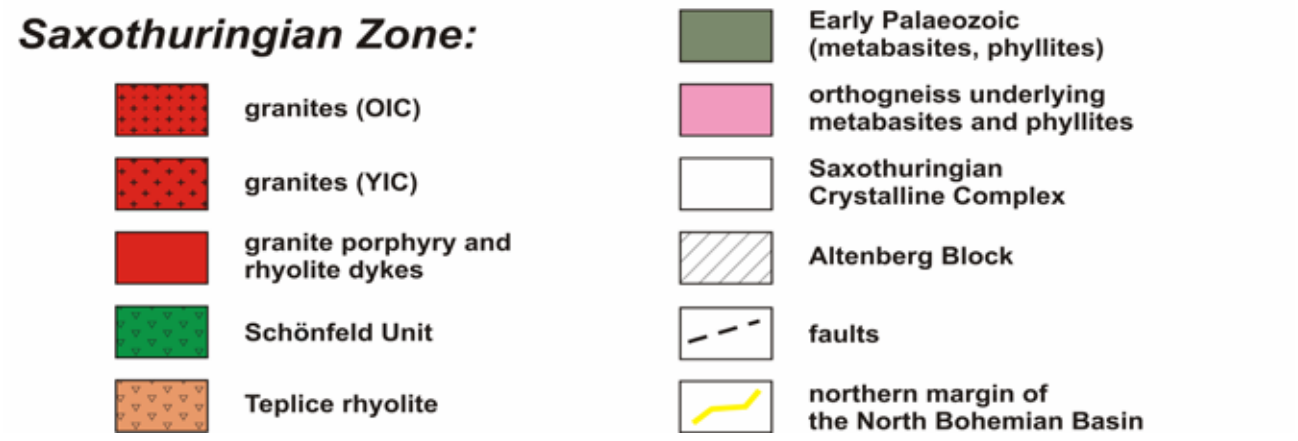

Fig. 1 Geological map of the Altenberg–Teplice Caldera area (after Mlčoch ed. 1989; Hoth et al. 1995) with the selected significant boreholes.

(2007) and, most recently, by Förster and Romer (2010). The age determinations are problematic because there are only a few available geochronological data for the ATC, which differ considerably from each other according to different authors and/or dating methods.

2. Geological setting

Thick granite porphyry dykes referred to as the Altenberg–Frauenstein microgranite (Müller and Seltmann 2002) mark the caldera border from Frauenstein to Loučná in the west. They submerge further to the southeast under the sediments of the North Bohemian Basin and continue to the southern margin of the Teplice rhyolite body. The dykes also rim the eastern margin of the Teplice rhyolite (e.g. Altenberg dyke) and can be considered as a component of the caldera. The granite porphyry dykes, together with the Teplice rhyolite, form a giant elliptical structure 18×35 km across (Fig. 1) of gravity trap-door character with the maximal subsidence in its southeastern part. The intrusion of marginal granite porphyry dykes marked the final phase of the ATC evolution, filling the ring faults. The Altenberg Block (the sunken roof pendant of the crystalline basement) is tilted to the east. Volcanic sequences in the hanging wall in the western part of the caldera underwent denudation. They are preserved only to limited extent in some places of the northern part of the Altenberg Block.

2.1. Saxothuringian Zone – Saxothuringian Crystalline Complex – Altenberg Block

The Altenberg Block represents a roof pendant covering the western part of the ATC. It consists predominantly of paragneisses belonging to the Saxothuringian Crystalline Complex. Due to the occurrence of remnants of low-grade Early Palaeozoic rocks, it was previously considered to be down-thrown relative to the surrounding area. Paragneisses, possibly at a rather deep erosion level, occur in the southern part of the Altenberg Block. A sharp tectonic boundary is evident between the orthogneisses of the Catherine Dome (in the W) and the paragneisses of the Altenberg Block exposed in the southern part of the Loučná–Fláje dyke (Mlčoch ed. 1989; Hoth et al. 1995). The relics of nappes of low-grade Lower Palaeozoic rocks (phyllites and metabasites) are preserved in the central and northern parts of the ATC (Fig. 1). They occur also in the basement of the Schönfeld Unit and represent the upper structural level of the Saxothuringian Zone. Intercalations of intensively shear-deformed orthogneisses occur in their footwall. A comparable sequence was documented also in the valley of the Labe River near Litoměřice (Porta Bohemica), which is the southernmost outcrop of the Saxothuringian Zone at the contact with the Teplá–Barrandian Unit (Mlčoch 2003; Mlčoch and Konopásek 2010).

2.2. Volcano–plutonic complex

The Fláje granite Massif represents the pre-caldera intrusion (OIC in earlier terminology), while the Cínovec–Krupka and the Schellerhau granite massifs, along with several small granite intrusions, belong to the younger magmatic suite (considered as YIC). The latter intrude the Teplice rhyolite (Chrt and Malásek 1984; Novák et al. 1991). The Fláje granite Massif at the western margin of the ATC crops out in an area of 7×9 km and is composed of two-mica and biotite granites. It reaches a depth of 9 km as shown by the reflection seismic data on the profile MVE-90 (DEKORP Research Group 1994).

The deep borehole Mi-4 (Mikulov) enabled to interpret the volcanic sequences of the Teplice rhyolite and provided lithogeochemical data presented by Breiter et al. (2001). These authors correlated dacites and intercalated sedimentary beds in the lower part of the Czech volcanic sequences with the Schönfeld Unit in Germany. The Teplice rhyolite body in the eastern ATC represents the most extensive outcrop of volcanic rocks (Fig. 1). In the basement of the North Bohemian Basin it continues as far to the Bílina river valley. The eastern margin of the Teplice rhyolite body is subvertical, rimmed by the Altenberg granite porphyry (microgranite) dyke. At the western margin the Teplice rhyolite and the Schönfeld Unit abut on the Altenberg Block at an angle of approximately 20–40°. The Carboniferous sediments in the Schönfeld Unit show the same dip. The maximal thickness of the Teplice rhyolite determined in the borehole TP-39 near Teplice is 1033 m. The oldest sequences, i. e. the basal rhyolite and dacite, are found in the northern and middle parts (a distinct belt on the western margin of the Teplice rhyolite body) of the ATC. The rhyolites in the southern part belong to the youngest volcanic phase. Sporadic occurrences of dacite (older sequence) below the Teplice rhyolite were determined in the borehole LH-31 (Mlčoch ed. 2001) southwest of Teplice (Fig. 1). In the north of the caldera, a deeper level of the volcanic sequences was probably exposed by erosion, compared with its southern part.

Different trends are observed in the dykes inside and outside the ATC. Inside the caldera, the granite porphyry dykes fill the approximately NNW–SSE to NW–SE oriented faults, which originated during the gravity collapse. In Czechia, these dominate the central part of the Altenberg Block and in the Teplice rhyolite body.

Outside-the-caldera dyke swarms predominantly trend ENE–WSW to NE–SW and are generally perpendicular

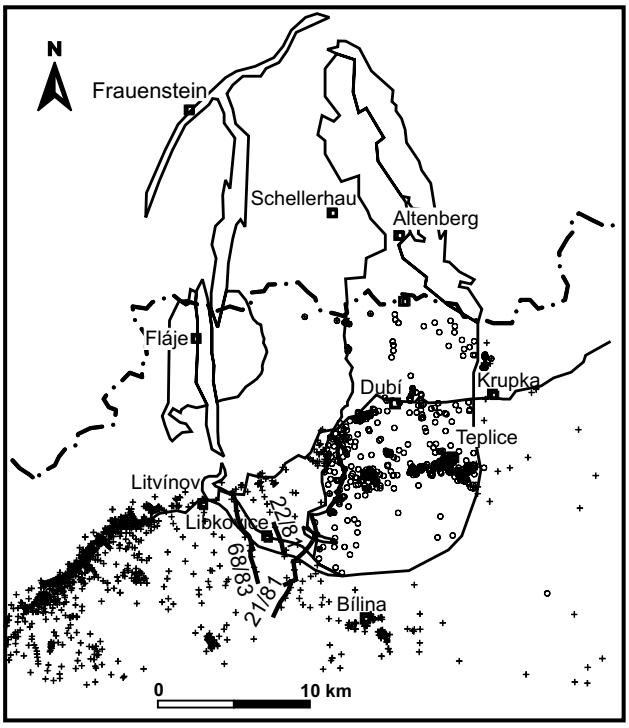

Fig. 2 Location of the boreholes and seismic profiles (crosses – surface of the crystalline complex, circles – surface of the Teplice rhyolite).

to the caldera's elongation. They are concentrated into several dyke swarms, which do not continue into the interior of the caldera. Rhyolitic dykes (Sayda–Berggiesshübel swarm) are most frequent at the northern margin of the caldera. Second large dyke swarm occurs in the Czech part of the eastern Krušné hory Mts./Erzgebirge. The origin of the dykes west of the ATC can be linked with the volcanic activity also, e.g. dykes between Hora Svaté Kateřiny and Steinbach (see Hoth et al. 1995).

3. Methods

The geometry of the Czech part of the ATC was reconstructed mainly from the borehole data, the field relations (detailed geological mapping at 1:25 000 scale, Mlčoch ed. 1989; Jiránek ed. 1991; Schovánek et al. 2004) and the geophysical data (Fig. 2). The latter include seismic reflection data used for the determination of the depth of the contact plane between the sediments and the Teplice rhyolite on the one hand, and the vertical extent of the crystalline complex on the other. A digital elevation model of the ATC volcano–plutonic complex and of the crystalline basement below the sedimentary cover of the North Bohemian Basin was constructed using the re-evaluated borehole database of the Czech Geological Survey-Geofond (*https://www.geofond.cz/mapsphere/EEARTH/*) and other sources (mining companies). In total we have utilized 2066 boreholes for the 3D modelling (727 boreholes for the Teplice rhyolite, and 27 boreholes for the crystalline relief in the basement of the rhyolite). All data were re-processed and checked for coordinates, depth and rock type. The surface of the ATC and of the crystalline relief was defined in each borehole (altitude, rock type, geological unit) and filed into the database. We also used the information on the hidden granite massif (proved by 21 boreholes) in the eastern part of the ATC. Lastly, data from the previous studies and available as a contour map (Chrt and Malásek 1984, Malásek ed 1987) were also utilized. The final digital elevation model for the study area was constructed by the combination of the modelled subsurface crystalline relief and Teplice rhyolite from boreholes and outcrops. The present-day relief was digitised from contour lines with an interval of 5 m.

The Surfer software by the Golden Software Inc. was used for the 3D modelling. The XYZ data of the final 3D model were interpolated by kriging into a regular grid with a spacing of 100 × 100 m.

4. Results

4.1. Seismic data

Seismic refraction survey (common-depth-point) was carried out in the North Bohemian Basin district in the years 1981 and 1983 (Jihlavec et al. 1983, 1984) as a part of the geological mapping and exploration for brown coal deposits (Figs 2 and 3). In total three Slalom line profiles

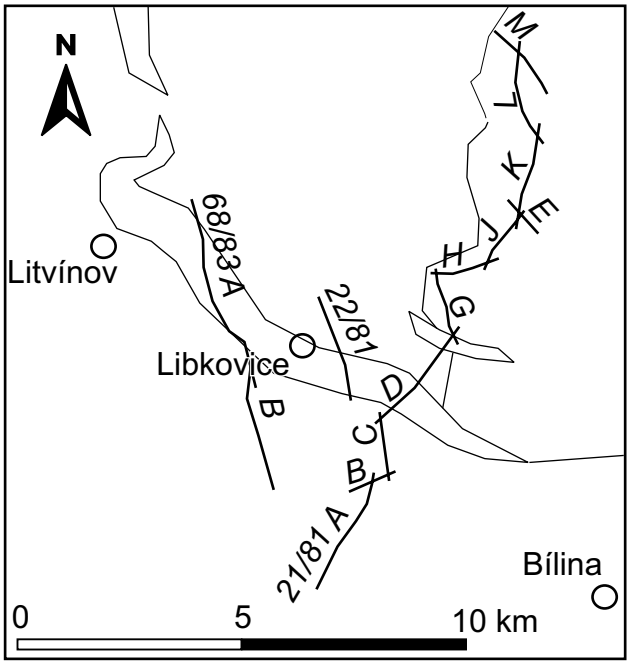

Fig. 3 Location of seismic profiles.

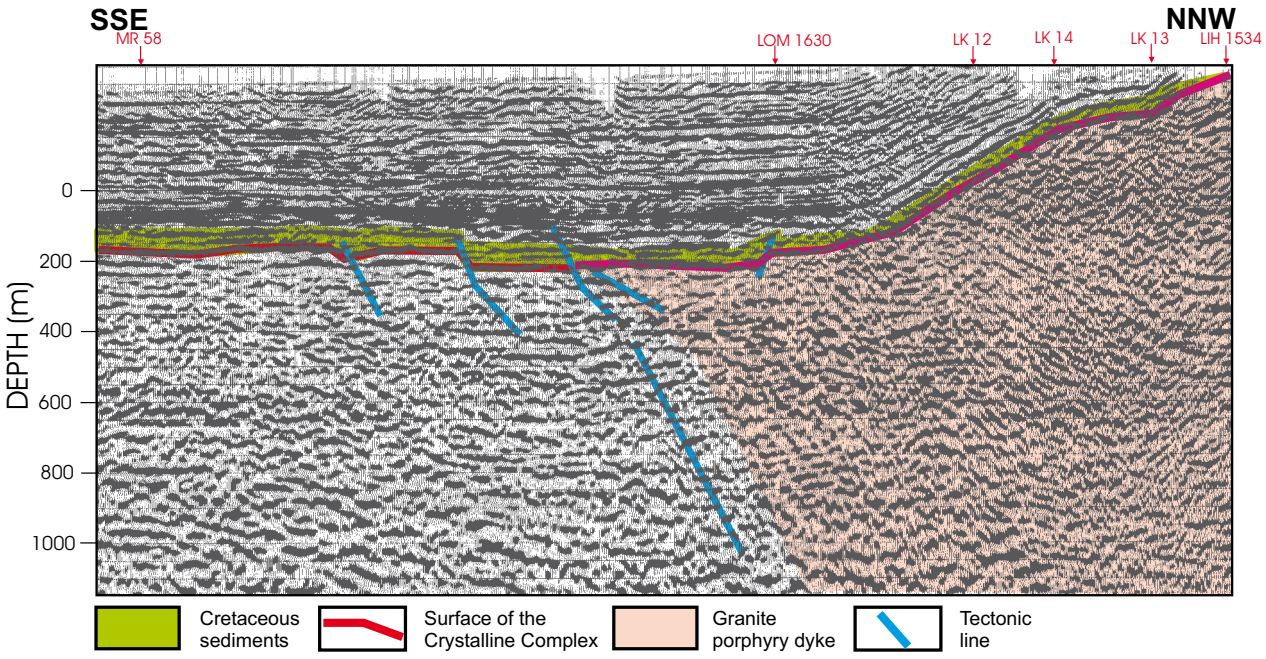

Fig. 4 Depth reflection seismic section 68/83 and its interpretation.

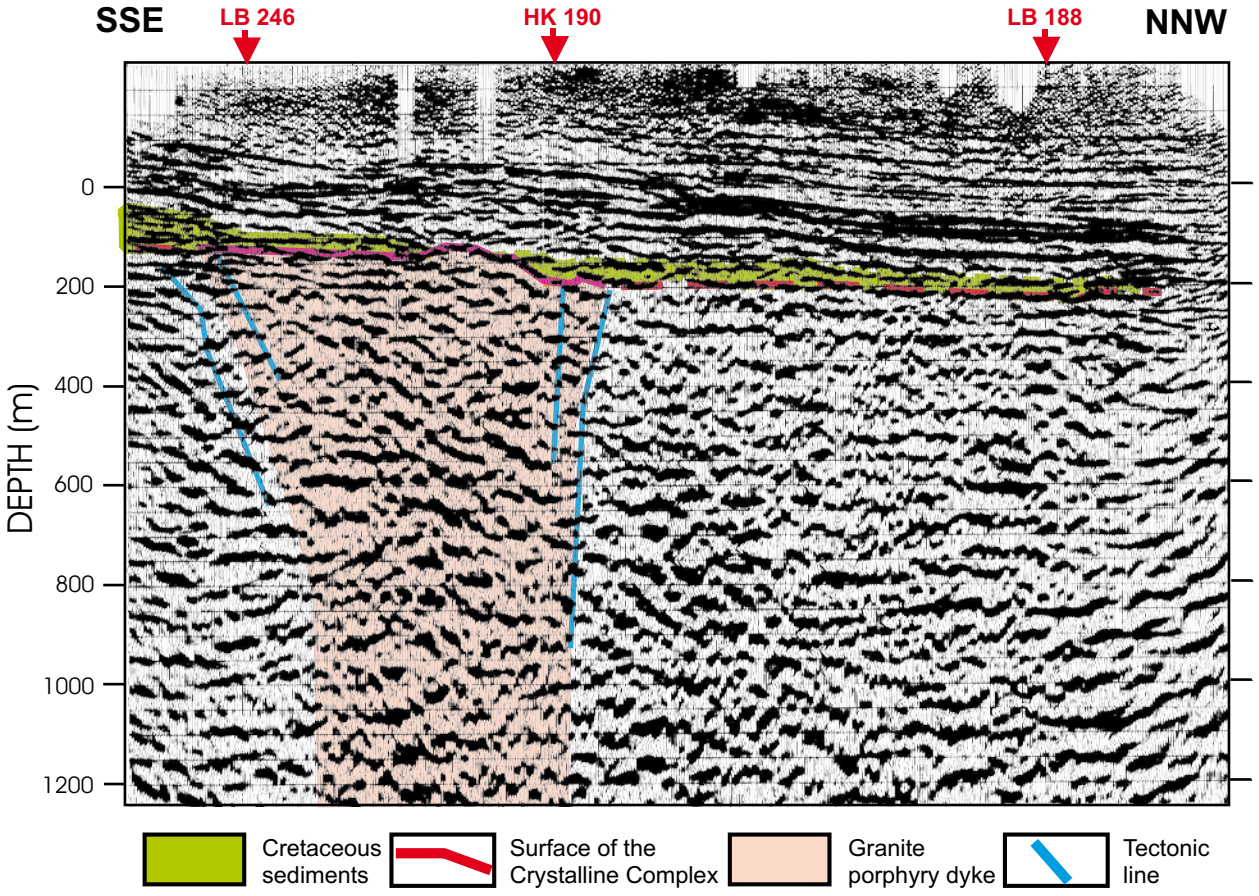

Fig. 5 Depth reflection seismic section 22/81 and its interpretation.

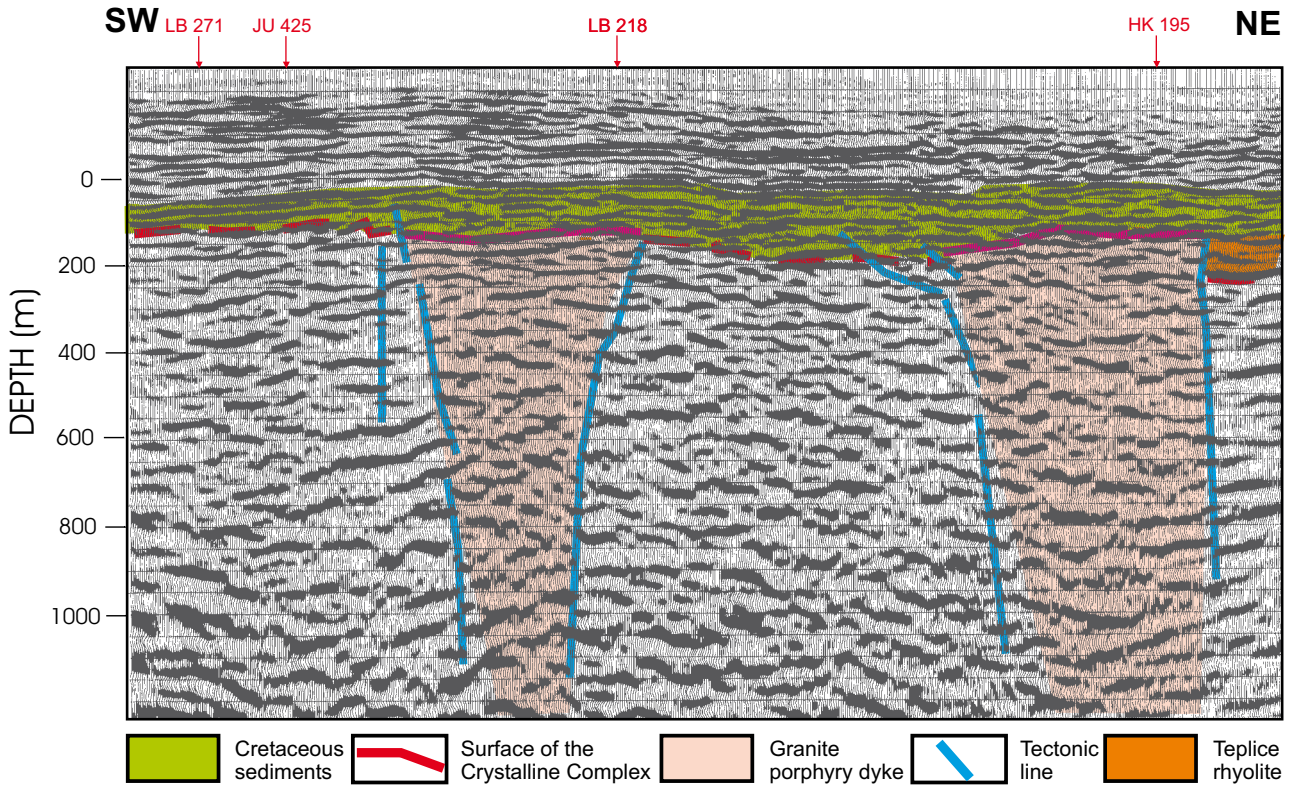

Fig. 6 Depth reflection seismic section 21D/81 and its interpretation.

were measured: 22/81, 68/83 and 21/81, which were combined from 10 sections. The quality of the primary data is good, so that they could be used for the study of the tectono-structural relations in the Tertiary sedimentary basin using new software (Rajchl et al. 2003).

The image and interpretation of the individual reflection interfaces were employed in this study, above all, for the 3D modelling of the crystalline complex and the Teplice rhyolite concealed below the Tertiary and Cretaceous sediments. The depth data acquired from seismic sections were correlated with new borehole logs and used for geological interpretation of the crystalline basement (Mlčoch 1994). Thus the reflection interfaces could be interpreted with a great accuracy along the entire profile length, including radial tectonic structures. The granite porphyry dyke documented between Litvínov and Libkovice (Mlčoch ed. 1989) is characterized by the changes of amplitude and frequency of seismic signal and area represented by missing reflections. Previous interpretation (Rajchl et al. 2003) assumed a presence of solely subvertical faults here.

The profile 68/83 was situated in the westernmost part of the studied area. In the north it nearly reaches the crystalline complex exposed on the slopes of the Krušné hory Mts. The re-interpreted data from the LIH1534, LK12, LK13, LK14 and LOM1630 boreholes (Fig. 1) identified a granite porphyry dyke within the crystalline complex underlying the sedimentary sequences at the end of profile (Fig. 4). In the original seismic interpretation, the seismic manifestation of this dyke was described as a fault system inclined to the NNW in the gneiss complex. New interpretation designates radial faults as the southern margin of the Litvínov–Libkovice granite porphyry dyke, which is a continuation of the Fláje–Loučná dyke further north (Fig. 1).

An analogous case represents also the 22/81 seismic profile, situated further to the east (Fig. 5), where the HK 190 and LB-246 boreholes in the basement also reached a granite porphyry dyke. The previous interpretations of the 22/81 seismic section (Rajchl et al. 2003) disclosed only vertical tectonic structures. Our new interpretation located a probable granite porphyry dyke, marked by area of missing reflection of the seismic signal on the both its margins.

A rather complicated is the interpretation of the 21/81 profile, in particular in its 21D/81 segment (Fig. 6), which intersects two granite porphyry dykes at the southern margin of the Teplice rhyolite. In this seismic section, the southern part of the Litvínov–Libkovice granite porphyry dyke (borehole LB 218) was newly recorded as was a small sub-parallel granite porphyry dyke at the southwestern margin of the Teplice rhyolite

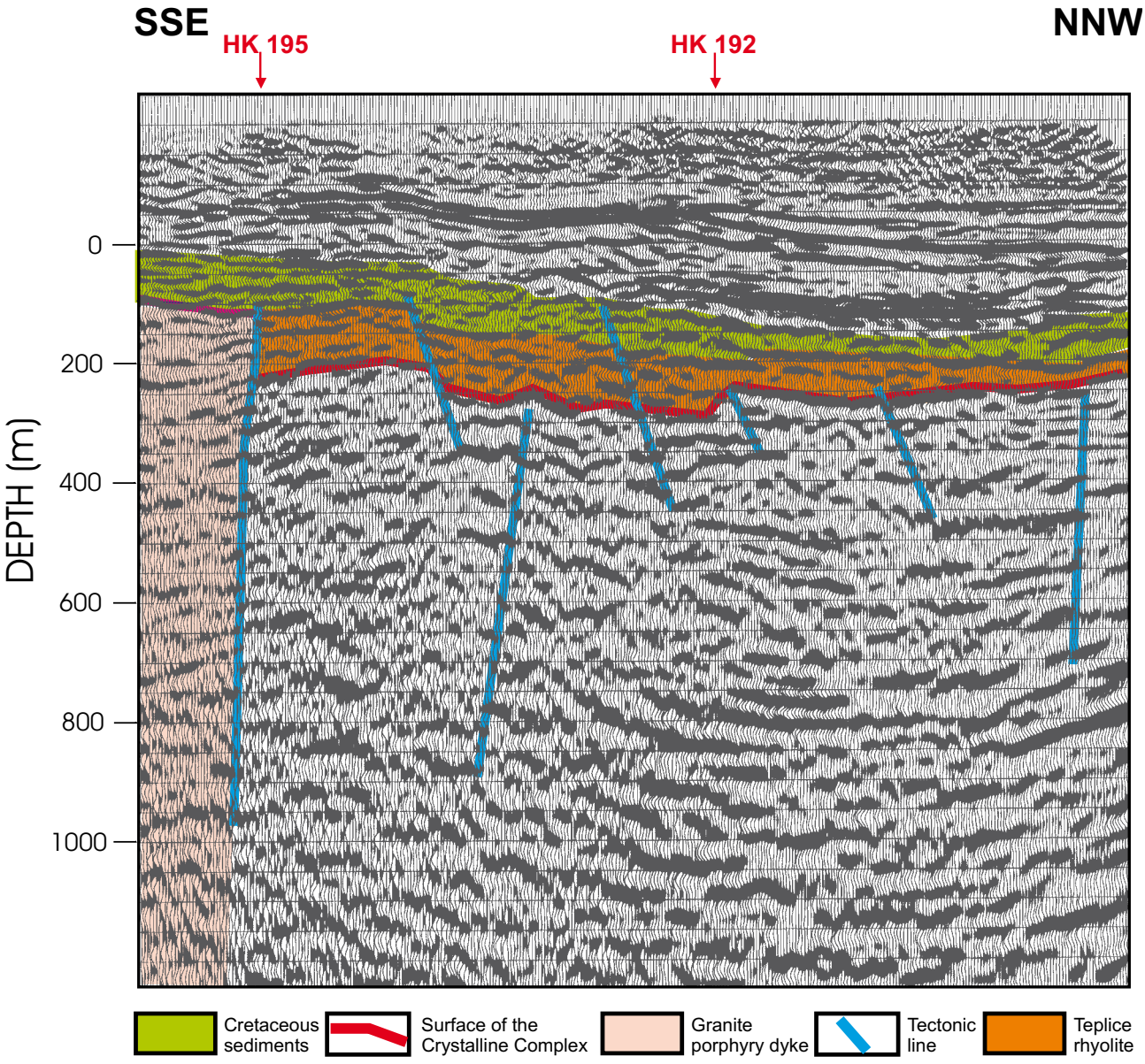

Fig. 7 Depth reflection seismic section 21G/81 and its interpretation.

body (HK 195). In the seismic section both these dykes are tectonically predisposed, filling the ring faults. In the northeastern part of the 21D profile, two interfaces were detected: the upper one corresponding to the rhyolite surface, and the lower one to the limit of the crystalline basement. The relief of the crystalline basement can be only partially determined along the whole 21/83 profile. It is very indistinct and can be correlated with a segment of the 21G/81 profile (Fig. 7), which indicated both the relief of Teplice rhyolite and of the crystalline complex (paragneiss of the Altenberg Block). A relatively short distance between both the interfaces (*c.* 50 to 100 m) probably caused a poor resolution of the depth indicators.

4.2. Borehole data and 3D model of the Czech part of the Altenberg–Teplice Caldera

We made use of 1339 boreholes for the 3D modelling of the crystalline relief and 727 for the Teplice rhyolite respectively. Most of them are from the Czech Geological Survey-Geofond database. The borehole-log evaluation provided additional information regarding the depth of a hidden granite body in the eastern part of the ATC. The final 3D model of the ATC is shown in Fig. 8. The recent surface relief (Fig. 8a), denotes the actual outcrops of the ATC, where the boundaries of granite bodies, granite porphyry dykes and of the Teplice rhyolite could be mapped

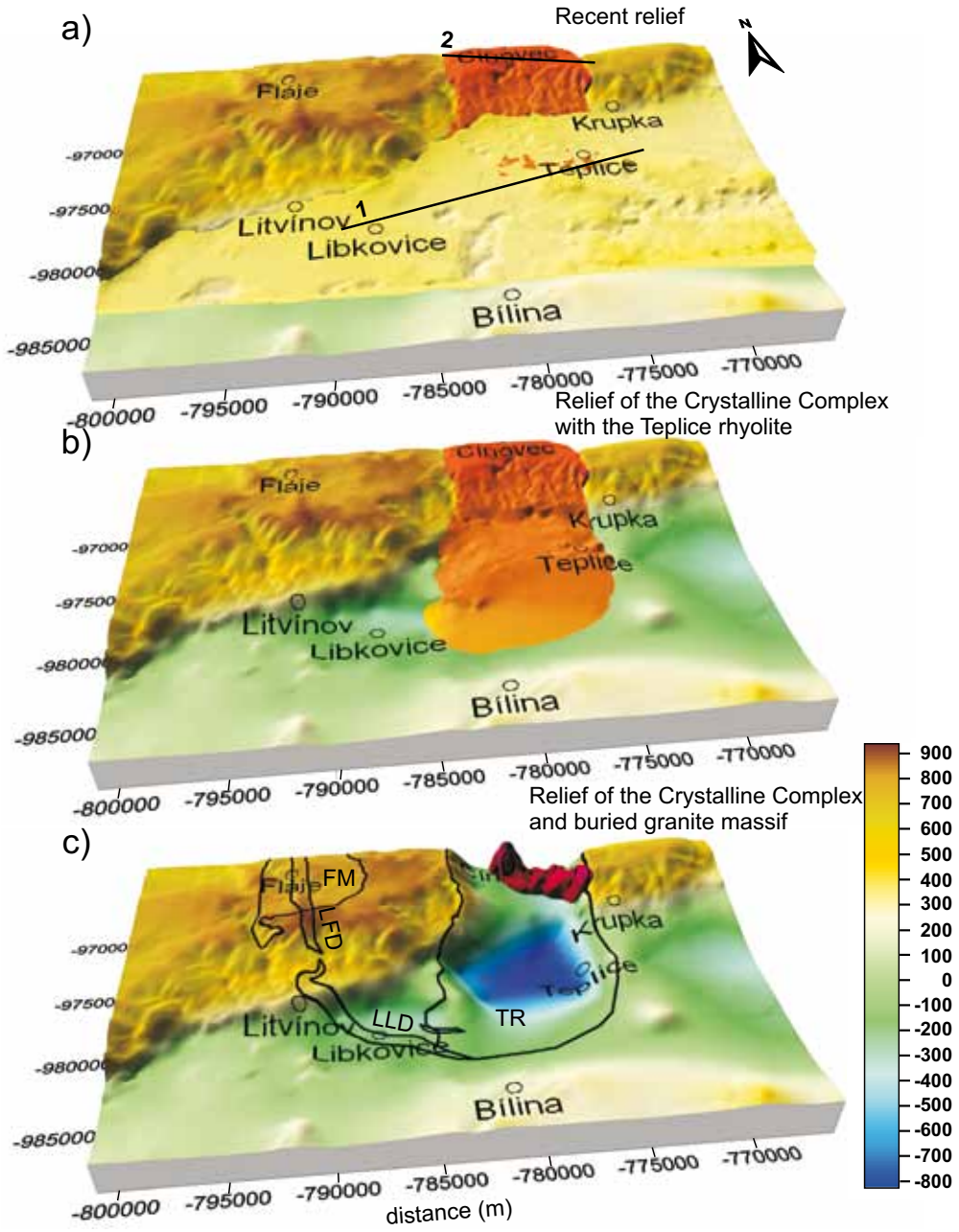

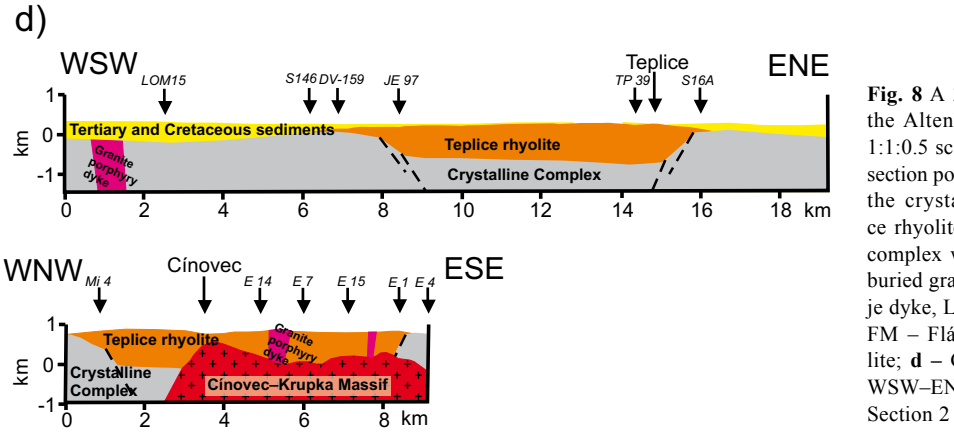

Fig. 8 A 3D model of the Czech part of the Altenberg–Teplice Caldera (x:y:z = 1:1:0.5 scaling). **a** – recent relief with the section position; **b** – contact plane between the crystalline complex and the Teplice rhyolite; **c** – surface of the crystalline complex with the marked position of the buried granite pluton. LFD – Loučná–Fláje dyke, LLD – Litvínov–Libkovice dyke, FM – Fláje Massif, TR – Teplice rhyolite; **d** – Geological interpretation of the WSW–ENE Section 1 and the WNW–ESE Section 2 (in Fig. 8a).

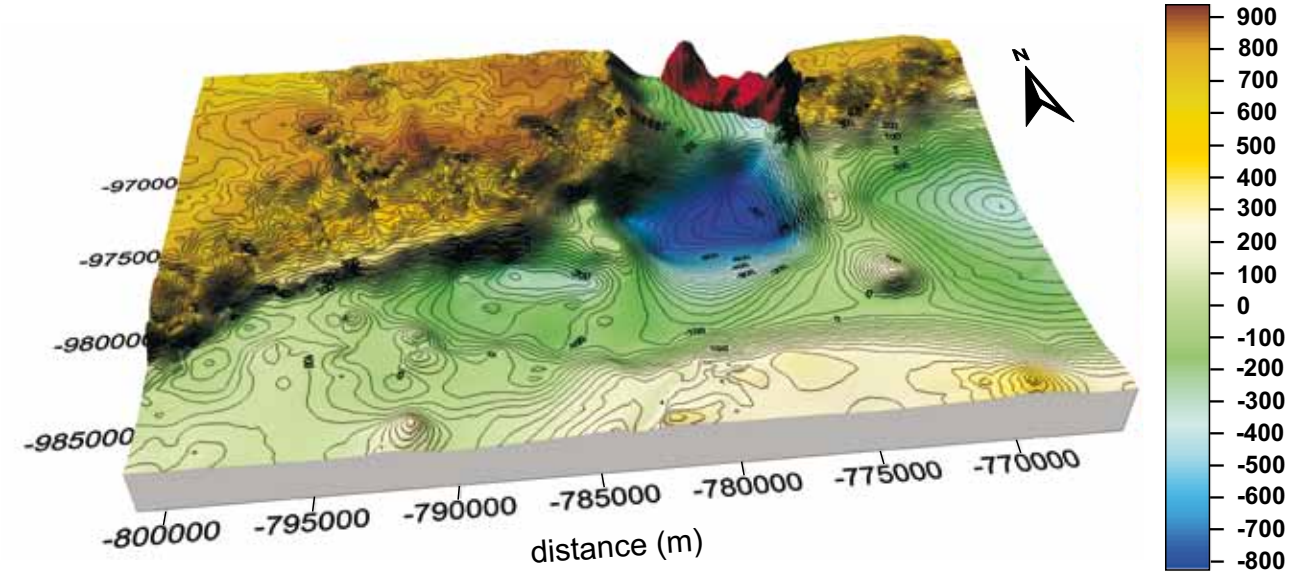

Fig. 9 Isolines of crystalline basement in the 3D model of the Czech part of the ATC (see also Fig. 8c).

in detail. The southern ATC is completely covered by Tertiary and Cretaceous sediments and only near the namesake town, the Teplice rhyolite is exposed on the Lahošť Ridge. The 3D model without sedimentary cover (Fig. 8b) shows the Teplice rhyolite body almost reaching the southern margin of the North Bohemian Basin. Thanks to a number of boreholes drilled to the base of the Teplice rhyolite body (e.g. Mi-4, TP-39, JE-97, HK-191, HK-184), it was possible to construct an estimated 3D model (Figs 8c and 9) of the crystalline complex–Teplice rhyolite contact plane. The maximal thickness of the rhyolite body was determined in the southeastern part of the ATC, where the surface of the crystalline relief is deeper than 800 m below sea level. This depression is probably delimited by faults in the east and west (Fig. 8d). In the west, the crystalline block is downthrown by more than 600 m over a distance of 2 km. The eastern margin of the Teplice rhyolite overlies the Altenberg Block at a moderate angle. The crystalline basement forms a ridge, whose flanks plunge steeply. In the south, in accordance with the 3D model (Fig. 9), the base of the Teplice rhyolite probably rises gradually towards the surface. In the north, the granite intrusion seen underneath the Teplice rhyolite may belong to the Cínovec–Krupka Massif exposed partly on the surface. The western boundary of this granite is not entirely clear. According to gravity data and the Mi-4 borehole, the limitation of the granite massif should be located at the northwestern margin of a gravity minimum, approximately along the Cínovec–Dubí line.

Regional gravity low in the ATC area (Fig. 10) indicates a deep source of the low-density rocks (an equivalent of the acid volcanic rocks). The regional gravity low extends beyond the marginal porphyry dykes that intruded along the ring faults, which means that the light rocks are located deeper under the caldera. This is in agreement with the seismic research (DEKORP Research Group 1994), which constrained the existence of granite bodies (sources of the Fláje and Schellerhau granite massifs, Teplice rhyolite and granite porphyry) to a depth

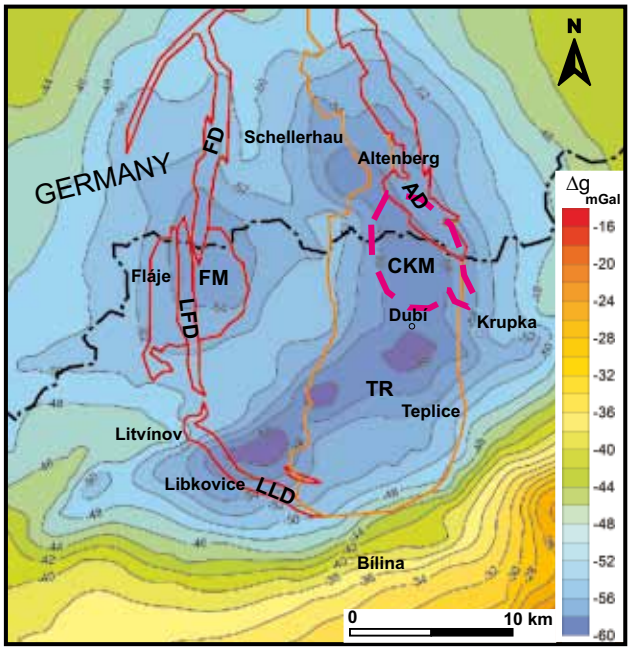

Fig. 10 Map of the Bouguer anomaly (modified after Sedlák et al. 2009) in ATC with the boundaries of the main geological units (FM – Fláje Massif, CKM – Cínovec–Krupka Massif, TR – Teplice rhyolite, AD – Altenberg dyke, FD – Frauenstein dyke, LFD – Loučná–Fláje dyke, LLD – Litvínov–Libkovice dyke).

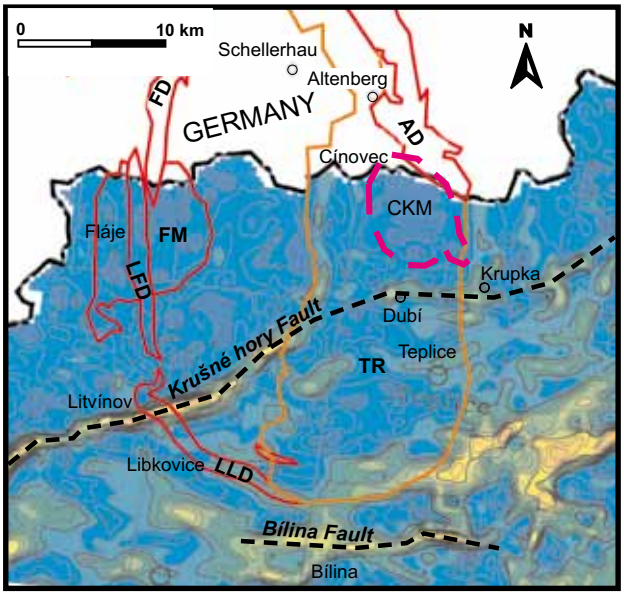

Fig. 11 Map of the horizontal gravity gradient (after Šrámek in Mlčoch ed. 2001) in the ATC with the boundaries of the main geological units (abbreviations the same as in Fig. 10).

of *c.* 15 km. The Fláje granite Massif is documented as a gravity minimum (less than -54 mGal) at the western margin of the caldera. In the eastern ATC, the sources of gravity low are identified as the Teplice rhyolite and the Cínovec–Krupka granite Massif. Cretaceous and Tertiary sediments of the North Bohemian Basin affect the course of geologic boundaries in the southern part of the caldera. Nevertheless, similarly to the 3D model, the down-faulted block of the crystalline complex is also reflected in gravity data. The rhyolitic rocks filling this depression at the eastern ATC generated an extensive gravity low elongated in the N–S direction. The local minimum north of Teplice (less than -59 mGal) can be interpreted as a deep source area of the Teplice rhyolite intrusion because the thickness of the sediments is relatively low (100–160 m) compared to north of Libkovice (550 m). The thickness of the sedimentary cover north of Teplice is 100–160 m and thus the sediments cannot be held responsible for the local gravity minimum (-59 m Gal).

The map of the horizontal gravity gradient (Fig.11) indicates a lateral density contrast close to Krušné hory and Bílina faults as well as at the steeply dipping contact between the Saxothuringian Crystalline Complex on the one hand, and Teplice rhyolite (N–S trend in the north) with the Litvínov–Libkovice porphyry dykes (NW–SE trend in the south) on the other.

5. Discussion

The ATC represents an ancient volcanic structure, which is not easy to reconstruct. At the beginning of the volcanic activity, this region was probably levelled relief of the Saxothuringian Zone, which is documented by the existence of sediments deposited in shallow terrestrial depressions. The deeper part of the caldera (eroded caldera structure) of Carboniferous age is exposed on the surface and beneath the sediments. Because the ATC is large and intersects geological structures, erosion has not affected all its parts with equal intensity. Recent image of the caldera is also complicated by an asymmetrical gravitational trapdoor collapse. It is evident from the geological maps (e.g. Mlčoch ed. 1989; Hoth et al. 1995) that in each quadrant of the caldera, obvious differences in its geological structure exist, which correspond to different depth levels of the original caldera (Fig. 12). Distinct structural stages of the caldera development are seen, which do need not correspond to the depth of erosion.

The differences in the depth of erosion existed between the northern and southern parts of the caldera basement already at the onset of the volcanic activity. In the north, the relics of nappes of Early Palaeozoic rocks (phyllites and metabasites) were preserved in the hanging wall of the sheared orthogneisses (probably also nappes). The Early Palaeozoic rocks were identified from the volcanic sequences revealed in the Mi-4 borehole. Analogous situation was observed at the contact of the Saxothuringian Zone with the Teplá–Barrandian Unit (Mlčoch and Konopásek 2010). In the southern part of the caldera, the Saxothuringian Crystalline Complex is formed by paragneisses. Low-grade Early Palaeozoic rocks have not been found even in the boreholes reaching the basement of the Teplice rhyolite. The depth of the Altenberg Block downthrow can also be seen along its western margin. In the south, the Fláje–Loučná and Litvínov–Libkovice granite porphyry dykes sharply separate the paragneisses of Altenberg Block from the orthogneisses of the Catherine Dome, while in the north, the nappes of Early Palaeozoic rocks continue even beyond the caldera. The Teplice rhyolite consisting mostly of ignimbrites of the main volcanic phase reaches the maximum thickness (up to 1200 m) in the southeastern quadrant of the caldera. This fact is readily apparent from the 3D model shown in Fig. 8. Older volcanic sequences have not been found, except for the dacite from the LH-31 borehole (Mlčoch ed. 2001). The thickness of the ignimbrites in the northeastern quadrant is significantly lower and older volcano–sedimentary sequences are preserved in their footwall (the Schönfeld Unit). The remnants of ignimbrites occur also in the northwestern quadrant. Although the northern part of the caldera represents a "deeper" level of the volcanic apparatus (with preserved older volcano–sedimentary sequences) it does not need to correspond to a "deeper" level of erosion. The thickness of ignimbrites was probably not comparable to that in the south to start with.

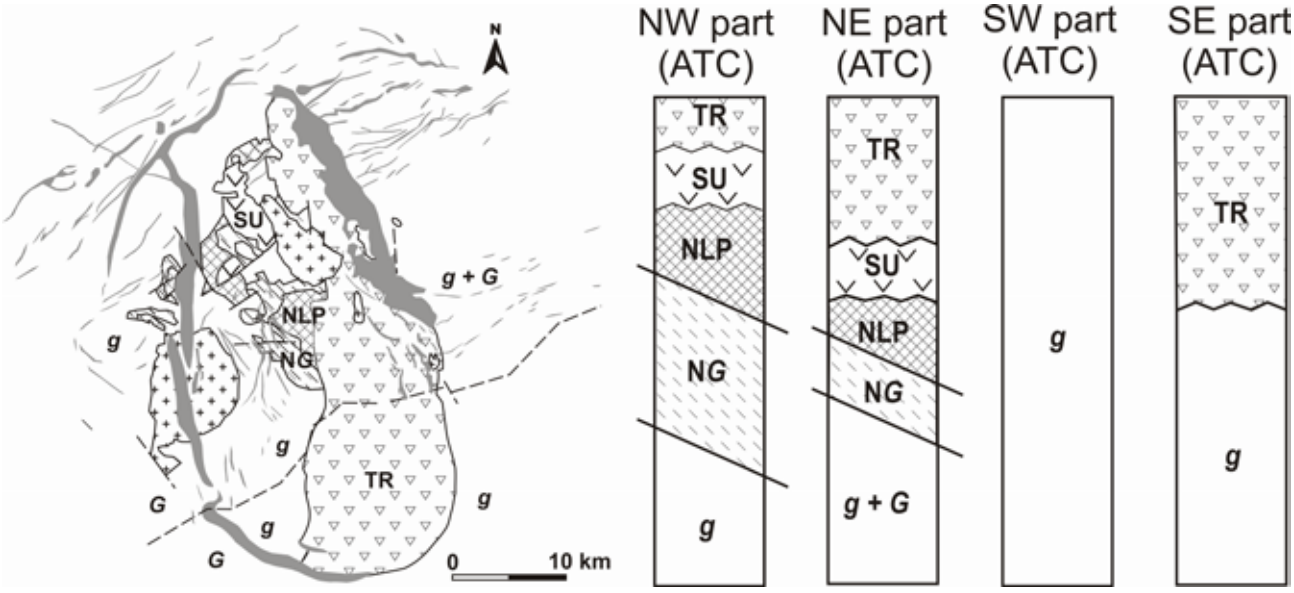

Fig. 12 Schematic distribution of the main geological units in four quadrants of the ATC (TR – Teplice rhyolite, SU – Schönfeld Unit, NLP – Lower Palaeozoic nappes, NG – orthogneiss nappes, g – paragneisses of the Saxothuringian Crystalline Complex, G – orthogneisses of the Saxothuringian Crystalline Complex).

Significant information about the caldera evolution can be inferred from the existence of granite porphyry and rhyolite dyke swarms within, and outside, the ATC. Uplift of the caldera structure is highlighted by the external radial dykes striking predominantly WSW–ENE in the middle part. Some dykes of SW–NE trend in the north run generally perpendicularly to the elongation of the caldera. The majority of these granite porphyry and rhyolitic dykes are therefore older than the gravitational collapse of the caldera. In the north, in the Sayda–Bergiesshübel dyke swarm three generations of rhyolitic dykes can be distinguished (Winter et al. 2008), some of them probably also related to a later phase of the caldera evolution. The granite porphyry dykes within the caldera plugged the faults trending approximately NNW–SSE to N–S, which had originated during the gravitational collapse. The dykes in the Altenberg Block and in the Teplice rhyolite dip to the east and are linked with a unilateral subsidence (of the eastern part) and the occurrence of the fault fissures. The ATC subsided asymmetrically bringing about a trapdoor-type collapse perceptible especially in the 3D model for the crystalline relief (Fig. 8c). The subsidence proceeded probably gradually from the west to the east as indicated by the dyke swarms. The Fláje granite Massif played a significant role in consolidation of the northwestern sector of the caldera. Moreover, it may have caused a difference in the caldera floor level of the collapsing block relative to its surroundings. The Fláje Massif was situated apparently close to the surface at the moment of the collapse (Müller and Seltmann 2002).

The final phase of the caldera subsidence gave rise to granite porphyry dykes filling the ring-faults (e.g. Altenberg, Frauenstein, Fláje–Loučná, Litvínov–Libkovice). These include the dykes in the caldera's centre (both in the Teplice rhyolite and Altenberg Block), which are subparallel with the ring faults and filled fractures generated during the caldera collapse. The Litvínov–Libkovice dyke and second small dyke at the southern rim below Tertiary and Cretaceous sediments were found in boreholes (Mlčoch 1994) and verified by a new interpretation of the seismic reflection survey (Figs 4–7).

In its western part, the Teplice rhyolite body covers the crystalline complex of the Altenberg Block and is only 30–50 m thick. An abrupt down-throw is found from the boreholes and it is visible in the 3D model (Fig. 8c) only near the centre of the caldera (1 to 2 km from the margin of the Teplice rhyolite). This fault could have been contemporaneous with the effusion of the Teplice rhyolite, as corroborated by the absence of any younger dykes filling this fault and intruding the rhyolite body. The down-throw reaches a depth of about 690 m b.s.l. (borehole JE-97), which is comparable with the maximum vertical movement in the east (TP39). The borehole data at the southeastern margin of the ATC are sufficient to detect the Teplice rhyolite body but are not adequate for the modelling of the crystalline basement surface. This is also obvious from the 3D model (moderately rising trend of the basement southwards). Lastly, a younger Cínovec–Krupka granitic intrusion occurs below the rhyolite in the north, in the mountainous part.

Rhyolite tuffs and ignimbrites are also documented outside the ATC as distinct strata in the Permo–Carboniferous sequences of the Tharandt Caldera, as well as in the Döhlend, Brandov and Erzgebirge basins. Some relics are seen also in the basement of Cretaceous sediments at the southeastern margin of the České středohoří Mts. (Porta Bohemica). A part of them may have originated from the ATC, but possibly also from other volcanic centres.

6. Conclusions

The presented 3D digital model based on borehole and geophysical data enables, together with the current geological, geochemical and petrological data, new interpretation of the Altenberg–Teplice Caldera (ATC) evolution. Seismic reflection profiles 21/83, 22/83 a 68/83 were used to determine the depth of the crystalline complex and the Teplice rhyolite below the Cretaceous and Tertiary sediments. The Teplice rhyolite relief and occurrence of granite porphyry dykes were identified by the new interpretation. Moreover, seismic data verified the position of the Litvínov–Libkovice granite porphyry dyke in the basement of the Most Basin.

The geology of the crystalline relief revealed a different level of erosion between the northern and southern parts of the ATC. Based on their relation to the ATC, several generations of granite porphyry and rhyolite dykes can be distinguished. The oldest would be the uplift-related dykes trending perpendicularly to the caldera's elongation, especially in its middle part. The gravity collapse was accompanied by the emplacement of the youngest ring dykes, which had bounded the caldera area, and by additional sub-parallel dykes inside the caldera or in its vicinity.

The geometry of the ATC correlates with the asymmetrical trapdoor gravity collapse event, whereby the western margin was influenced by the existence of the Fláje Massif. The 3D model of the ATC indicates a sunken block of the Altenberg Crystalline Complex limited by faults from the east and the west. Their origin was probably contemporaneous with the main volcanic phase of the Teplice rhyolite effusion. The down-throw was enormous in the southeastern part, as shown by the maximal thickness of the rhyolite body near Teplice (over 1000 m).

Acknowledgements. This research was financially supported by Ministry of Education, Youth and Sports of the Czech Republic through the Research Centre 1M0554 "Advanced Remedial Technologies and Processes" and project No A300460602 of the Grant Agency of the Academy of Sciences of the Czech Republic. Thanks are due to the reviewers R. Seltmann, M. Lapp and handling editor M. Štemprok for their comments and suggestions.

References

Benek R (1991) Aspekte einer Volumenbilanz paläovulkanischer Förderprodukte – Beispiel Teplice Rhyolith (Ostdeutschland). Z geol Wiss 19: 379–389

Breiter K (1997) The Teplice rhyolite (Krušné hory Mts., Czech Republic) – chemical evidence of a multiply exhausted stratified magma chamber. Bull Czech Geol Surv 72: 205–213

Breiter K, Novák JK, Chlupáčová M (2001) Chemical evolution of volcanic rocks in the Altenberg–Teplice caldera (Eastern Krušné hory Mts., Czech Republic, Germany). Geolines 13: 17–22

Chrt J, Malásek F (1984) The buried relief of the Rudohoří (Erzgebirge) granites between Cínovec and Krupka. Geol Průzk 26: 305–309 (in Czech)

Cole J W, Milner DM, Spinks KD (2005) Calderas and caldera structures: a review. Earth Sci Rev 69: 1–26

DEKORP Research Group (1994) The deep reflection seismic profiles DEKORP 3/MVE–90. Z geol Wiss 22: 627–824

Förster H J, Romer RL (2010) Carboniferous magmatism. In: Linnemann U, Romer RL (eds) Pre-Mesozoic Geology of Saxo–Thuringia from the Cadomian Active Margin to the Variscan Orogen. Schweizerbart, Stuttgart, pp 287–308

Holohan EP, Benjamin WV, Troll VR (2008) Analogue models of caldera collapse in strike–slip tectonic regimes. Bull Volcanol 70:773–796

Holub FV (1980) Petrography of the samples from the Deep Borehole Le –127 (B) In: Final Report of the project Barbora II. Part F. Final Report of Geoindustria. Unpublished manuscript, Czech Geological Survey – Geofond, Prague, pp 1–81 (in Czech)

Hoth K, Wasternack J, Berger H J, Breiter K, Mlčoch B, Schovánek P (1995) Geologische Karte Erzgebirge/Vogtland 1 : 100 000. Sächsisches Landesamt für Umwelt und Geologie, Freiberg

Jihlavec F, Chudomel J, Jakeš O, Kadlečík J, Novák J, Piller S (1983) Final Report – Seismic Survey in the SE part of the Most Basin in 1981–1982, Barbora–Maxim Gorkij Profile. Unpublished manuscript, Geofyzika, Brno, pp 1–30 (in Czech)

Jihlavec F, Chudomel J, Filková V, Hikl V, Horová M, Jakeš O, Novák J (1984) Seismic Survey in the KOH-I-NOOR Opet Pit Mine in the years 1983–84. Unpublished manuscript, Geofyzika, Brno, pp 1–29 (in Czech)

Jiránek J ed (1991) Geological map ČSSR 1 : 25 000, sheet 02–322 Krupka. Czech Geological Survey, Prague

Jiránek J, Kříbek B, Mlčoch B, Procházka J, Schovánek P (1987) Complex Geological Study of the Teplice Rhyolite. Final Report. Unpublished manuscript, Czech Geological Survey, Prague, pp 1–114 (in Czech)

Lange H , Tischendorf G, Pälchen W, Klemm I, Ossenkopf E (1972) Fortschritte der Metallogenic im Erzgebirge. B. Zur Petrographic und Geochemie der Granite des Erzgebirges. Geologie 21, 4/5, pp 491–520

Malásek F ed (1987) Report on Search of the Granite Elevation in the Eastern Part of the Krušné hory Mts. Mineral Deposit: Sn–W. Unpublished manuscript, Czech Geological Survey – Geofond, Prague, pp 1–56, 164 appendix folders (in Czech)

Mlčoch B ed (1989) Geological map ČSSR 1 : 25 000, sheet 02–314 Litvínov. Czech Geological Survey, Prague

Mlčoch B (1994) The geological structure of the crystalline basement below the North Bohemian brown coal Basin. KTB Report 94(3): 39–46. Niedersächsisches Landesamt für Bodenforschung, Hannover

Mlčoch B ed (2001) Research on the Crystalline Basement of Doupovské hory Mts. and Their Vicinity. Final Report. VAV 631/1/00. Unpublished manuscript, Czech Geological Survey, Prague, pp 1–120 (in Czech)

Mlčoch B (2003) Character of the contact between the Saxothuringian and Teplá–Barrandian Unit. Geolines 16: 75

Mlčoch B, Konopásek J (2010) Pre-Late Carboniferous geology along the contact of the Saxothuringian and Teplá–Barrandian zones in the area covered by younger sediments and volcanics (western Bohemian Massif, Czech Republic). J Geosci 55: 81–94

Moesta G (1928) Brüche und Porphyreffusionen im östlichen Erzgebirge. Z Dtsch geol Gesell 80: 343–408

Müller A, Seltmann R (2002) Plagioclase-mantled K-feldspar in the Carboniferous porphyric microgranite of Altenberg–Frauenstein, Eastern Erzgebirge/Krušné Hory. Bull Geol Soc Finland 74: 53–79

Müller A, Breiter K, Seltmann R, Pécskay Z (2005) Quartz and feldspar zoning in the eastern Erzgebirge Volcano–Plutonic Complex (Germany, Czech Republic): evidence of multiple magma mixing. Lithos 80: 201–227

Novák JK, Chrt J, Malásek F (1991) The hidden granite relief and its significance for prospection (as an example of the eastern part of the Krušné hory Mts). In: Kukal (ed) Proceedings of the 1st International Conference on the Bohemian Massif. Czech Geological Survey, Prague, pp 205–207

Rajchl M, Uličný D, Hubatka F (2003) Syn- and post-sedimentary tectonics of the Most Basin (Ohře Rift, Czech Republic); insights from reflection-seismic data. Geolines 16: 86

Romer RL, Thomas R, Stein HJ, Rhede D (2007) Dating multiply overprinted Sn-mineralized granites – examples from the Erzgebirge, Germany. Mineral Depos 42: 337–359

Schovánek P ed, Adamová M, Breiter K, Burda J, Cajz V, Elznic A, Fürych V, Godány J, Kořán V, Manová M, Nekovařík Č, Šalanský K, Šebesta J (2004) Explanatory text of Geological map of Czech Republic to sheets 02–321 Dubí and 02–143 Cínovec. Czech Geological Survey, Prague, pp 1–84 (in Czech)

Sedlák J, Gnojek I, Zabadal S, Scheibe R, Zabadal S (2009) Gravity response of igneous rocks in the northwestern part of the Bohemian Massif. J Geosci 54: 325–342

Seltmann R, Schilka W (1995) Late-Variscan crustal evolution in the Altenberg–Teplice caldera. Evidence from new geochemical and geochronological data. Terra Nostra 7/95: 120–124.

Spinks KD, Acoccella V, Cole JW, Bassett KN (2005) Structural control of volcanism and caldera development on the transtensional Taupo Volcanic Zone, New Zealand. J Volcanol Geotherm Res 144: 7–22

Štemprok M, Holub FV, Novák JK (2003) Multiple magmatic pulses of the Eastern Volcano–Plutonic Complex, Krušné hory/Erzgebirge Batholith, and their phosphorus contents. Bull Geosci 78: 277–296

Troll VR, Walter TR, Schmincke HU (2002) Cyclic caldera collapse: piston or piecemeal subsidence? Field and experimental evidence. Geology 30: 135–138

Walter T R, Troll VR (2001) Formation of caldera periphery faults: an experimental study. Bull Volcanol 63: 191–203

Winter C, Breitkreuz C, Lapp M (2008) Textural analysis of Late Palaeozoic coherent–pyroclastic rhyolitic dyke system near Burkerdorf (Erzgebirge, Saxony, Germany). In: Thomson K, Petford N (eds) Structure and Emplacement of High-Level Magmatic Systems. Geological Society of London Special Publications 302: 199–221

Journal of Geosciences, 55 (2010), 231–249 DOI: 10.3190/jgeosci.077

Original paper

Clinopyroxene from basaltic rocks of the Erzgebirge-Krušné hory Mts. – implications for modelling of the magmatic plumbing system

Roman RÖNICK[1], Axel D. RENNO[1*]

[1] *Technische Universität Bergakademie Freiberg, Institute of Mineralogy, Brennhausgasse 14, D-09596 Freiberg, Germany; axel.renno@mineral.tu-freiberg.de*

[*] *Corresponding author*

The Erzgebirge-Krušné hory area is part of the NW flank of the Eger-Ohře Rift. Within this rift-related area, basaltic rocks with low (< 3.5 wt. %) and high contents (> 3.5 wt. %) of TiO_2 occur. The distribution of these basaltic rock types shows strong spatial dependency. Ti-rich basalts are concentrated in the western Erzgebirge-Krušné hory Mts. with a sharp change at longitude 13.3 °E. Clinopyroxene and olivine are the most abundant phenocrysts. The zoning and chemistry of the clinopyroxene act as a recorder of the different stages of the magmatic plumbing systems. Seven different types of clinopyroxene phenocrysts are defined with four distinct chemical types: Cr-rich clinopyroxene, green-core pyroxene, Mg-rich clinopyroxene and finely zoned Ti-rich clinopyroxene with sector zoning.

Chemical and petrographic analysis of individual zones within clinopyroxenes allows the qualitative description of distinct steps of the multistage, regionally diverse processes yielding to the formation of both Ti-rich basalts in the W as well as Ti-poor basalts in the E. Two different types of asthenospheric melts are suggested, with increased activities of H_2O and potassium in the western Erzgebirge Mts. During ascent they incorporated xenoliths and xenocrysts of both the mantle (peridotite, olivine and Cr-rich clinopyroxene) and the crustal (granitic and gneissic rocks, quartz and feldspar) origin. Furthermore, green cores of clinopyroxene were introduced into the magmas. Fractionation processes took place within lithospheric magma chambers, having been accompanied by reaction of xenocrysts and xenoliths with the melt. The residence time in the magma chambers associated with the eastern and western parts of the Erzgebirge appears to have been totally different: short in the eastern and long in the western parts. Within the latter, no mantle-derived xenoliths, xenocrysts, or magmatic olivines are found. It is inferred that these xenoliths and crystals settled to the bottom of the magma chambers forming cumulates and therefore did not come to the surface. In contrast, the basaltic rocks of the East still contain mantle-derived xenoliths and xenocrysts as well as magmatic olivine. The size and amount of clinopyroxene phenocrysts in the West significantly exceed that of the East. Moreover, the crystallization of giant clinopyroxenes was restricted to the western region. Mixing of the magmas with Ti-rich melts, presumably derived from an eclogitic source, took place in crustal magma chambers. In any case, the proportion of Ti-rich melts in the West significantly exceeded that of the East.

Keywords: petrology, crystal chemistry, clinopyroxene, basalt, Erzgebirge-Krušné hory, green-core pyroxene
Received: 6 April 2010; accepted: 20 September 2010; handling editor: V. Rapprich/R. Skála
The online version of this article (doi: 10.3190/jgeosci.077) contains supplementary electronic material.

1. Introduction

Despite the eye-catching geochemical character of '*Ti-rich basalts*' it is unclear if this feature is a vagary of nature or an important geochemical fingerprint able to discriminate between different source regions of basaltic rocks. Besides well known High-Ti basalts from the moon (Papike et al. 1976; Papike and Vaniman 1978), which have no terrestrial equivalent, High-Ti basalts are found in different geotectonic settings, such as Continental Flood Basalts (CFB), Large Igneous Provinces (LIP) (Gibson et al. 1995), or rift-like intraplate settings (Pik et al. 1998). The occurrence of such basalts is not restricted to lavas; they appear also in dike systems (Essawy and El-Metwally 1999; Katzir et al. 2006) and intrusions of gabbroic rocks (Jama Aden and Frizzo 1996). Their age spans from the Archaean to recent. The origin in each of the geotectonic environments remains controversial. The proposed explanations in LIPs range from a high degree of fractionation (Fodor 1987), low degree of partial melting (Dupuy et al. 1988), crustal contamination (Fodor 1987), to the influence of subcontinental lithosphere mobilized by subduction (Duncan 1987; Murphy 1988). It is assumed that the effect of mantle plumes is the main cause for the genesis of Ti-rich rocks in rift-like settings (Pik et al. 2006).

A qualitative approach to understanding petrological processes responsible for the genesis of Ti-rich basalts through the comprehensive study of the microstructure and mineral chemistry of clinopyroxene is demonstrated in the

current paper. As a case study have been chosen Cenozoic basaltic rocks from the Eger-Ohře Rift (Erzgebirge-Krušné hory Mts, Bohemian Massif). Although we do not present a complete genetic model, this study does provide a basis for understanding the nature and genesis of the high-Ti basalts, both in this region and elsewhere.

2. Geological setting

According to Prodehl et al.(1995) the Eger-Ohře Rift, as part of the European Cenozoic Rift System (ECRS), is one of the major extensional structures in Central Europe. The structure itself is situated in Proterozoic to Paleozoic basement rocks of the Bohemian Massif (Malkovský 1987; Mlčoch and Konopásek 2010) and shows an elongation of roughly 300 km and a width up to ~ 30 km. The western part of the Eger Rift lies on a Variscan suture zone between two lithospheric blocks: the Saxothuringian and the Teplá–Barrandian terranes (Hrubcová et al. 2005; Babuška et al. 2007). The thermal thickness of the lithosphere at the level of the 1 300 °C isotherm has been modelled to be 110–170 km, whereas the mechanical thickness is only 65–90 km (Babuška and Plomerová 1992; Goes et al. 2000). Plomerová et al. (2007) with Babuška and Plomerová (this volume) found clear differences in the orientations of seismic anisotropy in the three major tectonic units (Saxothuringian, Moldanubian and Teplá–Barrandian), but no signs for the existence of plume-like structures in the mantle. The region shows evidence for repeated magmatic phases before the Tertiary but most of the Eger Rift lavas erupted between 30 and 15 Ma both within the rift and on its NW flank (Todt and Lippolt 1975; Pilot et al. 1984; Kaiser and Pilot 1986; Ulrych et al. 2002).

The NW-flank of the western part of the Eger Rift lies in the Erzgebirge-Krušné hory Mts. part of the Saxothuringian Zone of the Bohemian Massif, which is known to host volcanic rocks with distinct differences in the TiO_2 contents (Pfeiffer 1978; Niese et al. 1995; Shrbený 1995; Ulrych et al. 2005; Haase and Renno 2008). Detailed studies of the mineral chemistry of clinopyroxene in the basaltic rocks of the Eger Rift are rare so far (Ulrych 1986; Ulrych et al. 1990; Rapprich 2005) and the current manuscript aims to bring new data in this respect.

3. Sampling and methods

The first step of sampling was the verification of all outcrops of basaltic rocks evinced in the 1 : 25 000 geo-

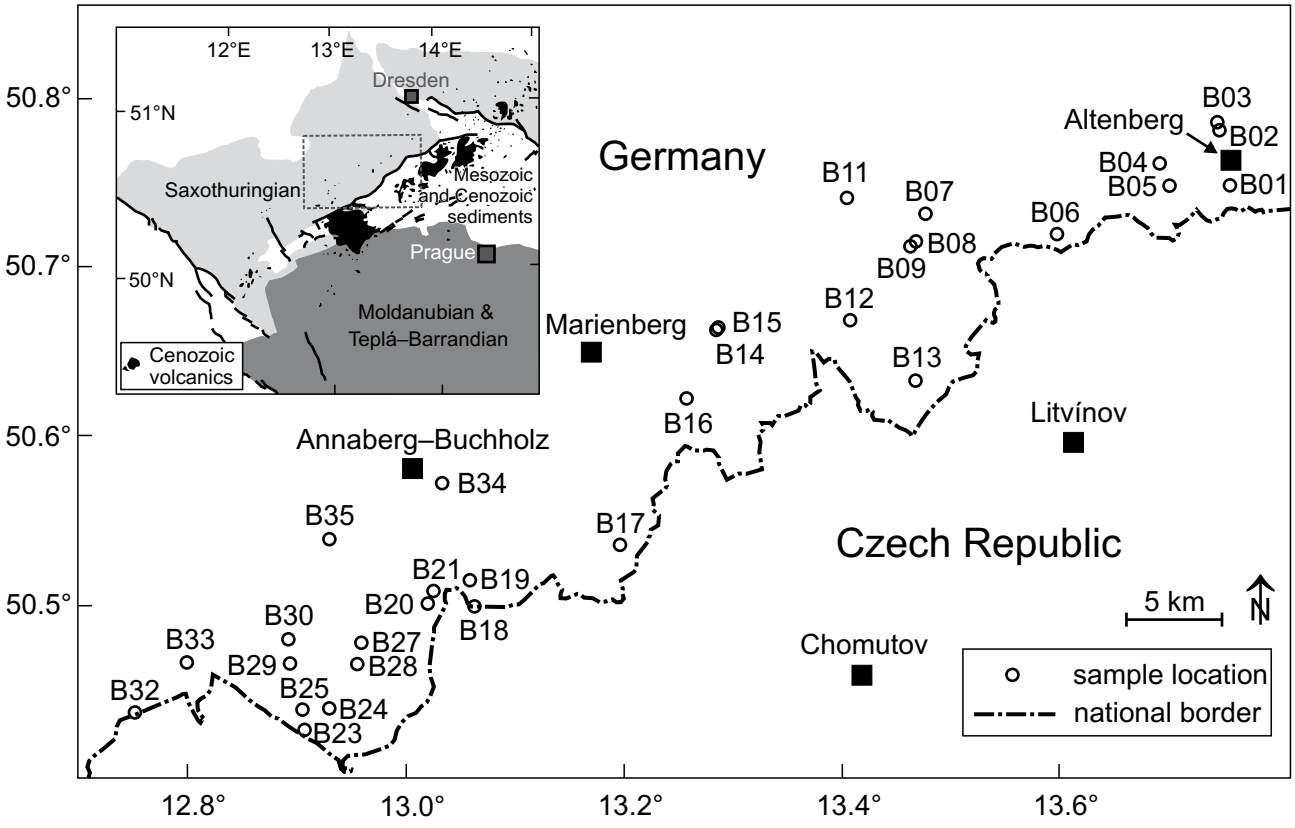

Fig. 1 Location of the samples. The locations, including GPS coordinates, are summarized in Tab. 1.

logical maps of the German part of the Erzgebirge. The eventual sampling covered 27 localities (Tab. 1 and Fig 1). The samples were selected on the basis of the major-element composition, i.e. only primitive rock types were chosen.

Fresh pieces were cut and washed in distilled water and an ultrasonic bath before crushing. The crushed rock sample was milled to powder in an agate ball mill. Whole-rock major-element analyses were measured with a Bruker "Tiger S8" X-ray fluorescence spectrometer at the Institut für Mineralogie, TU Bergakademie Freiberg using rock standards for calibration and quality control.

Mineral analyses were carried out using a JEOL JXA8900 electron microprobe at the Institut für Mineralogie, TU Bergakademie Freiberg. The analytical conditions for the minerals were an accelerating voltage of 15 keV, a beam current of 30 nA and a focused beam. Counting times were 20–50 s for peak and 10–25 s for background positions. An accelerating voltage of 20 keV and a beam current of 40 nA were used for X-ray concentration maps and concentration profiles. Natural mineral standards and the ZAF matrix correction was employed.

All data were visualized using the GCDkit software package (Janoušek et al. 2006).

4. Geochemistry

Representative whole-rock analyses of the lavas are presented in Tab. 1. All the analyzed basaltic rocks represent truly alkali basaltic rocks, mostly basanites and melanephelinites (Supp. 1), according to the total alkali vs. SiO_2 (TAS) classification scheme of Le Bas et al. (1986) and Le Maitre et al. (2005). We stuck to the proposals of Le Bas (1989) and Middlemost (1994) for further discrimination between basanite/tephrite and nephelinite/melanephelinite (Fig. 2).

4.1. Major elements and trace elements

All samples form a continuous trend with decreasing TiO_2, FeO^T, and CaO and increasing MgO, and Al_2O_3 with increasing SiO_2 (Fig. 3a–d and Supp. 2). With rising FeO^T/MgO, ratio, often used as a differentiation index, TiO_2, and CaO show a continuous increase, while Cr, and Ni drop sharply (Fig. 3e and Supp. 2). The lavas show two separate positive trends in binary diagram of FeO^T/MgO vs. Al_2O_3 (Fig. 3f). Some trace elements (e.g. Nb, V, and Zr) are positively correlated with TiO_2 (Fig. 3g and Supp. 2), whereas the ratio CaO/Al_2O_3 shows a clear splitting at *c.* 3.5 wt. % TiO_2 (Fig. 3h).

4.2. Regional variation

A striking feature is the regional dichotomy in whole-rock compositions of basalts from the eastern and western Erzgebirge. At a longitude of 13.3 °E we observed an abrupt change (Supp. 3), best exemplified by TiO_2 (Fig. 4). Despite a small overlap, TiO_2 (threshold value 3.5 wt. %) and CaO (threshold value 13.5 wt. %) drop eastwards, while Al_2O_3 (threshold value 12 wt. %),

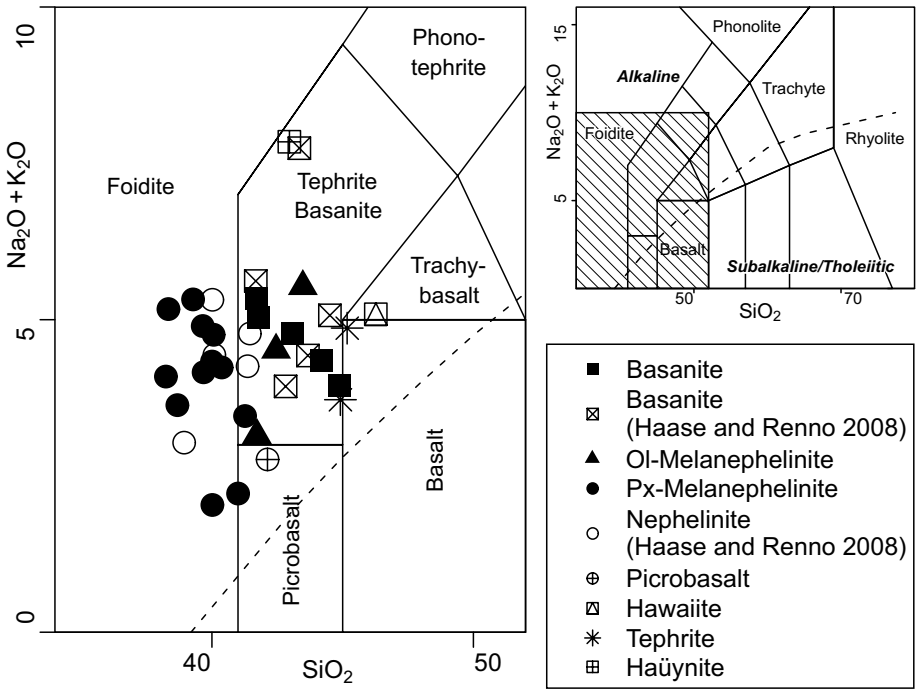

Fig. 2 Total alkali vs. SiO_2 (TAS) diagram for the analysed basaltic rocks and some additional samples from the same area (Haase and Renno 2008).

Tab. 1 Whole-rock major- and trace-element compositions for the studied basaltic rocks from the eastern and western Erzgebirge (Germany)

Sample	**B01**	**B02a**	**B03a**	**B05**	**B06**	**B07**	**B08**
Locality	NNW Zinnwald	SE Hirschsprung	Hirschsprung	road Altenberg–Rehefeld	Steinkuppe near Holzhau	Ziegenberg near Claußnitz	"Kreuztanne"
Latitude °N	50.749	50.782	50.786	50.749	50.720	50.730	50.715
Longitude °E	13.76	13.75	13.75	13.71	13.60	13.47	13.47
Rock type	basanite	basanite	basanite	Ol-Mn	Ol-Mn	Ol-Mn	hawaiite
SiO_2	42.29	40.97	40.71	40.27	42.34	41.75	45.13
TiO_2	2.72	3.71	3.59	3.37	3.14	3.07	3.20
Al_2O_3	12.68	13.72	13.11	12.66	13.44	13.26	13.63
Fe_2O_3t	12.39	13.36	13.27	13.91	12.37	12.92	12.25
MgO	12.17	9.93	10.84	9.99	9.18	10.57	8.80
MnO	0.19	0.19	0.19	0.23	0.20	0.21	0.22
CaO	11.67	11.75	11.46	13.39	11.73	12.74	9.88
Na_2O	3.32	3.75	3.63	2.55	4.25	3.59	3.66
K_2O	1.37	1.49	1.27	0.49	1.13	0.85	1.30
P_2O_5	0.60	0.73	0.71	1.06	0.83	0.68	0.69
L.o.I.	0.23	0.40	0.35	0.88	0.50	0.40	0.46
Total	99.63	100.01	99.13	98.79	99.11	100.03	99.22
B	76	128	134	100	112	97	112
F	491	897	776	252	898	528	869
S	190	270	230	190	260	240	470
Cl	179	250	218	bd	212	bd	bd
V	223	268	261	252	271	254	211
Cr	361	136	188	157	189	290	102
Co	51	46	48	43	41	48	40
Ni	209	108	152	130	110	138	90
Cu	48	61	53	31	38	43	35
Zn	97	97	97	97	97	97	97
Ga	17	18	17	17	18	17	18
As	2	3	3	5	8	4	19
Br	4	4	4	2	4	3	3
Rb	32	53	48	49	39	45	49
Sr	618	710	688	1344	782	701	707
Y	20	21	20	22	23	22	22
Zr	206	236	226	270	264	226	243
Nb	60	68	68	58	71	57	55
Mo	bd	1	4	2	4	2	4
Ag	bd	bd	bd	bd	bd	bd	bd
Cd	bd	bd	bd	bd	1	bd	1
Sn	5	7	5	9	4	6	4
Cs	0.6	2.4	1.2	bd	2.2	5.7	39.8
Ba	434	499	468	707	632	542	668
La	38	52	55	83	76	49	55
Ce	86	90	87	133	125	99	93
Pb	4	5	2	7	bd	4	bd
U	11.2	11.4	11.5	15.6	11.2	11.0	10.2

bd = below detection limit; Mn = melanephelinite

Tab. 1 Continued

Sample	B11b	B12b	B13	B14a	B15	B16	B17
Locality	Galgenberg (road way Voigtsdorf–Sayda)	Schafferholz (Heidersdorf)	Ahornberg (Seiffen)	SW Blumenau	SW Blumenau	Rabenberg (SE Zöblitz)	Hirtstein (N Satzung)
Latitude °N	50.740	50.668	50.632	50.662	50.663	50.622	50.536
Longitude °E	13.40	13.41	13.47	13.28	13.28	13.25	13.19
Rock type	basanite	basalt	basanite	Cpx-Mn	picrobasalt	Cpx-Mn	Cpx-Mn
SiO_2	43.74	47.24	43.63	39.63	41.23	39.23	39.13
TiO_2	2.98	2.72	2.36	3.88	3.83	4.32	4.04
Al_2O_3	12.40	13.48	11.09	10.16	10.30	11.17	10.42
Fe_2O_3t	11.75	11.12	12.01	14.31	14.22	14.94	14.47
MgO	10.53	8.27	16.01	9.07	9.36	8.26	8.85
MnO	0.18	0.18	0.18	0.21	0.20	0.22	0.22
CaO	12.29	11.31	9.66	17.97	16.75	15.54	16.45
Na_2O	2.95	3.12	3.07	1.63	1.91	2.95	2.83
K_2O	0.90	0.99	1.23	0.51	0.80	1.16	1.82
P_2O_5	0.93	0.50	0.70	0.72	0.70	0.86	0.90
L.o.I.	0.51	0.76	0.11	0.94	0.55	0.36	0.56
Total	99.17	99.68	100.06	99.03	99.84	99.01	99.67
B	115	109	88	126	118	146	146
F	505	375	bd	1344	1245	692	1385
S	300	240	110	910	580	300	320
Cl	bd	bd	85	396	170	bd	bd
V	242	237	183	383	371	416	393
Cr	299	272	549	185	193	100	100
Co	43	41	60	46	49	46	49
Ni	136	130	445	56	59	38	50
Cu	50	43	35	197	196	244	283
Zn	97	97	97	97	97	97	97
Ga	17	17	17	17	18	19	18
As	3	7	6	2	5	1	5
Br	3	3	4	4	3	3	3
Rb	38	207	32	58	45	49	43
Sr	768	548	765	701	729	790	804
Y	23	28	18	18	19	23	21
Zr	237	198	221	231	237	280	305
Nb	67	48	69	77	74	96	95
Mo	3	1	1	2	bd	bd	bd
Ag	bd	bd	bd	bd	bd	bd	bd
Cd	bd	bd	bd	bd	bd	bd	bd
Sn	4	6	6	6	6	3	3
Cs	1.5	5.5	0.7	1.7	2.2	bd	bd
Ba	602	867	448	585	898	978	531
La	70	42	55	63	64	84	83
Ce	124	83	125	113	117	148	135
Pb	4	6	5	6	5	3	6
U	11.3	6.0	12.5	10.4	8.1	7.9	11.7

bd = below detection limit; Mn = melanephelinite

Tab. 1 Continued

Sample	**B18c**	**B19**	**B21**	**B24**	**B25**	**B27a**	**B30b**
Locality	SW Jöhstadt (state frontier)	Klöfs–Berg (W Jöhstadt)	Bärenstein (W Bärenstein)	Wurzelbergstraße (Oberwiesenthal)	Einsberg (NE Tellerhäuser)	Morgenberg (W Neudorf)	Eisensteinberg (W Neudorf)
Latitude °N	50.501	50.516	50.508	50.442	50.439	50.479	50.481
Longitude °E	13.06	13.05	13.02	12.93	12.90	12.96	12.89
Rock type	Ol–Cpx-leucitite	Cpx-Mn	Cpx-Mn	tephrite	Cpx-Mn	haüynite	Cpx-Mn
SiO_2	40.79	38.91	38.18	43.74	40.31	41.56	38.76
TiO_2	3.95	4.37	5.02	3.75	4.68	4.12	4.75
Al_2O_3	10.71	10.38	11.04	12.99	11.55	13.79	11.24
Fe_2O_3t	13.89	16.09	16.23	12.92	15.01	12.65	14.74
MgO	10.11	8.31	7.05	6.74	7.26	4.32	8.25
MnO	0.18	0.21	0.27	0.20	0.22	0.28	0.23
CaO	14.81	16.64	14.61	12.42	15.91	12.36	15.58
Na_2O	2.27	2.79	3.93	3.59	2.60	4.20	3.30
K_2O	2.14	1.29	1.25	1.12	0.78	3.39	1.49
P_2O_5	0.62	0.69	1.26	0.65	0.87	1.33	0.88
L.o.I.	0.25	0.27	0.44	0.67	0.63	0.52	0.55
Total	99.72	99.95	99.28	98.79	99.83	98.52	99.76
B	112	146	160	126	162	180	169
F	560	1370	1643	1376	1443	1915	2155
S	330	410	270	1020	390	2100	600
Cl	bd	bd	bd	bd	bd	1517	200
V	369	454	408	324	410	352	393
Cr	270	26	12	62	37	10	88
Co	48	53	45	44	48	27	45
Ni	80	38	28	53	31	11	53
Cu	247	414	82	81	262	31	178
Zn	97	97	112	97	99	131	97
Ga	17	20	21	19	20	25	19
As	4	5	2	7	3	7	4
Br	3	4	3	3	3	7	4
Rb	70	36	40	46	82	77	37
Sr	456	833	899	788	731	1498	829
Y	20	19	27	23	22	38	22
Zr	220	262	377	247	306	523	293
Nb	76	89	107	76	89	157	94
Mo	bd	bd	bd	9	bd	3	bd
Ag	bd	bd	bd	bd	bd	bd	bd
Cd	bd	bd	1	bd	1	bd	bd
Sn	7	4	6	6	8	8	5
Cs	bd	0.6	bd	bd	bd	bd	bd
Ba	1024	697	511	664	439	954	621
La	62	76	108	74	72	148	86
Ce	123	117	169	121	117	260	142
Pb	4	6	bd	7	bd	16	5
U	4.4	10.5	12.9	10.9	11.6	14.4	11.3

bd = below detection limit; Mn = melanephelinite

Tab. 1 Continued

Sample	B30c	B32	B33a	B33b	B34	B35
Locality	Eisensteinberg (W Neudorf)	Glücksburg Berg (E Johanngeorgenstadt	Vordere Kohlung (S Rittersgrün)	Vordere Kohlung (S Rittersgrün)	Pöhlberg (E Annaberg–Buchholz)	Scheibenberg (E Scheibenberg)
Latitude °N	50.481	50.436	50.467	50.467	50.574	50.540
Longitude °E	12.89	12.75	12.80	12.80	13.03	12.92
Rock type	tephrite	Cpx-Mn	Cpx-Mn	Cpx-Mn	Cpx-Mn	Cpx-Mn
SiO_2	43.63	38.94	37.10	39.17	37.20	37.79
TiO_2	4.18	4.81	4.97	4.39	5.03	5.12
Al_2O_3	11.02	10.28	11.42	10.92	11.33	11.03
Fe_2O_3t	12.55	15.29	15.30	15.21	15.74	16.19
MgO	7.98	10.46	6.35	8.25	6.37	7.92
MnO	0.19	0.21	0.25	0.21	0.26	0.22
CaO	14.48	16.13	17.86	16.24	16.11	16.51
Na_2O	2.35	1.50	2.99	2.84	3.65	2.57
K_2O	1.27	0.49	0.98	1.40	1.36	0.98
P_2O_5	0.76	0.75	1.33	0.81	1.56	1.00
L.o.I.	0.77	1.01	0.45	0.34	0.42	0.58
Total	99.17	99.85	99.01	99.77	99.03	99.90
B	155	163	176	155	164	151
F	1734	1734	1671	1446	2466	2034
S	1940	530	960	470	1050	820
Cl	bd	115	bd	bd	425	bd
V	350	389	437	422	464	475
Cr	116	193	10	74	17	49
Co	42	52	44	50	52	54
Ni	60	82	12	39	21	39
Cu	148	213	295	330	186	287
Zn	97	97	104	97	122	106
Ga	17	17	20	19	24	22
As	5	5	4	3	5	5
Br	3	4	3	3	5	4
Rb	77	53	50	44	56	47
Sr	1009	667	998	857	822	807
Y	22	19	25	20	36	31
Zr	253	258	352	270	426	345
Nb	89	68	90	83	114	106
Mo	4	bd	1	bd	bd	2
Ag	bd	bd	bd	bd	2.3	bd
Cd	bd	bd	bd	1	bd	bd
Sn	8	7	6	7	7	6
Cs	0.3	bd	bd	bd	2.8	bd
Ba	662	540	745	903	302	610
La	79	74	95	74	98	89
Ce	135	131	173	136	179	144
Pb	6	5	8	1	12	10
U	12.6	10.4	11.6	9.1	12.9	10.1

bd = below detection limit; Mn = melanephelinite

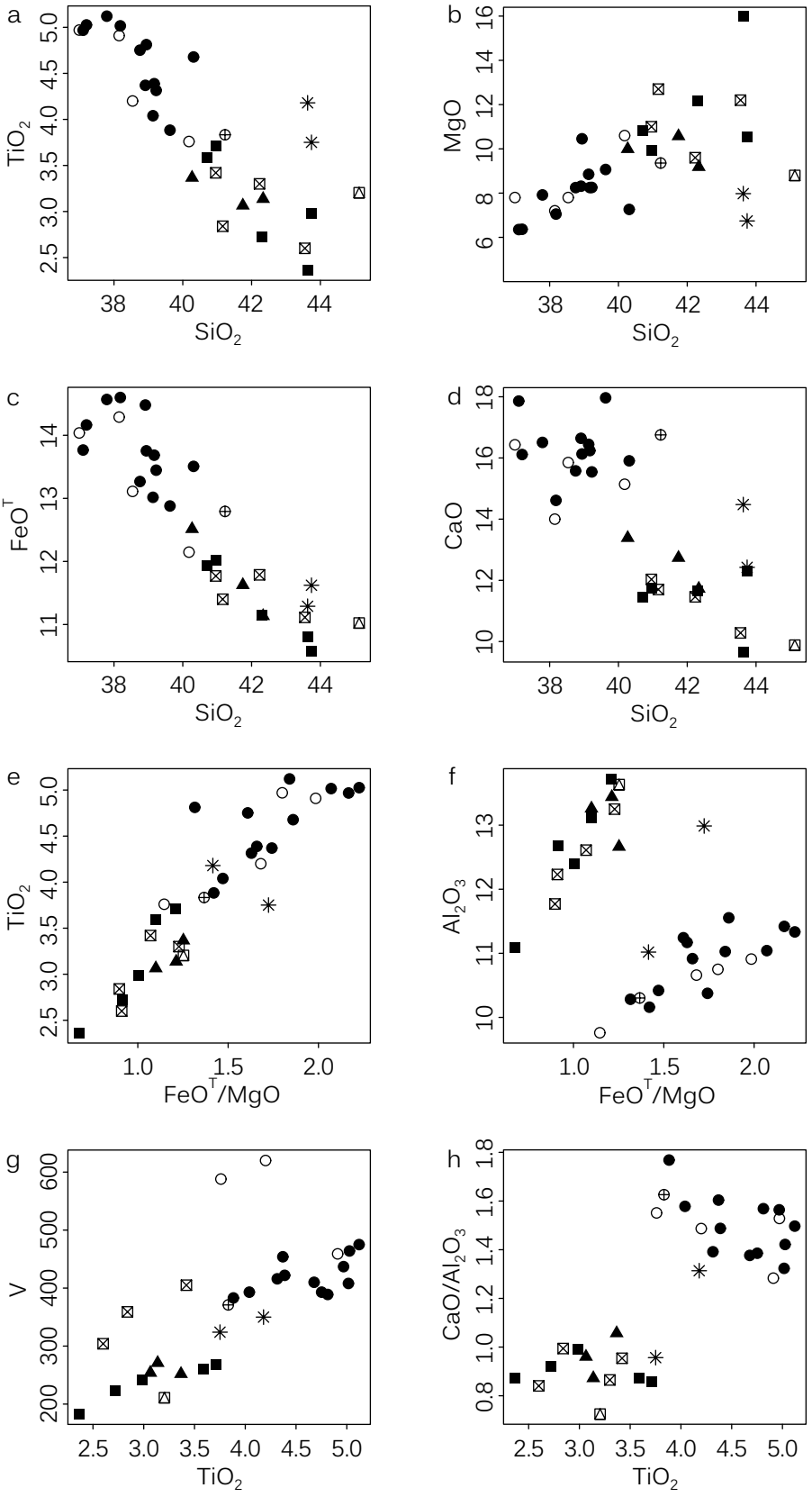

Fig. 3 Selected variation diagrams for the Erzgebirge basaltic rocks. Symbols and additional data sources as in Fig. 2. **a** – SiO_2 vs. TiO_2; **b** – SiO_2 vs. MgO; **c** – SiO_2 vs. FeO^T; **d** – SiO_2 vs. CaO; **e** – FeO^T/MgO vs. TiO_2; **f** – FeO^T/MgO vs. Al_2O_3; **g** – TiO_2 vs. V; **h** – TiO_2 vs. CaO/Al_2O_3.

and mg# (threshold value 58) increase. Such variations are known from other parts of the ECRS like the Vogelsberg (Bogaard and Wörner 2003) and the Rhön (Jung and Hoernes 2000).

5. Petrography

The petrography of all samples was described in detail by Rönick (2010). The main features are compiled in Supp. 1.

5.1. Groundmass

All rocks show a porphyritic microstructure with a fine-grained groundmass. This groundmass consists of small, elongate clinopyroxene and isometric opaque minerals. Some lavas show flow patterns or schlieren-like inhomogeneities. Additionally minerals of the sodalite-group, nepheline, perovskite, and analcime occur, predominantly in the rocks from the western part of the Erzgebirge. Lath-shaped plagioclase is typical of the lavas from the eastern Erzgebirge. Apatite is a common component of the groundmass, but can in some cases reach the size of a phenocryst. Tiny flakes of biotite (*c.* 0.02 mm) are found in many samples from both the eastern and the western Erzgebirge.

5.2. Phenocrysts

The most common phenocrysts are clinopyroxene and olivine; amphibole and biotite are of subordinate importance.

5.2.1. Olivine

Olivine is found almost exclusively in lavas from the eastern Erzgebirge and forms the main constituent of the phenocrysts in these rocks. Most of the olivine

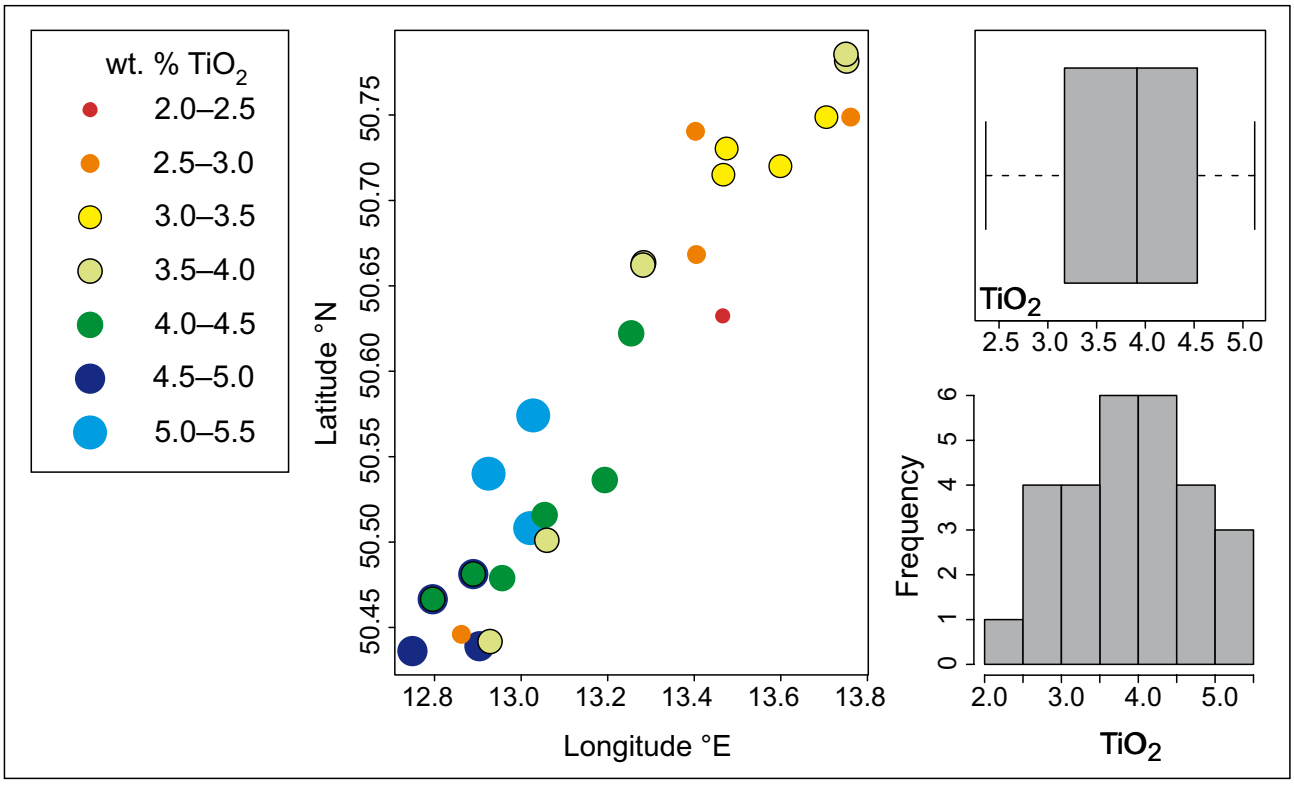

Fig. 4 Regional variation in the TiO_2 contents for the studied basaltic rocks.

crystals are subhedral; skeletal forms are rare. Many show signs of deformation. Visible zoning is restricted to the ultimate rim. Characteristic mineral inclusions are magnetite and brown spinel phases; typical alteration products are serpentine minerals and calcite.

5.2.2. Clinopyroxene

Generally, seven types of clinopyroxene phenocrysts occur in the studied rocks, of which six are shown in Fig. 5. Every type is characterized by the crystallization of an "outermost overgrowth" (**OMG**) of beige–brownish colour showing intense internal oscillatory zoning and sector growth features.

Type 1 Clinopyroxene with a light beige core (**LBC**) of subhedral to anhedral shape. The internal structure of the core shows dissolution features and reaction rims. These cores are always overgrown by the **OMG**.

Type 2 Similar features like Type 1 and additionally a thin fringe around the anhedral central core characterized by a weaker BSE intensity.

Type 3 Typical green-core clinopyroxenes (**GcCpx**) as noted by several authors (Huckenholz 1964, 1965, 1966; Duda and Schmincke 1985) with a size between 0.2 and 2 mm. The central green cores are anhedral and show dissolution features and reaction rims; in very rare cases these cores are zoned. The first overgrowth is by a LBC-type pyroxene followed by the OMG-type. The thickness of the respective zones varies.

Type 4 These form the smallest phenocrysts (0.5 mm) and show internal oscillatory zoning combined with sector zoning features. According to the mineral chemistry (see below) these phenocrysts belong to the **OMG**-type.

Type 5 Anhedral Cr-rich cores characterize this type as demonstrated by EMPA (see below) and show low BSE intensity (**CrCpx**). The first overgrowth is by the **LBC**-type followed by the **OMG**-generation. It is restricted to lavas from the eastern Erzgebirge.

Type 6 Shows the same features as type 5, but is overgrown merely by the **OMG**-type.

Type 7 This forms the so called "giant clinopyroxenes" (**GCpx**), reaching sizes of several centimetres, similar to the **LBC**-type. These megacrysts are overgrown by a very thin rim of the **OMG**-type and restricted to the western Erzgebirge.

5.2.3. Biotite

Biotite phenocrysts, up to 2 cm across, occur in some samples from the western Erzgebirge. These have an anhedral, rounded shape and show signs of bending and kinking. Reaction rims formed at the grain boundaries.

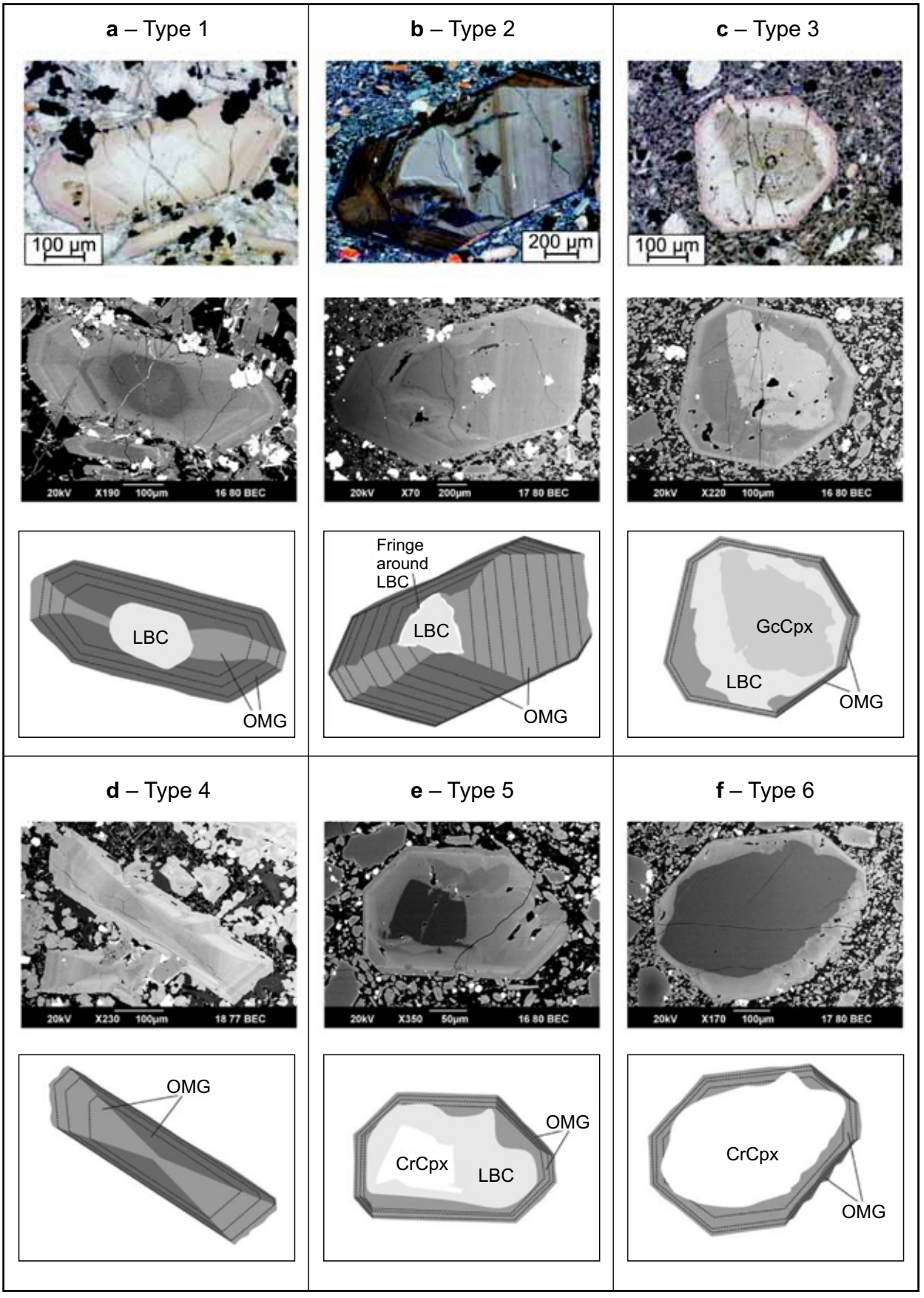
a – Type 1
b – Type 2
c – Type 3
100 µm
200 µm
100 µm
20kV X190 100µm 16 80 BEC
20kV X70 200µm 17 80 BEC
20kV X220 100µm 16 80 BEC
LBC
OMG
Fringe around LBC
LBC
OMG
GcCpx
LBC
OMG
d – Type 4
e – Type 5
f – Type 6
20kV X230 100µm 18 77 BEC
20kV X350 50µm 16 80 BEC
20kV X170 100µm 17 80 BEC
OMG
CrCpx
LBC
OMG
CrCpx
OMG

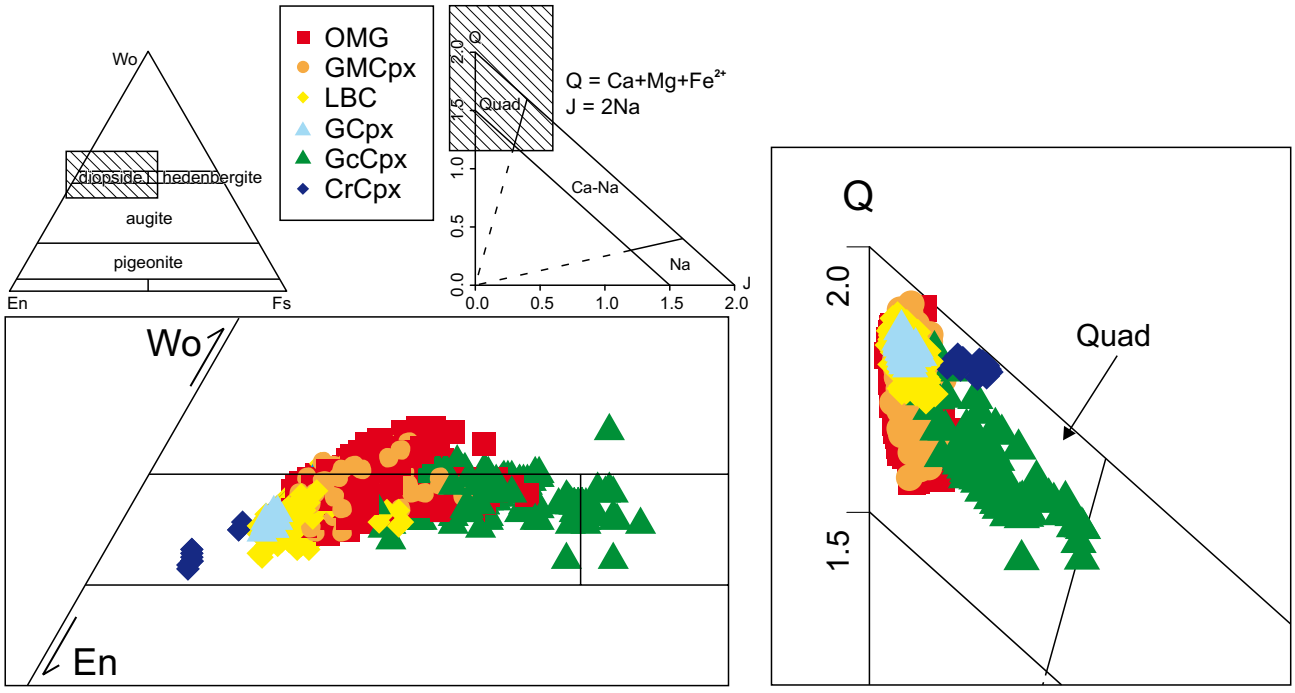

Fig. 6 Plot of analysed clinopyroxenes in classification diagram after Morimoto (1988).

Inclusions of opaque minerals and clinopyroxene are rare. Some of these biotites are intergrown with GCpx.

5.2.4. Amphibole

Two samples carry brownish-green subhedral amphibole crystals. These amphiboles are heterogeneous, but show no clear signs of zoning. Typical are inclusions of opaque minerals.

5.3. Xenoliths and xenocrysts

Many samples contain xenoliths and xenocrysts of crustal (granitoid, gneiss, and sandstone) and mantle origin (spinel lherzolite). The occurrence of mantle-derived material is restricted to samples from the eastern Erzgebirge.

⇦

Fig. 5 Clinopyroxene types in the Erzgebirge basaltic rocks (photomicrographs, back-scattered electron (BSE) images and sketches). **a** – Type 1 clinopyroxene **LBC** of subhedral to anhedral shape. The internal structure of the core shows dissolution features and reaction rims. The **LBC** is overgrown by the **OMG**-type Cpx; **b** – Type 2 resembling the Type 1 but showing additionally a thin fringe around the anhedral **LBC** core characterized by weaker BSE intensity; **c** – Type 3 is a typical green-core clinopyroxene (**GcCpx**). The green core is anhedral and shows effects of resorption and a reaction rim. The first overgrowth is by a **LBC**-type followed by the **OMG**-type clinopyroxene. The thickness of the individual zones varies; **d** – Type 4 forms the smallest phenocrysts and shows internal oscillatory zoning combined with sector growth features. These phenocrysts belong exclusively to the **OMG**-type; **e** – Type 5 characterized by anhedral Cr-rich core (**CrCpx**) with low BSE intensity. The first overgrowth is by the **LBC**-type followed by the **OMG**-generation; **f** – Type 6 shows the same features like Type 5 but is overgrown merely by the **OMG**-type.

6. Crystal chemistry of clinopyroxene

We analyzed 1236 points of the following clinopyroxene types (Tab. 2 and Supp. 4): OMG, groundmass clinopyroxene (**GMCpx**), GCpx, GcCpx, CrCpx and LBC.

In the conventional IMA classification diagram Morimoto (1988) the compositions of the studied clinopyroxenes plot almost exclusively in the diopside field (Fig. 6) and in the "forbidden" field with Wo > 50. In detail, the differences between the individual types are shown in the Mg# versus Si diagram (Fig. 7). The **GcCpx** have distinctive compositions, richest in iron (some crystals were classified as hedenbergite) and with very low Ti (*c.* 0.05 apfu) and relatively high Na (*c.* 0.11 apfu). The **CrCpx** show the highest Mg# (> 87) and Cr_2O_3 contents (up to 0.8 wt. %), and the same enriched Na values like the **GcCpx**. The **LBC** and **GCpx** combine relatively high MgO contents (13–15.1 wt. %) with comparably low Al_2O_3 and FeO concentrations (*c.* 5.5 and 5.7 wt. % respectively). The TiO_2 contents are generally lower than those of the **OMG** and **GMCpx** (*c.* 2 wt. %). Both types show the same crystal chemical features with the highest TiO_2 and Al_2O_3, accompanied by moderate MgO and FeO contents. It has to be stressed that the compositional ranges for individual samples of the given clinopyroxene type may, and often do, overlap significantly with the

Tab. 2 Compilation of electron microprobe analyses and crystal chemical formulae for the individual types of clinopyroxene phenocrysts

East

Type	**OMG** (n = 94)				**GMCpx** (n = 38)				**GcCpx** (n = 46)				**CrCpx** (n = 45)				**LBC** (n = 26)			
	mean	median	min	max	mean	median	min	max	mean	median	min	max	mean	median	min	max	mean	median	min	max
SiO_2	45.34	45.89	38.35	50.42	44.81	44.11	39.60	52.79	46.48	45.51	43.11	52.22	53.85	53.91	52.27	54.52	50.41	50.63	48.70	53.50
TiO_2	3.46	3.21	1.83	5.95	3.15	3.26	0.30	4.99	1.87	1.81	0.71	3.20	0.12	0.07	bd	0.69	1.67	1.74	0.37	2.60
Al_2O_3	8.57	8.49	4.80	13.06	8.33	8.72	0.81	12.34	8.29	9.11	3.02	10.72	2.93	2.77	2.57	4.54	5.37	5.32	3.28	7.01
Cr_2O_3	0.13	0.04	bd	0.81	0.08	0.02	bd	0.68	0.01	0.01	bd	0.07	1.14	1.14	0.90	1.33	0.45	0.45	0.06	0.91
MgO	12.23	12.39	10.01	14.51	12.10	11.83	10.23	14.96	8.86	8.43	6.11	13.03	16.96	17.04	15.26	17.32	14.03	14.06	12.99	15.14
FeO	6.97	7.02	5.39	8.18	7.39	7.44	6.09	8.70	11.81	12.20	8.69	12.94	2.83	2.76	2.60	3.95	5.68	5.69	4.92	6.28
MnO	0.08	0.09	bd	0.17	0.14	0.14	0.09	0.20	0.15	0.08	0.02	0.40	0.03	0.01	bd	0.14	0.10	0.10	0.02	0.22
CaO	23.09	23.09	21.91	23.81	23.22	23.22	22.48	23.96	21.51	21.56	20.32	23.34	20.14	19.79	19.00	22.29	23.43	23.56	22.46	23.89
Na_2O	0.54	0.53	0.34	0.88	0.57	0.56	0.40	0.87	1.49	1.53	0.73	2.48	1.32	1.37	0.94	1.46	0.57	0.54	0.38	0.79
atoms per formula unit Σ = 4																				
Si	1.68	1.69	1.46	1.84	1.67	1.65	1.50	1.96	1.74	1.72	1.66	1.90	1.96	1.96	1.89	1.97	1.83	1.83	1.76	1.92
$Al^{(IV)}$	0.32	0.31	0.16	0.54	0.33	0.35	0.04	0.50	0.26	0.28	0.10	0.34	0.04	0.04	0.03	0.11	0.17	0.17	0.08	0.24
$Fe(III)^{(IV)}$	0.00	0.00	0.00	0.00	0.00	0.00	0.00	0.01	0.00	0.00	0.00	0.00	0.00	0.00	0.00	0.00	0.00	0.00	0.00	0.00
$Al^{(VI)}$	0.05	0.05	0.01	0.09	0.04	0.03	0.00	0.10	0.11	0.13	0.02	0.16	0.08	0.08	0.06	0.10	0.06	0.05	0.02	0.11
$Fe(III)^{(VI)}$	0.11	0.11	0.01	0.19	0.16	0.16	0.06	0.26	0.16	0.16	0.07	0.20	0.02	0.01	0.00	0.04	0.05	0.06	0.01	0.09
Cr	0.00	0.00	0.00	0.02	0.00	0.00	0.00	0.02	0.00	0.00	0.00	0.00	0.03	0.03	0.03	0.04	0.01	0.01	0.00	0.03
Ti	0.10	0.09	0.05	0.17	0.09	0.09	0.01	0.14	0.05	0.05	0.02	0.09	0.00	0.00	0.00	0.02	0.05	0.05	0.01	0.07
Mg	0.67	0.68	0.56	0.80	0.67	0.65	0.58	0.80	0.49	0.47	0.34	0.71	0.92	0.93	0.82	0.94	0.76	0.76	0.71	0.81
Fe(II)	0.10	0.11	0.04	0.16	0.07	0.07	0.00	0.18	0.22	0.22	0.12	0.30	0.07	0.07	0.04	0.09	0.12	0.12	0.08	0.17
Mn	0.00	0.00	0.00	0.01	0.00	0.00	0.00	0.01	0.00	0.00	0.00	0.01	0.00	0.00	0.00	0.00	0.00	0.00	0.00	0.01
Ca	0.92	0.92	0.88	0.94	0.93	0.92	0.90	0.96	0.86	0.86	0.83	0.93	0.78	0.77	0.74	0.86	0.91	0.91	0.87	0.93
Na	0.04	0.04	0.02	0.06	0.04	0.04	0.03	0.06	0.11	0.11	0.05	0.18	0.09	0.10	0.07	0.10	0.04	0.04	0.03	0.06
Mg#	75.62	75.57	69.20	82.75	74.34	74.34	68.87	81.41	56.89	56.11	47.62	72.00	91.44	91.69	87.32	92.10	81.47	81.56	79.01	84.23
IMA end-members Σ = 100 %																				
En	37.24	37.64	32.18	42.70	36.59	36.24	32.78	42.58	28.41	27.81	21.66	37.39	51.35	51.96	45.49	53.07	41.11	41.08	38.91	43.09
Fs	12.10	12.22	9.08	14.80	12.80	12.84	9.90	15.29	21.74	21.99	14.59	24.62	4.84	4.73	4.46	6.76	9.52	9.49	8.13	10.62
Wo	50.66	50.66	47.37	53.36	50.61	50.97	47.52	52.82	49.85	50.00	47.05	54.01	43.81	43.35	41.86	47.76	49.37	49.39	47.68	51.03

Tab. 2 Continued

West

Type	**OMG** (n = 466)				**GMCpx** (n = 97)				**GCpx** (n = 46)				**GcCpx** (n = 71)				**Cr Cpx** (n = 1)	**LBC** (n = 196)			
	mean	median	min	max	mean	median	min	max	mean	median	min	max	mean	median	min	max		mean	median	min	max
SiO_2	44.67	44.76	37.05	52.03	46.42	46.53	40.93	52.30	49.39	49.60	47.76	50.56	45.39	45.27	41.18	48.56	52.38	48.9	48.79	45.43	51.50
TiO_2	4.10	4.02	1.24	8.10	3.70	3.76	1.73	5.97	1.59	1.56	1.31	2.05	2.10	2.11	0.61	4.57	0.97	2.10	2.00	1.17	3.76
Al_2O_3	7.42	7.45	1.06	11.84	6.27	6.43	1.63	10.42	4.32	4.31	3.94	4.80	6.98	7.1	4.18	10.34	2.84	4.63	4.63	3.01	7.54
Cr_2O_3	0.01	0.01	bd	0.37	0.01	bd	bd	0.04	0.03	0.01	bd	0.55	0.01	bd	bd	0.07	0.79	0.05	0.02	bd	0.53
MgO	12.27	12.28	8.8	14.56	12.70	12.8	10.47	14.51	14.41	14.31	13.62	15.49	9.13	9.56	6.79	12.31	16.02	14.16	14.16	12.17	15.72
FeO	6.97	6.93	5.37	9.53	6.87	6.82	5.34	8.46	5.82	5.92	4.87	6.71	11.51	10.93	7.95	14.95	4.16	5.78	5.82	4.64	6.99
MnO	0.09	0.09	0.01	0.26	0.13	0.12	0.05	0.25	0.07	0.07	0.02	0.11	0.35	0.34	0.15	0.59	0.05	0.08	0.08	0.01	0.15
CaO	23.89	23.97	21.99	25.21	23.76	23.85	22.21	24.51	23.61	23.42	22.90	24.30	21.94	22.24	19.94	23.48	23.92	23.80	23.77	22.2	24.83
Na_2O	0.42	0.40	0.22	0.92	0.47	0.44	0.27	0.88	0.44	0.42	0.36	0.59	1.46	1.33	0.61	2.44	0.34	0.42	0.41	0.22	0.71
atoms per formula unit Σ = 4																					
Si	1.67	1.67	1.42	1.95	1.72	1.73	1.54	1.91	1.82	1.83	1.79	1.86	1.73	1.72	1.55	1.83	1.89	1.81	1.80	1.68	1.87
$Al^{(IV)}$	0.32	0.32	0.05	0.52	0.27	0.27	0.07	0.45	0.17	0.17	0.14	0.21	0.27	0.27	0.17	0.42	0.11	0.19	0.19	0.13	0.32
$Fe(III)^{(IV)}$	0.01	0.00	0.00	0.07	0.01	0.00	0.00	0.05	0.00	0.00	0.00	0.01	0.00	0.00	0.00	0.04	0.00	0.01	0.00	0.00	0.05
$Al^{(VI)}$	0.01	0.00	0.00	0.07	0.01	0.00	0.00	0.06	0.01	0.01	0.00	0.04	0.04	0.04	0.00	0.12	0.01	0.01	0.01	0.00	0.06
$Fe(III)^{(VI)}$	0.12	0.13	0.00	0.20	0.10	0.11	0.01	0.18	0.10	0.11	0.04	0.14	0.22	0.22	0.07	0.33	0.04	0.09	0.09	0.00	0.18
Cr	0.00	0.00	0.00	0.01	0.00	0.00	0.00	0.00	0.00	0.00	0.00	0.00	0.00	0.00	0.00	0.00	0.02	0.00	0.00	0.00	0.02
Ti	0.12	0.11	0.03	0.23	0.10	0.10	0.05	0.17	0.04	0.04	0.04	0.06	0.06	0.06	0.02	0.13	0.03	0.06	0.06	0.03	0.10
Mg	0.68	0.68	0.50	0.81	0.70	0.71	0.59	0.79	0.79	0.79	0.75	0.84	0.52	0.54	0.39	0.69	0.86	0.78	0.78	0.67	0.85
Fe(II)	0.08	0.08	0.00	0.23	0.11	0.10	0.03	0.23	0.08	0.07	0.05	0.14	0.15	0.14	0.03	0.27	0.08	0.08	0.08	0.00	0.16
Mn	0.00	0.00	0.00	0.01	0.00	0.00	0.00	0.01	0.00	0.00	0.00	0.00	0.01	0.01	0.00	0.02	0.00	0.00	0.00	0.00	0.00
Ca	0.96	0.96	0.88	1.02	0.94	0.95	0.88	0.99	0.93	0.94	0.91	0.96	0.89	0.91	0.82	0.96	0.93	0.94	0.94	0.88	0.98
Na	0.03	0.03	0.02	0.07	0.03	0.03	0.02	0.06	0.03	0.03	0.03	0.04	0.11	0.10	0.05	0.18	0.02	0.03	0.03	0.02	0.05
Mg#	75.71	75.99	62.21	82.79	76.63	76.80	69.13	82.13	81.51	81.06	78.87	84.69	58.5	60.83	44.74	73.40	87.28	81.33	81.3	75.63	85.42
IMA end-members Σ = 100 %																					
En	36.94	37.02	28.93	42.28	37.81	38.02	33.06	41.48	41.56	41.35	39.68	44.22	28.88	29.74	22.78	36.95	45.03	41.08	41.27	36.13	44.58
Fs	11.26	11.27	6.69	17.80	11.28	11.15	8.48	14.48	9.51	9.70	8.12	10.54	21.14	19.65	12.98	29.13	6.64	9.29	9.32	6.38	11.80
Wo	51.80	51.82	47.90	56.30	50.91	50.96	47.46	54.54	48.93	48.91	47.66	50.86	49.98	50.23	46.85	52.22	48.33	49.64	49.58	46.94	52.10

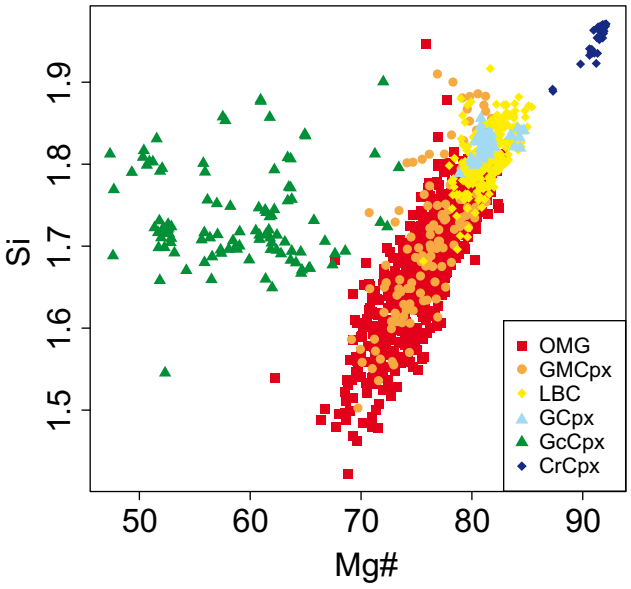

Fig. 7 Binary plot of mg# vs. Si (formula units) for the six clinopyroxene types.

chemical compositions of the other clinopyroxene types. This is shown, for example, in Fig. 8. All groups have invariably wide range of Ca contents varying between 0.8 and 0.99 apfu.

The X-ray concentration maps (Supp. 5) provide a good overview of the microstructural and crystal chemical features of the individual clinopyroxene types.

7. Discussion

The respective chemical and microstructural data for the clinopyroxene phenocrysts bear a witness of multistage, regionally diverse processes leading to the formation of the Ti-rich as well as Ti-poor basalts in the western and eastern Erzgebirge. It is impossible to constrain rates and mass balances with the data available. In particular, we lack high-resolution age determinations of the lavas as well as trace-element and isotope data for the clinopyroxene. Therefore the following hypothesis remains a tentative one. The presumed origin and evolution of the basaltic rocks in the eastern and western Erzgebirge are summarized in Fig. 9.

The first step was the generation of asthenospheric melts (**S1** and **S1***) probably from mantle regions with enhanced activities of H_2O and potassium for the western Erzgebirge, as can be seen from the formation of amphibole and biotite phenocrysts limited to this region.

The chemical characteristics of the **CrCpx** are very similar to data from clinopyroxenes of peridotite xenoliths found in some basalts of the eastern Erzgebirge (A. Renno, unpublished data). Together with xenolithic olivine crystals and mantle-derived peridotite xenoliths, these clinopyroxene crystals were incorporated into the asthenospheric primitive melts **S1** and **S1*** rising rapidly to transient magma chambers or directly to the surface.

The genesis of **GcCpx** is uncertain with several possibilities: (1) crystallization from a geochemically evolved alkaline melt in the upper mantle (Tappe 2004), (2) nucleation from quartz-bearing magmas in a crustal magma chamber (Bédard et al 1988) or (3) formation at the crust–mantle-boundary (Duda and Schmincke 1985). A multistage process involving crystallization from a melt and subsequent reaction with another melt of contrasting composition seems highly probable. We suggest that these **GcCpx** were incorporated as xenocrysts into the first magma batches stored in the lithospheric mantle chambers (**M1A** and **M1b**). They have reacted with the melts **S1** and **S1***, whereby they were overgrown by the **LBC**. Simultaneously, the LBC formed independent, newly grown crystals in these magma chambers. The residence time in the magma chambers associated with the eastern and western parts of the Erzgebirge appears to have been totally different. A short residence demonstrated by the occurrence of mantle-derived xenoliths and xenocrysts in the eastern part (**M1a**) is in contrast with the western part, where long residence times presumably allowed the settling with complete removal of such xenoliths and xenocrysts as well as the formation of the **GCpx** in **M1b**.

The fractionated melts **S2a** and **S2b** rose to the shallower magma chambers **M2a** and **M2b**, situated probably at a crustal level. These areas appear to be locations of intense magma mixing of the melts **S2a** or **S2b** with Ti-rich melts **S3a** and **S3b**. The existence of these Ti-rich melts in both parts of the Erzgebirge is demonstrated by the crystallization of the chemically mutually identical **OMG** and **GMCpx** phases. The **LBC**, **GCpx**, **GcCpx**, biotite phenocrysts and the mantle-derived olivine xenocrysts all reacted with the newly formed melt. The existence of schlieren-like heterogeneities in the groundmass of some of the lavas suggests that these mixing processes lasted for considerable time and were themselves multistage in character. The geochemical differences among the basaltic rocks demonstrate the significantly lower involvement of the hypothetical Ti-rich melt **S3a** in these mixing processes in the east.

The ultimate origin of the Ti-rich melts **S3a** and **S3b** remains unexplained. Eclogite-derived melts appear as a viable possibility. Melting experiments e.g., by Klemme et al. (2002) showed that the partial melting of eclogite at temperatures similar to, or exceeding 1300 °C and a pressure of 3 GPa could yield melts enriched in Ti and Na. Eclogites derived from subducted oceanic crust

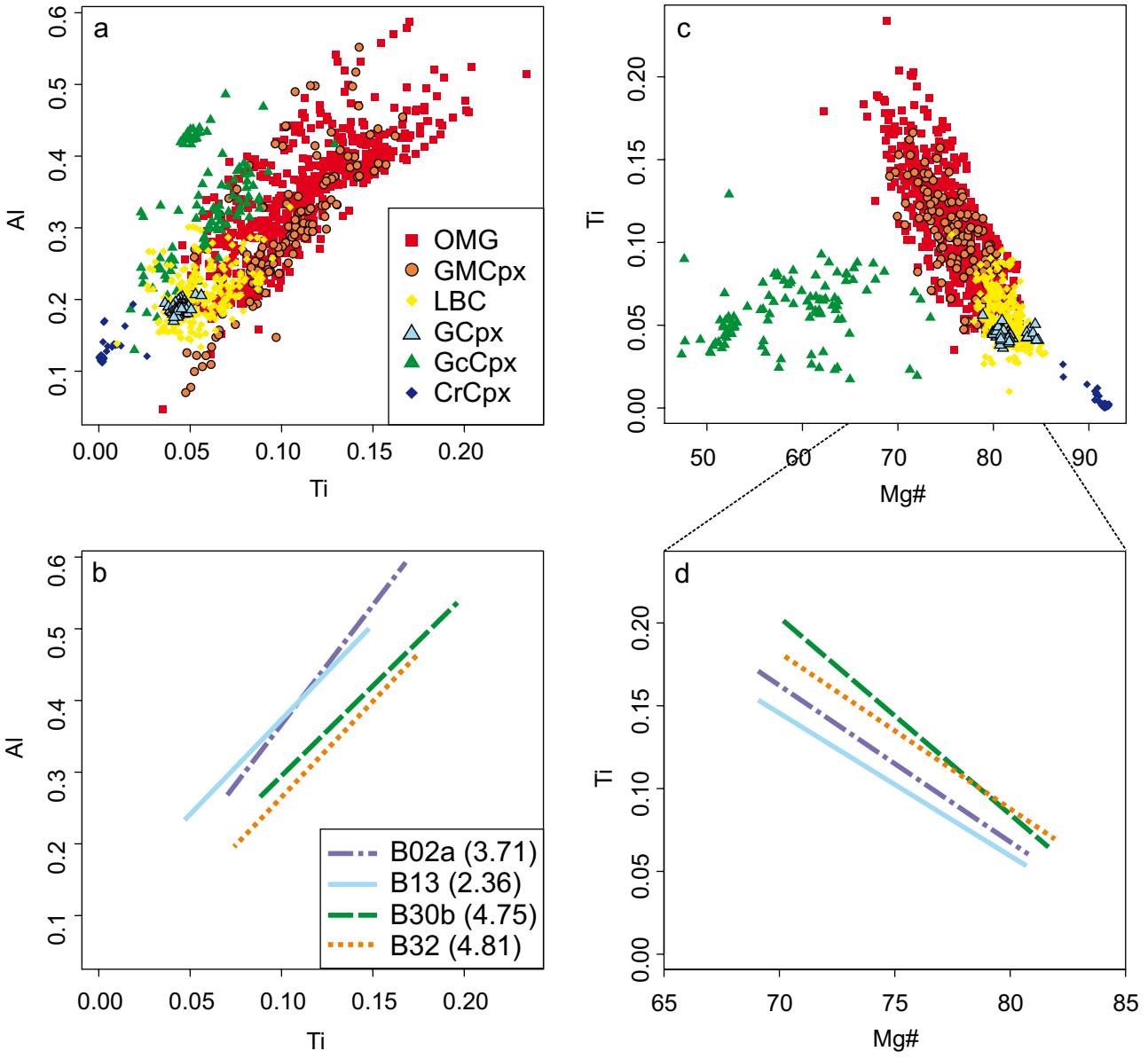

Fig. 8a – Ti vs. Al (formula units) diagram of the individual clinopyroxene types; **b** – Ti vs. Al (formula units) diagram showing the variability of data for the **OMG**-type Cpx using four selected samples as an example (whole-rock TiO_2 contents in parentheses); **c** – Mg# vs. Ti (formula units) diagram of the individual clinopyroxene types; **d** – Mg# vs. Ti (formula units) diagram showing the range of data for the **OMG**-type Cpx using four selected samples as an example (whole-rock TiO_2 contents in parentheses).

represent an important component of the Saxothuringian lithosphere, as demonstrated by the common presence of exhumed eclogites in the upper crust (e.g., Schmädicke et al. 1992; Konopásek and Schulmann 2005). The mixing of these very hot melts with the **S1** and **S2** magmas in the shallow magma chambers should have triggered the resorption of the **GcCpx** and the **LCB** as well as the assimilation of continental crustal material. Indeed, the crustal contamination (biotite flakes and crustal xenoliths) was likely coeval with the mixing in the magma chambers **M2a** and **M2b**.

8. Conclusions

The synopsis of the petrographic, microstructural and chemical features of several types of clinopyroxenes from cenozoic basaltic rocks in the eastern and the western Erzgebirge demonstrated that the origin of the parental Ti-poor and Ti-rich basaltic melts was a multistage process. At least three different melts were involved in fractionation, assimilation and magma-mixing in two magma chamber systems at different depths, in the lithospheric mantle and in the crust. The regional dichotomy

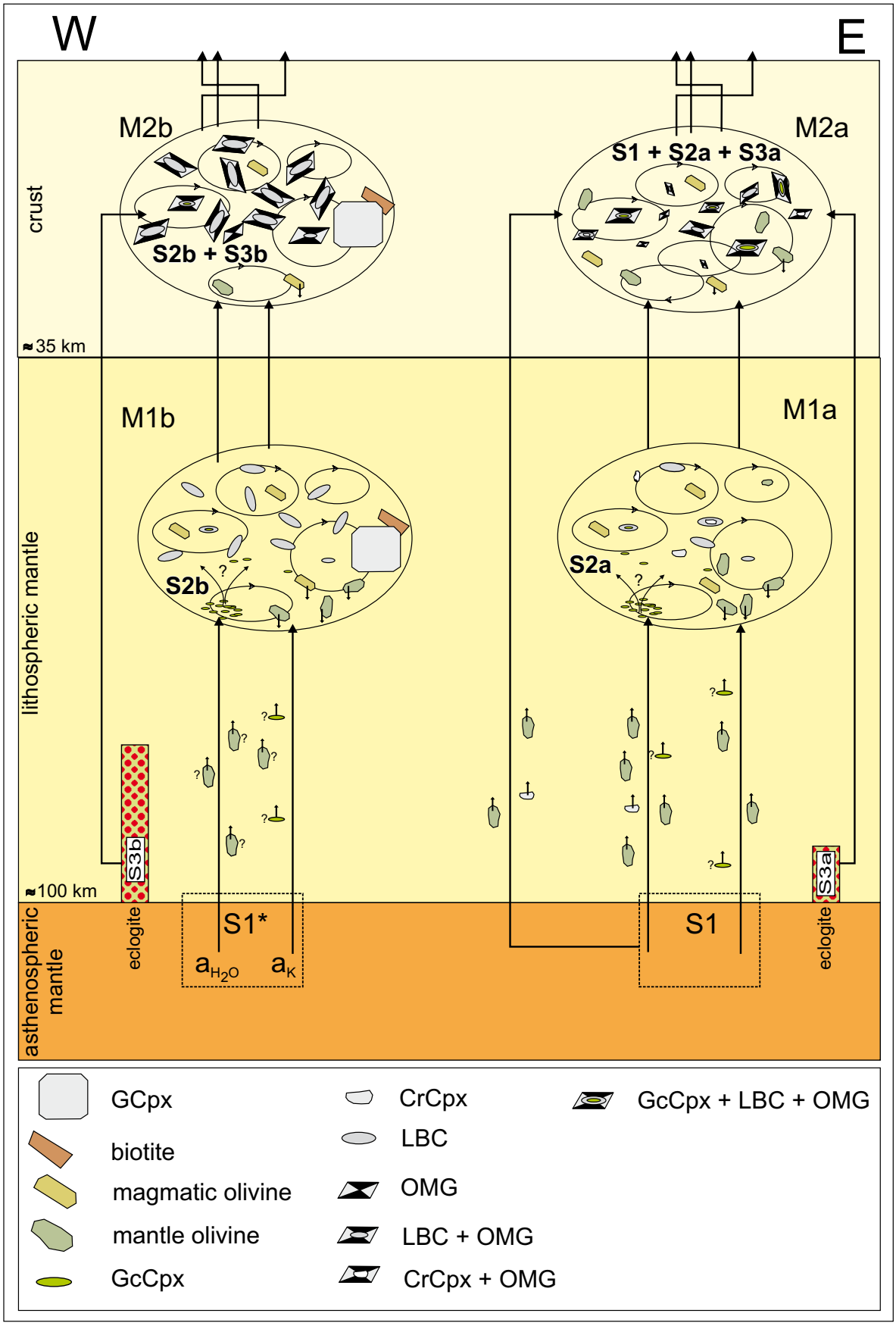
W
E
M2b
M2a
S1 + S2a + S3a
S2b + S3b
crust
≈35 km
M1b
M1a
S2b
S2a
lithospheric mantle
≈100 km
S3b
S3a
eclogite
eclogite
S1*
S1
a_{H_2O}
a_K
asthenospheric mantle
GCpx
biotite
magmatic olivine
mantle olivine
GcCpx
CrCpx
LBC
OMG
LBC + OMG
CrCpx + OMG
GcCpx + LBC + OMG

between the eastern and western Erzgebirge basaltic rocks is interpreted by differences in the residence time of the parental magmas in the transient magma chambers, as well as variable mixing with hot Ti-rich melts, possibly derived from an eclogitic source.

Acknowledgements. We gratefully acknowledge the help of A. Pleßow, T. Tschöpe, K. Treptow, and E. Rüdiger with the analytical work. We express our thanks to Jaromír Ulrych and Stanislav Vrána for their careful reviews and to the guest editor Vladislav Rapprich for the subtle and stringent editorial handling of the manuscript. Matthew Huber improved the English style and grammar. This work was funded by the DFG through grant Ha 2568/10-1.

Electronic supplementary material. The GPS coordinates and a map of the sampling sites, detailed petrographic features for the analysed basaltic rocks, the complete set of variation diagrams for the Erzgebirge basaltic rocks including a compilation of the regional variation in major elements and mg#, all mineral compositional data for clinopyroxene and X-ray concentration maps for several typical clinopyroxene crystals are available online at the Journal web site *(http://dx.doi.org/10.3190/jgeosci.077)*.

References

Babuška V, Plomerová J (1992) The lithosphere in central Europe – seismological and petrological aspects. Tectonophysics 207: 141–163

Babuška V, Plomerová J (2010) Mantle lithosphere control of crustal tectonics and magmatism of the western Ohře (Eger) Rift. J Geosci 55: 171–186

Babuška V, Plomerová J, Fischer T (2007) Intraplate seismicity in the western Bohemian Massif (central Europe): a possible correlation with a paleoplate junction. J Geodyn 44: 149–159

Bédard JH, Francis DM, Ludden J (1988) Petrology and pyroxene chemistry of Monteregian dykes; the origin of concentric zoning and green cores in clinopyroxenes from alkali basalts and lamprophyres. Can J Earth Sci 25: 2041–2058

⇦

Fig. 9 Tentative model for the formation of the basaltic rocks in the western (W, labelled by 'a') and eastern (E, labelled by 'b') Erzgebirge, respectively. **S1** = primary asthenospheric melt (E Erzgebirge); **S1*** = primary asthenospheric melt with higher a_{H2O} and a_K (W Erzgebirge); **S2a, S2b** = fractionated melts from the first magma chamber system in the lithospheric mantle; **S3a, S3b** = eclogite-derived melts; **M1a, M1b** = first magma chamber in the lithospheric mantle; **M2a, M2b** = second (crustal) magma chamber systems.

Bogaard PJF, Wörner G (2003) Petrogenesis of basanitic to tholeiitic volcanic rocks from the Miocene Vogelsberg, Central Germany. J Petrol 44: 569–602

Duda A, Schmincke H–U (1985) Polybaric differentiation of alkali basaltic magmas: evidence from green-core clinopyroxenes (Eifel, FRG). Contrib Mineral Petrol 91: 340–353

Duncan AR (1987) The Karoo Igneous Province – a problem area for inferring tectonic setting from basalt geochemistry. J Volcanol Geotherm Res 32: 13–34

Dupuy C, Marsh J, Dostal J, Michard A, Testa S (1988) Asthenospheric and lithospheric sources for Mesozoic dolerites from Liberia (Africa): trace element and isotopic evidence. Earth Planet Sci Lett 87: 100–110

Essawy MA, El-Metwally AA (1999) Petrogenesis of a high TiO_2 mafic dyke swarm from southwest Sinai. J Afr Earth Sci 29: 551–565

Fodor RV (1987) Low- and high-TiO_2 flood basalts of southern Brazil: origin from picritic parentage and a common mantle source. Earth Planet Sci Lett 84: 423–430

Gibson SA, Thompson RN, Dickin AP, Leonardos OH (1995) High-Ti and low-Ti mafic potassic magmas: Key to plume-lithosphere interactions and continental flood-basalt genesis. Earth Planet Sci Lett 136: 149–165

Goes S, Loohuis JJP, Wortel MJR, Govers R (2000) The effect of plate stresses and shallow mantle temperatures on tectonics of northwestern Europe. Global Planet Change 27: 23–38

Haase KM, Renno AD (2008) Variation of magma generation and mantle sources during continental rifting observed in Cenozoic lavas from the Eger Rift, Central Europe. Chem Geol 257: 192–202

Hrubcová P, Środa P, Špičák A, Guterch A, Grad M, Keller GR, Brueckl E, Thybo H (2005) Crustal and uppermost mantle structure of the Bohemian Massif based on CELEBRATION 2000 data. J Geophys Res B Solid Earth 110: 1–21, DOI: 10.1029/2004JB003080

Huckenholz HG (1964) Der petrogenetische Werdegang der Klinopyroxene in den tertiären Vulkaniten der Hocheifel I. Die Klinopyroxene der Alkaliolivinbasalt–Trachyt–Assoziation. Contrib Mineral Petrol 11: 138–195

Huckenholz HG (1965) Der petrogenetische Werdegang der Klinopyroxene in den tertiären Vulkaniten der Hocheifel II. Die Klinopyroxene der Basanitoide. Contrib Mineral Petrol 11: 415–448

Huckenholz HG (1966) Der petrogenetische Werdegang der Klinopyroxene in den tertiären Vulkaniten der Hocheifel. Contrib Mineral Petrol 12: 73–95

Jama Aden A, Frizzo P (1996) Geochemistry and origin of low and high TiO_2 mafic rocks in the Barkasan Complex: a comparison with common Neoproterozoic gabbros of northern Somali crystalline basement. J Afr Earth Sci 22: 43–54

Janoušek V, Farrow CM, Erban V (2006) Interpretation of whole-rock geochemical data in igneous geochemistry: introducing Geochemical Data Toolkit (GCDkit). J Petrol 47: 1255–1259

Jung S, Hoernes S (2000) The major- and trace-element and isotopic (Sr, Nd, O) geochemistry of Cenozoic alkaline rift-type volcanic rock from the Rhön area (central Germany): petrology, mantle source characteristics and implications for asthenosphere–lithosphere interactions. J Volcanol Geotherm Res 99: 27–53

Kaiser G, Pilot J (1986) Weitere K–Ar-Datierungen an jungen Vulkaniten. Z geol Wiss 14: 121–124

Katzir Y, Litvinovsky B, Eyal M, Zanvilevich A, Vapnik Y (2006) Four successive episodes of Late Pan-African dikes in the central Elat area, southern Israel. Isr J Earth Sci 55: 69–93

Klemme S, Blundy JD, Wood BJ (2002) Experimental constraints on major and trace element partitioning during partial melting of eclogite. Geochim Cosmochim Acta 66: 3109–3123

Konopásek J, Schulmann K (2005) Contrasting Early Carboniferous field geotherms: evidence for accretion of a thickened orogenic root and subducted Saxothuringian crust (Central European Variscides). J Geol Soc, London 162: 463–470

Le Bas MJ (1989) Nephelinitic and basanitic rocks. J Petrol 30: 1299–1312

Le Bas MJ, Le Maitre RW, Streckeisen A, Zanettin B, IUGS Subcomission on the Systematics of Igneous Rocks (1986) A chemical classification of volcanic rocks based on the total alkali–silica diagram. J Petrol 27: 745–750

Le Maitre RW, Streckeisen A, Zanettin B, Le Bas MJ, Bonin B, Bateman P (2005) Igneous Rocks: A Classification and Glossary of Terms: Recommendations of the International Union of Geological Sciences Subcommission on the Systematics of Igneous Rocks. Cambridge University Press, Cambridge, pp 1–252

Malkovský M (1987) The Mesozoic and Tertiary basins of the Bohemian Massif and their evolution. Tectonophysics 137: 31–42

Middlemost EAK (1994) Naming materials in the magma/igneous rock system. Earth Sci Rev 37: 215–224

Mlčoch B, Konopásek J (2010) Pre-Late Carboniferous geology along the contact of the Saxothuringian and Teplá–Barrandian zones in the area covered by younger sediments and volcanics (western Bohemian Massif, Czech Republic). J Geosci 55: 81–94

Morimoto N (1988) Nomenclature of pyroxenes. Bull Minéral 111: 535–550

Murphy JB (1988) Late Precambrian to Late Devonian mafic magmatism in the Antigonish Highlands of Nova Scotia: multistage melting of a hydrated mantle. Can J Earth Sci 25: 473–485

Niese S, Pfeiffer L, Gleisberg GB (1995) Geochemie sächsischer Tertiärmagmatite. Z geol Wiss 23: 317–330

Papike JJ, Vaniman DT (1978) The Lunar Mare Basalt suite. Geophys Res Lett 5: 433–436

Papike JJ, Hodges FN, Bence AE, Cameron M, Rhodes JM (1976) Mare basalts: crystal chemistry, mineralogy, and petrology. Rev Geophys 14: 475–540

Pfeiffer L (1978) Beitrag zur Petrochemie der sächsischen Tertiärvulkanite. Freiberg Forsch H C333: 1–164

Pik R, Deniel C, Coulon C, Yirgu G, Hofmann C, Ayalew D (1998) The northwestern Ethiopian Plateau flood basalts: classification and spatial distribution of magma types. J Volcanol Geotherm Res 81: 91–111

Pik R, Marty B, Hilton DR (2006) How many mantle plumes in Africa? The geochemical point of view. Chem Geol 226: 100–114

Pilot J, Pfeiffer L, Rösler HJ, Schlichting M, Kaiser G (1984) Zur genetischen Problematik der tertiären Vulkanite von der Lausitz und des Erzgebirges auf Grund von Strontiumisotopenverhältnissen, Rb–Sr- und K–Ar-Altern. Freiberg Forsch H C389: 84–92

Plomerová J, Achauer U, Babuška V, Vecsey L (2007) Upper mantle beneath the Eger Rift (Central Europe): plume or asthenosphere upwelling? Geophys J Int 169: 675–682

Prodehl C, Müller S, Haak V (1995) The European Cenozoic rift system. In: Olsen KH (ed) Continental Rifts: Evolution, Structure, Tectonics. Elsevier, Amsterdam, pp 133–212

Rapprich V (2005) Compositional variation of clinopyroxenes of basaltic, essexitic and tephriphonolitic rocks from the Doupovské hory Volcanic Complex, NW Bohemia. J Czech Geol Soc 50: 119–132

Rönick R (2010) Geochemisch-petrologische Untersuchungen an Ti-reichen Basalten des Erzgebirges. Unpublished Diploma thesis, TU Bergakademie Freiberg – Institut für Geologie, pp 1–124

Schmädicke E, Okrusch M, Schmidt W (1992) Eclogite-facies rocks in the Saxonian Erzgebirge, Germany: high pressure metamorphism under contrasting P–T conditions. Contrib Mineral Petrol 110: 226–241

Shrbený O (1995) Chemical composition of young volcanites of the Czech Republic. Czech Geol Survey Spec Pap 4: 1–53

Tappe S (2004) Mesozoic mafic alkaline magmatism of southern Scandinavia. Contrib Mineral Petrol 148: 312–334

Todt W, Lippolt HJ (1975) K–Ar Altersbestimmungen an Vulkaniten bekannter paläomagnetischer Feldrichtung II Sachsen. J Geophysics 41: 641–650

Ulrych J (1986) Clinopyroxenes in the Cenozoic volcanics of the České středohoří Mts.: a review. Acta Univ Carol, Geol 1986: 117–131

Ulrych J, Pivec E, Rutšek J, Povondra P (1990) Olivines–monticellites and clinopyroxenes in melilitic rocks,

Ploučnice River region, Czechoslovakia. Acta Univ Carol, Geol 1990: 141–164

Ulrych J, Svobodová J, Balogh K (2002) The source of Cenozoic volcanism in the České středohoří Mts., Bohemian Massif. Neu Jb Mineral, Abh 177: 133–162

Ulrych J, Lloyd FE, Balogh K, Hegner E, Langrová A, Lang M, Novák JK, Řanda Z (2005) Petrogenesis of alkali pyroxenite and ijolite xenoliths from the Tertiary Loučná–Oberwiesenthal Volcanic Centre, Bohemian Massif in the light of new mineralogical, geochemical, and isotopic data. Neu Jb Mineral, Abh 182: 57–79

Journal of Geosciences, 55 (2010), 251–278 DOI: 10.3190/jgeosci.074

Original paper

Petrology and geochemistry of the Tertiary alkaline intrusive rocks at Doupov, Doupovské hory Volcanic Complex (NW Bohemian Massif)

František V. HOLUB[1,*], Vladislav RAPPRICH[2], Vojtěch ERBAN[2], Zoltán PÉCSKAY[3], Bedřich MLČOCH[2], Jitka MÍKOVÁ[2]

[1] *Institute of Petrology and Structural Geology, Faculty of Science, Charles University in Prague, Albertov 6, 128 43 Prague 2, Czech Republic; frholub@natur.cuni.cz*
[2] *Czech Geological Survey, Klárov 3, 118 21 Prague 1, Czech Republic*
[3] *Institute of Nuclear Research, Hungarian Academy of Sciences, Bem tér 18/C, H-4001 Debrecen, Hungary*
[*] *Corresponding author*

Field observations, petrography, geochemical data and the results of K–Ar dating are presented for Oligocene (*c.* 30–29 Ma) alkaline intrusions at the former township of Doupov (Duppau) in the central part of the Doupovské hory Volcanic Complex (DHVC).

The Doupov Intrusive Complex (DIC) is a very limited in area (< 2 km^2) but is petrographically highly variable. Several phaneritic rock types have been identified, including clinopyroxenite (both the clinopyroxenite-dominated breccia and xenoliths in younger intrusive phases), essexite, sodalite-bearing monzodiorite, sodalite monzosyenite to nepheline–sodalite syenite, and highly mafic to felsic nephelinolites (melteigite–ijolite–urtite). These rocks are accompanied by vent breccias, and a thermal and metasomatic aureole with zones of pervasive phlogopitization. Phaneritic intrusions and their host rocks are cut by thin aphanitic dykes ranging from mafic alkaline lamprophyres to felsic trachytes and phonolites. All the intrusions are characterized by undersaturated alkaline compositions with high abundances of incompatible elements.

Geochemical variations and also subtle differences in the isotopic compositions of Sr and Nd suggest that the less undersaturated essexitic rocks and sodalite syenitoids do not form a common evolutionary line with highly undersaturated nephelinolites. Nephelinolites are isotopically close to the "European Asthenospheric Reservoir" or the "Common Mantle Reservoir" compositions and interaction of their parental magmas with the continental crust was negligible. Magmatic evolution of nephelinolites with "dry" mineral assemblages was dominated by fractionation of clinopyroxene accompanied at the early stage by olivine, and later by titanite, magnetite and apatite. Essexite is isotopically more different though still within the field of mafic lavas from DHVC and other volcanic complexes in Central and Western Europe. Either its parental magma originated in heterogeneous mantle with more distinct lithospheric signature or this magma reacted with the continental crust during its ascent and fractionation. Sodalite monzosyenite displays significantly higher $^{87}Sr/^{86}Sr$ ratios and its parental magma probably interacted even more intensively with the crustal rocks.

The K–Ar ages of phaneritic intrusive rocks from Doupov are *c.* 30–29 Ma. Intrusions are older than the tephrite–basanite and foidite lavas forming the upper parts of the DHVC.

The rock association resembles that accompanying many carbonatite intrusions around the world. However, brecciation and high-temperature metasomatic overprint including the extensive phlogopitization may be related to ijolitic magma. Nevertheless, the presence of carbonatite at some deeper level cannot be excluded.

Keywords: alkaline rocks, nephelinolite, petrology, geochemistry, Ohře Graben, Bohemian Massif
Received: 24 June 2010; accepted: 15 September 2010; handling editor: E. Jelínek
The online version of this article (doi: 10.3190/jgeosci.074) contains supplementary electronic material.

1. Introduction

Many alkaline volcanic complexes around the world are accompanied by phaneritic intrusive members, some of them also with carbonatites. Such intrusions of plutonic appearance are rather rare within the volcanic complexes associated with the European Cenozoic Rift System. These were described namely from the Kaiserstuhl situated within the S part of the Rhine Graben (Germany), where ultramafic to felsic highly undersaturated intrusive rocks are accompanied by both intrusive and volcanic carbonatites (Wimmenauer 1974; Keller 1981).

The Bohemian Massif contains two large volcanic complexes including subvolcanic intrusions – the larger České středohoří Volcanic Complex in the NE part and the less voluminous Doupovské hory Volcanic Complex

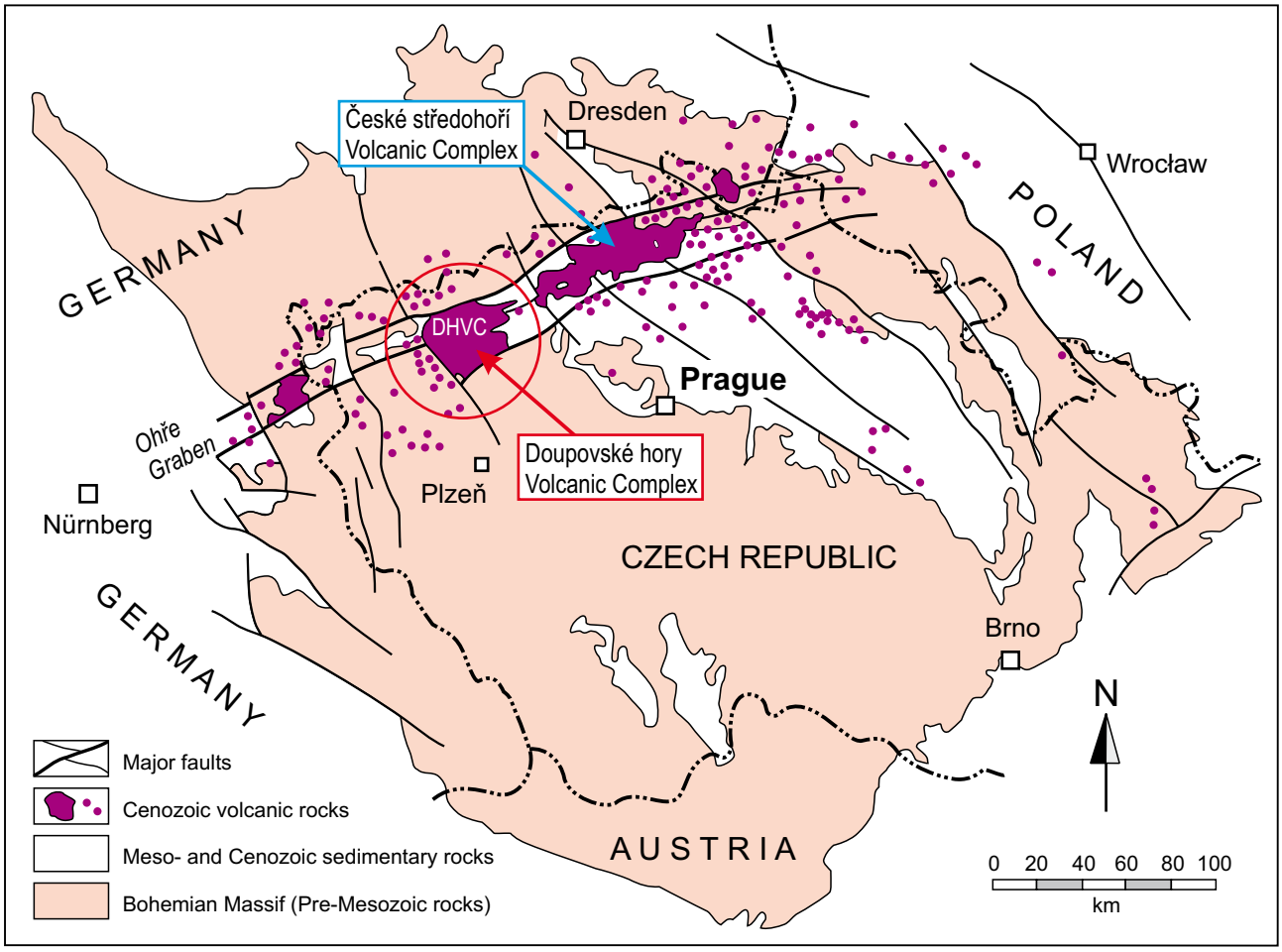

Fig. 1 Geological sketch of the Bohemian Massif showing the Ohře Graben, outlines of major Cenozoic volcanic complexes therein, and schematic position of significant scattered localities of the Cenozoic volcanism (small circles).

(DHVC) in the south-western part of the Ohře (Eger) Graben (Fig. 1). Present paper is focused on the DHVC whose intrusive members are still poorly known. These rocks crop out at the locality called Flurbühl (or Flurhübl in some older papers), a small hill (648.5 m above sea level) located in the close SW vicinity of the former small town of Doupov (Duppau). The locality is situated in the central part of the DHVC (Fig. 2) in the middle of a large military training area.

This paper presents the most important data on the petrography, whole-rock major- and trace-element geochemistry and a limited number of Sr and Nd isotopic analyses for alkaline intrusive rocks of the Doupov Intrusive Complex. New K–Ar ages were also determined for selected samples. Additional data including mineral analyses are given in the Supplementary electronic material (Supplements S1 to S8). A more detailed study focusing on the mineralogical development of ijolitic rocks can be found in Haloda et al. (this volume).

2. Geological setting

2.1. Doupovské hory Volcanic Complex

The NE branch of the European Cenozoic Rift System (ECRIS, Dèzes et al. 2004) is formed by the Ohře (Eger) Graben. It runs across the western part of the Bohemian Massif in the ENE–WSW direction (Fig. 1), roughly following the Variscan suture between the Saxothuringian and Teplá–Barrandian domains of the Bohemian Massif (see Mlčoch and Konopásek 2010).

In the south-western part of the Ohře (Eger) Graben is situated the Doupovské hory Volcanic Complex (DHVC) covering an area of nearly 600 km^2. Several geological units join in the basement of the DHVC in the form of a heterogeneous crustal mosaic. The Saxothuringian Unit (paragneisses, felsic granulites, orthogneisses, mica schists, and phyllites) extends in the basement of the DHVC from the north as far as to the Střezov and Petrov

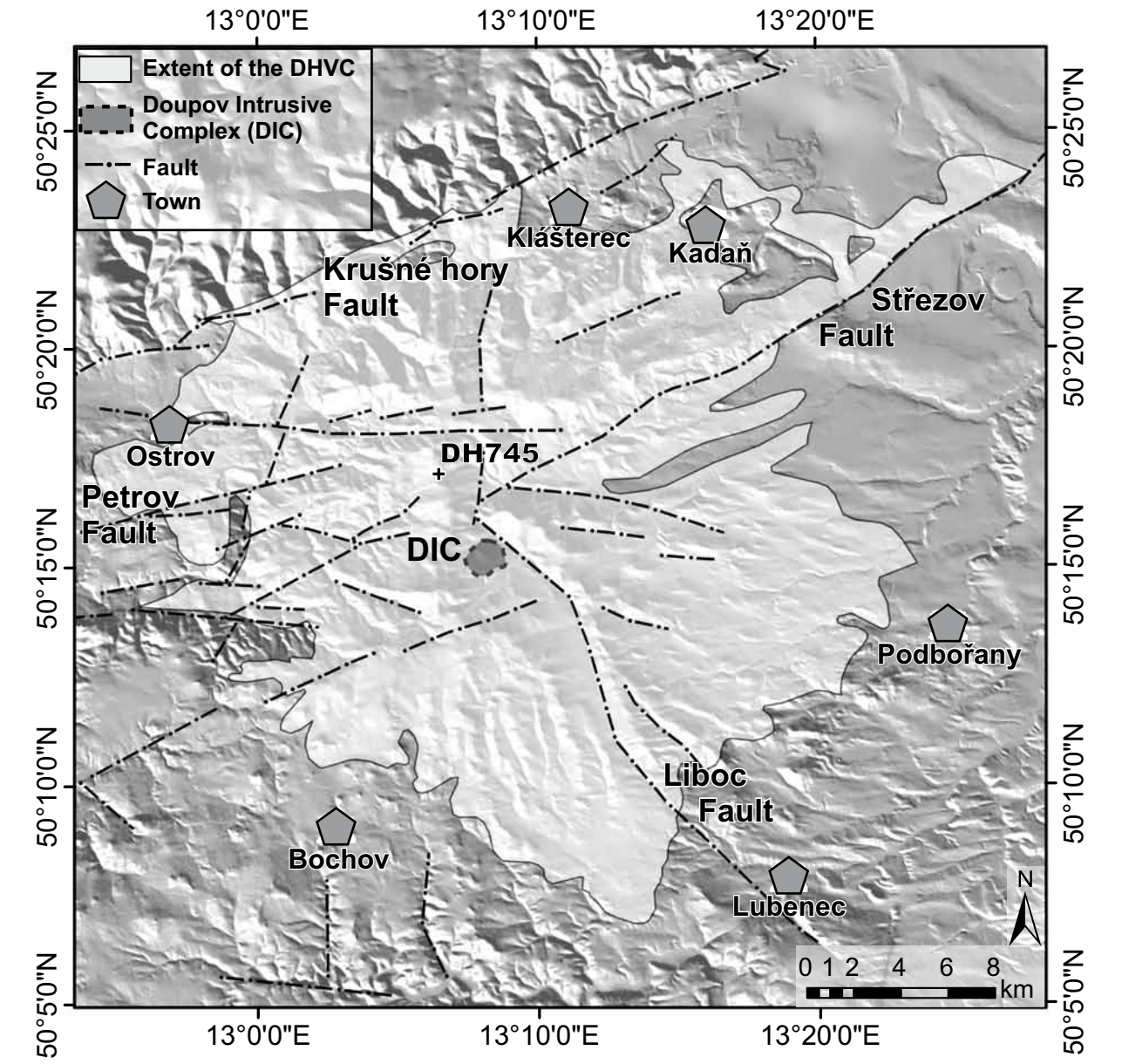

Fig. 2 Position of the Doupov Intrusive Complex (DIC) within the Doupovské hory Volcanic Complex (DHVC) with the regional fault pattern. Location of the sample DH745 (haüyne-phyric phonolite dyke) is shown NW of the DIC.

faults (Fig. 2). Variscan granites (Nejdek–Eibenstock Pluton) plunge beneath the DHVC from the west. Metamorphic rocks of the Teplá–Barrandian Unit (garnet–kyanite gneisses, micaschists and phyllites) form the fundament to the south. Metamorphosed basic and ultrabasic rocks (amphibolites, eclogites, and peridotites to serpentinites, equivalent to the Mariánské Lázně Complex – Mlčoch and Konopásek 2010) occur beneath the central part of the DHVC (Mlčoch 2003, 2006). The south-eastern sector of the DHVC (delimited by the Střezov and Liboc faults – Fig. 2) is underlain by a thick sequence of Late-Palaeozoic sedimentary rocks covering the Teplá–Barrandian Unit basement.

Formation of the DHVC started during the Lowermost Oligocene (mammal zone MP-21: Fejfar and Kaiser 2005) and lasted up to the Lower Miocene. The complex consists of alkaline volcanic rocks, namely foidites, basanites and tephrites. Weak erosion preserved superficial products dominated by sequences of mafic lavas with subordinate concomitant volcaniclastics, whereas the subvolcanic systems mostly remained hidden.

The DHVC was formerly interpreted as a huge stratovolcano (e.g., Zartner 1938; Šantrůček et al. 1967; Kopecký 1987–88). However, voluminous pyroclastic material was produced only during the early stages of volcanic evolution (Hradecký 1997). Subsequent, almost purely effusive activity from a number of local vents (e.g., Hradecký 1997; Cajz et al. 2006) and sequences of gently dipping lava flows forming the upper parts of the DHVC (e.g., Rapprich and Holub 2008), indicate a cluster of shield volcanoes rather than a single stratovolcano.

2.2. Doupov Intrusive Complex

The occurrence of relatively coarse-grained, subvolcanic intrusive rocks originally referred to as theralites in the close south-western vicinity of Doupov has been known since the beginning of the 20th century (Becke 1900; Wiesbaur 1901; Bauer 1903). For a long time, these intrusions were considered to mark the position of a major stratovolcano conduit or "volcanic centre" within the "central crater" or caldera (e.g., Šantrůček et al. 1967; Kopecký 1988).

Kopecký (1988) briefly described the major intrusion at Doupov as a vertical stock 450 × 100 m in a NW–SE elongated outcrop, which is composed largely of essexite, locally grading to theralite. This stock is surrounded by pyroxenite and pyroxenite breccia built by partially phlogopitized augite and penetrated by small dykes of nepheline to sodalite syenite. Another variety of pyroxenite has been characterized as jacupirangite dominated by clinopyroxene and also containing about 30 % nepheline, opaque minerals and an accessory amount of garnet. Kopecký (1988) estimated the total outcrop area of the complex including marginal pyroxenites to be *c.* 1300 × 300 m.

The whole composite intrusion is called the Doupov Intrusive Complex (DIC) in this paper. Its size is definitely larger and the distribution of the various rock types appears much less regular compared to Kopecký's description. We have found rocks assigned to, or believed to be genetically linked with, the DIC at and around the Flurbühl Hill within an area of *c.* 1500 × 1200 m.

Contacts of the intrusive rocks are not exposed. Weathered vent or diatreme breccia containing phlogopite megacrysts occurs adjacent to the eastern border of phaneritic intrusive rocks and perhaps represents the immediate host rock of intrusions. This breccia brought abundant amphibolite xenoliths, originally interpreted as an outcrop of basement rocks (Zartner 1938). Fine-grained breccia is present secondarily in the DP-3 borehole located close to the NW border of DIC. Breccia-looking but otherwise massive rocks are present also in the roof of phaneritic intrusions. These observations imply the possibility that massive intrusions were emplaced into a pre-existing diatreme.

The coordinates of the sampling sites and their location within proposed outline of the DIC are given in Supplements S1 and S2. Sampling sites including two drillings (DB-2 and DP-3) from 1968 are commented in Supplement S3.

3. Analytical methods

3.1. Mineral chemistry

The composition of the anhydrous rock-forming minerals was studied using the CamScan 3400 electron microprobe (Czech Geological Survey, Prague) at an operation current of 2.5–3 nA, voltage of 15 kV and 100 s counting time. An Energy Dispersive System (EDS – Link ISIS 300) was employed to acquire quantitative analyses. The foid minerals were analysed by a defocused beam to omit alkali loss during the analyses. The advantage of real-time control on running EDS analyses was crucial for study of the feldspathoid composition, as the stability of the alkali signal could have been controlled simultaneously with the analysis.

The (OH, F)-bearing minerals (micas and amphiboles) were analysed largely using the Cameca SX 100 wavelength-dispersive electron microprobe at the Geological Institute, Academy of Sciences of the Czech Republic. The operation current was 10 nA and the voltage 15 kV. The diameter of the focused beam varied from 1 to 2 μm.

Selected mineral analyses are tabulated in the supplementary electronic material.

3.2. Whole-rock geochemistry

Samples were analysed for major- and trace-element contents in the Activation Laboratories, Ltd. (Ancaster, Ontario). Prior to the analysis, the samples were mixed with a lithium metaborate and lithium tetraborate flux and fused in an induction furnace. The melt was poured into a solution of 5% nitric acid containing an internal standard, and mixed continuously until completely dissolved. The samples were run for major oxides and Sc, Sr, Ba, V on a combination simultaneous/sequential Thermo Jarrell-Ash ENVIRO II ICP-OES or a Spectro Ciros ICP-OES; all the remaining trace elements including REE were determined using the Perkin Elmer SCIEX ELAN 6000 or 6100 ICP-MS. The estimated analytical uncertainties for concentrations of <100 ppm vary from element to element but are commonly better than ± 10 %. Detailed tables of control analyses of reference

materials together with certified values are available as supplementary electronic material.

Moreover, selected samples were also analyzed for major elements by wet chemistry in the laboratories of the Czech Geological Survey (Prague Barrandov). When available, these wet analyses are preferred.

Whole-rock analytical data were processed using the Geochemical Data Toolkit (GCDkit) (Janoušek et al. 2006).

3.3. Sr–Nd isotopes

Selected samples were analysed for the Sr and Nd isotopic compositions in the laboratories of the Czech Geological Survey in Prague. Each sample was dissolved by combined HF–HCl–HNO_3 decomposition. Strontium was isolated by ion exchange chromatography using the Sr.spec Eichrom resin, neodymium with TRU.spec and Ln.spec Eichrom resins (see Míková and Denková 2007 for details). Isotopic analyses of Sr and Nd were performed on a Finnigan MAT 262 Thermal Ionization Mass Spectrometer in a dynamic mode using single and double Re filament assemblies, respectively. The Sr and Nd ratios were corrected for mass fractionation assuming $^{146}Nd/^{144}Nd = 0.7219$ and $^{86}Sr/^{88}Sr = 0.1194$. The precision and external reproducibility are demonstrated by repeated analyses of the La Jolla [$^{143}Nd/^{144}Nd = 0.511852 \pm 14$ (2σ; n = 23)] and NBS 987 [$^{87}Sr/^{86}Sr = 0.710247 \pm 26$ (2σ; n = 25)] isotopic reference materials.

3.4. K–Ar dating

Three selected whole-rock samples and two samples of separated phlogopite were dated using the potassium–argon method. The geochronological analyses were performed in the ATOMKI Laboratories, Debrecen, Hungary. After acid digestion and 0.2M HCl dissolution of the samples, the potassium content was determined by flame photometry with a Na buffer and Li internal standard. Measurements were checked by inter-laboratory standards (Asia 1/65, LP-6, HD-B1 and GL-O). Argon was extracted from the samples by radiofrequency fusion in Mo crucibles under vacuum conditions. A ^{38}Ar-spike was added to samples prior to gas-cleaning in Ti and SAES getters and liquid nitrogen traps, respectively. The isotope ratios of argon were measured in the static mode using a 15 cm radius magnetic sector-type mass spectrometer in Debrecen. Balogh (1985) and Odin (1982) described the methods employed in detail. Age calculations were based on constants proposed by Steiger and Jäger (1977). Results of K–Ar dating are given with 1σ errors.

4. Petrographic types

4.1. Overview of the petrographic variability

Within the limits of the DIC, we have found vent or diatreme breccias with phlogopite megacrysts and basement xenoliths, heterogeneous breccias cemented by a fine-grained rock resembling dense basanitic lava (Fig. 3a–b), clinopyroxenite breccias infiltrated by syenitic veinlets (Fig. 3c), variable mafic to felsic nephelinolites, essexites, foid monzodiorite and foid monzosyenite dykes with variable mafic to clinopyroxene-dominated ultramafic xenoliths (Fig. 3d–e). Moreover, these breccias and phaneritic intrusive rocks are crosscut by thin aphanitic dykes with lamprophyric and trachytic to phonolitic compositions (Fig. 3f). Similar dykes also occur in the surrounding lavas.

Phaneritic intrusive rocks consist of various combinations and proportions of clinopyroxene (diopside), hornblende (kaersutite to pargasite), biotite (phlogopite to magnesian biotite) and olivine as mafic minerals. Nepheline, sodalite *sensu lato* (including nosean, haüyne), plagioclase and K-feldspar (sanidine) are the main felsic minerals. Typical accessory minerals are magnetite, ilmenite, titanite and apatite. Limited amounts of epidote, pyrite, analcime, calcite, and zeolite minerals may be present as alteration products of post-magmatic origin. However, most samples are practically devoid of low-temperature minerals.

Magmatic mineral assemblages are both "dry" (lacking significant amounts of hydrous mafic minerals like hornblende) and "wet" (involving abundant hornblende and/or biotite). Typical mineral assemblages of the individual rock types are presented in Tab. 1. Modal analyses of representative samples are given in Tab. 2. Microprobe analyses of main groups of mafic rock-forming minerals (clinopyroxene, hornblende and biotite) can be found in the Supplementary electronic material (Supplements S4–6).

4.2. Nephelinolites (melteigite–ijolite–urtite)

Nephelinolites were found as loose blocks in the eastern and western marginal parts of the complex. They are absent both around the summit of the Flurbühl Hill and in the DB-2 borehole. The colour indices of nephelinolites are highly variable, enabling us to distinguish olivine-bearing melteigite (melanocratic variety, probably referred to as jacupirangite by Kopecký 1988), ijolite and, finally, urtite with less than 30 vol. % of mafic minerals (see Le Maitre et al. 2002). Leucocratic rock classified as urtite (leucocratic nephelinolite) has been found only as a small loose block (sample DR051B). Nephelinolites

Fig. 3 Field photos of studied rocks. **a**–**b** – Vent (?) breccia from the roof of the DIC (wall of a wayside shrine on the top of the Flurbühl Hill); **c** – Clinopyroxenite breccia intruded by thin veinlets of sodalite syenite (drill core DB-2); **d** – Essexite–sodalite monzosyenite intrusive breccia; **e** – Essexite-dominated intrusive breccia crosscut by a dyke of sodalite monzosyenite; **f** – Hornblende-rich essexite intruded by aphanitic trachyte to phonolite (drill core DB-2). *Bar is 10 cm, coin 2.5 cm in diameter.*

Tab. 1 Mineral assemblages of phaneritic intrusive rocks from the Doupov Intrusive Complex

	C.I.	Olivine	Cpx	Hbl	Bt	Foids	Kfs	Plg
Clinopyroxenite	90–100	○	●●●●	○/●	○/●●	// Sdl	//	○
Melteigite	>70	● $Fo_{85–72}$	●●● mg 84–74	○/▪ (mg 58)	○/▪ mg 58–90	●● Ne	●	○
Ijolite	50–70	○/● $Fo_{85–83}$	●●● mg 85–71	○/▪ mg 50–57	○/●● mg 52–64	●● Ne (Sdl)	●	○
Urtite	<30	○	● mg 57–78	○	▪ mg 57–82	●●● Ne > Sdl	●●	○
Essexite	40–70	(●)/○	●● mg 81–64	●●● mg 38–62	●● mg 45–52	● Ne	●	●● $An_{54–44}$
Monzodiorite	30–40	○	●●	▪	●●	● Sdl	●	●●●
Sodalite monzonite	25–35	○	●●	●	●●	● Sdl	●●	●●
Sodalite monzosyenite	<25	○	● mg 64–77	● mg 42–60	● mg 56–70	●● Sdl (Ne)	●●●	●● $An_{< 33}$

C.I. – Colour Index (vol. % of mafic minerals); mg = 100 Mg/(Mg + Fe_{tot})
Symbols for presence and abundance of mineral constituents: ○ – absent; ▪ – may be present sporadically; ● – present; ●● – present as typical constituent; ●●● – abundant; ●●●● – highly dominant; // – only in veinlets or small pockets
Abbreviations for minerals: Cpx – calcic clinopyroxene (diopside); Hbl – hornblende (kaersutite, pargasite); Bt – biotite; Kfs – K–feldspar; Plg – plagioclase; Sdl – sodalite group mineral; Ne – nepheline

Tab. 2 Modal analyses (vol. %) of selected phaneritic intrusive rocks from the Doupov Intrusive Complex

	1	2	3	4	5	6	7	8
Sample	DH1330	DH1319	DR052	DR051B	TV52	DB2	TV54	DB2
Rock	Melteigite	Ijolite	Mica ijolite	Urtite	Essexite	Sodalite monzodiorite	Sodalite monzosyenite	Clinopyroxenite
Olivine	4	–	3	–	2	–	–	–
Clinopyroxene	63	58	46	15	29	23	5	79
Hornblende	trace	trace	–	trace	18	2	7	1
Biotite	1	3	12	trace	10	10	5	8
Plagioclase	–	–	–	–	21	48	24	–
K-feldspar	7	8	2	20	5	3	38	1
Nepheline	18	24	25	44	3	1	–	–
Sodalite *s. l.**	–	–	2	15	–	6	13	3
Analcime	–	–	–	–	1	trace	–	–
Zeolites	–	–	–	–	1	–	–	–
Titanite	0.1	+	3	2	4	2	3	–
Magnetite	5	4	4	2	4	3	2	5
Ilmenite	1	1	trace	trace	trace	trace	trace	trace
Apatite	0.9	1.5	3	2	2	2	2	3
Sum	100	99.5	100	100	100	100	99	100
Colour index	73	65	68	19	67	40	23	93

* including its alteration products

are plagioclase-free but contain K-feldspar and sodalite (Tab. 1). The absence of (OH, F)-bearing mafic minerals, namely amphiboles, is typical of most samples of these rocks.

4.2.1. Olivine melteigite and ijolite

Ijolitic rocks are mesocratic to melanocratic rocks dominated by subhedral to almost euhedral, purplish Ti-rich clinopyroxene (titanian diopside) with Ti-poor crystal cores (Fig. 4a). However, olivine with normal zoning ($Fo_{85–73}$) has been found in several samples. The main felsic mineral is relatively coarse but anhedral and interstitial K-bearing nepheline (4.8–5.5 wt. % K_2O). Nepheline may be accompanied by subordinate sodalite, which is commonly altered. Magnetite, titanite, ilmenite and apatite are common accessory phases. Apatite forms abundant euhedral needles.

A variety of olivine-bearing ijolite with abundant phlogopite was found as a loose block in the westernmost part of the Doupov Intrusive Complex (sample DR052).

The clinopyroxenes from mafic phaneritic rocks (melteigite, ijolite and essexite) display similar features. The individual grains are compositionally and optically zoned. Their cores contain more magnesium and lower amounts of both TiO_2 and Al_2O_3 compared to the surrounding oscillatory growth zones and crystal rims. The rims have slightly higher contents of TiO_2 and $A1_2O_3$ but lower FeO_{tot}, MgO and Cr_2O_3 than the cores. Compositional variations of pyroxene and the problems associated with its classification were discussed by Rapprich (2005). He concluded that large crystals of clinopyroxene from essexite compositionally resemble phenocrysts in tephritic lavas and display the same evolutionary trend. The compositions of aluminian diopside in the cores and titanian aluminian subsilicic diopside in marginal parts of crystals are typical.

Amphiboles only rarely found in ijolite to melteigite correspond to kaersutite with 5.3–6.3 wt. % TiO_2.

4.2.2. Urtite

Urtite DR051B is a greyish-white rock macroscopically similar to fine-grained syenite. Felsic constituents are dominated by euhedral nepheline (0.2–0.6 mm; Fig. 4b), subordinate sodalite or yellowish products of its alteration, and interstitial K-feldspar. Clinopyroxene in small subhedral grains is variable in colour (Z – brown–violet to greenish) and corresponds to diopside with Mg/(Mg + Fe + Mn) = 0.57–0.78. Small grains included in euhedral nepheline are rich in TiO_2 and Al_2O_3 (up to 9.3 and 5.8 wt. %, respectively), whereas discrete grains in the matrix are poor in these oxides. Matrix diopside may be more magnesian, perhaps due to contemporary crystallization of magnetite. The contents of Na_2O and the aegirine component are generally low (commonly less than 1.2 wt. % and 4.5 mol. %, respectively). Scarce mica (several small anhedral grains per thin section) corresponds to phlogopite with less magnesian cores (Mg/Fe 1.3–1.5) and highly magnesian rims (2.9–4.7). This "inverse" type of zoning of both phlogopite and clinopyroxene reflects the increasing oxidation and co-precipitation of magnetite. Titanite, magnetite, and apatite (<1 vol. %) are accessory minerals.

4.3. Essexites

Essexitic rocks are common in limited outcrops W and N of the Flurbühl hill-top but very subordinate in the DB-2 borehole. Essexites display typically "wet" mafic mineral assemblage with abundant hornblende and great textural and mineralogical variability. Large amphibole crystals (Fig. 3f) are important for the appearance of relatively coarse varieties of the rock. Abundance of amphibole is the major criterion for distinguishing essexitic rocks from mafic nephelinolites in the field.

Most typical essexite samples are composed of clinopyroxene, amphibole, biotite (phlogopite to magnesian biotite) and various amounts of plagioclase (labradorite to andesine), K-feldspar and nepheline. Some varieties contain variously altered sodalite instead of nepheline; the presence of a limited amount of analcime is much less common. Magnetite, titanite and apatite are the most common accessory to minor constituents.

Clinopyroxene is subhedral to almost euhedral and strongly zoned with evolutionary trends similar to those in tephritic lavas (Rapprich 2005). The almost homogeneous crystal cores of diopside low in TiO_2 are surrounded by oscillatory growth zones of titanian diopside with purplish colour (Fig. 4c). Hornblende (Fig. 4d) is commonly larger (up to 7 mm in some varieties) and constitutes individual poikilitic crystals as well as overgrowths on clinopyroxene. The predominant parts correspond to kaersutite and titanian pargasite. It is deep reddish brown along the Z-direction, and there are marginal zones that are deeply brownish–green coloured. The filling of the spaces between the mafic phases is dominated by large, tabular to anhedral plagioclase, accompanied by irregularly distributed interstitial K-feldspar and nepheline.

Many essexite samples display irregular mineral distribution with patchy concentrations of minerals. In some thin sections (e.g., DI3), small (several mm in diameter) patches of ijolitic assemblage clinopyroxene + nepheline are present, surrounded by common "wet" assemblages rich in hornblende.

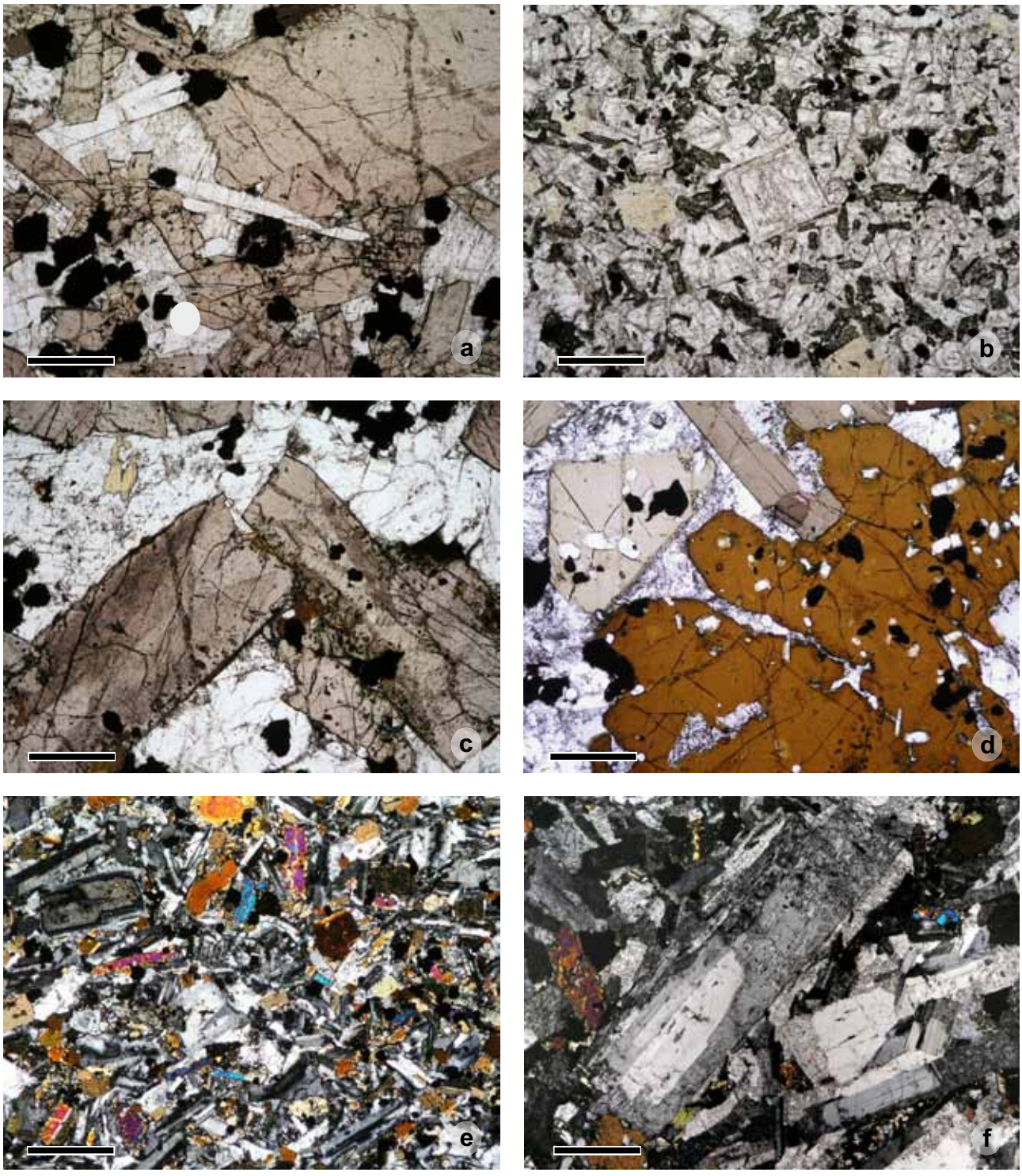

Fig. 4 Photomicrographs of mafic to felsic phaneritic rocks of the Doupov Intrusive Complex. **a** – Melteigite (melanephelinolite DH1550); **b** – Urtite (leuconephelinolite DR051B) rich in euhedral nepheline; **c** – Essexite (KY20A), a domain dominated by zoned clinopyroxene and anhedral nepheline; **d** – Essexite (KY20A), prevailing part rich in kaersutitic amphibole and interstitial plagioclase; **e** – Texture of monzodiorite with tabular plagioclase (crossed nicols); **f** – Porphyritic variety of sodalite monzosyenite with plagioclase overgrown by K-feldspar (crossed nicols). *Bar is 0.5 mm, plane-polarized light if not indicated otherwise.*

4.4. Sodalite monzodiorite and similar varieties

Sodalite-bearing monzodiorite occurs as small (<1 m) medium- to fine-grained dykes intruding clinopyroxenite breccias and other rocks in drill-core DB-2. The rock is dominated by plagioclase and the amount of interstitial K-feldspar is highly variable. Mafic minerals consist of clinopyroxene and biotite, whereas hornblende occurs only rarely as inclusions in some plagioclase grains. Sodalite-bearing monzodiorite (Fig. 4e) may gradually pass into sodalite-bearing or sodalite monzonite.

4.5. Sodalite-bearing monzosyenite to nepheline–sodalite (monzo)syenite

Sodalite-bearing to sodalite monzosyenite constitutes one relatively thick (~4 m) dyke exposed within a small old quarry NW of the summit Flurbühl (DI-4). Findings of rare homogeneous syenitic blocks (e.g., DR054) argue for existence of another relatively wide dyke(s) in the area. There are almost ubiquitous, innumerable, very thin dykes and veinlets crosscutting other rock types (Fig. 3c).

Relatively homogeneous syenitoids are felsic rocks dominated by sanidine, with less abundant plagioclase (andesine to oligoclase–andesine, commonly overgrown by sanidine), variable amounts of the sodalite group mineral(s) (nosean to sodalite, commonly euhedral but frequently altered) and rarely also nepheline (DH1322). Mafic minerals are minor and represented by dark mica (phlogopite to magnesian biotite; e.g., DH1322), brown hornblende (DR054) or by a combination of clinopyroxene, hornblende and mica (TV54). Accessory minerals consist of euhedral titanite, magnetite, ilmenite and tiny acicular apatite. The grain-size is variable but lengths of K-feldspar laths ~1–3 mm are common. In a weakly porphyritic variety of sodalite syenite, plagioclase forms cores of K-feldspar phenocrysts (Fig. 4f) set in a finer grained, nearly trachytic matrix.

Thin dykes and veinlets (1–X0 mm in width) are commonly irregular, inhomogeneous and frequently rich in sodalite, especially in the marginal parts.

4.6. Clinopyroxenites and clinopyroxenite breccias

These rocks are very poorly exposed. On the present surface, they occur mostly as small xenoliths in other intrusive rocks or as small loose blocks without known original position. However, clinopyroxenites are the most widespread rock type in drill core DB-2 and seem to represent the oldest recognizable rock group intruded by sodalite-bearing monzodioritic to syenitic rock types and aphanitic dyke rocks.

Clinopyroxenites consist essentially of subhedral to anhedral clinopyroxene, which corresponds to almost unzoned or only weakly and irregularly zoned diopside. Clinopyroxene is commonly accompanied by variable amounts of phlogopite and magnetite, and much less frequently also apatite. Kaersutitic amphibole is present in some clinopyroxenite xenoliths (Fig. 5a) associated to essexite and sodalite syenite and representing ultramafic cumulate.

Clinopyroxenites in the DB-2 borehole are variable in grain size and texture even on a thin section scale. Phlogopite and magnetite are commonly present in various amounts (Fig. 5b). Some samples also contain apatite, pyrite and other minerals.

Brecciation of clinopyroxenites is accompanied by shattering of individual pyroxene grains. These crystals display an irregular network of microcracks marked by very fine phlogopite. Phlogopite may also form clusters of relatively coarse, often deformed flakes, in places with abundant and very sharp kink bands oriented in various directions (Fig. 5c).

Small felsic pockets (several mm in diameter) and veinlets are dominated at the margins by a sodalite mineral or its alteration products involving carbonate. The inner parts may approach the composition of sodalite syenite. These pockets and veins are frequently rimmed by kaersutitic amphibole and/or phlogopite, which partially replace the surrounding clinopyroxene grains.

4.7. Phlogopite–clinopyroxene metasomatic rock ("pseudolamprophyre") and other products of thermal and metasomatic aureole

Phlogopite-rich rock of lamprophyric appearance (macroscopically resembling coarse minette) occurs as large blocks at the eastern border of the DIC in close spatial association with ijolitic rocks and a thin dyke of nepheline–sodalite syenite. However, the microtexture strongly contrasts with lamprophyres and corresponds to a product of a metasomatic process superimposed on a pre-existing igneous, probably volcanic rock. Phlogopite flakes 1 to 10 mm and also clinopyroxene megacrysts (1–4 mm) are surrounded by a fine-grained, extremely inhomogeneous matrix. Phenocrystic clinopyroxenes are strewed with a network of microcracks invaded by fine-grained phlogopite (Fig. 5d) in the same manner as in clinopyroxenite breccias. "Phenocrystic" phlogopite may be deformed and, in places, partly replaced by fine-grained phlogopite aggregates. Other relatively large phlogopite

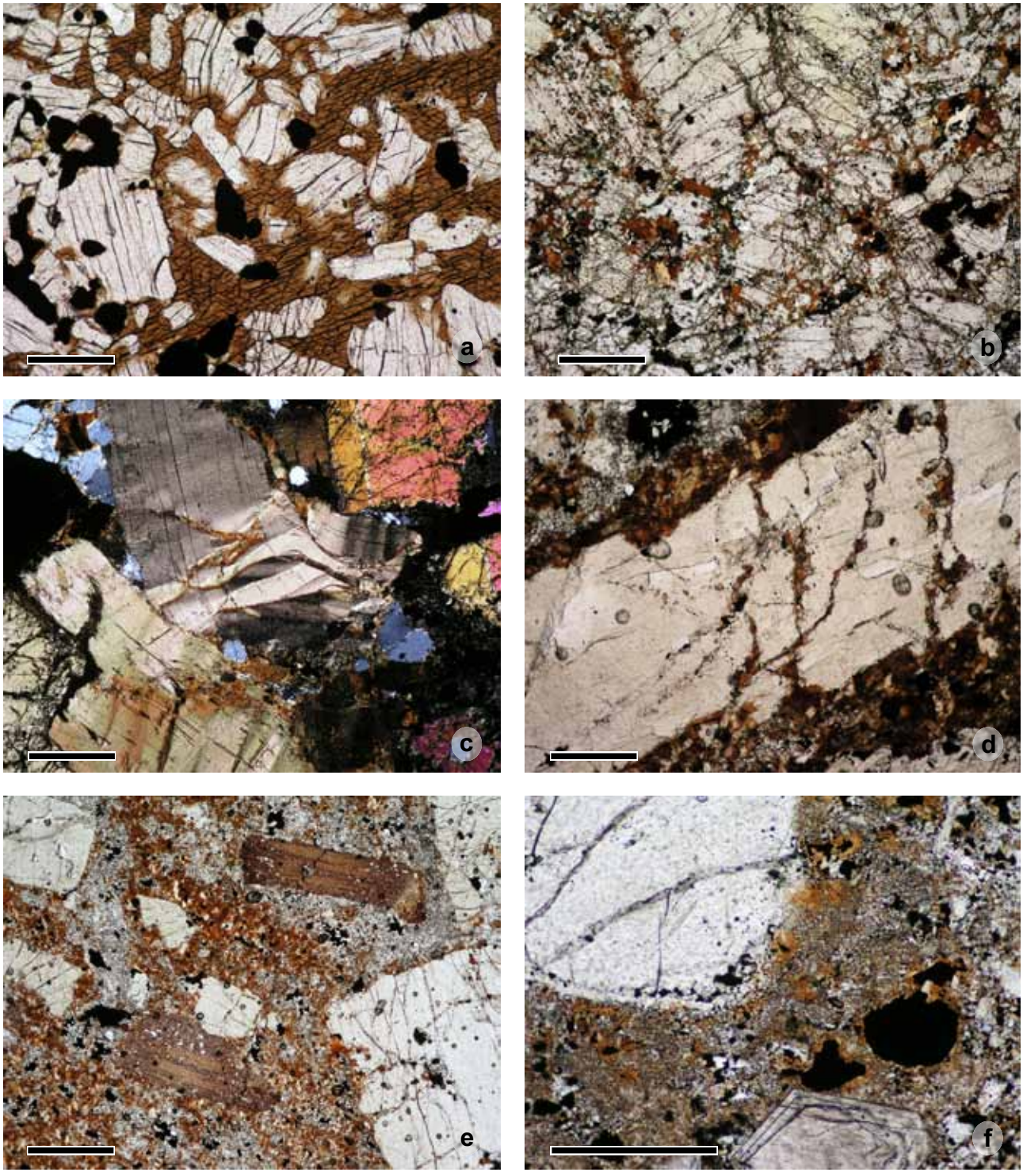

Fig. 5 Photomicrographs (plane-polarized light) of clinopyroxenites and metasomatized rocks of the Doupov Intrusive Complex. **a** – Clinopyroxenite with large interstitial and poikilitic kaersutite; **b** – Phlogopite-bearing clinopyroxenite with fine-grained phlogopite along grain boundaries and cracks within clinopyroxene grains; **c** – Large deformed phlogopite in coarse-grained clinopyroxenite, DB-2; **d** – Brittle deformation and partial phlogopitization along cracks of large clinopyroxene grain in metasomatic "pseudolamprophyre"; **e** – Phlogopitized matrix and large phlogopite flakes in metasomatized "pseudolamprophyre"; **f** – Phlogopitization of matrix in thermally affected microbreccia (matrix of vent breccia) from the top of Flurbühl. *Bar is 0.5 mm.*

crystals are undeformed but markedly poikilitic with minute clinopyroxene and magnetite inclusions. The matrix is fine-grained and inhomogeneous with some small domains highly dominated by phlogopite (Fig. 5e) and other completely devoid of this mineral, composed of pale greenish–yellow clinopyroxene (0.015–0.05 mm) with subordinate interstitial sodalite or its alteration products (zeolites with dispersed carbonate). Magnetite is minor, while iron sulphides and apatite represent accessory constituents.

The other samples are much poorer in fine phlogopite with mica forming individual poikilitic grains. Their fine-grained matrix is mostly "dry" with clinopyroxene dominating over fine magnetite and interstitial sodalite or K-feldspar plus sodalite. There are also irregular veins with a predominance of poikilitic K-feldspar enclosing many small euhedral inclusions of sodalite. Exactly the same fine-grained rock with scattered poikilitic flakes of phlogopite was found as small xenoliths in the sodalite monzodiorite dyke from the DB-2 borehole.

Breccias from the top of Flurbühl, i. e. located higher than essexite outcrops, contain fragments X mm to 10 cm in size corresponding to highly variable fine-grained clinopyroxene-phyric mafic rocks that may represent chilled intrusive varieties of tephritic to basanitic composition and also monchiquitic lamprophyres. These fragments and also olivine and clouded clinopyroxene xenocrysts are cemented in a dense, aphanitic but highly inhomogeneous matrix resembling a microbreccia that was affected by thermal recrystallization. This matrix is characterized by the presence of finely scattered and locally concentrated biotite (Fig. 5f).

This unusual breccia type probably represents the fill of a pre-existing explosive conduit which was thermally reworked and metasomatized in the roof of the phaneritic alkaline intrusions.

4.8. Lamprophyric dykes

Thin dykes (1 cm to > 0.5 m) of lamprophyric rocks were found in abandoned drill-cores from the DP-3 borehole. The DB-2 drill-core contains lamprophyric rocks within the clinopyroxenite-dominated breccia as small, very irregular bodies that may be dykes or fragments.

Lamprophyres from DP-3 are aphanitic to fine-grained with very sharp, strongly chilled contacts. They contain phenocrysts of phlogopite, clinopyroxene and rare olivine 0.5 to 3 mm across. The groundmass contains various proportions of small acicular or blade-shaped crystals of phlogopite, amphibole and/or clinopyroxene set in a felsic matrix dominated by analcime, with dispersed fine-grained calcite and magnetite, and frequently also K-feldspar. There are common occurrences of carbonate-bearing zeolitic pseudomorphs, possibly replacing sodalite. Some samples contain small round ocelli rimmed with tangentially arranged biotite and filled by analcime, carbonate, and frequently brown amphibole needles in a very fine felsic matrix.

4.9. Felsic aphanitic dykes: trachytes to phonolites

Trachytes, sodalite-bearing trachytes and phonolites were found as thin, very irregular dykes in drill-core DB-2. They are porphyritic with very fine-grained to aphanitic groundmass and consequently resemble effusive rocks. Judging from their textural features, these dykes intruded the already cold host rocks.

Trachytic varieties contain mafic phenocrysts of clinopyroxene plus hornblende or clinopyroxene (diopside) plus biotite. Other phenocrysts are sanidine and plagioclase (andesine to oligoclase) with sanidine overgrowths, in most cases also sodalite mineral(s), less frequently apatite and titanite. Some samples contain higher proportion of the sodalite mineral and pass into sodalite phonolite.

Sample DH745 from the NW vicinity of the Doupov Intrusive Complex represents an unusual variety of dyke phonolite with abundant euhedral phenocrysts of haüyne set in an extremely fine to cryptocrystalline, probably devitrified matrix. Clinopyroxene, which forms minute microliths, is rich in the aegirine component.

5. Whole-rock geochemistry

Selected representative whole-rock major- and trace-element analyses are presented in Tabs 3 and 4. A larger set of analyses, including those from the literature, is used for construction of variation diagrams (Figs 6–7) and other geochemical plots including that with chondrite-normalized rare-earth element patterns (Fig. 8).

The analysed **ijolitic rocks** with "dry" mineral assemblage are strictly ultrabasic, extremely undersaturated with *Ne* + *Lc* + *Cs* ("larnite") in their CIPW norms, and metaluminous. The primitive nature of these rocks is expressed in the MgO contents, which are significantly higher than in essexites. Both melteigite DH1330 and ijolite DH1329 have very high contents of CaO with TiO_2 but their Na_2O and K_2O are lower than in essexites. Melteigite and ijolite plot into the picrobasalt (close to foidite) and foidite fields, respectively. When comparing "dry" melteigite and ijolite, the latter is lower in SiO_2 and MgO as well as compatible trace elements, namely Cr, but higher in TiO_2, Al_2O_3, total Fe, Na_2O, K_2O, P_2O_5 and the whole spectrum of incompatible trace elements.

Olivine–phlogopite ijolite DR052 has MgO similar to the "dry" ijolite DH 1329 but is higher in SiO_2, Al_2O_3, Na_2O, K_2O and lower in TiO_2, FeO_{tot}, CaO and P_2O_5. Its

Tab. 3 Selected major-element data for the studied alkaline intrusive rocks (wt. %)

	1	2	3	4	5	6	7
Sample	DH1330	DH1329	DR052	DR051B	DI-8B	DI-3	TV52
Rock	Melteigite	Ijolite	Mica ijolite	Urtite	Essexite	Essexite	Essexite
SiO_2	40.74	38.05	41.78	47.63	40.63	42.28	43.88
TiO_2	4.629	5.453	3.79	1.67	4.15	3.98	3.755
Al_2O_3	9.57	10.71	12.26	22.05	11.87	13.33	13.28
Fe_2O_3	5.97	6.69	5.49	2.75	14.91*	13.53*	12.57*
FeO	6.62	6.85	6.22	1.76	n.a.	n.a.	n.a.
MnO	0.176	0.200	0.184	0.128	0.223	0.224	0.185
MgO	11.06	8.28	8.41	0.99	6.27	6.01	5.96
CaO	16.74	16.43	12.86	4.31	12.73	12.1	11.99
SrO	n.a.	n.a.	0.09	0.41	n.a.	n.a.	n.a.
BaO	n.a.	n.a.	0.11	0.21	n.a.	n.a.	n.a.
Li_2O	n.a.	n.a.	0.00	0.00	n.a.	n.a.	n.a.
Na_2O	1.47	1.60	2.70	7.58	2.74	2.99	3.25
K_2O	1.24	1.57	2.80	6.13	2.40	2.60	2.90
P_2O_5	0.44	1.15	0.59	0.15	1.23	0.94	0.66
F	0.131	0.176	0.169	0.124	n.a.	n.a.	0.142
CO_2	0.10	0.50	0.03	0.08	n.a.	n.a.	0.15
SO_3	n.a.	n.a.	n.a.	n.a.	n.a.	n.a.	0.11
S	0.017	0.017	0.09	0.04	n.a.	n.a.	0.147
$H_2O(+)$	n.a.	n.a.	1.88	3.18	n.a.	n.a.	n.a.
$H_2O(-)$	0.12	0.22	0.20	0.35	n.a.	n.a.	0.13
LOI	0.77	1.53	n.a.	n.a.	1.55	0.93	0.92
Total	100.40	99.52	99.66	99.55	98.71	98.92	99.35
mg	61.8	53.0	59.2	29.4	45.4	46.8	48.4
K_2O/Na_2O	0.84	0.98	1.04	0.81	0.88	0.87	0.89
NK/A	0.39	0.40	0.61	0.87	0.60	0.58	0.64

	8	9	10	11	12	13	14
Sample	DI-8C	TV54	DR048E	DB2 48.8 m	DH1321	DR048C	DH745
Rock	Essexite	Sdl. mnz-syenite	Vent breccia	Breccia	Metasom. rock	Monchiquite	Phonolite
SiO_2	48.71	56.00	37.84	37.49	40.49	41.29	52.06
TiO_2	2.72	1.256	3.988	4.42	4.25	3.12	0.30
Al_2O_3	15.23	18.51	9.53	11.05	9.98	11.93	20.18
Fe_2O_3	9.94*	2.67	12.19*	10.75	5.67	5.75	2.60
FeO	n.a.	1.91	n.a.	8.34	6.64	5.80	1.01
MnO	0.189	0.126	0.145	0.241	0.159	0.181	0.256
MgO	4.38	1.21	8.51	7.96	11.60	6.99	0.23
CaO	9.82	4.82	13.31	12.49	14.17	12.62	2.60
SrO	n.a.	n.a.	n.a.	0.078	0.046	0.09	0.253
BaO	n.a.	n.a.	n.a.	0.060	0.079	0.09	0.168
Li_2O	n.a.	n.a.	n.a.	0.002	0.001	0.00	0.006
Na_2O	3.67	4.78	1.58	1.93	0.77	2.94	10.03
K_2O	3.37	5.43	2.10	2.03	2.86	2.48	7.04
P_2O_5	0.57	0.20	0.32	0.30	0.279	0.66	0.038
F	n.a.	0.136	n.a.	0.14	0.131	0.132	0.106
CO_2	n.a.	0.66	n.a.	0.21	0.23	2.82	0.26
SO_3	n.a.	0.06	n.a.	0.18	n.a.	n.a.	1.07
S	n.a.	0.036	0.023	0.22	0.725	0.12	0.026
$H_2O(+)$	n.a.	n.a.	n.a.	1.59	1.45	2.17	1.92
$H_2O(-)$	n.a.	0.34	n.a.	0.24	0.24	0.43	0.32
LOI	1.19	2.41	9.18	n.a.	n.a.	n.a.	n.a.
Total	99.78	99.61	98.69	99.73	99.72	99.61	99.39
mg	46.6	33.0	58.0	46.0	63.8	53.2	10.5
K_2O/Na_2O	0.92	1.14	1.33	1.05	3.71	0.84	0.70
NK/A	0.64	0.74	0.51	0.49	0.45	0.63	1.16

LOI – loss on ignition given for ICP-OES analyses from Activation Laboratories, Ltd.; *mg* = 100Mg/(Mg + Fe_{tot}) from atomic proportions; K_2O/Na_2O based on wt. %; NK/A = $(Na_2O + K_2O)/Al_2O_3$ from molar values; * – total Fe as Fe_2O_3 (ICP-OES analyses); n.a. – not analysed

Tab. 4 Selected trace-element data (ppm) for the studied alkaline intrusive rocks

	1	2	3	4	5	6	7
Sample	DH1330	DH1329	DR052	DR051B	DI-8B	DI-3	TV52
Rock	Melteigite	Ijolite	Mica ijolite	Urtite	Essexite	Essexite	Essexite
Ba	389	450	802	2171	579	856	780
Co	52	51	43	7	52	38	44
Cr	278	79	254	<5	<20	20	37
Cs	0.2	1.2	0.6	0.7	3.1	1.3	0.9
Ga	20	23	20	26	24	22	22
Hf	8.2	10.2	7.2	9.1	9.3	8.3	7.8
Nb	61	71.4	87.1	333	72.3	68.1	83.4
Ni	100	60	73	4	50	40	30
Pb	2	5	4	3	9	9	5
Rb	27	38	65	84	64	67	69
Sc	62	43	33.9	1.5	28	24	27.1
Sr	563	735	780	3352	738	1126	844
Ta	4.22	5.36	6.29	20.70	5.29	5.52	5.98
V	483	644	404	124	474	438	449
Y	20.5	29.1	20.3	25.2	27.1	27.9	23.5
Zr	317	420	312	601	340	316	311
U	1.08	1.31	1.97	6.94	2.13	2.21	2.33
Th	3.90	4.89	6.37	20.60	7.53	7.03	8.50
La	39.0	65.4	53.6	96.8	72.1	71.2	63.4
Ce	89.1	148	112	175	151	145	130
Pr	11.8	19.4	13.5	17.4	17.7	17.4	15.5
Nd	42.0	69.5	51.8	52.5	70.5	69.0	57.9
Sm	8.15	12.50	9.29	7.99	12.00	11.90	10.40
Eu	2.49	3.65	2.62	2.42	3.78	3.68	2.84
Gd	7.27	11.20	6.80	5.66	9.07	9.04	7.76
Tb	0.93	1.38	0.94	0.91	1.28	1.29	1.07
Dy	4.43	6.33	4.58	4.96	6.21	6.29	5.36
Ho	0.69	0.99	0.80	0.94	1.04	1.05	0.96
Er	1.72	2.50	2.03	2.74	2.61	2.72	2.42
Tm	0.213	0.314	0.250	0.397	0.347	0.359	0.324
Yb	1.21	1.77	1.50	2.51	2.01	2.14	1.93
Lu	0.170	0.233	0.201	0.343	0.275	0.297	0.267

Underlined data were determined by INAA, others excepting Sc by ICP-MS, Sc by ICP-OES

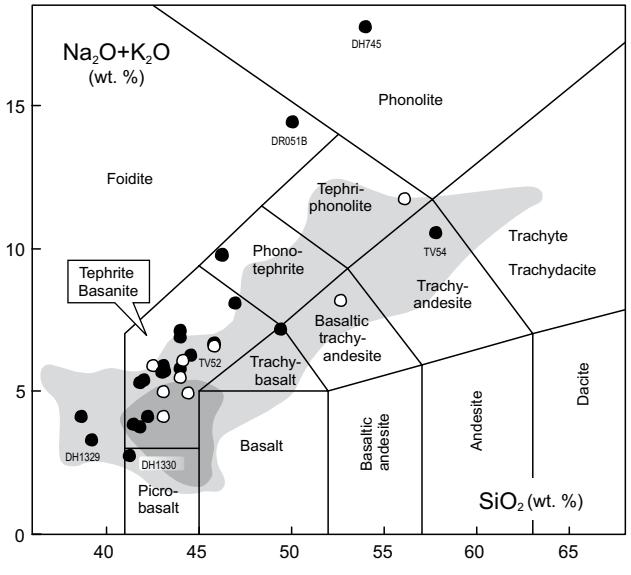

Fig. 6 Total-Alkali vs. Silica (TAS) diagram for phaneritic intrusions, breccias and aphanitic dyke rocks from the Doupov Intrusive Complex (black circles with numbers represent new samples, white circles are older analyses from literature). Compositional variability of lavas from the Doupovské hory Volcanic Complex is shown for comparison (shaded fields represent all literature analyses, dark one denotes the highest frequency of analyses). The IUGS classification grid for volcanic rocks is from Le Maitre et al. (2002).

Tab. 4 continued

	8	9	10	11	12	13	14
Sample	DI-8C	TV54	DR048E	DB2 48.8 m	DH1321	DR048ch	DH745
Rock	Essexite	Sdl. mnz–syenite	Vent breccia	Breccia	Metasom. rock	Monchiquite	Phonolite
Ba	927	987	660	529	564	689	2593
Co	28	7	63	70	53	51	2
Cr	60	<20	157	45	113	169	7
Cs	2.0	5.0	0.3	0.8	0.6	0.7	4.5
Ga	26	24	21	23	18	23	41
Hf	10.0	9.6	6.1	8.2	6.4	4.4	7.6
Nb	102	93.8	50.4	76.2	58.2	66.7	173
Ni	40	7	70	120	70	52	11
Pb	14	20	<3	10	<5	8	25
Rb	95	153	52	44	68	54	200
Sc	19	4.2	61.2	49	67	36.9	<1
Sr	1179	971	381	627	396	780	2531
Ta	7.85	5.46	3.50	5.90	3.86	5.03	2.48
V	309	136	447	603	413	393	87
Y	33.7	19.5	14.7	23.3	17.2	20.6	5.9
Zr	389	459	217	305	245	201	656
U	3.56	4.54	1.10	1.44	0.73	1.74	13.50
Th	12.80	17.10	4.01	4.75	3.79	5.92	43
La	95.9	76.6	28.1	46.6	29.3	42.1	148
Ce	196	136	66.3	101	72.4	96.8	206
Pr	21.4	14.3	8.79	12.5	9.78	12.4	15.1
Nd	80.2	46.6	39.5	50.2	35.5	52.9	35.5
Sm	13.10	7.13	7.25	9.41	6.98	9.10	2.72
Eu	3.83	1.85	2.05	2.62	2.07	2.61	0.74
Gd	9.54	5.21	5.32	6.87	6.10	6.90	1.24
Tb	1.42	0.74	0.72	0.96	0.76	0.92	0.17
Dy	7.12	3.88	3.41	4.90	3.74	4.59	0.80
Ho	1.25	0.75	0.60	0.82	0.60	0.83	0.17
Er	3.28	2.05	1.46	2.15	1.45	2.08	0.52
Tm	0.451	0.303	0.151	0.283	0.186	0.237	0.082
Yb	2.68	1.91	1.10	1.71	1.07	1.66	0.57
Lu	0.375	0.276	0.148	0.257	0.143	0.226	0.099

chemistry is more primitive (high MgO, Cr) but otherwise similar to the essexites.

Urtite (DR051B) is higher in silica (47.75 wt. %) and much higher in alumina (22 %) and alkalis (sum 13.7 %) compared to ijolitic rocks. It is highly undersaturated and dominated in the CIPW norm by *Or* and *Ne*. It is also metaluminous, although the molar $(Na_2O + K_2O)/Al_2O_3$ ratio is moderately elevated (0.83). Of the incompatible trace elements, Ba, Sr, Zr, Nb and Ta are strongly enriched, not only compared to mafic rocks, but also to the sodalite syenite. Compared with the rest of the dataset, this sample displays the lowest Ti/Nb (30) and has a highly superchondritic Zr/Hf ratio (66). No negative Eu-anomaly was observed (the slightly elevated Eu/Eu* value of 1.05 may be due to analytical uncertainty).

Essexites are alkaline, ultrabasic, rarely also basic, but invariably undersaturated (*Ne*-normative) rocks. The silica contents are in the range of 40.6–48.7 wt. % in the uncorrected analyses and 41.6–49.4 wt. % (mostly < 45 %) after recalculation to a volatile-free basis. The contents of MgO vary from 6.3 % in the most primitive variety to 4.4 % in the most evolved one. The *mg* values calculated as $100Mg/(Mg + Fe_{total})$ decrease with MgO from 48 to 40. At the same time, the contents of Al_2O_3 and both Na_2O and K_2O increase, the latter from 2.4 to 3.4 wt. %. The K_2O/Na_2O ratios equal 0.75–0.92. The contents of TiO_2 and P_2O_5 decrease with decreasing MgO and they behave as compatible trace elements. All highly incompatible elements including Rb, Ba, Th, U, Nb, Ta, and LREE have high contents, typically *c.* 100× enriched in respect to the "primordial mantle" composition (Fig. 9).

Sodalite monzosyenite TV54, together with an older silicate analysis from the same locality (Shrbený 1982; values in parentheses), plots into the trachyandesite (or tephriphonolite) field of the Total Alkali–Silica diagram

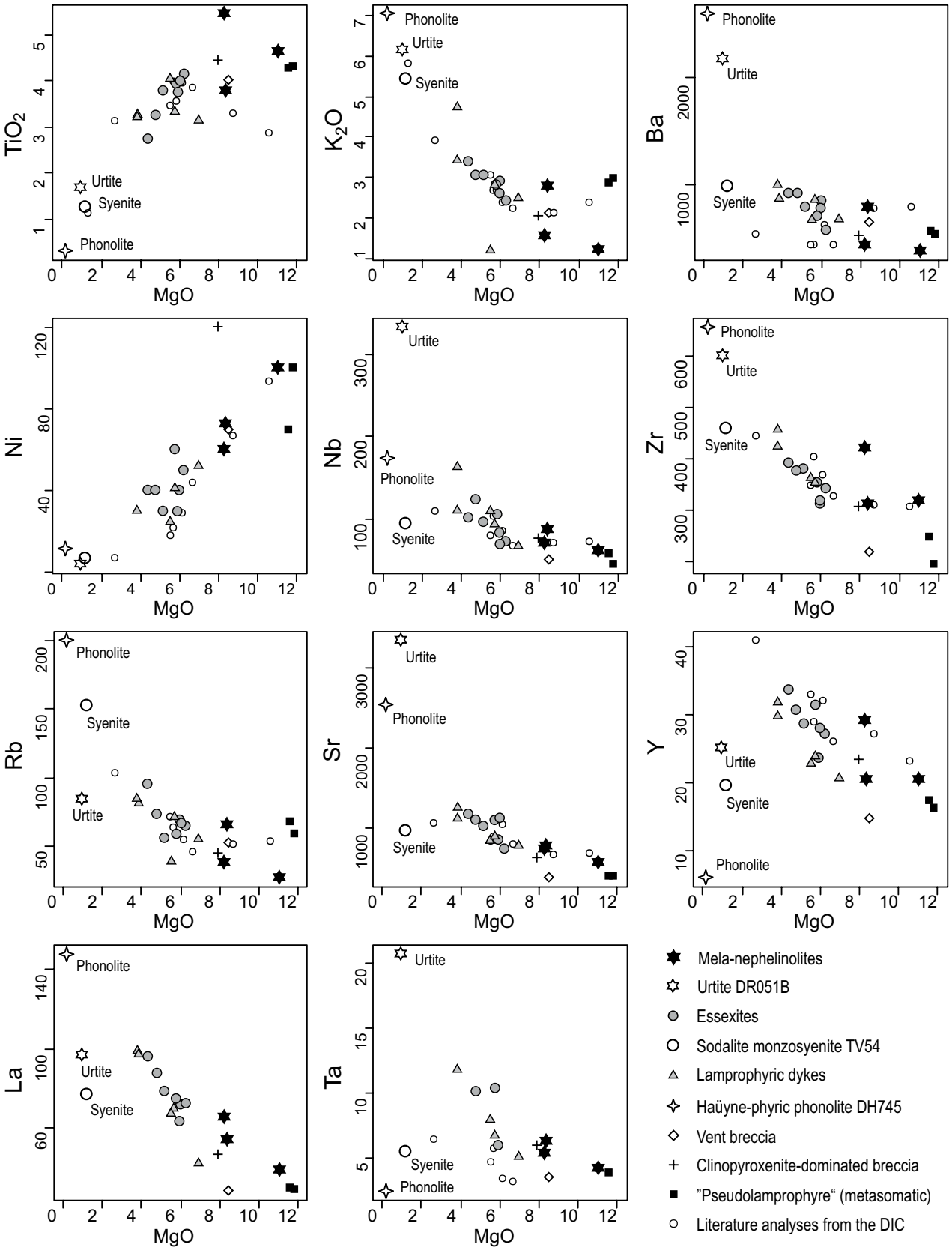

Fig. 7 Multiple variation diagrams of selected minor oxides (wt. %) and trace elements (ppm) *versus* MgO (wt. %) for all analyzed rocks from the Doupov Intrusive Complex and phonolite dyke DH745.

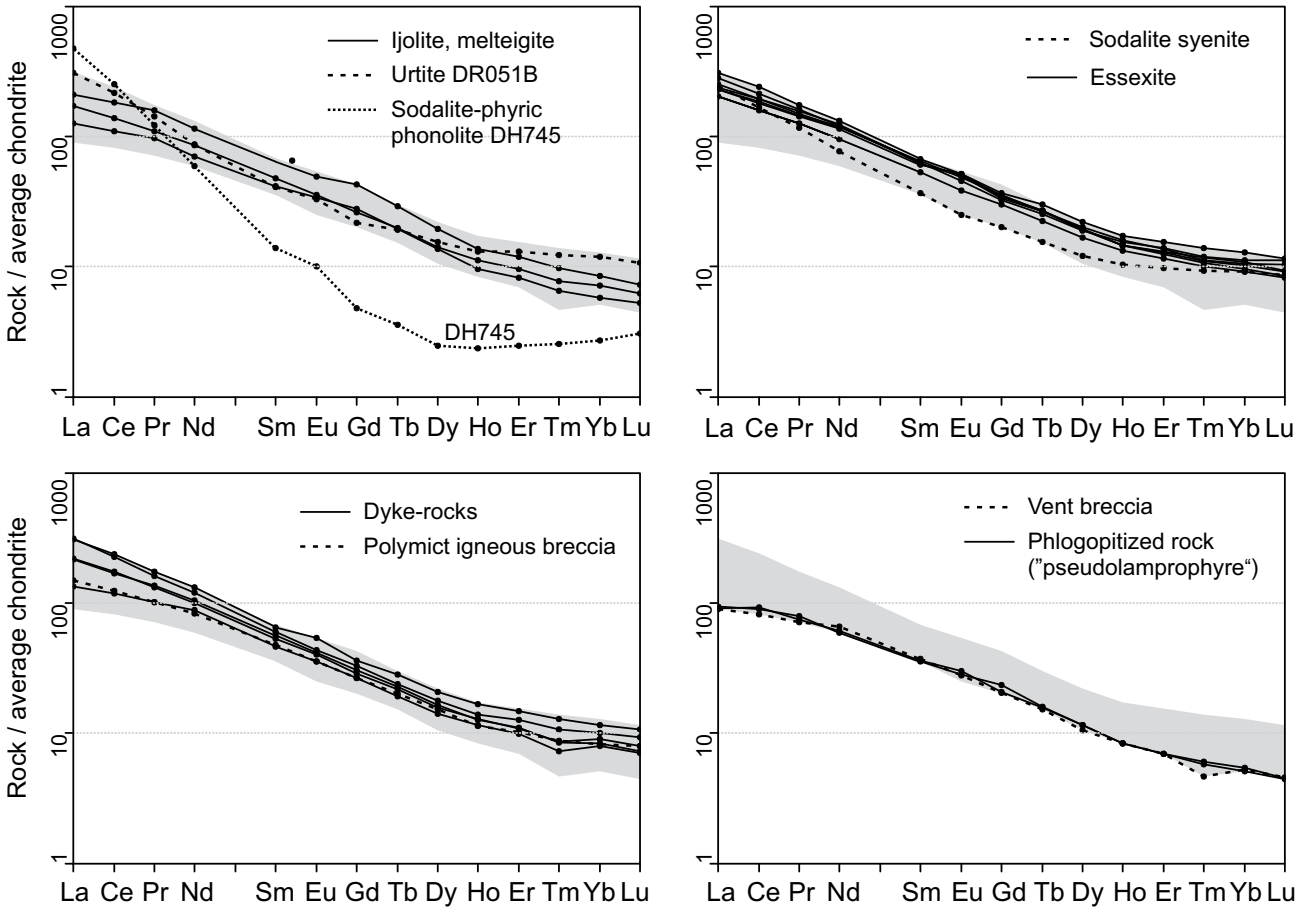

Fig. 8 Chondrite-normalized REE patterns of rocks from the Doupov Intrusive Complex. The grey field includes all samples apart for the sodalite-phyric phonolite dyke (DH745) from a locality NW of the DIC (Fig. 1). Normalization values are from Boynton (1984).

(Fig. 6). It is an alkaline intermediate rock containing 56.00 (54.75) wt. % SiO_2 and 10.2 (11.4) wt. % of total alkalis with the K_2O/Na_2O ratio of 1.14 (1.03). Sodalite monzosyenite is geochemically similar to trachytic rocks occurring as rare dykes in the surrounding lava sequences. It is metaluminous and An-normative with molar $(Na_2O + K_2O)/Al_2O_3 < 1$ (0.74). Normative *Ne* is low (~ 3.5 wt. %) and the CIPW norm is dominated by *Ab* and *Or*. Syenite is poor in compatible trace elements Cr, Co and Ni; V is rather high (136 ppm) although about three-times lower than in essexites. The contents of mantle-incompatible trace elements are roughly similar to those in essexite except for Rb, Cs, Pb, Th, and U, which have greatly elevated contents. Syenite displays only a weak negative Eu-anomaly (Eu/Eu* ~ 0.9, Fig. 8).

Phlogopite–clinopyroxene rock ("pseudolamprophyre") DH1321 is ultrabasic and highly magnesian (even more than melteigite). In a strong contrast to other mafic samples, it has ultrapotassic composition with K_2O/Na_2O approaching 4. The contents of numerous trace elements are similar to other highly mafic rocks, except for Sr, Zr, Hf, Th, U and LREE, which are the lowest in the whole dataset.

6. Isotopic composition (Sr–Nd)

The results of isotopic analyses are listed in Tab. 5. Isotopic data display subtle variations. The initial $^{143}Nd/^{144}Nd$ ratios, back-calculated for reference age of 30 Ma, display minimal differences (0.51268–0.51279). The initial $^{87}Sr/^{86}Sr$ ratios fall within a broader range between 0.70358 and 0.70487. The lowest value of $^{87}Sr/^{86}Sr$ (0.70358) was found for urtite (DR051B). The "wet" rock varieties tend to higher $^{87}Sr/^{86}Sr$ (>0.7042), whereby the sodalite monzosyenite has the highest ratio (0.70487).

Mafic phaneritic rocks isotopically correspond to the published Sr–Nd data for lavas of the DHVC. Felsic varieties of both phaneritic and aphanitic intrusions display greater scatter (Fig. 10), perhaps due to lack of isotopic data from equivalent felsic lavas.

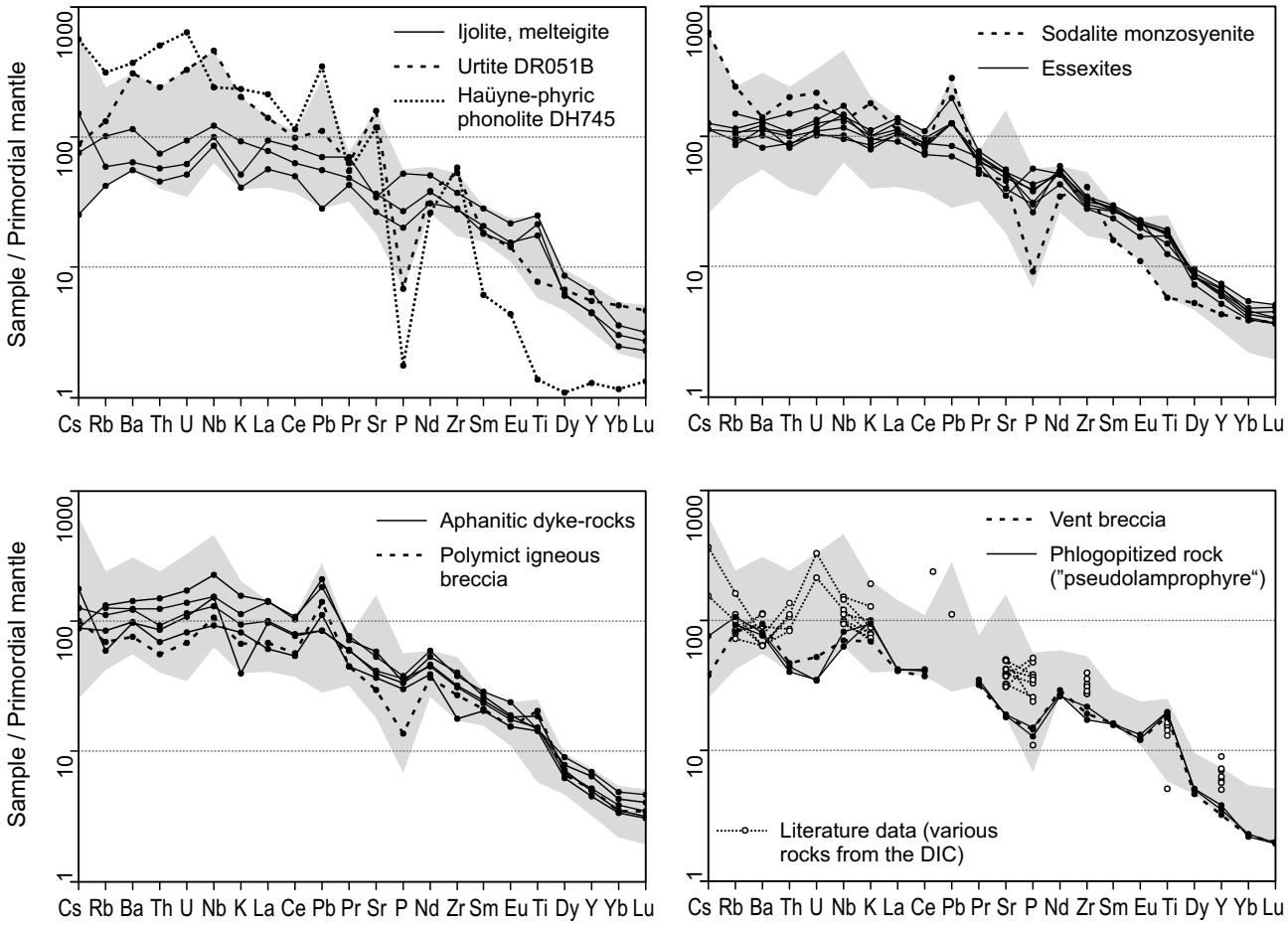

Fig. 9 Trace-element concentrations normalized to the composition of the primordial mantle (Sun and McDonough 1989). Grey field contains all samples but the evolved phonolite dyke DH745.

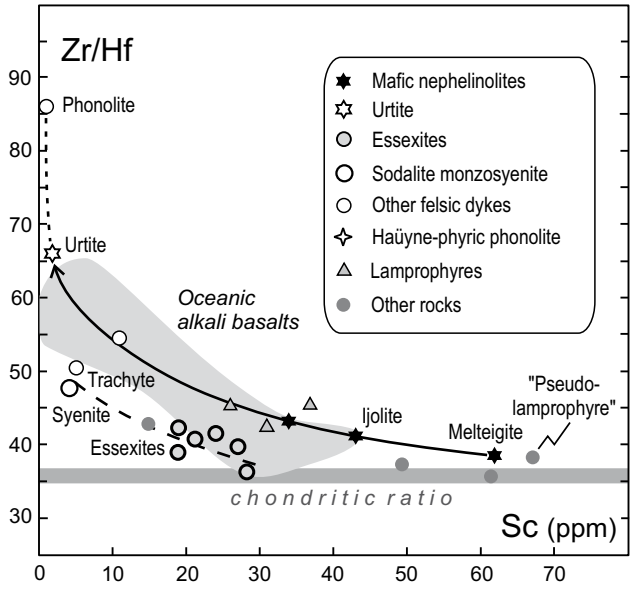

Fig. 10 Plot of Zr/Hf ratios against Sc contents in rocks from the Doupov Intrusive Complex. Shown is also field for oceanic alkali basalts *sensu lato* and their derivatives (grey) after David et al. (2000).

7. K–Ar geochronology

Three bulk samples of intrusive rocks (melteigite, essexite and sodalite syenite), one metasomatically reworked igneous rock ("pseudolamprophyre") and also phlogopite megacrysts separated from vent breccia on the eastern margin of the DIC were dated using the K–Ar method (Tab. 6).

All these five age determinations resulted in a very narrow time span from about 30.1 ± 1.1 to 28.0 ± 0.9 Ma and rank among the oldest published ages for the whole DHVC (cf. Ulrych et al. 2003; Rapprich and Holub 2008).

The new K–Ar ages are nearly identical within analytical errors and cannot reflect temporal relations between individual intrusive pulses. The sodalite monzosyenite (30.00 ± 0.94 Ma) is, in fact, geologically younger than essexite (27.96 ± 0.89 Ma), even though their K–Ar ages are statistically undistinguishable.

Tab. 5 Sr–Nd isotopic data for the studied alkaline intrusive rocks

Sample	DH1330	DR051B	TV52	TV54	DH1321	DH745
Rock type	Melteigite	Urtite	Essexite	Sodalite monzosyenite	Metasom. r. "Pseudolamprophyre"	Haüyne-phyric phonolite
$^{87}Sr/^{86}Sr$ (measured)	0.703823	0.703608	0.704384	0.705060	0.704241	0.703884
1 sigma	0.000066	0.000078	0.000068	0.000063	0.000082	0.000037
2 S(M)	0.000010	0.000015	0.000013	0.000009	0.000016	0.000010
$^{143}Nd/^{144}Nd$ (measured)	0.512793	0.512789	0.512729	0.512694	0.512811	0.512722
1 sigma	0.000045	0.000061	0.000040	0.000065	0.000052	0.000039
2 S(M)	0.000011	0.000011	0.000009	0.000019	0.000013	0.000008
$(^{87}Sr/^{86}Sr)_{30}$	0.703766	0.703577	0.704283	0.704866	0.704029	0.703787
$(^{143}Nd/^{144}Nd)_{30}$	0.512507	0.512565	0.512464	0.512469	0.512521	0.512609

$(^{87}Sr/^{86}Sr)_{30}$ and $(^{143}Nd/^{144}Nd)_{30}$ are initial ratios corrected to the mean age of 30 Ma
2 S(M) – two standard errors of the mean

Tab. 6 Results of K–Ar dating

Sample	DH1330	DI-3	TV54	DH1321	DH1364
Rock type	Melteigite	Essexite	Sodalite monzosyenite	"Pseudolamprophyre"	Vent breccia
Material	bulk-rock	bulk-rock	bulk-rock	mica	mica
K (%)	0.96	1.94	4.47	4.54	6.56
$^{40}Ar_{rad}$ (ccSTP/g)	1.092×10^{-6}	2.125×10^{-6}	5.254×10^{-6}	5.349×10^{-6}	7.472×10^{-6}
$^{40}Ar_{rad}$ (%)	51.5	70.8	76.0	49.8	73.3
K–Ar age (Ma)	29.03 ± 1.03	27.96 ± 0.89	30.00 ± 0.94	30.06 ± 1.09	29.07 ± 0.91

Ages are given at 1σ confidence level

8. Discussion

8.1. Comparison of the Doupov Intrusive Complex with other alkaline intrusive complexes associated with Cenozoic volcanic activity in the Bohemian Massif

8.1.1. České středohoří

Shallow subvolcanic intrusive bodies of essexite, rongstockite (*Ne*-normative clinopyroxene–biotite monzodiorite) and sodalite syenite compositions from several localities within the so-called Roztoky Intrusive Centre or "main volcanic centre of České středohoří" are well known (e.g., Hibsch 1899, 1902; Ulrych et al. 1983; Ulrych 1998; Ulrych and Balogh 2000). Except for numerous dyke rocks displaying broader scatter of K–Ar ages, the major intrusive bodies forming the so-called "Hypabyssal Weakly Alkaline Series" range from 33.1 to 28.2 Ma (Ulrych and Balogh 2000). Even though there is some non-systematic scatter, most of the data fall close to 30 Ma.

Despite the apparent parallelism in petrographic features of the essexitic and sodalite syenitic rocks in the two areas, some compositional differences do exist. The average composition of the Roztoky essexite is, e.g., higher in SiO_2 but lower in CaO and P_2O_5, whereas sodalite syenite is lower in SiO_2 but higher in CaO and P_2O_5 (see Ulrych 1998; Ulrych and Balogh 2000) compared to our analyses from Doupov. There is also a tendency towards lower K_2O/Na_2O in the intrusive rocks from the Roztoky Intrusive Centre.

Xenoliths of plutonic alkaline rocks (hornblendite to amphibole clinopyroxenite, nepheline syenite) and also products of various stages of fenitization were found in the vent breccia of Košťál near Košťálov at the S margin of the České středohoří (Kopecký 1966; Kopecký et al. 1970). Nephelinolites and larger bodies of clinopyroxenite *in situ* (except for small clinopyroxene-rich xenoliths) were not reported from the České středohoří area.

8.1.2. Loučná

Xenoliths up to 10 cm in size of phlogopite-bearing alkali clinopyroxenite and ijolite to urtite were described from the Loučná–Oberwiesenthal Volcanic Centre in the Krušné hory (Erzgebirge) Mts. (Ulrych et al. 2005). The locality is situated only 20 km NW of the Doupov Intrusive Complex. The results of K–Ar dating of various rocks from the complex vary significantly, ranging from

51 to 31.2 Ma (Pfeiffer et al. 1990) or 76.6 to 28.1 Ma (Ulrych et al. 2005), most likely due to problems with trapped excess argon. Perhaps the most reliable age determination for a pyroxenite xenolith and thus also the host nephelinite is 29.7 ± 1.2 Ma (phlogopite from a clinopyroxenite xenolith; Ulrych et al. 2005). Therefore, at least some of the coarse-grained xenoliths were roughly contemporaneous with members of the Doupov Intrusive Complex. However, in contrast to the geological position of phaneritic rocks from Doupov, clinopyroxenite to ijolite and urtite xenoliths from the Loučná–Oberwiesenthal Volcanic Centre are currently interpreted as being derived from a (layered) mafic alkaline complex underplating the Variscan felsic basement at the crust–mantle boundary (Ulrych et al. 2005) or which was situated within the deep crust (Ulrych et al. 2006).

Published and newly presented geochronological data thus lead to interestingly similar ages for all the three centres – Roztoky, Loučná and Doupov – containing phaneritic alkaline rocks of plutonic appearance. Compositionally variable intrusive rocks from Doupov can be considered as counterparts of both the Hypabyssal Weakly Alkaline Series *sensu* Ulrych and Balogh (2000) from České středohoří and the highly undersaturated plutonic rocks forming xenoliths in the Loučná Volcanic Centre.

8.2. Compositional relations between intrusive rocks and lavas of the DHVC

Essexitic and ijolitic rocks from the Doupov Intrusive Complex roughly correspond to basanites–tephrites and foidites, respectively (see, e.g., analyses of lavas in Shrbený 1982). Also the ranges of Sr and Nd isotopic compositions in intrusive rocks (except for Sr in syenite) are the same as those for "basaltic" lavas from the DHVC published by Vokurka (1997).

However, there is an apparent tendency towards a higher "Total Alkali" parameter in intrusive rocks from Doupov (Fig. 6). This is largely due to higher K_2O contents in the mafic intrusive rocks compared to compositionally similar lavas of the DHVC. This contrast can be explained by distinct mineral assemblages and their ability to fix potassium. Lavas containing glass and/or leucite are susceptible to low-temperature alterations involving exchange of alkalis with water and replacement of leucite by analcime; as a consequence, many lavas of the DHVC display a partial loss of K (cf. Rapprich 2003). Contrary to lavas, phaneritic intrusive rocks have K_2O fixed in amphiboles, biotite, K-bearing nepheline and K-feldspar. Their K_2O contents may thus reflect the original contents in the parental magmas better than in the lavas. Some phaneritic rocks, however, may represent cumulates and their composition does not have to correspond to that of the original magma. Moreover, the composition of intrusive rocks, namely those with "wet" mineralogy, may be affected by metasomatic processes leading to significant redistribution of elements. In the Doupov Intrusive Complex proper, we have to consider operation of potassic metasomatism, which is manifested by partial phlogopitization of clinopyroxene and some other minerals.

8.3. Constraints on the mantle sources for mafic magmas

The alkaline, undersaturated compositions and the incompatible trace-element patterns with high contents of HFSE (see the multielement normalization "spider" plots, Fig. 9) are in accord with the anorogenic, extensional (rift-related) intraplate setting of the Doupov intrusive rocks as well as the whole DHVC and also a number of other volcanic complexes and occurrences over Western and Central Europe (see, e.g., Wilson and Downes 1991, 2006; Lustrino and Wilson 2007).

The nature of the mantle sources can be evaluated from composition of the most primitive mafic igneous rocks. For instance, Lustrino and Wilson (2007) selected only analyses with MgO > 7 wt. %. These rocks are rare in the DIC and some of them are far from representing the original magma composition, being rather heterogeneous breccias, cumulitic or metasomatized rocks.

The most primitive mafic rocks in the DIC are highly mafic nephelinolites – melteigite (DH 1330) and ijolites (DH1329 and DR052). The latter sample is, however, "wet" with abundant mica and also geochemically different from the "dry" nephelinolites.

Mafic melts with various degrees of undersaturation can be theoretically derived from a homogeneous peridotitic source by various degrees of partial melting; such simple relationships between mafic magmas occurring even within a limited area are, however, seldom the case (Bogaard and Wörner 2003) and an origin in geochemically heterogeneous mantle sources must be taken into account.

Although mafic nephelinolites and essexites share many geochemical features, there are some subtle differences, e.g., in their Zr/Hf ratios (Fig. 11) and also in evolution of this parameter towards more fractionated rocks. There are two evolutionary trends, one involving the more undersaturated nephelinolites and their counterparts among dykes, the other consisting of essexites and relatively less undersaturated felsic rocks. Systematic differences also appear in some other elemental ratios, such as Ce/Pb, Nb/U (both being higher in nephelinolites) and Ba/Nb (higher in essexites), which apparently confirm some distinctness of the two rock varieties.

Dupuy et al. (1992) explained the increased Zr/Hf ratios in some undersaturated mafic lavas from oceanic

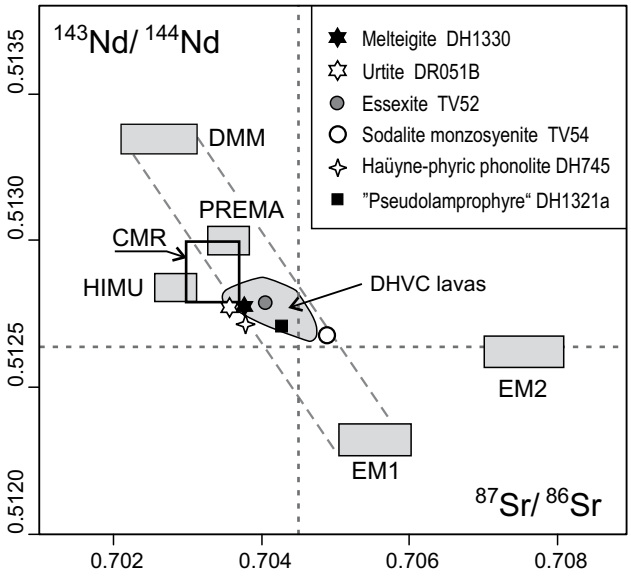

Fig. 11 Diagram of $^{143}Nd/^{144}Nd$ vs. $^{87}Sr/^{86}Sr$ in various rock types from the Doupov Intrusive Complex. Mantle components as defined by Zindler and Hart (1986): DMM – Depleted MORB Mantle; PREMA – Prevalent Mantle; HIMU – high μ ($^{238}U/^{204}Pb$) component of ocean island basalts; EM I – component of Enriched Mantle with a low Sm/Nd ratio leading to low $^{143}Nd/^{144}Nd$; EM II – component of Enriched Mantle with high Rb/Sr and $^{87}Sr/^{86}Sr$. Other abbreviations: CMR – Common Mantle Source (Lustrino and Wilson 2007); DHVC – field of published isotopic data for lavas from the Doupovské hory Volcanic Complex.

islands in terms of carbonatitic metasomatism in their mantle source. According to Fujinawa and Green (1997), these increased Zr/Hf ratios may reflect not only the mantle source metasomatically overprinted by interaction with carbonatite fluid, but also the presence of residual hornblende in the source domain. On the other hand, David et al. (2000) came to the conclusion that not the mantle heterogeneity, but a different extent of melting may be the major factor controlling the Zr/Hf variations in primitive magmas.

Isotopic data (Sr and Nd) for rocks of the DIC do not deviate from those published for lavas of the DHVC, České středohoří and other alkaline volcanic rocks of the Bohemian Massif. They appear as relatively primitive in the whole isotopic data scatter for mafic lavas of the anorogenic Central and West European Cenozoic igneous province (Lustrino and Wilson 2007). Nephelinolites from Doupov including the evolved urtite (DR051B) are isotopically very close to the European Asthenospheric Reservoir (EAR, Cebriá and Wilson 1995; Wilson and Downes 2006) or the Common Mantle Reservoir (CMR, Lustrino and Wilson 2007), representing a dominant, sub-lithospheric magma source region beneath the Central and Western European volcanic complexes (Fig. 10).

Isotopic composition of urtite is very similar to highly mafic melteigite DH1330. The $^{87}Sr/^{86}Sr$ ratio of the urtite is even the lowest among all the analysed samples. Therefore, the modification of urtite composition by contamination with continental crust was likely negligible. The highly undersaturated urtite can be interpreted as a fractionation product of the parental ijolitic magma.

The remaining samples have Sr isotopic compositions significantly more radiogenic. Such shift to higher $^{87}Sr/^{86}Sr$ ratios may imply contamination with more evolved crustal material. Increased Sr isotopic ratios (0.70443–0.70465) were documented from trachybasaltic lavas of the Upper Formation in the České středohoří Mts. and interpreted in terms of fractionation combined with crustal contamination (Cajz et al. 1999; Ulrych et al. 2002). On the other hand, as demonstrated by Downes (2001), the compositional extent of enriched domains within the European lithospheric mantle spans up to $^{87}Sr/^{86}Sr \sim 0.706$. This implies that even melts with such high values can simply be derived by partial melting of the local mantle source, without any assimilation of the crust. Therefore, the sole essexite sample displays a more apparent lithospheric signature in terms of its Sr isotopic ratio but its crustal contamination cannot be proved.

8.4. Petrogenetic relations between various phaneritic intrusive rocks in the Doupov Intrusive Complex

8.4.1. Mafic nephelinolite

Nephelinolites are the most undersaturated rocks of the Doupov Intrusive Complex. The "dry" varieties form a distinct group that probably evolved separately and can be evaluated independently from the "wet" rocks. The most primitive sample with *mg* ~ 62, Cr 278 ppm, Ni 100 ppm and Sc 62 ppm is melteigite DH1330. The composition of ijolite DH1329 is characterized by lower *mg* (53), Cr, Ni, and Sc (79, 60 and 43 ppm, respectively) and systematically higher contents of all the typically incompatible elements.

If there is a direct petrogenetic link between these two compositions, we can consider three possibilities: (1) melteigite was derived from the ijolite magma through accumulation of mafic phases, (2) both ijolite and melteigite originated by crystal accumulation from a common parental magma, and (3) ijolite represents a more evolved composition generated from the parental melteigite magma by crystal fractionation. This latter scenario is preferred and modelled in detail by Haloda et al. (this volume).

Going from melteigite DH1330 to ijolite DH1329, the drop in the Cr contents accompanied by a significant decrease in Ni and Sc are consistent with loss of ultramafic cumulates dominated by clinopyroxene but also containing some olivine at an early stage (see Haloda et al. this volume). The fractionation model can even per-

fectly explain the lower silica content in ijolite compared with melteigite, as the crystal extract has SiO_2 higher than the parental magma composition (see also the Total Alkali – Silica plot, Fig. 6). There are, however, some discrepancies in P_2O_5 (being too high in ijolite) and in the enrichment factors of various strongly incompatible elements (e.g., LREE are enriched in the ijolite sample systematically more than K, Rb, Ba, Th and U). Cobalt with nearly the same contents in both melteigite and ijolite is also rather problematic; when we consider the high olivine/melt partition coefficient for Co (e.g., Lemarchand et al. 1987), mildly incompatible behaviour of Co in the clinopyroxene/liquid equilibrium is required. The distribution of Cs is quite erratic and cannot be modelled by crystal fractionation.

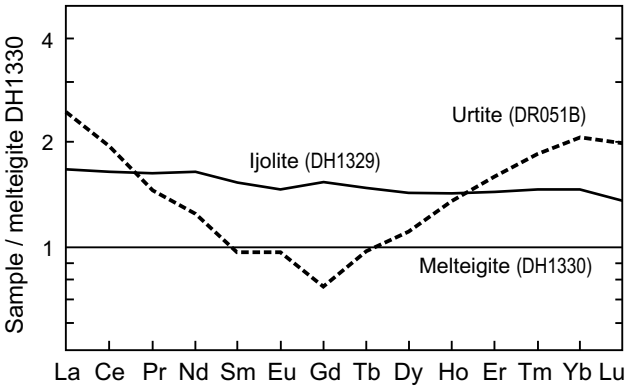

Fig. 12 Abundances of rare-earth elements in ijolite and urtite normalized by concentrations in melteigite DH1330. The convex-down curve of urtite is explained by fractionation of titanite.

8.4.2. Urtite

Urtite is a highly undersaturated felsic rock type and could seldom be petrogenetically linked with the much less undersaturated rocks of the Doupov Intrusive Complex. Therefore, we propose derivation of urtite from a more mafic and highly undersaturated magma of ijolitic or melteigitic composition. However, the geochemical features of urtite correspond to a highly evolved melt and the compositional gap between ijolite and urtite or melteigite is too large for quantitative modelling of fractional crystallization.

When we compare the compositions of urtite and melteigite, the enrichment factors of incompatible elements (concentration in urtite/concentration in melteigite) are very variable. The highest value (6.43) is displayed by uranium, which can be considered to be an "almost perfectly" incompatible element during fractionation. Uranium is closely followed by Sr (5.95), Ba (5.58), Nb (5.46) Th (5.28), and Ta (4.91). Urtite is also highly enriched in Na (5.16) and K (4.94) but less enriched in Cs (3.5) and Rb (3.1). Even lower enrichment factors are typical of Zr (1.90) and Hf (only 1.11). Both LREE and HREE are moderately enriched whereas the middle rare earth elements (MREE) are depleted in urtite compared to melteigite.

The highly superchondritic Zr/Hf ratio combined with very low Sc content in urtite (Fig. 11) argue for strong fractionation of clinopyroxene in the same manner as in alkaline basaltic magmas from oceanic islands (see David et al. 2000). This is caused by the significantly higher partition coefficient for Hf than for Zr in clinopyroxene (e.g., Lemarchand et al. 1987; Hart and Dunn 1993). The effect could be further enhanced by co-precipitation of titanite and magnetite.

Urtite displays a weak tendency towards a convex-down curve of chondrite-normalized REE concentrations in Fig. 8. This feature is enhanced and much more obvious in Fig. 12, where normalization with the most primitive melteigite is employed. Here it is apparent that the origin of the convex-down curve for ijolite requires fractionation of some mineral with strong preference for the middle rare-earth elements (MREE). Green and Pearson (1986) and Lemarchand et al. (1987) have shown that the convex-down partitioning pattern with strong favouring of the middle rare earths (MREE) is typical of titanite. Moreover, titanite strongly favours Ta and its fractionation will increase Nb/Ta ratio in the melt (Tiepolo et al. 2002). An increase in Nb/Ta is also observable in urtite. As titanite in variable amounts and relatively large, well-shaped crystals is typically present in our rocks, we consider its significant role in the relatively late stages of the fractionation process to be proven.

The increase in the silica content towards urtite cannot be explained by fractionation of clinopyroxene alone and the effect of titanite is insufficient due to its limited quantity. Therefore, fractionation of the mineral phases with low or negligible SiO_2 is required. The most important candidate is magnetite, which was definitely accompanied by a limited amount of apatite, as the only explanation for the obvious decrease in P_2O_5.

Evolution of melteigite magma represented by DH1330 to the composition of urtite DR051B through fractionation of the above-mentioned anhydrous minerals cannot explain the variations in K, Rb and Cs. Either phlogopite/biotite concentrating Rb and Cs played a subordinate role or these three elements were partially redistributed in a fluid phase.

The strongly undersaturated dyke of phonolite DH745 representing the only sample of peralkaline chemistry is also isotopically close to phaneritic nephelinolites. It can be considered to be an extremely evolved composition (the *mg* value is only about 10) derived by prolonged fractional crystallization from a nephelinolitic parental magma to similar to that for the urtite. Its very high Zr/Hf, very strongly convex-down REE pattern and greatly

increased Nb/Ta ratio argue for advanced clinopyroxene and titanite fractionation during a late evolutionary stage of felsic alkaline magma. The subtle decrease in Al_2O_3 and the origin of the weakly peralkaline character may be due to late fractionation of haüyne.

8.4.3. Essexite

Essexites are typically "wet" and their most mafic samples have MgO ~ 6 wt.%. Their low *mg* values (< 48.5) as well as low Cr and Ni are far from values typical of primary melts equilibrated with the mantle sources and indicate significantly more evolved composition compared to mafic nephelinolites. Essexites are less undersaturated than nephelinolites and it is highly probable that also their parental mafic magmas shared this feature. The relatively low Ni and *mg* values in essexites as a group argue for prior separation of olivine-rich cumulates, which would be left within a deeper magma chamber or at the walls of deep channels for magma ascent. The chemical changes from the most to least mafic varieties of essexites may be attributed to the fractionation of clinopyroxene accompanied by some titanite, magnetite, and apatite. However, the existence of considerable scatter in elemental abundances and ratios is inconsistent with a simple evolutionary trend common for all the analysed varieties of essexitic rocks.

8.4.4. Sodalite monzosyenite

In contrast to urtite, which is similarly evolved in terms of low *mg* values and contents of compatible elements, sodalite monzosyenite is much less undersaturated. Moreover, it is poorer in some incompatible elements, namely Ba, Sr, Nb, and Zr but richer in some others, especially Rb. Moreover, the rock displays a weak negative Eu-anomaly. Such geochemical features are interpreted in terms of a different parental magma (weakly undersaturated) and fractionation of feldspars as well as mafic minerals.

Although there is some geochemical affinity to the group of essexitic rocks, a true genetic relationship can hardly be established. Syenite is definitely intrusive into essexites at the present erosion level and the possible existence of a common parental magma at depth is obscured by younger processes. The isotopic composition of the sodalite monzosyenite TV54 is significantly shifted away from the CMR field towards the magmas of dominantly lithospheric sources or contaminated by crustal material (Fig. 10). As such a composition has no counterpart among more mafic rocks from the whole DHVC (including essexite TV52), this shift may be ascribed to limited contamination by the (upper) continental crust.

Small volumes of sodalite syenite forming thin dykes and veinlets in mafic and ultramafic rocks may have locally evolved from dykes of sodalite monzodiorite. Insufficient data are currently available for these rocks.

8.4.5. Clinopyroxenite and clinopyroxenite breccia

Due to their extreme composition and by analogy with many other alkaline complexes over the world, clinopyroxenites may be considered to be ultramafic cumulates derived from mafic alkaline magmas. Their textural features argue for accumulation of magnetite, apatite and phlogopite in addition to the highly dominant clinopyroxene.

Clinopyroxenites in the Doupov Intrusive Complex could be genetically linked to both the ijolitic and essexitic parental magmas. A genetic link with foidite and basanite–tephrite lavas is also possible. However, such a small and very shallow intrusive complex can hardly be interpreted as a magma chamber in which crystal fractionation processes could have operated effectively.

Another possibility is origin of clinopyroxenite cumulates within a long-lasting deeper magma chamber or a system of feeding channels, with subsequent explosive destruction of cumulates and quick transport of clinopyroxenite fragments and hot fluids as a fluidized system up to the present position. Some petrographic and geological features of clinopyroxenites are consistent with this idea, especially:

- extensive brecciation of clinopyroxenites,
- very frequent presence of abundant microcracks within individual clinopyroxene grains,
- strong deformation of large phlogopite flakes (cumulus mica) present in some samples,
- relative temporal relations – where geological relationships are observable, clinopyroxenites behave as the oldest member of the complex (namely in the DB-2 drill core) and are intruded by sodalite (monzo-) diorite to sodalite syenite,
- widespread evidence that these rocks were invaded by very hot fluids and melts shortly after but perhaps even during their emplacement.

8.5. Presence of carbonatite intrusion beneath Flurbühl: fact or fiction?

Kopecký (e.g., 1987, 1987–1988, 2010; Kopecký et al. 1970) took great pains to demonstrate the presence of carbonatites in České středohoří Mts. Kopecký (1988) expressed his belief that carbonatite intrusions are also present below the Loučná and Doupov volcanic centres.

The DHVC was not found to contain any rock type that could be considered to be carbonatite. Therefore, we can discuss the problem only from these two viewpoints: (1) silicate rock association of the Doupov Intrusive Complex, and (2) record of metasomatic processes that could be eventually ascribed to carbonatite.

8.5.1. Rock association

The clinopyroxenite–foid syenite, melteigite–ijolite–urtite and also essexite–foid syenite are rock assemblages that are very frequently associated with intrusive carbonatites (Wooley 2003; Wooley and Kjarsgaard 2008). The clinopyroxenite breccias are "classic" counterparts of many carbonatite intrusions of variable ages and in various parts of the world including, e.g., the Palaeozoic Kola carbonatite province of Baltica. Felsic alkaline rocks in carbonatite–silicate rock associations are either peralkaline nephelinolites and foid syenites including strongly agpaitic nepheline syenites, or metaluminous including miaskitic nepheline syenites and monzosyenites. Therefore, the fact that alkaline rocks from the DIC are metaluminous (apart from the dyke of the extremely fractionated sodalite phonolite DH745 with agpaitic chemistry) is not contradictory to potential presence of carbonatite.

8.5.2. Metasomatism

Carbonatite intrusions are typically accompanied by metasomatic aureoles of fenitized country rocks. Fenitization represents a variable, typically polyphase processes of alkali metasomatism progressively removing silica and producing alkali feldspars, commonly also alkali amphibole or aegirine, and occasionally nepheline; the overall character of fenitization may be sodic or potassic (Le Bas 2008 and references therein).

Potassic fenitization is commonly interpreted as being related with shallow carbonatite intrusions (see, e.g., Heinrich 1966; Gittins et al. 1975; Le Bas 2008). Zones of potassic fenitization are also frequently associated with brecciation (Le Bas 2008). The presence of carbonate minerals in metasomatic rocks is not necessary and many typical fenites highly dominated by alkali feldspar (albite or K-feldspar) do not contain any.

Kopecký (1988) mentioned finding a xenolith of carbonatized syenite fenite with relics of quartz replaced by carbonate in the DP-3 borehole. According to its character, such a xenolith could represent fenitized basement rock or clastic sediment from underneath the DHVC. However, no sample is available and no detailed documentation of the xenolith and its host-rock petrography has been published. No other fenitized xenolith has been identified among a number of basement xenoliths studied in the past decade.

The products of alkali metasomatic overprint on the alkaline igneous rocks are currently observable in the Doupov Intrusive Complex. Even though typical sodic metasomatism leading to albitization or the origin of Na-rich mafic minerals is definitely lacking at the present erosion level of the DIC, phlogopitization associated with brecciation of clinopyroxenites and some other rocks argues for the action of K-rich metasomatic fluids. This typically potassic metasomatism was pervasive; however, thin sections from the DB-2 drill-core document that it later changed to more channelized invasion of fluids producing essentially sodalite minerals accompanied by K-feldspar and minor apatite. The latter process closely preceded intrusions of innumerable veinlets of sodalite syenite and dykes of monzodiorite to sodalite monzosyenite.

An extreme result of strong pervasive phlogopitization is represented by the "pseudolamprophyre" that is spatially associated with olivine ijolite at the eastern margin of the DIC. Chemically, this "pseudolamprophyre" (DH1321) is similar to melteigite except for being even more mafic and particularly much higher in K but low in Na. Incompatible trace elements also display a very similar pattern with consistently lower contents in "pseudolamprophyre". Rubidium and Cs, which are enriched similarly to K, and also Ba, which is enriched much less than K, are the sole exceptions.

Although much less common than typical fenitization, extensive phlogopitization has been reported from many localities around the world for carbonatites that came into contact with highly mafic and ultramafic rocks (Heinrich 1966, 1970; Gittins et al. 1975; Le Bas 2008, and many others). Gittins et al. (1975) considered phlogopitization of pyroxenites to be a special type of fenitization.

Sodalite is not a very common and important mineral in fenites, although such cases do rarely exist, e.g. around ferrocarbonatite at Swartbooisdrif in Namibia (Thompson et al. 2002; Drüppel et al. 2005). However, those sodalite-rich fenites have albite as the major mineral and the whole metasomatic alteration is typically sodic.

Pervasive phlogopitization together with the freshness of the phlogopite without any secondary alterations and the abundance of sodalite minerals in the DIC are noteworthy. The almost total absence of typical low-temperature minerals in phaneritic rocks including clinopyroxenite and heterogeneous breccias is a very interesting feature of the whole complex. The only exceptions are disseminated secondary carbonates partially replacing early sodalite minerals at the margins of the sodalite monzodiorite dykes and sodalite syenite veinlets, and also the presence of accessory epidote at the contacts, or in the close proximity, of these veins. Therefore, we assume that the fluids responsible for the origin of secondary phlogopite were high-temperature and of rather special composition.

Hot fluids responsible for metasomatism at Doupov might not necessarily be related to any hidden carbonatite intrusion. Metasomatic, frequently potassic aureoles are also known around highly alkaline intrusions of ijolitic composition. The ijolitic-type fluids have relatively low XCO_2, high activities of alkalis, SiO_2 and Al_2O_3, and low activity of CaO (Morogan 1994), the characteristics compatible with origin of phlogopite in mafic rocks.

Ultimate resolution of the "carbonatite problem" in Doupov is, however, hardly possible without new drill hole(s) reaching significantly greater depths than those from the late sixties of the last century.

9. Conclusions

1. Phaneritic intrusive rocks from Doupov are more variable than those from the České středohoří Volcanic Complex. In addition to essexites, sodalite-bearing monzodiorites and sodalite monzosyenites with "wet" mineral assemblages, the Doupov Intrusive Complex also includes clinopyroxenites and highly undersaturated nephelinolites ranging from olivine melteigite to ijolite to rare urtite, predominantly with "dry" mineral assemblages.
2. As the phaneritic intrusive rocks (~ 30 Ma) are older than the overlying lava sequences, the Doupov Intrusive Complex provides proof for the polyphase evolution of the whole Doupovské hory Volcanic Complex.
3. The geochemical and isotopic data suggest that the less undersaturated "wet" essexitic rocks and the more undersaturated nephelinolites (melteigite–ijolite–urtite) with predominantly "dry" mineralogy evolved independently and their parental mafic magmas were derived from distinct mantle sources.
4. The melteigite–ijolite–urtite group is isotopically close to the "European Asthenospheric Reservoir" or the "Common Mantle Source".
5. Less undersaturated rocks display more pronounced lithospheric mantle source fingerprints. The sodalite monzosyenite may be also contaminated by rocks of the continental crust.
6. Fractional crystallization of both mafic groups was dominated by clinopyroxene with an increasing role of titanite and also apatite in the late stages. In contrast to sodalite syenite, the evolved urtite composition displays no indication of feldspar fractionation.
7. Clinopyroxenites may represent cumulates from both ijolitic and essexitic mafic magmas. Brecciation of clinopyroxenites and deformation of both clinopyroxene and phlogopite may be due to explosive release of hot magmatic fluids from an evolving deeper magma reservoir. Clinopyroxenite fragments were transported to a very shallow level and breccias were invaded by metasomatizing hot fluids and residual melts.
8. Some features of the Doupov Intrusive Centre (widespread brecciation, locally strong phlogopitization) are not contradictory to the former hypothesis assuming the presence of a carbonatite intrusion at depth, beneath the alkaline silicate intrusions. However, the source of metasomatizing fluids could have been the ijolitic magmas themselves.

Acknowledgements.This research was financially supported by the Grant Agency of the Academy of Sciences of the Czech Republic (Project No. IAA300130612 "Combined magnetostratigraphic studies of Cenozoic volcanics, Bohemian Massif"), the Ministry of Education, Youth and Sports of the Czech Republic (Research Plan No. MSM0021620855, Faculty of Science, Charles University in Prague), and the Ministry of the Environment of the Czech Republic (Research Plan MZP0002579801, Czech Geological Survey). The K–Ar analytical works were partly supported by the Hungarian National Scientific Foundation (OTKA No. K68153). P. Hradecký (Czech Geological Survey) is acknowledged for providing old thin sections from Flurbühl. We are greatly indebted to two anonymous reviewers for their constructive criticism that helped us to considerably improve the manuscript. The text also profited from a language check by M. Štulíková and the editorial work of V. Janoušek.

Electronic supplementary material. The GPS coordinates and a map of the sampling sites, mineral composition data for clinopyroxene, hornblende and biotite from the intrusive rocks, and a table documenting accuracy of the whole-rock analyses are available online at the Journal web site *(http://dx.doi.org/10.3190/jgeosci.074)*.

References

Balogh K (1985) K/Ar Dating of Neogene Volcanic Activity in Hungary: Experimental Technique, Experiences and Methods of Chronologic Studies. ATOMKI Rep., D/1: 277–288

Bauer F (1903) Petrographische Untersuchung des Duppauer Theralithvorkommens. Zts Krist Mineral Petrogr 22: 266–296

Becke F (1900) Vorläufige Mitteilung über die Auffindung von Theralith am Flurhübl bei Duppau. Verh K–kön geol Reichanst 13/14: 351–353

Bogaard PJF, Wörner G (2003) Petrogenesis of basanitic to tholeiitic volcanic rocks from the Miocene Vogelsberg, Central Germany. J Petrol 44: 569–602

Boynton WV (1984) Cosmochemistry of the rare earth elements: meteorite studies. In: Henderson P (ed) Rare Earth

Element Geochemistry. Developments in Geochemistry. Elsevier, Amsterdam–New York, pp 63–114

Cajz V, Vokurka K, Balogh K, Lang M, Ulrych J (1999) The České středohoří Mts.: volcanostratigraphy and geochemistry. Geolines 9: 21–28

Cajz V, Rapprich V, Radoň M (2006) Volcanics on the periphery of the Doupovské hory Mts. – a volcanological study of the Dětaň paleontological site. Zpr geol Výzk v R 2005: 13–16

Cebrià JM, Wilson M (1995) Cenozoic mafic magmatism in Western/Central Europe: a common European asthenospheric reservoir. Terra Nova Abstract Suppl 7: 162

David K, Schiano P, Allègre CJ (2000) Assessment of the Zr/Hf fractionation in oceanic basalts and continental materials during petrogenetic processes. Earth Planet Sci Lett 178: 285–301

Dèzes P, Schmid SM, Ziegler PA (2004) Evolution of the European Cenozoic Rift System: interaction of the Alpine and Pyrenean orogens with their foreland lithosphere. Tectonophysics 389: 1–33

Downes H (2001) Formation and modification of the shallow sub-continental lithospheric mantle: a review of geochemical evidence from ultramafic xenolith suites and tectonically emplaced ultramafic massifs of Western and Central Europe. J Petrol 42: 233–250

Drüppel K, Hoefs J, Okrusch M (2005) Fenitizing processes induced by ferrocarbonatite magmatism at Swartbooisdrif, NW Namibia. J Petrol 46: 377–406

Dupuy C, Liotard JM, Dostal J (1992) Zr/Hf fractionation in intraplate basaltic rocks: Carbonate metasomatism in the mantle source. Geochim Cosmochim Acta 56: 2411–2423

Fejfar O, Kaiser TM (2005) Insect bone-modification and paleoecology of Oligocene mammal-bearing sites in the Doupov Mountains, northwestern Bohemia. Palaeon Electron 8.1.8A: 1–11, *http://palaeo-electronica.org/2005_1/fejfar8/fejfar8.pdf*

Fujinawa A, Green TH (1997) Partitioning behaviour of Hf and Zr between amphibole, clinopyroxene, garnet and silicate melts at high pressure. Eur J Mineral 9: 379–391

Gittins J, Allen CR, Cooper AF (1975) Phlogopitization of pyroxenite; its bearing on the composition of carbonatite magmas. Geol Mag 112: 503–507

Green TH, Pearson NJ (1986) Rare-earth element partitioning between sphene and coexisting silicate liquid at high pressure and temperature. Chem Geol 55: 105–119

Haloda J, Rapprich V. Holub FV, Halodová P, Vaculovič T (2010) Crystallization history of ijolitic rocks from the Doupovské hory Volcanic Complex (Oligocene, Czech Republic). J Geosci 55: 279–297

Hart SR, Dunn T (1993) Experimental Cpx/melt partitioning of 24 trace elements. Contrib Mineral Petrol 113: 1–8

Heinrich EWM (1966) The Geology of Carbonatite. Rand McNally & Co, Chicago, pp 1–555

Heinrich EWM (1970) The Palabora carbonatitic complex; a unique copper deposit. Canad Mineral 10: 585–598

Hibsch JE (1899) Geologische Karte des Böhmischen Mittelgebirges, Blatt II (Rongstock – Bodenbach). Alfred Hölder, Wien, pp 1–101

Hibsch JE (1902) Über Sodalithaugitsyenit im Böhmischen Mittelgebirge und über die Beziehungen zwischen diesem Gestein und dem Essexit. Tschermaks Mineral Petrogr Mitt 21: 157–170

Hradecký P (1997) The Doupov Mountains. In: Vrána S, Štědrá V (eds) Geological Model of Western Bohemia Related to the KTB Borehole in Germany. Sbor geol Věd, Geol 47: 125–127

Janoušek V, Farrow CM, Erban V (2006) Interpretation of whole-rock geochemical data in igneous geochemistry: introducing Geochemical Data Toolkit (GCDkit). J Petrol 47: 1255–1259

Keller J (1981) Carbonatitic volcanism in the Kaiserstuhl alkaline complex: evidence for highly fluid carbonatitic melts at the Earth's surface. J Volcanol Geotherm Res 9: 423–431

Kopecký L (1966) The find of fenites and alkaline rocks in the České středohoří Mts. Věst Ústř Úst geol 41: 121–124 (in Czech, English abstract)

Kopecký L (1987) The Roztoky pseudotrachyte caldera in the České středohoří Mts., Czechoslovakia. In Kopecký L (ed) Proceedings of the First Seminar on Carbonatites and Alkaline Rocks of the Bohemian Massif and Ambient Regions. Geological Survey, Prague, pp 119–156

Kopecký L (1987–88) Young volcanism of the Bohemian Massif. Geol Hydrometal Uranu, 11(3): 30–67; 11(4): 3–44; 12(1): 3–40; 12(2): 3–56; 12(3): 3–40; 12(4): 3–40 (in Czech)

Kopecký L (1988) Young volcanism of the Bohemian Massif, Part 3. Geol Hydrometal Uranu 12(3): 3–40 (in Czech)

Kopecký L (2010) České Středohoří Mts. and Ambient Young Alkaline Volcanic Complexes in the Ohře Rift, Czech Republic: Volcanology, Petrology and Rift Evolution. Czech Geological Survey, Prague, pp 1–188

Kopecký L, Dobeš M, Fiala J, Šťovíčková N (1970) Fenites of the Bohemian Massif and the relations between fenitization, alkaline volcanism and deep fault tectonics. Sbor geol Věd, Geol 16: 51–112

Le Bas MJ (2008) Fenites associated with carbonatites. Canad Mineral 46: 915–932

Le Maitre RW (ed), Streckeisen A, Zanettin B, Le Bas MJ, Bonin B, Bateman P, Bellieni G, Dudek A, Efremova S, Keller J, Lameyre J, Sabine PA, Schmid R, Sørensen H, Wooley AR (2002) Igneous Rocks. A Classification and Glossary of Terms. Recommendations of the International Union of Geological Sciences Subcommission on the Systematics of Igneous Rocks. 2nd Edition, Cambridge University Press, Cambridge–New York, pp 1–193

Lemarchand F, Villemant B, Calas G (1987) Trace element distribution coefficients in alkaline series. Geochim Cosmochim Acta 51: 1071–1081

Lustrino M, Wilson M (2007) The circum-Mediterranean anorogenic Cenozoic igneous province. Earth Sci Rev 81: 1–65

Míková J, Denková P (2007) Modified chromatographic separation scheme for Sr and Nd isotope analysis in geological silicate samples. J Geosci 52: 221–226

Mlčoch B (2003) Character of the contact between the Saxothuringian and Teplá–Barrandian Unit. Geolines 16: 75

Mlčoch B (2006) Ultrabasic rocks of the basement below the Tertiary volcanites of the Doupovské hory Mts. Zpr geol výzk v R 2005: 25–26 (in Czech)

Mlčoch B, Konopásek J (2010) Pre-Late Carboniferous geology along the contact of the Saxothuringian and Teplá–Barrandian zones in the area covered by younger sediments and volcanics (western Bohemian Massif, Czech Republic). J Geosci 55: 81–94

Morogan V (1994) Ijolite versus carbonatite as sources of fenitization. Terra Nova 6: 166–176

Odin GS (1982) Numerical Dating in Stratigraphy. John Wiley and Sons, New York, pp 1–1040

Pfeiffer L, Wenzel T, Eckstein L (1990) Neue Alterswerte vom Oberwiesenthaler Eruptivstock im Westerzgebirge und ihre geologischen Konsequenzen. Freiberg Forsch H C 441: 115–119

Rapprich V (2003) Analcimized leucites and Ti-phlogopite from Doupovské hory Mts. Zpr geol Výzk v R 2002: 180–181 (in Czech, English abstract)

Rapprich V (2005) Compositional variation of clinopyroxenes of basaltic, essexitic and tephriphonolitic rocks from the Doupovské hory Volcanic Complex, NW Bohemia. J Czech Geol Soc 50: 119–132

Rapprich V, Holub FV (2008) Geochemical variations within the Upper Oligocene–Lower Miocene lava succession of Úhošť Hill (NE margin of Doupovské hory Mts., Czech Republic). Geol Quart 52: 253–268

Shrbený O (1982) Chemistry of alkaline volcanic rocks of the Doupovské hory Mts., Bohemia. Čas Mineral Geol 27: 139–158

Steiger RH, Jäger E (1977) Subcommission on Geochronology: convention on the use of decay constants in geo- and cosmochronology. Earth Planet Sci Lett 36: 359–362

Sun SS, McDonough WF (1989) Chemical and isotopic systematics of oceanic basalts; implications for mantle composition and processes. In: Saunders AD, Norry MJ (eds) Magmatism in the Ocean Basins. Geological Society of London Special Publications 42: 313–345

Šantrůček P, Bůžek Č, Kopecký L, Malecha A, Václ J (1967) Tertiary Basins and Young Volcanics of the Bohemian Massif. International Geological Congress, XXIII Session Prague 1968, Guide to Excursion 13 AC, pp 1–53

Thompson RN, Smith PM, Gibson SA, Mattey DP, Dickin AP (2002) Ankerite carbonatite from Swartbooisdrif, Namibia: the first evidence for magmatic ferrocarbonatite. Contrib Mineral Petrol 143: 377–395

Tiepolo M, Oberti R, Vannucci R (2002) Trace-element incorporation in titanite: constraints from experimentally determined solid/liquid partition coefficients. Chem Geol 191: 105–119

Ulrych J (1998) Geochemistry of subvolcanic alkaline rock series of the Roztoky Intrusive Centre, České středohoří Mts., Bohemia. Erlanger Beitr Petr Min 8: 1–42

Ulrych J, Balogh K (2000) Roztoky Intrusive Centre in the České středohoří Mts.: differentiation, emplacement, distribution, orientation and age of dyke series. Geol Carpath 51: 383–397

Ulrych J, Pivec E, Fiala J, Lang M (1983) Petrology of the alkaline subvolcanic rocks from the Roztoky area (České středohoří Mts.). Rozpravy ČSAV, Ř mat přír Věd 93 (8): 1–85

Ulrych J, Svobodová J, Balogh K (2002) The source of Cenozoic volcanism in the České středohoří Mts., Bohemian Massif. Neu Jb Mineral, Abh 177: 133–162

Ulrych J, Lloyd FE, Balogh K (2003) Age relations and geochemical constraints of Cenozoic alkaline volcanic series in W Bohemia: a review. Geolines 15: 168–180

Ulrych J, Lloyd F E, Balogh K, Hegner E, Langrová A, Lang M, Novák J K, Řanda Z (2005) Petrogenesis of alkali pyroxenite and ijolite xenoliths from the Tertiary Loučná–Oberwiesenthal Volcanic Centre, Bohemian Massif in the light of new mineralogical, geochemical, and isotopic data. Neu Jb Mineral, Abh 182: 57–79

Ulrych J, Nižňanský D, Pertlik F, Giester G, Ertl A, Brandstätter F (2006) Clinopyroxene from an alkali pyroxenite xenolith, Loučná–Oberwiesenthal Volcanic Centre, Bohemian Massif: crystal chemistry and structure. Geol Quart 50: 257–264

Vokurka K (1997) Neodymium and strontium isotopes of basalts from the Doupovské hory Mts. (Bohemia). J Czech Geol Soc 42: 17

Wiesbaur JB (1901) Theralith im Duppauer Gebirge. Lotos 21: 62–71

Wilson M, Downes H (1991) Tertiary–Quaternary extension-related alkaline magmatism in Western and Central Europe. J Petrol 32: 811–849

Wilson M, Downes H (2006) Tertiary–Quaternary intraplate magmatism in Europe and its relationship to mantle dynamics. In: Gee DG, Stephenson RA (eds) European Lithosphere Dynamics. Geological Society London Memoirs 32: 147–166

Wimmenauer W (1974) The alkaline province of Central Europe and France. In: Sørensen H (ed) The Alkaline Rocks. Wiley, London, pp 238–271

Wooley AR (2003) Igneous silicate rocks associated with carbonatites: their diversity, relative abundances, and implications for carbonatite petrogenesis. Periodico Mineral 72: 9–17

Wooley AR, Kjarsgaard BA (2008) Paragenetic types of carbonatite as indicated by the diversity and relative abundances of associated silicate rocks: evidence from a global database. Canad Mineral 46: 741–752

Zartner WR (1938) Geologie des Duppauer Gebirges. I. Nördliche Hälfte. Abh Dtsch Akad Wiss Kunste, mat–naturwiss Abt 2: 1–132

Zindler A, Hart SR (1986) Chemical geodynamics. Ann Rev Earth Planet Sci 14: 493–571

Journal of Geosciences, 55 (2010), 279–297 DOI: 10.3190/jgeosci.076

Original paper

Crystallization history of Oligocene ijolitic rocks from the Doupovské hory Volcanic Complex (Czech Republic)

Jakub HALODA[1*], Vladislav RAPPRICH[1], František V. HOLUB[2], Patricie HALODOVÁ[1], Tomáš VACULOVIČ[3]

[1] *Czech Geological Survey, Klárov 3, 118 21 Prague 1, Czech Republic; jakub.haloda@geology.cz*
[2] *Institute of Petrology and Structural Geology, Faculty of Science, Charles University, Albertov 6, 128 43 Prague 2, Czech Republic*
[3] *Institute of Chemistry, Faculty of Science, Masaryk University, Kotlářská 2, 611 37 Brno, Czech Republic*
[*] *Corresponding author*

Ijolitic rocks of the Flurbühl Composite Intrusion rank to the most primitive intrusive rocks found within the Doupovské hory Volcanic Complex. Studies of mineral chemistry together with crystallization modelling of melteigite and ijolite brought new information about the evolution of ijolitic magmas and their ascent. Crystallization modelling affirms the absence of accumulated minerals and confirms that the recalculated major-element bulk-rock analyses reflect the compositions of their original parental magmas accurately. Melteigite developed by early equilibrium crystallization under pressure of approximately 4 kbar (estimated minimum cooling rate is ~0.02 °C/hr) and subsequent fractional crystallization under much lower pressure (~0.2 kbar). Ijolite originated by fractional crystallization of a slightly more evolved magma batch under lower pressures probably at the final emplacement level. The results of crystallization modelling and estimates of REE contents in parental melts suggest a close genetic relationship between both rock suites. The olivine-bearing melteigite was postulated as a possible parental magma composition for derivation of the olivine-free ijolite.

Keywords: Nephelinolite, melteigite, ijolite, crystallization modelling, fractional crystallization, Doupovské hory Mts.
Received: 16 April 2010; accepted: 19 September 2010; handling editor: D. Dolejš

1. Introduction

High-level intrusions are rather common in mafic alkaline volcanic complexes. However, they are mostly hidden and even where they crop out thanks to advanced erosion of the volcanic edifices, their original features are frequently obscured by alteration processes. Therefore, detailed research and models of magmatic evolution in such intrusions are rather scarce.

We have investigated intrusive rocks from the central part of the Doupovské hory Volcanic Complex (the Flurbühl Composite Intrusion) that provide the possibility to study the sub-surface magmatic processes related to formation and evolution of the still preserved superficial volcanic complex. The petrology and bulk-rock chemistry of the entire subvolcanic suite with two observed differentiation trends is described by Holub et al. (this volume). From the whole association of alkaline rocks we selected for detailed examination of mineral chemistry and crystallization history the very fresh ijolitic rocks with nearly anhydrous mineral assemblages.

The major aims of this contribution are to unravel the crystallization history of these intrusive rocks rich in mafic minerals, to evaluate a possible role of mafic mineral accumulation in the genesis of the melteigite, and to decipher its relationship to ijolites with lower abundances of the mafic phases.

2. Geological setting

The Doupovské hory Volcanic Complex (DHVC) occupies the western part of the northeast-southwest-trending Eger (Ohře) Graben (EG) in northwestern Bohemia (Czech Republic; Fig. 1). The EG belongs to the system of Cenozoic rifts in central and western Europe (European Cenozoic Rift System *sensu* Dèzes et al. 2004 – ECRIS). The EG follows the older Variscan suture between the Saxothuringian and Teplá–Barrandian domains (Babuška et al. 2010; Mlčoch and Konopásek 2010) in the northwestern part of the Bohemian Massif. It is interpreted as an incipient rift structure formed during two distinct phases of extension (Rajchl et al. 2009). The first phase lasted from the late Eocene until the early Miocene. It was characterised by the NNE–SSW to N–S oriented horizontal extension, oblique to the rift axis. The palaeostress field of the oblique extension most probably reflected lithospheric doming due to thermal perturbation of the lithosphere (Dèzes et al. 2004), which resulted also in extensive OIB-like magmatism within the EG. The later, orthogonal extensional phase is explained by stretching along the crest of a growing regional-scale anticlinal feature, which supports the recent hypothesis of the lithospheric folding in the Alpine–Carpathian foreland (Dèzes et al. 2004; Bourgeois et al. 2007; Rajchl et al. 2009).

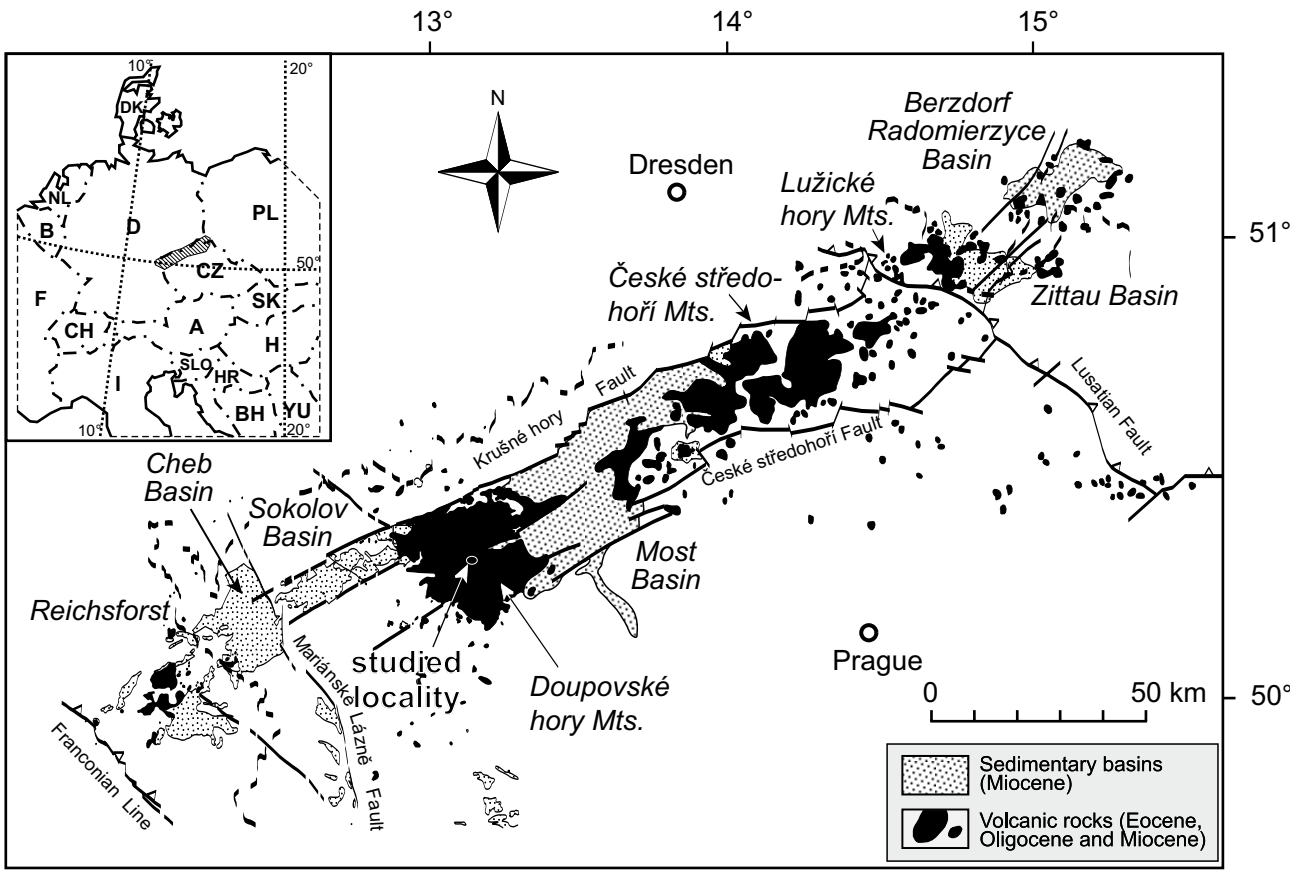

Fig. 1 Location of the Doupovské hory Volcanic Complex and the Flurbühl Composite Intrusion.

The volcanic activity of the DHVC started in the earliest Oligocene (mammal zone MP-21; Fejfar and Kaiser 2005) and lasted until the early Miocene (Rapprich and Holub 2008). The Flurbühl body, which also includes the studied ijolites, intruded into the early DHVC volcanic edifice at about 29–30 Ma (Holub et al. this volume).

The setting and composition of the DHVC are similar to many other Cenozoic intra-plate volcanic complexes of central and western Europe (The Circum-Mediterranean Anorogenic Cenozoic Igneous Province *sensu* Lustrino and Wilson 2007 – CiMACI). The DHVC is dominated by mafic alkaline lavas corresponding to (olivine-) foidites, basanites, tephrites and picrobasalts to alkali basalts. Moderately differentiated rocks (trachybasalts to trachyandesites) are subordinate and phonolitic rocks occur only scarcely, mostly in the form of NW–SE trending dykes (Skácelová et al. 2009). Subvolcanic rocks building up the Flurbühl body (Wiesbaur 1901) are represented by clinopyroxenites, various nephelinolites (melteigite to ijolite with rare urtite), essexite, sodalite monzodiorite to monzosyenite and sodalite syenite (Holub et al. this volume).

Most of the mafic volcanic and intrusive rocks are depleted in compatible elements (Cr, Ni) suggesting that these rocks already experienced significant crystal fractionation. The most mafic rocks with the highest mg# values and compatible element contents are picrobasalts. However, abundance of large olivine and clinopyroxene phenocrysts (exceeding 1 cm) together with positive correlation between SiO_2 and MgO point to a semi-cumulate origin of these rocks (Rapprich and Holub 2008).

Among intrusive rocks of the Flurbühl body, the most mafic, apart from the extremely heterogeneous clinopyroxenite breccias, are ijolitic rocks, namely the olivine-bearing melteigite (melanephelinolite). Though these rocks are present at the current surface only as loose blocks, local road construction works temporarily exposed two types of these primitive alkaline intrusive rocks at the eastern margin of the Flurbühl Intrusion. The first type, olivine-bearing melteigite, is described in Holub et al. (this volume) as samples DH1330 and DH1319A. The second type, olivine-free ijolite, is represented by their sample DH1329.

3. Methods

3.1. Scanning electron microscopy and microanalysis

Two polished thin sections (21×34 mm and 20×38 mm) from an olivine-bearing melteigite and one (24×38 mm)

from an olivine-free ijolite were prepared. Textural and mineralogical characteristics were studied using a LEICA DMLP petrographic microscope.

Backscattered electron (BSE) images and elemental X-ray intensity maps were produced using a CamScan 3200 scanning electron microscope fitted with an Oxford Instruments Energy Dispersive Spectral unit at the Czech Geological Survey in Prague. The elemental X-ray maps were generated using an accelerating voltage of 20 kV and 25 nA beam current. Mineral modes were determined using the Area Measurement software (Oxford Instruments) and digital processing of BSE images and elemental X-ray maps.

Mineral compositions were acquired using quantitative X-ray wavelength dispersive spectral analysis on an MICROSPEC 3PC X-ray wavelength dispersive system on a CamScan 3200 scanning electron microscope at the Czech Geological Survey. The analyses were performed using an accelerating voltage of 15 kV, 20 nA beam current, 1 μm beam size and ZAF correction procedures. The counting times were 20 or 30 s for all analyzed elements. To avoid Na volatilization during the analysis of nepheline and sanidine, the beam diameter was defocused to 5 μm. A combination of natural and synthetic standards was used for calibration. Relative uncertainties are calculated to be less than 1 % at the >10 wt. % level, <12 % at the ~1 wt. % level and >20 % at the <0.5 wt. % level.

3.2. Electron backscattered diffraction

Crystallographic orientations of olivine were determined by electron backscattered diffraction (EBSD). The thin sections used for EBSD applications were prepared by the process of chemo-mechanical polishing using colloidal silica suspension. The crystallographic orientation data were obtained from automatically indexed EBSD patterns collected by a HKL Technology Nordlys II EBSD system (Schmidt and Olensen 1989) on a CamScan 3200 scanning electron microscope at the Czech Geological Survey. Analytical conditions were 33 mm working distance, 20 kV accelerating voltage and 5.0 nA beam current. Obtained EBSD patterns were indexed by using the CHANNEL 5 software from HKL Technology.

3.3. Laser ablation ICP-MS

The concentrations of selected trace elements (including REE) in clinopyroxene and olivine phenocrysts were analysed by mass spectrometer with inductively coupled plasma equipped with laser ablation (LA-ICP-MS) hosted at the Institute of Chemistry, Masaryk University in Brno. Instrumentation for LA-ICP-MS consists of a laser ablation system UP 213 (New Wave, USA) and an ICP-MS spectrometer Agilent 7500 CE (Agilent, Japan). A commercial Q-switched Nd:YAG laser ablation device works at the 5th harmonic frequency which corresponds to the wavelength of 213 nm. The ablation device is equipped with programmable XYZ-stages to move the sample along a programmed trajectory during ablation. Target visual inspection as well as photographic documentation is accomplished by means of a built-in microscope/CCD-camera system. A sample was enclosed in the SuperCell (New Wave, USA) and was ablated by the laser beam, which was focused onto the sample surface through a quartz window. The ablation cell was flushed with helium (carrier gas), which transported the laser-induced aerosol to the inductively coupled plasma. A sample gas flow of argon was admixed to the helium carrier gas flow behind the laser ablation cell to achieve the total gas flow of 1.6 l/min.

For LA-ICP-MS measurements, a hole drilling mode (fixed sample position during laser ablation) was used for 60 s at each spot. Laser ablation was performed with a laser spot diameter 65 μm, laser fluence 5.0 J cm^{-2} and repetition rate 10 Hz. The NIST612 glass standard (Hollocher and Ruiz 1995) was used for calibration purposes.

4. Results

4.1. Petrography and mineral chemistry

4.1.1. Melteigite

The studied melteigite (olivine-bearing melanephelinolite; samples DH1330 and DH1319A) has a coarse-grained porphyritic magmatic texture consisting mainly of clinopyroxene (63 vol. %), olivine (4 vol. %), Ti-rich magnetite (5 vol. %), nepheline (18 vol. %) and sanidine (7 vol. %) (Fig. 2). Accessory minerals include apatite (0.9 vol. %), ilmenite (1 vol. %), rare chromite, titanite (< 0.1 vol. %), Mg-biotite (1 vol. %), analcime, and rare calcite. The distribution of silicate minerals is relatively homogeneous.

Olivine. Olivine in the melteigite forms euhedral to subhedral phenocrysts (1.8–4.0 mm, typically > 2.5 mm) with equant shapes. The olivine grains show normal symmetric zoning with Mg-rich cores and less magnesian rims (Fig. 2c). The early-formed olivines often have inclusions of chromite or crystallized melt inclusions consisting of fine-grained clinopyroxene, nepheline, Ti-rich magnetite, ilmenite and apatite.

Electron microprobe data of 48 olivine spot analyses were collected to obtain the true range of Fo component ($Fo_{85.5–72.3}$). Representative compositions of olivine are listed in Tab. 1. Variation of Fo component within select-

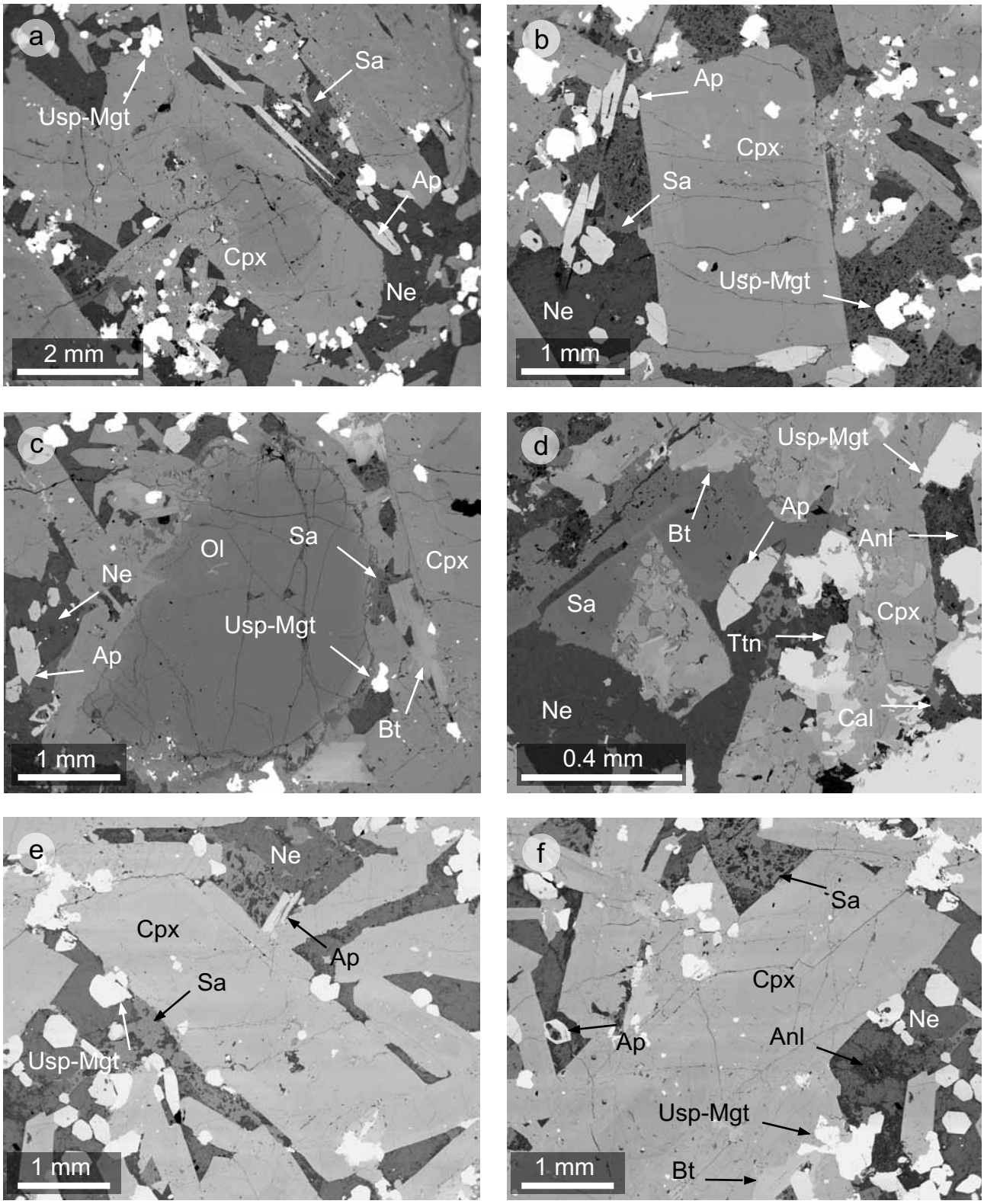

Fig. 2 Back-scattered electron images illustrating the texture and mineralogy of the studied samples. **Melteigite: a–b** – Coarse-grained magmatic texture with zoned pyroxene phenocrysts; **c** – Detailed view of a large zoned olivine phenocryst; **d** – Detailed view of late-stage mineral association. **Ijolite: e** – Coarse-grained magmatic texture with clinopyroxene phenocryst; **f** – Detail of a large zoned clinopyroxene phenocryst. Mineral abbreviations after Kretz (1983).

Tab. 1 Representative electron microprobe analyses (wt. %) and crystallochemical formulae of representative rock-forming minerals

	melteigite							ijolite				
Phase	Olivine (core)	Olivine (rim)	Mg-rich clinopyroxene (core)	Ca–Fe–Al–Ti-rich clinopyroxene (mantle)	Ca–Mg-rich clinopyroxene (rim)	Titanomagnetite	Ilmenite	Mg-rich clinopyroxene (core)	Ca–Fe–Al–Ti-rich clinopyroxene (mantle)	Ca–Mg-rich clinopyroxene (rim)	Titanomagnetite	Ilmenite
SiO_2	39.86	38.11	51.71	44.11	47.51	0.32	bd	50.43	44.75	45.34	1.95	0.35
TiO_2	0.03	0.03	1.15	4.68	3.36	17.79	51.48	1.77	4.47	4.27	20.52	54.90
Al_2O_3	0.06	0.05	3.75	9.37	6.63	5.89	0.12	3.71	8.33	7.85	1.01	0.22
Cr_2O_3	0.01	0.01	0.86	0.03	0.20	0.41	bd	0.42	0.12	0.10	0.15	bd
Fe_2O_3	nd	nd	0.08	1.28	0.16	29.18	nd	0.58	1.44	1.77	23.67	nd
MgO	45.16	37.89	15.41	11.23	12.13	5.12	2.07	14.80	11.27	11.75	0.13	8.88
CaO	0.37	0.36	22.63	23.57	23.46	bd	bd	24.12	23.74	23.61	bd	0.29
MnO	0.24	0.60	0.09	0.06	0.08	0.77	1.81	0.03	0.05	0.08	0.67	1.19
FeO	13.94	22.75	4.13	5.52	6.25	40.33	44.12	4.18	5.70	5.02	52.10	34.14
Na_2O	nd	nd	0.25	0.25	0.40	nd	nd	0.09	0.27	0.38	nd	nd
NiO	0.12	0.08	nd	nd	nd	nd	nd	nd	nd	nd	nd	nd
Total	99.79	99.88	100.06	100.10	100.17	99.81	99.60	100.13	100.14	100.18	100.19	99.98
Oxygen basis	4	4	6	6	6	4	3	6	6	6	4	3
Si	0.999	0.998	1.893	1.652	1.772	0.011	–	1.859	1.678	1.695	0.072	0.008
Ti	0.001	0.001	0.032	0.132	0.094	0.473	0.970	0.049	0.126	0.120	0.573	0.977
Al	0.002	0.002	0.162	0.414	0.291	0.245	0.004	0.161	0.368	0.346	0.044	0.006
Cr	0.000	0.000	0.025	0.001	0.001	0.011	–	0.012	0.004	0.003	0.004	–
Fe^{3+}	–	–	0.002	0.036	0.004	0.776	–	0.016	0.041	0.050	0.663	–
Mg	1.689	1.479	0.841	0.627	0.674	0.269	0.077	0.813	0.630	0.654	0.007	0.313
Ca	0.010	0.010	0.888	0.946	0.937	–	–	0.953	0.954	0.945	–	0.008
Mn	0.005	0.013	0.003	0.002	0.002	0.023	0.028	0.001	0.002	0.003	0.021	0.024
Fe^{2+}	0.292	0.498	0.126	0.173	0.195	1.191	0.924	0.129	0.179	0.157	1.617	0.676
Na	–	–	0.018	0.019	0.029	–	–	0.005	0.018	0.029	–	–
Ni	0.002	0.002	–	–	–	–	–	–	–	–	–	–
Total	3.000	3.003	3.990	4.001	4.000	3.000	2.004	3.999	3.998	4.001	3.002	2.012
Fo (%)	85.0	74.2										
En (%)			45.3	35.2	37.2			42.6	34.9	36.2		
Wo (%)			47.8	53.1	51.8			49.9	52.9	52.3		

nd = not determined, bd = below detection limit

ed single olivine grain was also investigated along two orthogonal profiles (see section 4.3 for more discussion). A BSE image of the measured olivine grain is shown in Fig. 3a and variation of Fo component within this grain is plotted in Fig. 3b–c.

Concentrations of CaO vary from 0.29 to 0.42 wt. %, TiO_2 is less than 0.03 wt. %, Cr_2O_3 is below 0.01 wt. % and the MnO range is 0.11–0.60 wt.%.

Clinopyroxene. Clinopyroxene is the most abundant mineral phase, occurring mainly as euhedral, elongated phenocrysts (3–7.5 mm) and also as finer later crystallized euhedral and subhedral grains (Fig. 2a–b). All clinopyroxenes are characterized by remarkable symmetric chemical zoning. Clinopyroxenes contain inclusions of common Ti-rich magnetite, as well as of rare chromite and apatite.

The chemical composition of clinopyroxene shows strong variations in terms of Mg, Fe, Si, Al and Ti contents (Fig. 4). Representative analyses of the main compositional types of clinopyroxene are listed in Tab. 1. Two representative orthogonal chemical profiles across one selected clinopyroxene phenocryst are shown in Fig. 4. Characteristic zoning of the earliest formed clinopyroxene phenocrysts is represented by Mg-rich diopsidic cores with very homogeneous compositions (En_{45}, Wo_{48}), mantles enriched in Ca, Fe, Al and Ti ($En_{35–40}$, $Wo_{50–53}$) and rims enriched in Ca and Mg ($En_{35–37}$, $Wo_{53–52}$). The core-to-mantle enrichment in Ca, Fe, Al and Ti of clinopyroxene grains is not continuous. This feature reflects a discontinuity in the chemical composition between Mg-rich diopside and Al–Ti-rich diopside (Fig. 4). The majority of clinopyroxene phenocrysts, and all clinopyroxene grains that crystallized later, have the composition of Ca–Fe–Al–Ti-rich diopside and do not contain Mg-enriched diopsidic cores. The wollastonite content of the Ca–Fe–Al–Ti-rich diopside is generally higher than 50 mol. % due to extreme enrichment in non-quadrilateral components (Al and Ti in Ca-Tschermak's molecules – e.g., Rapprich 2005) and such diopside shows depletion in Si.

The chemical composition of Mg-rich diopsidic clinopyroxene cores can be used for estimation of pressure at the time of their initial crystallization from the parental magma. We employed the method of Nimis (2007) based on element occupation of clinopyroxene structural positions. It yielded approximately 4 kbar for the early crystallized Mg-rich cores of larger clinopyroxene crystals and also for Mg-rich clinopyroxene inclusions in olivine. This estimation can be interpreted as the prevailing pressure during initial clinopyroxene crystallization from the parental melt in a relatively deep-seated magma chamber.

Ti-rich magnetite. Ti-rich magnetite in the melteigite occurs as euhedral and subhedral grains (100–500 μm), commonly with exsolved ilmenite. Representative compositions of Ti-rich magnetite, ulvöspinel and exsolved ilmenite are given in Tab. 1. Early crystallized cores have ulvöspinel compositions typically of Mgt_{35} Usp_{65}.

4.1.2. Ijolite

The ijolite has a coarse-grained porphyritic magmatic texture similar to that of the melteigite (Fig. 2e–f) and is dominated by clinopyroxene (58 vol. %) but free of olivine. Other rock-forming minerals are Ti-rich magnetite (4 vol. %), nepheline (24 vol. %), sanidine (8 vol. %) and apatite (1.5 vol. %). Accessory minerals include Mg-rich biotite (3 vol. %), ilmenite (1 vol. %), titanite (< 0.1 vol. %), analcime and rare calcite. Similarly to the melteigite, the ijolite is homogeneous at the thin-section scale.

Clinopyroxene. Clinopyroxene is the most abundant phase occurring mainly as euhedral, elongated phenocrysts (3.5–7 mm) (Fig. 2e–f) and also as smaller later crystallized euhedral and subhedral grains. All clinopyroxenes possess characteristic symmetric chemical zoning with significant sector zoning (hourglass structure).

The chemical composition of ijolite clinopyroxenes varies widely in terms of Mg, Fe, Si, Al, and Ti contents (Fig. 5). However these are much smaller than the compositional variations of the melteigite clinopyroxene (Fig. 4). Representative compositions of the main types of clinopyroxene are listed in Tab. 1. Two representative orthogonal chemical profiles across one selected clinopyroxene phenocryst are shown in Fig. 5. The characteristic zoning of the clinopyroxene phenocrysts is represented by Mg-enriched, homogeneous diopsidic cores ($En_{43–41}$, $Wo_{50–51}$), mantles rich in Ca, Fe, Al and Ti ($En_{40–35}$, $Wo_{51–53}$) and Ca–Mg-rich rims ($En_{36–37}$, $Wo_{52–51}$). All ijolite clinopyroxenes are richer in Ca, Fe, Al, and Ti than those in the melteigite.

Ti-rich magnetite. Ti-rich magnetite in ijolite occurs as euhedral and subhedral grains (80–500 μm), commonly with exsolved ilmenite. Representative compositions of Ti-rich magnetite, ulvöspinel and exsolved ilmenite are listed in Tab. 1. Early crystallized cores have ulvöspinel compositions typically of $Mgt_{32}Usp_{68}$.

4.2. Crystallization modelling

4.2.1. Melteigite

For crystallization modelling we used whole-rock analyses by Holub et al. (in this volume). These were recalculated on the basis of total FeO, whereby the proportion of Fe_2O_3 was adjusted to the oxygen fugacity value used for the modelling (Tab. 2). Roeder and Emslie (1970) showed that the distribution coefficient K_d for partitioning of iron and magnesium between olivine and a co-existing liquid

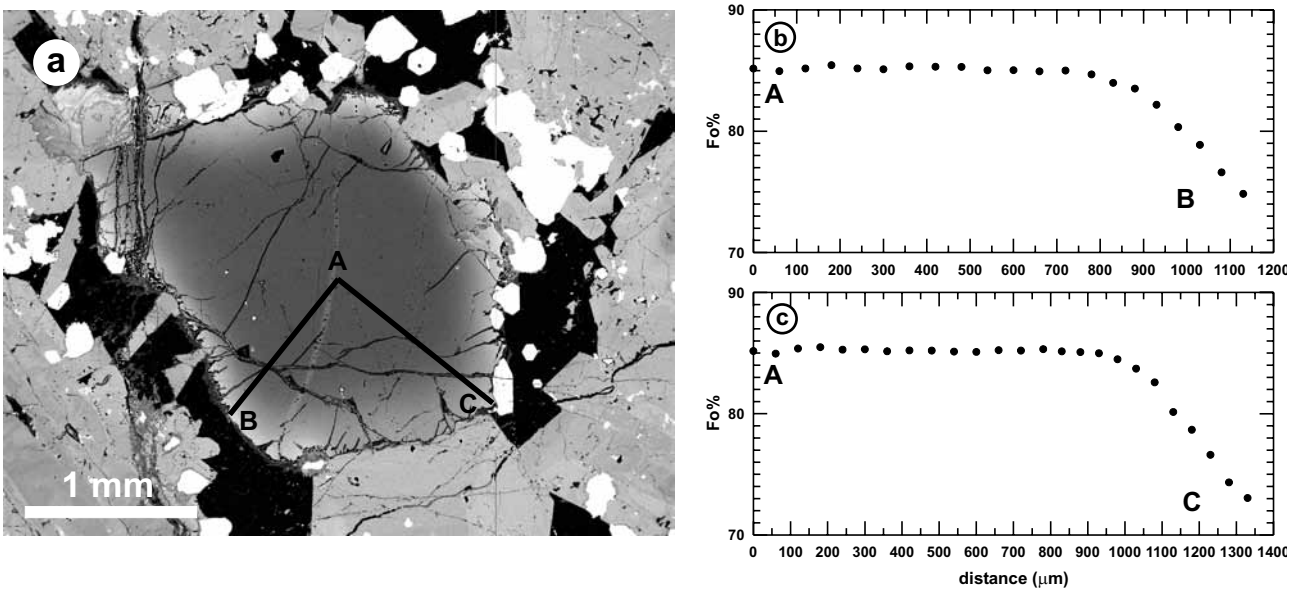

Fig. 3a Back-scattered electron image of single olivine grain from melteigite with lines indicating two orthogonal profiles chosen for investigation of the chemical zoning; **b–c** – Plots of Fo content variations along these profiles A–B and A–C.

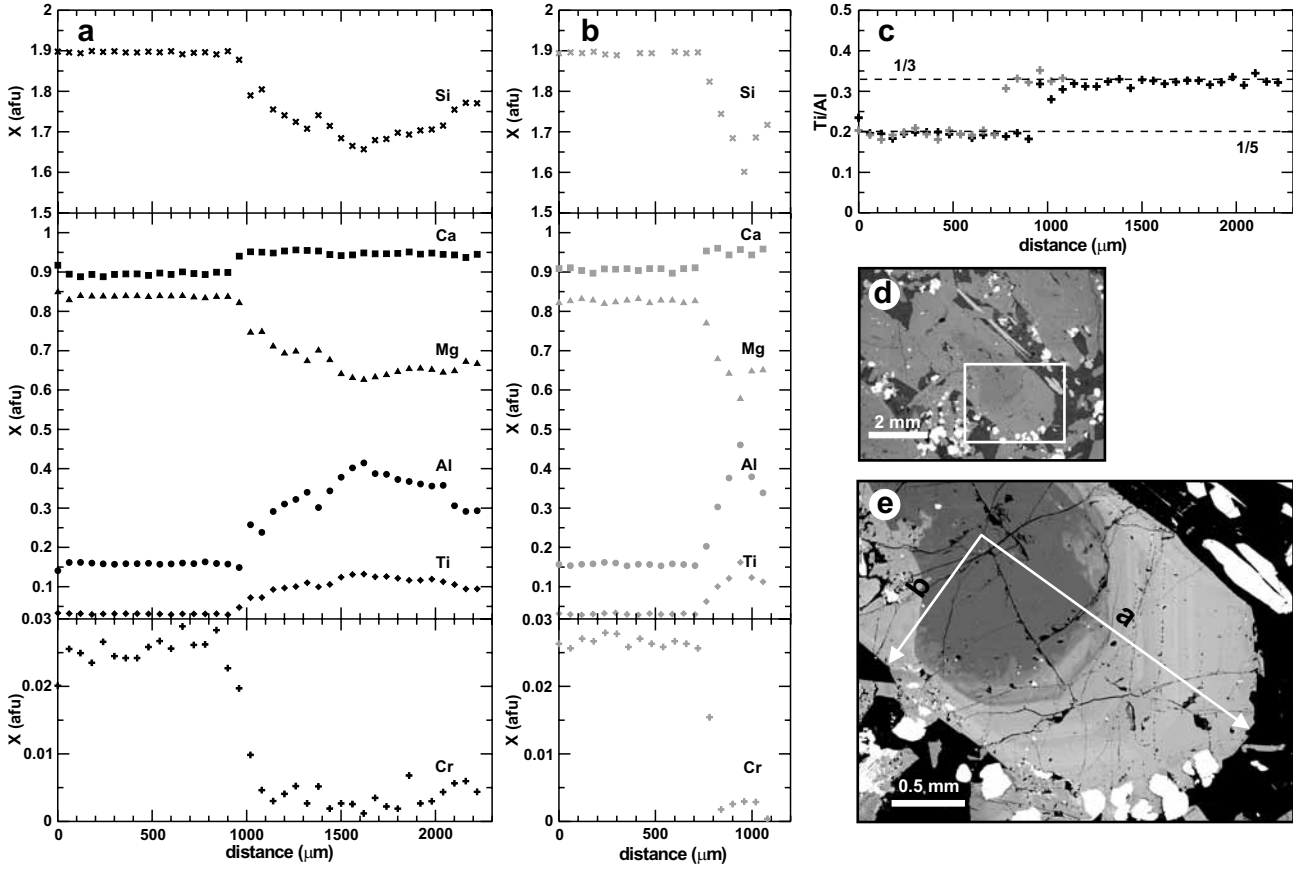

Fig. 4a–b Chemical variation of clinopyroxene from melteigite along two orthogonal profiles (see Figs 4d–e for their location) showing the changes in chemical composition during crystallization; **c** – Ti/Al ratio values (black crosses – profile a, gray crosses – profile b); **d–e** – Back-scattered electron images of analysed clinopyroxene phenocryst with lines indicating the location of the two profiles.

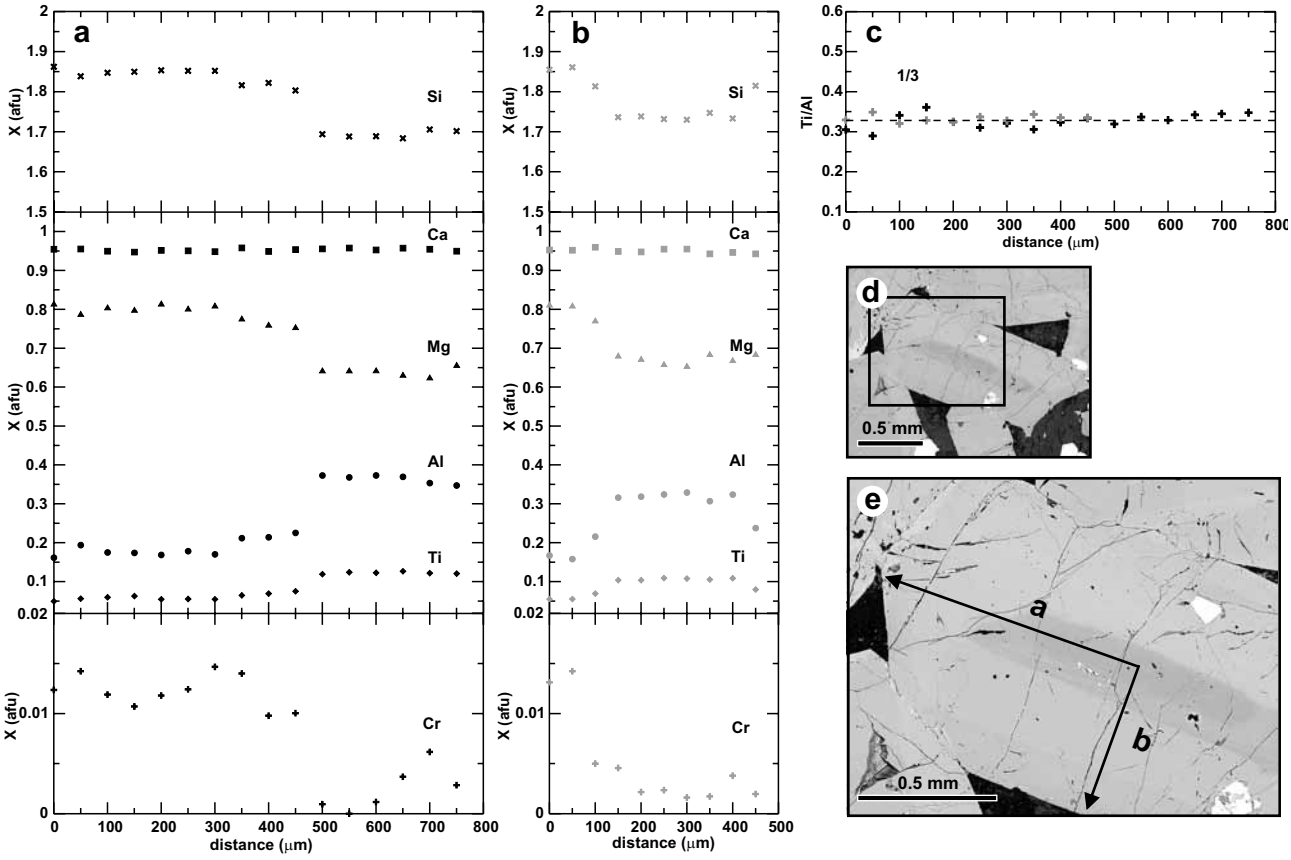

Fig. 5a–b Chemical variation of clinopyroxene from ijolite along two orthogonal profiles (see Figs 5d–e for their location) showing the changes in chemical composition during crystallization; **c** – Ti/Al ratio values (black crosses – profile a, gray crosses – profile b); **d–e** – Back-scattered electron images of analysed clinopyroxene phenocryst with lines indicating the location of the two profiles.

is relatively insensitive to temperature, melt composition and oxygen fugacity, with a value of 0.3 ± 0.03. For calculation of the Fo_{eq} content of olivine in equilibrium with bulk-rock mg# the equation described by Roeder and Emslie (1970) was used.

The Fo_{eq} content of olivine in melteigite with the recalculated bulk-rock mg# of 64.7 was calculated to be $Fo_{eq,86}$ (Tab. 2). This Fo_{eq} value is in good agreement with the highest measured Fo content in olivine ($Fo_{85.5}$) of this rock and supports the assumption that this mineral does not have a cumulate origin. Therefore, we used the recalculated melteigite major-element bulk-rock composition for crystallization sequence modelling using the PELE software (Boudreau 1999) based on the algorithms and database of Ghiorso (1985) and Ghiorso and Sack (1994).

The modelling started with calculated liquidus temperature of 1233 °C, pressure of 4 kbar, determined from clinopyroxene core compositions (see above), and an oxygen fugacity one log unit below the quartz–fayalite–magnetite (QFM) buffer. This oxygen fugacity value was determined according to the method of Buddington and Lindsley (1964). For the change of fO_2 with temperature the model of Kress and Carmichael (1988) was used. Since the mineral assemblage is essentially anhydrous, we consider the melt to be relatively H_2O-poor, hence H_2O was neglected in our calculations. The predicted crystallization sequence for equilibrium and fractional crystallization was compared with analysed chemical compositions of minerals. Thereafter, a final model of crystallization was computed in two steps. The first invoked early equilibrium crystallization of olivine and clinopyroxene cores, having simulated the presence of equilibrated Mg-rich cores of early-crystallized olivines and clinopyroxenes. The second step included fractional crystallization of residual liquid under a pressure of 0.2 kbar (assumed for the intrusion emplacement). The results of this crystallization model are shown in Fig. 6a–b.

4.2.2 Ijolite

As in the case of the melteigite, the recalculated bulk-rock composition (Tab. 2) was used for crystallization modelling of ijolite. However, the early-crystallized olivine is not present in this rock. Therefore we used the

Tab. 2. Bulk-rock compositions used for crystallization modelling

	real bulk-rock compositions†		modelled bulk-rock compositions‡	
	melteigite	ijolite	melteigite	ijolite
wt. %				
SiO_2	40.74	38.05	41.38	39.16
TiO_2	4.63	5.45	4.70	5.61
Cr_2O_3	0.06	0.01	0.06	0.01
Al_2O_3	9.57	10.71	9.72	11.02
Fe_2O_3	5.97	6.69	1.35	1.67
FeO	6.62	6.85	10.92	11.73
MnO	0.18	0.20	0.18	0.21
MgO	11.06	8.28	11.23	8.52
CaO	16.74	16.43	17.00	16.91
Na_2O	1.47	1.60	1.49	1.65
K_2O	1.24	1.57	1.26	1.62
P_2O_5	0.44	1.15	0.45	1.18
F	0.13	0.18	0.13	0.18
CO_2	0.10	0.50	0.10	0.51
S	0.02	0.02	0.02	0.02
LOI	0.77	1.53	–	–
Total	99.73	99.22	100.00	100.00
mg#	62.2	53.4	64.7	56.4
K_d	–	–	0.3	–
Fo_{eq}	–	–	85.9	–
$T_{Ol–liq}$ (°C)	–	–	1 232	–
$(En, Wo)_{mod}$	–	–	–	43.0, 49.8
$T_{Cpx–liq}$ (°C)	–	–	–	1 123
$\log fO_2$	–	–	–11	–11

† Published analyses of Holub et al. (this volume). Melteigite: sample DH1330, ijolite: sample DH1329.

‡ Recalculated bulk-rock compositions used for modelling

PELE software to calculate the chemical composition of the first clinopyroxene that could have crystallized from the modelled magma composition. The predicted clinopyroxene composition is En_{43}, Wo_{50} (Tab. 2) and the highest Mg-value measured from clinopyroxene core composition is $En_{43.1}$, $Wo_{49.5}$. This agreement was fundamental for crystallization modelling and suggests that the first clinopyroxene crystallized from the liquid was in equilibrium with the parental magma and that clinopyroxenes having this composition are not of cumulate origin.

The ijolite crystallization modelling started with calculated liquidus temperature of 1 123 °C, pressure of 0.2 kbar (assumed emplacement pressure) and oxygen fugacity equivalent to one log unit below the quartz–fayalite–magnetite (QFM) buffer. The oxygen fugacity changes were treated as suggested by Kress and Carmichael (1988).When the models for fractional and equilibrium crystallization are compared, fractional crystallization yields a better agreement between the predicted and observed compositional ranges for studied mineral phases. The results of fractional crystallization modelling of ijolite are shown in Fig. 6c–d.

4.3. Cooling rate estimation

The chemical zoning preserved in olivine grains can be used to estimate cooling rate and thermal history of the given rock during its crystallization. The minimum cooling rates necessary for the preservation of measured compositional zoning in olivine grains of melteigite were determined following the kinetic model of Taylor et al. (1977) with interdiffusion coefficient for the Mg^{2+} and Fe^{2+} determined by Buening and Buseck (1973). The variations of Fo content in a selected olivine grain (Fig. 3), measured along mutually orthogonal profiles across the grain, were used to estimate the minimum cooling rates. The effects of crystallographic orientation (determined from EBSD analyses) on Mg–Fe diffusion in the olivine grains were taken into account in the calculations. Based on the procedure of Taylor et al. (1977) the calculated minimal cooling rate of these olivine crystals is ~0.02 °C/hr, or 175 °C/yr.

4.4. REE concentrations in clinopyroxenes

Based on the large observed variations of major elements in the clinopyroxenes of melteigite and ijolite, the composition of REE in several clinopyroxene grains from both rocks was further investigated using the LA-ICP-MS (Tab. 3). The analyses of specific parts of the clinopyroxene grains were carried out to cover the wide range of clinopyroxene's major-element variation observed.

Rare earth element concentrations correlate with major-element abundances (Fig. 7), whereby the cores of clinopyroxene grains (Cpx-1, Cpx-2 for both rocks, see Tab. 3) have consistently lower REE concentrations than the mantles (Cpx-3, Cpx-5 for melteigite and Cpx-3 for ijolite) and the rims (Cpx-4, Cpx-6 for melteigite and Cpx-4 for ijolite). Measured clinopyroxenes are clearly enriched in light REE (LREE) relative to heavy REE (HREE) without a Eu anomaly. Chondrite-normalized ratios $[La/Lu]_n$ (normalization after Anders and Grevesse 1989) for studied melteigite clinopyroxenes vary in the range of 2.05–12.34 and for ijolite clinopyroxenes between 7.89 and 10.43.

5. Discussion

5.1. Clinopyroxene composition as a record of crystallization processes

During the crystallization of a basaltic magma, the Al/Ti ratios in clinopyroxene vary depending upon appearance and disappearance of other liquidus phases and changes in crystallization conditions. Thus, the co-variation between Al and Ti in clinopyroxene may provide useful information about the crystallization sequence.

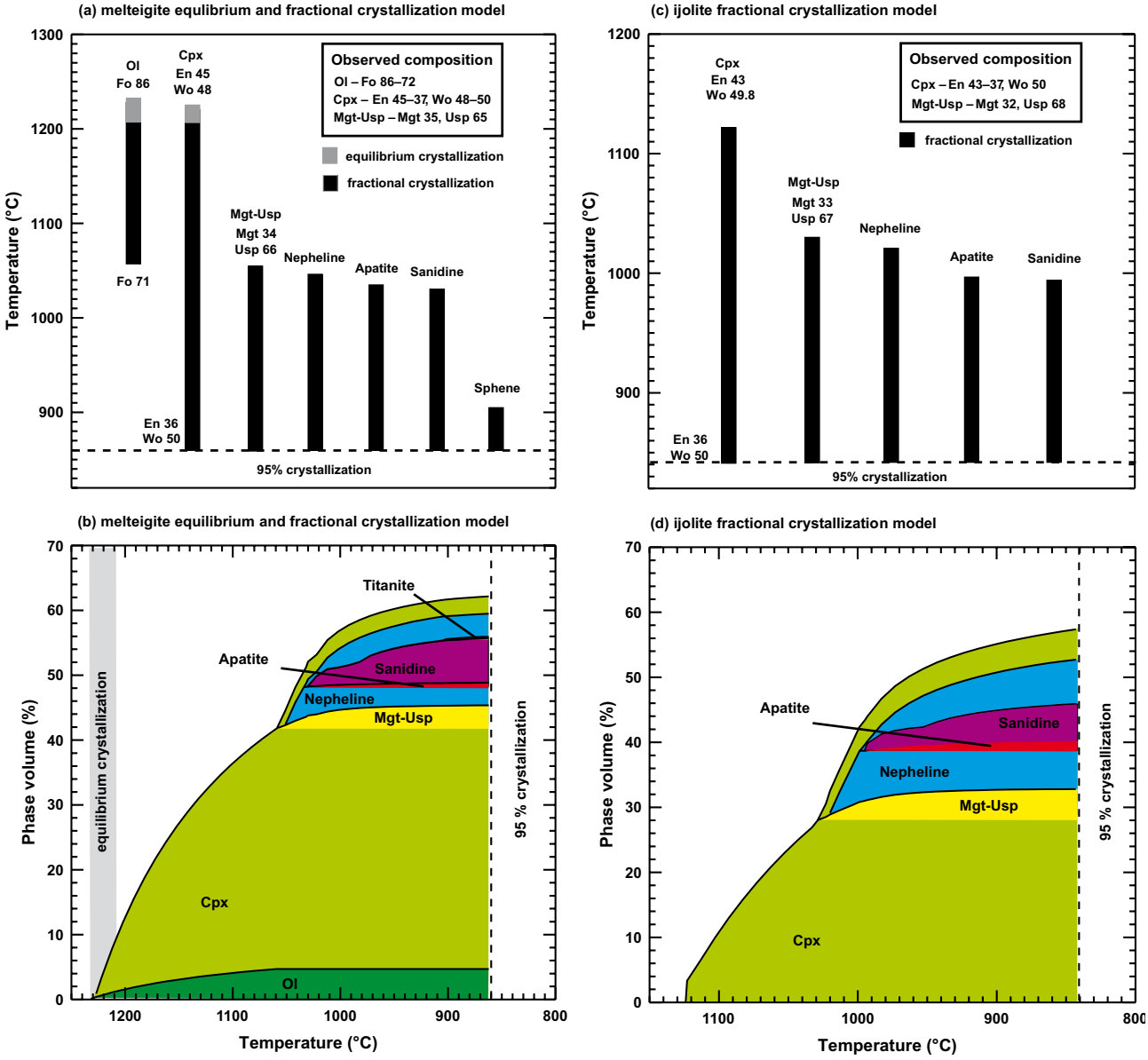

Fig. 6 Results of crystallization modelling of melteigite (**a–b**) and ijolite (**c–d**). Upper diagrams (a, c) in both cases show the modelled crystallization intervals of mineral phases with decreasing temperature and the ranges of their calculated/measured chemical compositions. Lower diagrams (b, d) illustrate the modelled volumes of the crystallized phases appearing with the dropping temperature.

5.1.1. Melteigite

Magnesian cores of clinopyroxene grains are depleted in Al and high field-strength elements (HFSE) with Σ(Al, Ti, Cr) ≈ 0.21 apfu (based on 6 oxygens) relative to the mantles (Σ(Al, Ti, Cr) ≈ 0.45) and rims (Σ(Al, Ti, Cr) ≈ 0.30) (Tabs 1, 3). The Ti/Al ratios in Mg-rich clinopyroxene cores are ~ 0.2 and reflect initial diopsidic Cpx crystallization (Fig. 4). Furthermore, these Mg-rich cores show only negligible variability in chemical composition. Clinopyroxene mantles enriched in Ca–Fe–Al–Ti have higher concentrations of Al and Ti and lower Si (Tabs 1, 3 and Fig. 4). This trend suggests a combination of substitutions with overall stoichiometry Fe^{2+} + Ti^{4+} + 2 Al for 2 Mg + 2 Si, leading to the idealized end-member $CaFe_{0.5}Ti_{0.5}AlSiO_6$. For crystallization of such Ti–Al-rich diopsides, the favourable conditions would be low pressure, high activity of TiO_2 and low fO_2 (Tracy and Robinson 1977). The change in Ti/Al due to the substitution described above most probably indicates a rapid drop in pressure during magma rise to the final emplacement level. Subsequent decrease in Ti and Fe concentrations recorded in clinopyroxene (Fig. 4) can be interpreted as an appearance of Ti-rich magnetite on the liquidus, whereby

Tab. 3. Major- and trace-element analyses of representative clinopyroxene grains

	melteigite												ijolite							
	Cpx-1 ($En_{45.1}Wo_{48.2}$)		Cpx-2 ($En_{45.2}Wo_{48.5}$)		Cpx-3 ($En_{37.9}Wo_{51.4}$)		Cpx-4 ($En_{36.1}Wo_{52.9}$)		Cpx-5 ($En_{42.7}Wo_{50.0}$)		Cpx-6 ($En_{35.8}Wo_{52.8}$)		Cpx-1 ($En_{42.9}Wo_{49.8}$)		Cpx-2 ($En_{41.7}Wo_{50.3}$)		Cpx-3 ($En_{36.1}Wo_{50.7}$)		Cpx-4 ($En_{38.6}Wo_{50.9}$)	
wt. %		±2σ		±2σ		±2σ		±2σ		±2σ		±2σ		±2σ		±2σ		±2σ		±2σ
SiO_2	52.00	0.12	51.70	0.12	46.66	0.13	46.12	0.12	50.70	0.11	44.83	0.11	50.63	0.12	49.55	0.12	44.09	0.11	47.98	0.11
TiO_2	1.11	0.03	1.21	0.03	3.58	0.03	4.23	0.05	1.89	0.05	4.51	0.05	1.76	0.03	2.21	0.06	4.53	0.05	3.08	0.05
Al_2O_3	3.60	0.02	3.37	0.02	6.89	0.02	7.77	0.03	3.94	0.02	8.96	0.03	3.70	0.02	4.59	0.03	8.57	0.02	5.86	0.02
Cr_2O_3	0.71	0.01	0.69	0.01	0.15	0.01	0.12	0.01	0.46	0.01	0.09	0.01	0.63	0.02	0.38	0.01	0.03	0.01	0.06	0.01
MgO	15.34	0.08	15.60	0.07	12.52	0.07	11.50	0.08	14.62	0.06	11.45	0.08	14.83	0.08	14.26	0.07	11.75	0.05	12.87	0.03
CaO	22.80	0.03	23.32	0.03	23.63	0.03	23.46	0.06	23.78	0.06	23.46	0.06	23.96	0.05	23.93	0.07	22.97	0.06	23.61	0.05
MnO	0.12	0.01	0.16	0.01	0.02	0.01	0.16	0.01	0.08	0.01	0.04	0.01	0.03	0.01	0.01	0.01	0.01	0.01	0.05	0.01
FeO	4.05	0.08	3.89	0.08	6.36	0.09	6.28	0.08	4.45	0.08	6.48	0.07	4.47	0.08	4.93	0.06	7.65	0.08	6.22	0.09
Na_2O	0.21	0.01	0.18	0.01	0.16	0.01	0.31	0.01	0.05	0.01	0.26	0.01	0.05	0.01	0.11	0.01	0.34	0.01	0.29	0.01
Total	99.95		100.13		99.97		99.95		99.98		100.09		100.07		99.96		99.93		100.02	
ppm		±1σ		±1σ		±1σ		±1σ		±1σ		±1σ		±1σ		±1σ		±1σ		±1σ
Sc	105	7.33	88	7.33	129	7.33	105	7.33	158	7.33	112	7.33	162	9.92	101	9.92	146	9.92	138	9.92
V	182	2.22	135	2.22	209	2.22	174	2.22	138	2.22	486	2.22	166	1.93	254	1.93	180	1.93	171	1.93
Co	27	2.48	24	2.48	23	2.48	18	2.48	24	2.48	40	2.48	37	2.70	28	2.70	24	2.70	21	2.70
Ni	375	11.03	283	11.03	356	11.03	193	11.03	97	11.03	61	11.03	133	12.11	74	12.11	43	12.11	35	12.11
Y	4	0.48	5	0.48	13	0.48	21	0.48	7	0.48	26	0.48	8	0.48	21	0.48	12	0.48	9	0.48
La	1.88	0.39	3.53	0.39	9.30	0.39	25.07	0.39	3.81	0.39	20.17	0.39	3.38	0.41	8.61	0.41	18.14	0.41	12.17	0.41
Ce	6.13	0.31	11.86	0.31	31.16	0.31	70.03	0.31	11.49	0.31	65.79	0.31	12.63	0.67	28.36	0.67	44.97	0.67	36.37	0.67
Pr	1.24	0.34	2.44	0.34	5.27	0.34	11.64	0.34	1.87	0.34	9.78	0.34	2.42	0.46	4.52	0.46	9.51	0.46	6.63	0.46
Nd	6.17	0.35	12.48	0.35	31.33	0.35	53.15	0.35	11.28	0.35	61.13	0.35	14.09	0.35	28.77	0.35	44.68	0.35	35.81	0.35
Sm	2.86	0.50	3.83	0.50	9.11	0.50	15.61	0.50	2.55	0.50	12.79	0.50	2.83	0.50	6.68	0.50	11.45	0.50	12.92	0.50
Eu	0.96	0.01	1.19	0.01	2.86	0.01	3.90	0.01	0.81	0.01	3.84	0.01	0.88	0.02	2.02	0.02	3.21	0.02	2.98	0.02
Gd	2.83	0.41	3.68	0.41	6.86	0.41	10.91	0.41	2.70	0.41	10.45	0.41	2.52	0.48	4.28	0.48	8.54	0.48	7.39	0.48
Tb	0.49	0.12	0.58	0.12	1.24	0.12	1.92	0.12	0.53	0.12	1.83	0.12	0.39	0.12	0.69	0.12	1.57	0.12	1.30	0.12
Dy	1.43	0.32	1.35	0.32	4.22	0.32	8.73	0.32	1.68	0.32	6.51	0.32	1.89	0.32	4.09	0.32	7.61	0.32	6.77	0.32
Ho	0.23	0.08	0.26	0.08	0.76	0.08	1.59	0.08	0.28	0.08	1.14	0.08	0.39	0.08	0.62	0.08	1.08	0.08	1.00	0.08
Er	0.56	0.11	0.72	0.11	1.76	0.11	3.30	0.11	0.59	0.11	2.55	0.11	0.92	0.12	1.40	0.12	1.73	0.12	1.47	0.12
Tm	0.09	0.03	0.08	0.03	0.24	0.03	0.48	0.03	0.10	0.03	0.36	0.03	0.11	0.03	0.16	0.03	0.30	0.03	0.18	0.03
Yb	0.50	0.16	0.67	0.16	1.44	0.16	2.05	0.16	0.48	0.16	1.92	0.16	0.66	1.11	0.88	1.11	1.21	1.11	0.78	1.11
Lu	0.10	0.03	0.11	0.03	0.20	0.03	0.26	0.03	0.07	0.03	0.17	0.03	0.04	0.27	0.05	0.27	0.20	0.27	0.13	0.27

σ = standard deviation

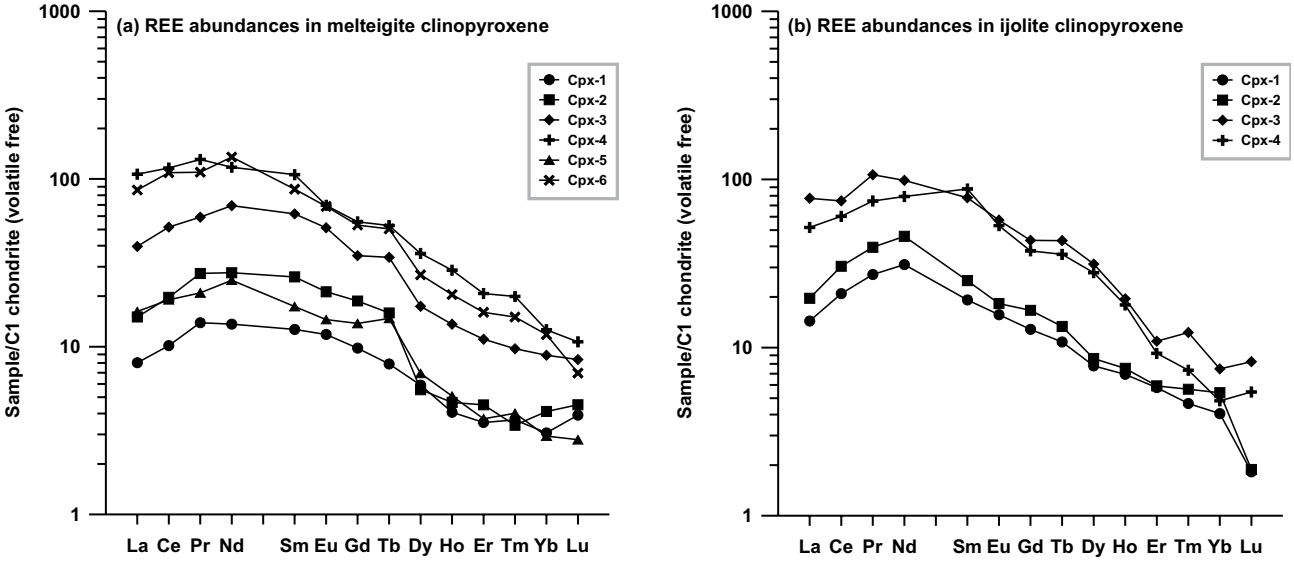

Fig. 7 The REE abundances in clinopyroxene from melteigite (**a)** and ijolite (**b**). Normalization values are from Anders and Grevesse (1989).

the amount of Ti and Fe uptake into the clinopyroxene structure would be controlled by the declining Fe and Ti contents in the melt. Also the simultaneous decrease of Al concentration in clinopyroxene (Fig. 4) indicates an onset of nepheline and sanidine crystallization. Thus, crystallization of magnetite together with nepheline, sanidine and clinopyroxene presumably lead to depletion in Fe, Ti and Al in the residual magma as well as an increasing Mg uptake to the clinopyroxene structure.

Furthermore the concomitant decrease of Al, Ti and Fe (see orthogonal profiles Fig. 4) indicate that magnetite, nepheline and sanidine begun to crystallize probably at the same time during crystallization of clinopyroxene. The melteigite crystallization sequence of major mineral phases, derived from variations in Ti and Al contents and clinopyroxene chemical zoning, can be proposed as follows: Ol → Ol + Cpx → Cpx + Mgt → Cpx + Mgt + Ne → Cpx + Mgt + Ne + Sa. Coexisting magnetite–ilmenite pairs indicate log $fO_2 = -11$, calculated using the method of Buddington and Lindsley (1964). This is slightly more reducing than the quartz–fayalite–magnetite buffer.

5.1.2. Ijolite

Similarly to the melteigite, the Mg-rich cores of clinopyroxene grains are also depleted in Al and HFSE with Σ(Al, Ti, Cr) ≈ 0.25 apfu (based on 6 oxygens) relative to the mantles (Σ(Al, Ti, Cr) ≈ 0.51) and the rims (Σ(Al, Ti, Cr) ≈ 0.35) (Tabs 1, 3). This indicates that the clinopyroxenes of ijolites are more enriched in the HFSE than those of melteigites. Furthermore the Ti/Al ratio is the same for Mg-rich cores and mantles enriched in Ca, Fe, Al, and Ti, having a consistent value of 0.33 (Fig. 5). This fact documents that ijolite clinopyroxene crystallized from a more fractionated magma that was enriched in Al and Ti in respect to the melteigite. This assumption is also supported by the bulk-rock composition, lower mg# (Tab. 2) and absence of strongly Mg-enriched clinopyroxene cores with low abundances of Al and Ti. The uniform Ti/Al values for Mg-rich cores and Ca, Fe, Al, Ti-rich mantles also indicate substitution of $Fe^{2+} + Ti^{4+} + 2$ Al for 2 Mg + 2 Si during the whole crystallization interval of the parental magma that led to a significant enrichment of Al and Ti, especially in clinopyroxene mantles. This observation is consistent with clinopyroxene crystallization from magma enriched in Al and Ti under lower pressure, i.e. at its final emplacement level.

A subsequent decrease in Ti and Fe concentrations recorded in clinopyroxene rims (Fig. 5) can be interpreted (identically to the case of melteigite) as an appearance of Ti-rich magnetite on the liquidus, when the amount of Ti and Fe uptake into the crystal structure was affected by simultaneous crystallization of Ti-rich magnetite. Furthermore, concomitant decrease in clinopyroxene Al contents (Fig. 5) indicates the onset of nepheline and sanidine crystallization. Crystallization of magnetite together with nepheline, sanidine and clinopyroxene presumably led to the Fe, Ti and Al depletion of the residual melt.

The crystallization sequence of major mineral phases, derived from Ti/Al values and clinopyroxene chemical zoning, is: Cpx → Cpx + Mgt → Cpx + Mgt + Ne → Cpx + Mgt + Ne + Sa. This crystallization sequence is in good agreement with the results of crystallization modelling (see section 5.2.2.).

5.2. Crystallization modelling

5.2.1. Melteigite

Numerical modelling can provide significant information for understanding the crystallization processes of the studied melteigite. When the resulting two-step model is compared with mineral chemistry data, the model yields a very good fit between predicted and observed compositional ranges for both olivine and clinopyroxene (Fig. 6). The first step of the model is equilibrium crystallization for the recalculated bulk composition of melteigite at 4 kbar (Tab. 2, Fig. 6) predicting the olivine (Fo_{86}) as a first phase to crystallize from the cooling liquid at 1 232 °C, followed by diopsidic pyroxene (En_{45}, Wo_{48}) at 1 227 °C. This first crystallization phase finished at 1 209 °C (olivine Fo_{85} + clinopyroxene En_{44}, Wo_{48}). The modelled olivine and clinopyroxene compositions correspond to the compositional variation in our samples (see above and Fig. 4).

The second step is assumed to have taken place at a pressure of 0.2 kbar. The fractional crystallization model infers crystallization of olivine (Fo_{85}) and clinopyroxene (En_{41}, Wo_{50}). The end of olivine crystallization (Fo_{71}) predicted at 1058 °C was followed by crystallization of ulvöspinel (Mgt_{34}, Usp_{66}) at 1 057 °C, nepheline at 1 047 °C, apatite at 1 035 °C, sanidine at 1 030 °C and titanite at 905 °C.

The predicted and observed mineral chemistries are in good mutual agreement (Fig. 6). The sudden drop in pressure and onset of substitution of Fe^{2+} + Ti^{4+}+ 2 Al for 2 Mg + 2 Si in clinopyroxene explain the predicted and observed compositional gap in the clinopyroxene (Fig. 4). The two-step crystallization model is consistent with the crystallization sequence derived from Ti/Al variations in clinopyroxenes (section 5.1.1 and Fig. 4) and provides us with a very detailed insight into the crystallization evolution of melteigite from the parental magma. The melteigite crystallization model also excludes the presence of accumulated minerals and, together with other lines of evidence (e.g., type of chemical zoning of olivine and clinopyroxene – section 4.1.1; strong REE variations between core and rim for clinopyroxene grains – section 4.4), reflects the role of fractional crystallization processes during crystallization of the magma.

5.2.2. Ijolite

When we compare the results of fractional crystallization modelling of the studied ijolite at a pressure of 0.2 kbar, the very good fit between predicted and observed chemical compositions of main mineral phases is apparent (Figs 5–6). Diopsidic pyroxene (En_{43}, Wo_{50}) is the first phase that was modelled to have crystallized from the cooling parental magma at 1 123 °C followed by ulvöspinel (Mgt_{32}, Usp_{68}) at 1 029 °C, nepheline at 1 020 °C, apatite at 999 °C and sanidine at 995 °C. Similarly to the melteigite, the agreement between the predicted and observed compositions of the early-crystallized clinopyroxene excludes any significant presence of accumulated minerals. The predicted limited temperature range of the beginning of Ti-rich magnetite, nepheline, apatite and sanidine crystallization corresponds well with the chemical record in pyroxene. The Fe^{2+} + Ti^{4+} + 2 Al for 2 Mg + 2 Si substitution was already significant in the clinopyroxene core, confirming that low-pressure fractional crystallization was effective throughout the whole crystallization interval. The results of crystallization modelling for both studied rocks suggest that, after final emplacement of parental magmas, they crystallized under similar conditions. However, the chemical compositions of these parental magmas were slightly different (Tab. 2). The melteigite model, together with the observed chemical composition of the clinopyroxene, records also an early equilibrium crystallization history of olivine and clinopyroxene at higher pressure, whereas the slightly more fractionated ijolite magma crystallized entirely at a lower pressure.

5.3. Character of the parental magmas

5.3.1. Melteigite

The rare-earth element concentrations of melteigite clinopyroxenes measured by LA-ICP-MS show significant variations (Fig. 7a) suggesting an extensive fractional-crystallization history of the melteigite magma. The REE compositions of clinopyroxene can be therefore used to estimate the composition of the liquid with which they were in equilibrium at the time of crystallization (e.g., McSween et al. 1996). As shown by these authors, good agreement between bulk-rock and estimated equilibrium melt REE contents for the earliest-formed minerals could indicate evolution of the parental magma in a closed-system. On the other hand, it is also possible to detect the presence of minerals with cumulitic origin or potential escape of some REE-enriched residual melt expelled by the filter-pressing processes.

The studied clinopyroxenes have in their Mg-rich cores lower REE abundances than their Ca–Fe–Al–Ti-rich mantles and Ca–Mg-rich rims. The correlation of $(La/Lu)_n$ values with the Wo and En contents is illustrated in Fig. 8. In general, the $(La/Lu)_n$ values of Mg-rich cores are lower than those of mantles and rims. This observation can easily be explained as an increase in $(La/Lu)_n$ value with progressive magma fractionation. The lowest $(La/Lu)_n$ values seen in equilibrated Mg-rich cores (Fig. 8a–b) are in agreement with petrographic observations and numerical modelling, suggesting that this was the

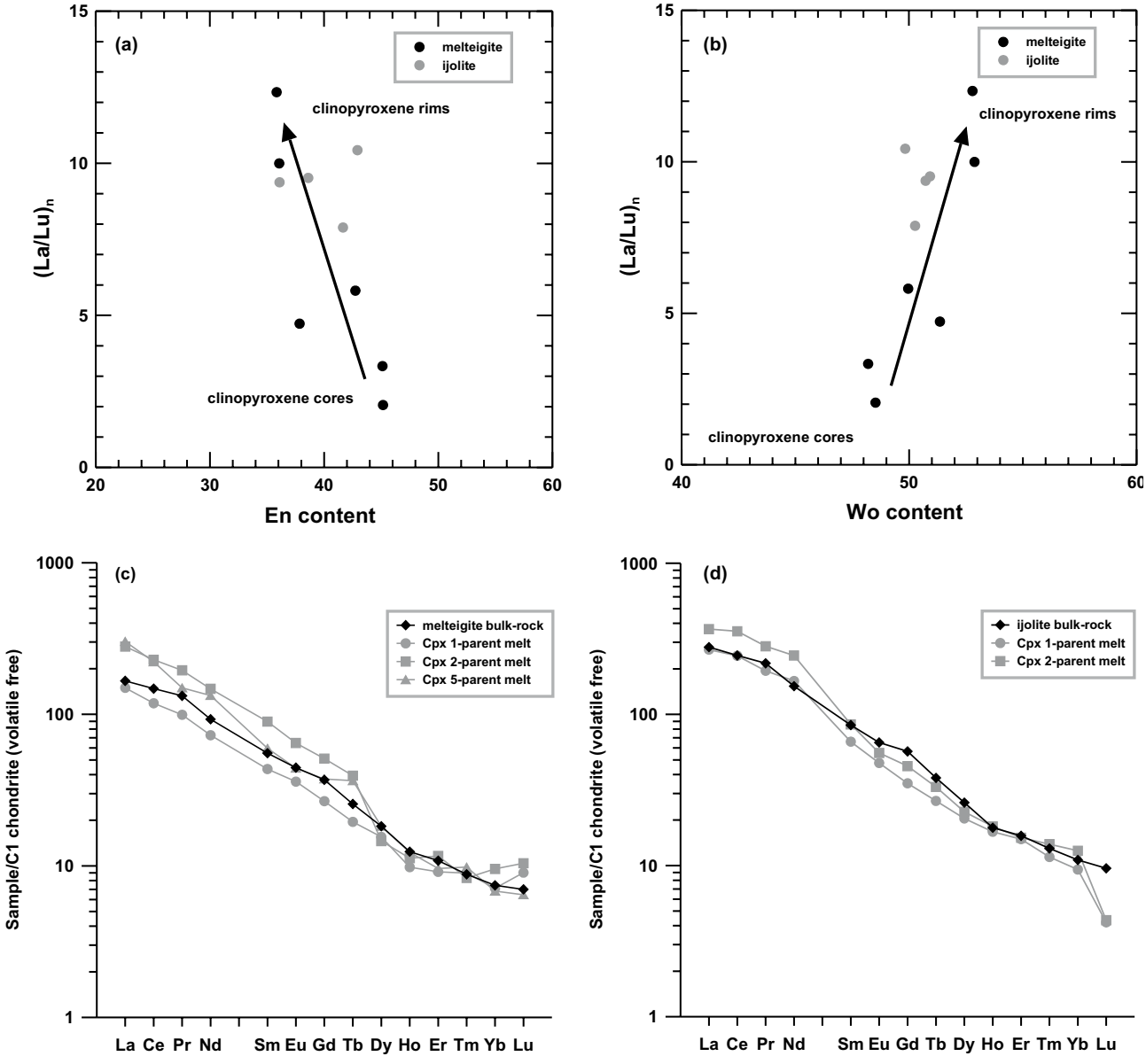

Fig. 8a–b – Correlation plots between $(La/Lu)_n$ and En and Wo contents in analysed clinopyroxenes; **c–d** Modelled REE abundances in melts parental to melteigite (c) and ijolite (d). Normalization values are from Anders and Grevesse (1989).

earliest clinopyroxene crystallizing from the melteigite parental magma.

In estimating the composition of the melteigite parental magma, REE partition coefficients between olivine and melt, published by Bédard (2005), appear to be too low. In our evaluation we therefore take into account the bulk-rock REE concentrations (Tab. 3.) published by Holub et al. (this volume), and the olivine modal abundance in this rock. The REE abundances in measured olivine grains are very low, often below the detection limit of LA-ICP-MS. In any case, this mineral could accommodate only <0.01 ppm of total REE and was therefore excluded from the calculation.

The equilibrium melt compositions have thus been calculated for the earliest formed Mg-rich diopsidic pyroxene having the lowest REE concentrations and consuming substantial amounts of REE from the parental magma (Cpx-1, Cpx-2, see Tab. 3 and Fig. 7a). The REE partition coefficients between diopsidic clinopyroxene and melt of Hart and Dunn (1993) were used. In addition, melt compositions in equilibrium with the Ca, Fe, Al and Ti-rich clinopyroxene (Cpx-5) with the highest

Tab. 4. The measured bulk-rock REE compositions and calculated equilibrium melt REE compositions for melteigite and ijolite

REE (ppm)	D_{Cpx}	melteigite bulk-rock	(melteigite bulk-rock)$_n$	melteigite earliest formed pyroxenes								
				Cpx-1	Cpx-1-pm	(Cpx-1-pm)$_n$	Cpx-2	Cpx-2-pm	(Cpx-2-pm)$_n$	Cpx-5	Cpx-5-pm	(Cpx-5-pm)$_n$
La	0.054	39.00	166.17	1.88	35.13	149.67	3.53	65.79	280.30	3.81	71.02	302.58
Ce	0.086	89.10	147.71	6.13	71.40	118.37	11.86	138.28	229.24	11.49	133.91	222.00
Pr	0.140	11.80	132.44	1.24	8.85	99.32	2.44	17.40	195.26	1.87	13.32	149.53
Nd	0.187	42.00	92.84	6.17	32.92	72.76	12.48	66.66	147.34	11.28	60.21	133.09
Sm	0.291	8.15	55.40	1.86	6.41	43.56	3.83	13.17	89.56	2.55	8.78	59.67
Eu	0.329	2.49	44.46	0.66	2.01	35.97	1.19	3.62	64.63	0.81	2.47	44.11
Gd	0.367	7.27	36.98	1.93	5.25	26.72	3.68	10.03	51.02	2.70	7.37	37.46
Tb	0.404	0.93	25.62	0.29	0.71	19.52	0.58	1.43	39.38	0.53	1.32	36.48
Dy	0.380	4.43	18.25	1.43	3.77	15.54	1.35	3.54	14.59	1.68	4.43	18.23
Ho	0.415	0.69	12.41	0.23	0.55	9.81	0.26	0.62	11.24	0.28	0.68	12.26
Er	0.387	1.72	10.82	0.56	1.45	9.13	0.72	1.85	11.63	0.59	1.53	9.61
Tm	0.409	0.21	8.80	0.09	0.22	8.96	0.08	0.20	8.33	0.10	0.24	9.82
Yb	0.430	1.21	7.45	0.50	1.16	7.12	0.67	1.55	9.55	0.48	1.11	6.82
Lu	0.433	0.17	7.00	0.10	0.22	9.03	0.11	0.25	10.41	0.07	0.16	6.44

REE (ppm)	D_{Cpx}	ijolite bulk-rock	(ijolite bulk-rock)$_n$	ijolite earliest formed pyroxene					
				Cpx-1	Cpx-1-pm	(Cpx-1-pm)$_n$	Cpx-2	Cpx-2-pm	(Cpx-2-pm)$_n$
La	0.054	65.40	278.65	3.38	62.97	268.32	4.61	86.03	366.53
Ce	0.086	148.00	245.36	12.63	147.21	244.04	18.36	213.93	354.66
Pr	0.140	19.40	217.73	2.42	17.31	194.29	3.52	25.17	282.51
Nd	0.187	69.50	153.63	14.09	75.21	166.25	20.77	110.89	245.12
Sm	0.291	12.50	84.98	2.83	9.71	66.00	3.68	12.63	85.89
Eu	0.329	3.65	65.18	0.88	2.67	47.69	1.02	3.11	55.60
Gd	0.367	11.20	56.97	2.52	6.88	34.99	3.28	8.94	45.45
Tb	0.404	1.38	38.02	0.39	0.97	26.75	0.49	1.20	33.10
Dy	0.380	6.33	26.08	1.89	4.97	20.49	2.09	5.50	22.66
Ho	0.415	0.99	17.81	0.39	0.93	16.73	0.42	1.01	18.15
Er	0.387	2.50	15.73	0.92	2.37	14.94	0.94	2.43	15.29
Tm	0.409	0.31	12.98	0.11	0.28	11.39	0.14	0.34	13.85
Yb	0.430	1.77	10.89	0.66	1.53	9.40	0.88	2.04	12.53
Lu	0.433	0.23	9.59	0.04	0.10	4.21	0.05	0.11	4.35

REE mineral–melt partition coefficients for diopsidic clinopyroxene (D) (Hart and Dunn 1993), REE concentrations and normalized REE concentrations in melteigite (DH1330) and ijolite (DH1329) adopted from Holub et al. (this volume), measured REE concentrations in Mg-rich clinopyroxene, calculated REE concentrations for parental melts in equilibrium (X-pm) and calculated normalized REE concentrations for parental melt in equilibrium (Xpm)$_n$. Normalization values are from Anders and Grevesse (1989).

En component (and with the lowest REE concentrations) have also been calculated in this model. The calculated equilibrium melt REE compositions are compared with measured bulk-rock REE contents (Holub et al. this volume) in Tab. 4 and Fig. 8c.

The bulk-rock REE concentrations of melteigite are very similar to the calculated equilibrium melt REE concentrations for Mg-rich diopsidic pyroxene (Cpx-1, Cpx-2, see Tab. 4, Fig. 8c). Furthermore, the REE composition of melts in equilibrium with early-formed diopsidic pyroxene and Ca, Fe, Al and Ti-rich clinopyroxene with the highest En component (Cpx-5), are also similar to each other, suggesting that both clinopyroxenes crystallized from similar melts. This calculation is consistent

with the results of crystallization modelling (see section 4.2.1) predicting the early equilibrium crystallization of olivine and Mg-rich diopsidic pyroxene and subsequent fractional crystallization of clinopyroxene enriched in Ca, Fe, Al and Ti.

The similarity between the measured bulk-rock and calculated equilibrium melt REE contents supports the assumption that the REE composition of the melteigite reflects that of the parental melt very well. This fact, together with the outcome of crystallization modelling, excludes the presence of any significant cumulate olivine/clinopyroxene or removal of REE-enriched residual melt. The results of the parental magma composition modelling thus indicate a closed-system crystallization of the melteigite parental magma.

5.3.2. Ijolite

The REE concentrations in ijolite clinopyroxenes measured by LA-ICP-MS showed also significant variations (Tab. 3, Fig. 7b). These clinopyroxenes have lower REE abundances in their Mg-rich cores than in their mantles and rims. The correlation of $(La/Lu)_n$ values with the Wo and En contents of clinopyroxenes also demonstrates an increasing degree of magma fractionation (Fig. 8a–b). However, the range of $(La/Lu)_n$ is in this case much more limited compared to that in the melteigite clinopyroxenes. This observation, together with the results of crystallization modelling and the chemical composition recorded in clinopyroxenes, reflects a generally simple low-P fractional crystallization history. Furthermore, the evolution of the ijolite magma implies also variations in REE between clinopyroxene cores, mantles and rims (Fig. 7b). The results of crystallization modelling suggest that the clinopyroxene with the highest En content should be the earliest phase to have crystallized from the parental magma. The REE contents of these clinopyroxenes were therefore used for the estimates of the parental liquid composition using the same method as applied to the melteigite clinopyroxene.

Good agreement between the observed bulk-rock and the estimated equilibrium melt REE compositions for the earliest formed clinopyroxenes once again indicates that these pyroxenes crystallized from magma with a composition resembling that of the bulk rock (Tab. 4, Fig. 8d). Moreover, this also indicates a closed-system fractional crystallization.

5.4. Genetic relationship between melteigite and ijolite

The results of crystallization modelling and REE parental melts composition estimations suggest the possibility of a close petrogenetic relationship between both studied ijolitic rocks from the Flurbühl Composite Intrusion. For verification of this theory we used the modelled bulk-rock melteigite composition (Tab. 2) as that of initial melt. Taking into account modal abundances of early crystallized olivine and clinopyroxene that originated during the equilibrium phase of crystallization (see section 5.1.1) and their chemical composition, 4 wt. % olivine and 10 wt. % clinopyroxene were removed, and the bulk composition of melteigite was recalculated (Tab. 5). After this first step, the recalculated bulk-rock composition was far from the fractionated ijolite bulk rock composition (Tab. 5, Fig. 9), thus indicating that the ijolite bulk-rock

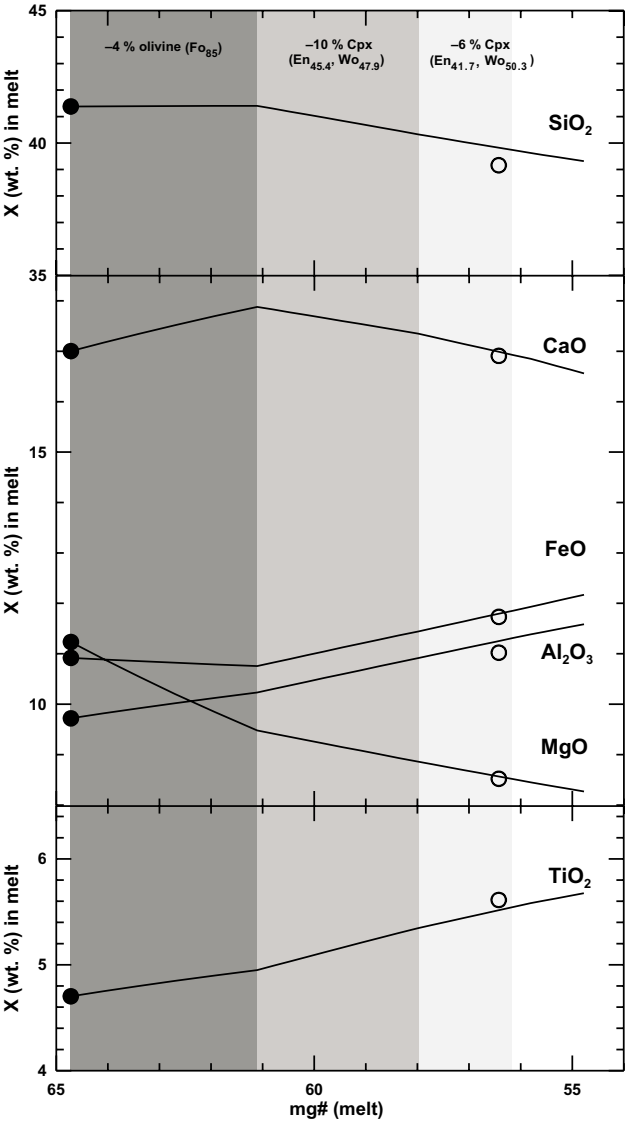

Fig. 9 Modelled evolution of SiO_2, CaO, FeO, Al_2O_3, MgO and TiO_2 contents in the melt after removal of 4 % Ol, 10 % Cpx and 6 % Cpx with the indicated chemical compositions. The initial chemistry of the melt (black dots) represents the recalculated melteigite bulk-rock composition. Recalculated real bulk-rock composition of ijolite (circles) is also plotted.

Tab. 5. Recalculated and modelled melteigite and ijolite bulk-rock compositions

	melteigite (recalculated bulk-rock composition)	1. step melteigite (–4 % Ol, –10 % Cpx)	2. step melteigite (–6 % Cpx)	ijolite (recalculated bulk-rock composition)	1. step Ol composition	1. step Cpx composition	2. step Cpx composition
wt. %							
SiO_2	41.41	40.33	39.73	39.16	40.88	52.08	49.73
TiO_2	4.70	5.35	5.55	5.61	–	1.15	2.22
Al_2O_3	9.73	10.91	11.32	11.02	–	3.72	4.60
Fe_2O_3	1.35	1.57	1.67	1.67	–	–	–
FeO	10.93	11.45	11.86	11.73	14.02	4.18	4.95
MnO	0.18	0.20	0.21	0.21	0.17	0.01	0.01
MgO	11.24	8.86	8.51	8.52	44.59	15.51	14.31
CaO	17.01	17.35	16.93	16.91	0.34	23.12	24.02
Na_2O	1.49	1.71	1.81	1.65	–	0.23	0.15
K_2O	1.26	1.46	1.56	1.62	–	–	–
P_2O_5	0.45	0.52	0.55	1.18	–	–	–
F	0.13	0.15	0.16	0.18	–	–	–
CO_2	0.10	0.12	0.13	0.51	–	–	–
S	0.02	0.02	0.02	0.02	–	–	–
Total	100.00	100.00	100.00	100.00	100.00	100.00	100.00
mg#	64.72	57.99	56.14	56.43			
Fo					85.0		
En						45.4	41.7
Wo						47.9	50.3

composition cannot be derived by fractionation of olivine and clinopyroxene from melteigite melt. Furthermore, melteigite crystallization modelling shows that to approach the REE concentrations of residual melt similar to those of the ijolite, solidification of *c.* 22 wt. % of parental melt is needed. Based on the fractional crystallization model, only clinopyroxene should have crystallized in this range (after removal of 14 wt. % olivine + clinopyroxene in the first step). At the second step of this simple model, 6 wt. % clinopyroxene was removed from the recalculated bulk rock composition; a representative Ca, Fe, Al and Ti-rich clinopyroxene composition (Tab. 5) was adopted for calibration of this model. Removing 6 wt. % clinopyroxene provides the best fit between modelled major-elements bulk-rock composition and the real ijolite analysis (Tab 5, Fig. 9). Total removal of 20 % olivine and clinopyroxene from the melteigite bulk rock composition is very close to the estimation based on modelled REE concentration evolution during equilibrium and fractional crystallization of the melteigite parental melt. It is apparent that derivation of ijolite parental melt from melteigite is possible only for conditions of olivine and clinopyroxene fractionation during the early crystallization phase and also with partial crystallization during magma ascent (that is, pressure decrease).

6. Conclusions

(i) Crystallization modelling of ijolitic rocks excludes the presence of any significant amounts of accumulated minerals and confirms that the modelled major-element bulk-rock compositions reflect their parental magma compositions very well.

(ii) Chemical zoning of clinopyroxenes in melteigite and ijolite resulted from substitution of $Fe^{2+} + Ti^{4+} + 2\ Al$ for $2\ Mg + 2\ Si$, which led most likely to significant enrichment of clinopyroxenes in Al and Ti in the course of the crystallization. Significance of this substitution mechanism points to a rapid pressure decrease associated with the magma ascent.

(iii) The chemical composition of melteigite clinopyroxenes, together with the results of crystallization modelling, indicates early equilibrium crystallization at *c.* 4 kbar followed by low-pressure fractional crystallization (~0.2 kbar). For ijolite, the results indicate solely low-pressure fractional crystallization, probably at the final emplacement level.

(iv) Strong REE variations between core, mantle and rim of clinopyroxene grains in both rock samples suggest formation of these rocks by fractional crystallization processes, and correspond very well with the results

of crystallization modelling. The limited compositional variability in Mg-rich clinopyroxene cores from melteigite indicates early equilibrium crystallization under higher temperature and pressure. Low minimum cooling rate estimated for melteigite (175 °C/yr; ~0.02 °C/hr), based on the variation of Fo content in olivine, suggests that this rock has been emplaced and crystallized at a greater depth.

(v) The correspondence between measured bulk-rock REE contents and calculated equilibrium melt REE compositions for melteigite and ijolite, suggests that the bulk-rock REE budget of both ijolitic rocks reflects the composition of the original parental melt accurately. The bulk-rock chemistry of these rocks excludes the presence of significant amounts of accumulated minerals and was not affected by removal of putative REE-enriched residual melt by filter-pressing after emplacement, neither. Therefore, these rocks were likely to have evolved solely by the closed-system fractional crystallization.

(vi) The results of crystallization modelling and parental melts REE composition estimations suggest a close genetic relationship between both studied ijolitic rocks. Removal of ~20 % of olivine and clinopyroxene from the initial melt provides a feasible mechanism for the derivation of fractionated ijolite magma from that of the melteigite.

Acknowledgements. This research was supported by project IAA300130612 granted by the Grant Agency of the Czech Academy of Sciences (GAAV). The study was conducted within the framework of research plans of the Czech Geological Survey (MZP0002579801) and Faculty of Science, Charles University in Prague (MSM0021622855). We would like to thanks to journal reviewers, Axel Renno and Alan Wolley, for their careful critical reviews as well as to Associate Editor David Dolejš for constructive comments and suggestions which significantly improved the quality of the paper.

References

Anders E, Grevesse N (1989) Abundances of the elements: meteoritic and solar. Geochim Cosmochim Acta 53: 197–214

Babuška V, Fiala J, Plomerová J (2010) Bottom to top lithosphere structure and evolution of western Eger Rift (central Europe). Int J Earth Sci 99: 891–907

Bédard JH (2005) Partitioning coefficients between olivine and silicate melts. Lithos 83: 394–419

Boudreau AE (1999) A version of the MELTS software program for the PC platform. Comput and Geosci 25: 21–203

Bourgeois O, Ford M, Diraison M, Le Carlier De Veslud C, Gerbault M, Pik R, Ruby N, Bonnet S (2007) Separation of rifting and lithospheric folding signatures in the NW-Alpine foreland. Int J Earth Sci 96: 1003–1031

Buddington AF, Lindsley DH (1964) Iron–titanium oxide minerals and synthetic equivalents. J Petrol 5: 310–357

Buening DK, Buseck PR (1973) Fe–Mg lattice diffusion in olivine. J Geophys Res 78: 6852–6862

Dèzes P, Schmid SM, Ziegler PA (2004) Evolution of the European Cenozoic Rift System: interaction of the Alpine and Pyrenean orogens with their foreland lithosphere. Tectonophysics 389: 1–33

Fejfar O, Kaiser TM (2005) Insect bone-modification and paleoecology of Oligocene mammal-bearing sites in the Doupov Mountains, northwestern Bohemia. Palaeon Electron 8.1.8A: 1–11, *http://palaeo-electronica.org/2005_1/fejfar8/fejfar8.pdf*

Ghiorso MS (1985) Chemical mass transfer in magmatic processes. I. Thermodynamic relations and numerical algorithms. Contrib Mineral Petrol 90: 107–120

Ghiorso MS, Sack RO (1994) Chemical mass transfer in magmatic processes. IV. A revised and internally consistent thermodynamic model for the interpolation and extrapolation of liquid–solid equilibria in magmatic systems at elevated temperatures and pressures. Contrib Mineral Petrol 119: 197–212

Hart SR, Dunn T (1993) Experimental Cpx/melt partitioning of 24 trace elements. Contrib Mineral Petrol 113: 1–8

Hollocher K, Ruiz J (1995) Major and trace element determinations on NIST glass standard reference materials 611, 612, 614 and 1834 by inductively coupled plasma-mass spectrometry. Geost Geoanal Res 19: 27–34

Holub FV, Rapprich V, Erban V, Pécskay Z, Mlčoch B (2010) Petrology and geochemistry of alkaline intrusive rocks at Doupov, Doupovské hory Mts. J Geosci 55: 251–278

Kress VC, Carmichael ISE (1988) Stoichiometry of the iron oxidation reaction in silicate melts. Amer Miner 73: 1267–1274

Kretz R (1983) Symbols for rock-forming minerals. Amer Miner 68: 277–279

Lustrino M, Wilson M (2007) The circum-Mediterranean anorogenic Cenozoic igneous province. Earth Sci Rev 81: 1–65

McSween HY, Eisenhour DD, Taylor LA, Wadhwa M, Crozaz G (1996) QUE94201 shergottite: crystallization of a Martian basaltic magma. Geochim Cosmochim Acta 60: 4563–4569

Mlčoch B, Konopásek J (2010) Pre-Late Carboniferous geology along the contact of the Saxothuringian and Teplá–Barrandian zones in the area covered by younger sediments and volcanics (western Bohemian Massif, Czech Republic). J Geosci 55: 81–94

Nimis P (2007) A clinopyroxene geobarometer for basaltic systems based on crystal-structure modeling. Contrib Mineral Petrol 121: 115–125

Rajchl M, Uličný D, Grygar R, Mach K (2009) Evolution of basin architecture in an incipient continental rift: the Cenozoic Most Basin, Eger Graben (Central Europe). Basin Res 21: 269–294

Rapprich V (2005) Compositional variation of clinopyroxenes of basaltic, essexitic and tephriphonolitic rocks from the Doupovské hory Volcanic Complex, NW Bohemia. J Czech Geol Soc 50: 119–132

Rapprich V, Holub FV (2008) Geochemical variations within the Upper Oligocene–Lower Miocene lava succession of Úhošť Hill (NE margin of Doupovské hory Mts., Czech Republic). Geol Quart 52: 253–268

Roeder PL, Emslie RF (1970) Olivine–liquid equilibrium. Contrib Mineral Petrol 29: 275–289

Schmidt NH, Olensen NO (1989) Computer-aided determination of crystal-lattice orientation from electron-channelling patterns in the SEM. Canad Mineral 28: 15–22

Skácelová Z, Rapprich V, Mlčoch B (2009) Effect of small potassium-rich dykes on regional gamma-spectrometry image of a potassium-poor volcanic complex: a case from the Doupovské hory Volcanic Complex, NW Czech Republic. J Volcanol Geotherm Res 187: 26–32

Taylor LA, Onorato PIK, Uhlmann DR (1977) Cooling rate estimations based on kinetic modeling of Fe–Mg diffusion in olivine. In: Proceedings of the 8th Lunar Science Conference, Lunar and Planetary Institute, Houston, pp 1581–1592

Tracy RJ, Robinson P (1977) Zoned titanian augite in alkali olivine basalt from Tahiti and nature of titanian substitutions in augite. Amer Miner 62: 634–645

Wiesbaur JB (1901) Theralith im Duppauer Gebirge. Lotos 21: 62–71